Universidad de Navarra

Facultades de Medicina y Ciencias

Gene therapy for Dravet Syndrome: evaluation of adenoviral vectors expressing *SCN1A* in a new mouse model

Lucía Mora Jiménez

2020

Universidad de Navarra

Facultades de Medicina y Ciencias

Gene therapy for Dravet Syndrome: evaluation of adenoviral vectors expressing *SCN1A* in a new mouse model

Memoria presentada por D./Dª Lucía Mora Jiménez para aspirar al Grado de Doctor por la Universidad de Navarra en el Programa de Doctorado de Medicina Aplicada y Biomedicina

(firma del Doctorando)

El presente trabajo ha sido realizado bajo la Dirección de los siguientes Profesores en el Departamento de Terapia Génica y Regulación de la Expresión Génica del CIMA y autorizamos su presentación ante el Tribunal que lo ha de juzgar.

Pamplona, 23 de octubre de 2020.

(firma del Director)

Dr. Rubén Hernández Alcoceba

(firma del Director)

Dra. Ana Lourdes Ricobaraza Abarquero

A Marc.

A Yago.

“We look at the world once, in childhood.

The rest is memory”

– Louise Glück

Agradecimientos

Agradecimientos

En primer lugar, quisiera agradecer al Centro de Investigación Médica Aplicada de la Universidad de Navarra por ofrecerme la oportunidad de realizar esta tesis doctoral.

También quiero referir un profundo agradecimiento a DD y a la Beca Pedro López Berastegui por apostar por la ciencia, por apostar por todos esos niños con Síndrome de Dravet, por confiar en este proyecto y por confiar en mí. Gracias a gestos y ayudas como estas poco a poco se hacen posibles muchos avances que logran un futuro mejor para todos, por eso creo que conviene recalcar la importancia de este tipo de contribuciones y el inmenso honor y gratitud con los que la he recibido.

Por supuesto, mi más sentido agradecimiento a mis directores, Ana y Rubén, por todo lo aprendido durante este tiempo, por depositar su confianza en mí, por su comprensión y por ayudarme a luchar y continuar en los momentos más duros. Sin vuestra coordinación y complementariedad este proyecto no habría sido posible. Rubén, gracias por todas las lecciones, tanto profesionales como personales, por tu infinita paciencia y por aportar calma y optimismo cuando las aguas estaban revueltas. Y a ti Ana, infinitas gracias por todo. No solo has sido mi directora, sino también mi compañera, una igual. He aprendido mucho, muchísimo de ti, además de compartir confidencias, sustos, microinfartos pero también risas y buenos momentos. Y pese a que algún que otro momento no fuese tan bueno, siempre has estado ahí, apoyándome, enseñándome y luchando al pie del cañón, dejándote la piel y el alma por este proyecto. Admiro mucho la pasión que demostráis por la ciencia y vuestra incansable e incombustible manera de trabajar, por eso esta tesis os la debo a vosotros y a vuestros esfuerzos.

Gracias también al resto del equipo, las que siguen y a las que ya no están. A la “constante” Manuela, por tus enseñanzas con los virus, por todos los buenos consejos que me has dado y los momentos compartidos hablando de buena música y aquellas maravillosas épocas que parecen tan lejanas en las que se podía ver conciertos en directo. ¡Ojalá podamos continuar con esas charlas o esos conciertos con una milnoh delante y la Alhambra de fondo! A María, no sólo por enseñarme mucho sobre el lab y los ratones, sino porque también he disfrutado enormemente con las conversaciones “culturetas”. Siempre es un placer coincidir con gente interesante que tiene algo guay que aportar y con la que además disfrutas trabajar. Gracias a Noemí por toda su dedicación al proyecto y en especial a Eva, que lo has dado todo con los ratones y has aportado mucha vidilla al lab con tus anécdotas e historias. Ha sido un placer chicas, por eso quiero agradeceros tanto y también deciros que no perdáis la esperanza, que aún puede que nos llegue nuestra carta de ingreso a Hogwarts y que volvamos a coincidir allí, esta vez trabajando con mandrágoras y dragones.

Y a Sara, mi Saru, mi hermana pequeña de lab pero que en realidad has cuidado más tú de mí que yo de ti. Gracias por ser mi máximo apoyo en todo momento, por decirme tantas veces que yo puedo y que yo lo valgo, y sobre todo por los momentos tan geniales y buenos que hemos compartido tanto dentro como fuera del lab. No era consciente de lo que te necesitaba hasta que apareciste y le diste una vuelta a mi vida aquí en Pamplona, así que gracias por aparecer. Dentro de no mucho será tu turno, así que sigue dándolo todo como hasta ahora que lo vas a conseguir y con creces. ¡Y llegado el momento, por supuesto, voy a querer las bonitas palabras que me vayas a dedicar!

Quiero agradecer también a muchas personas y grandes profesionales que han participado en este proyecto. A la Dra. Gloria González Aseguinolaza, a la Dra. Rocío Sánchez-Carpintero, a los Dres. Julio Artieda y Miguel Valencia junto a todo su equipo: Mariaje, Guille y Sandra e Ignacio aunque ya no estén. Al departamento de Farmacología de la Universidad de Navarra por la ayuda prestada tantas veces, sobre todo un especial agradecimiento a la Dra. Elena Puerta, por su incansable ímpetu y apoyo en el proyecto. Gracias a todos por tanto.

Y sobre todo, mi más eterno y profundo agradecimiento a mi madre, quién pese a todos los kilómetros de distancia que nos han separado todo este tiempo no me ha faltado nunca y ha creído en mí más que cualquier otra persona. Para mí eres el mayor ejemplo de fuerza y resiliencia que he conocido nunca, por eso quiero aprovechar para decirte el orgullo que supone que seas mi madre y mi mayor ejemplo de vida. Gracias por todo el amor incondicional, la fuerza y el apoyo que me has transmitido siempre. Y aunque no vaya a leer nunca estas palabras, también quiero agradecer profundamente a mi padre, que nunca ha dejado de acompañarme y está tan presente en esta tesis como en cualquier otro momento de mi vida. Él me enseñó el valor de la constancia, del trabajo y de la superación. Y sé que en este momento estaría orgulloso y feliz, con cada palabra escrita en esta tesis memorizada a fuego y llorando como una magdalena (aunque esto último lo negaría y trataría de ocultarlo). Por todo esto gracias de corazón, por ofrecerme lo mejor de vosotros, por hacer de mí quien soy y por haberme traído hasta este momento.

También a ti tata, a la que tanto echo de menos. Tú también me has criado y me has demostrado tantos momentos de fortaleza y superación que ojalá yo tuviera la mitad de esas virtudes. Y gracias por no cansarte nunca de decir lo orgullosa que estás de mí. Espero que tus hijos, a los cuales va dedicada esta tesis y que son dos de las personitas más importantes para mí en la vida, se parezcan a todo eso a ti y que tengan un futuro brillante y feliz.

Y por supuesto no me olvido de toda mi familia, con su eterno cariño y apoyo. También, como no, está esa otra familia que una elige, que va creciendo poco a poco, en distintos sitios y en distintas épocas, pero con la que sabes que no podrías vivir sin ella y que nunca te van a fallar.

Esa familia son mis incondicionales, las que me han sacado risas hasta en los peores momentos, las que hacen que se detenga el tiempo cuando estamos separadas y que todo vuelva a ser igual cuando nos juntamos. Las que nunca se han hartado de darme ánimos y de estar a mi lado en las buenas buenísimas y en las malas malísimas. A mi PDP, que espero ver pronto y reírme eternamente con ellas.

A Sheila, mi "partner in crime", gracias por la complicidad, las miles de risas y los momentos geniales. ¡Empieza una época en que esto va a ser a diario! A Joana, a la que ya tanto echo de menos y que me ha aportado mucho cariño, serenidad y cordura en los momentos de mi vida que más falta me hacía. A Andrea, por ser esa maravillosa excepción que rompe la regla. A la otra Andrea por la buena música y los momentos divertidos. A Dani, por tantas buenas charlas serias, absurdas y terapéuticas. A Álex, Germán, Laura, Montse, Aina…y tantos más. A los de no hace tanto pero al fin y al cabo "a los de siempre". Gracias por ser mi familia en Pamplona, por las aventuras y las locuras y por formar este "Consejo de predocs" tan increíble.

Gracias Bea por tus innumerables consejos y por ayudarme a creer en mí. A Silvia, por tu apoyo y tu aprecio infinito y en definitiva a todas las personas que de una forma u otra han formado parte de mi vida y me han ayudado a llegar hasta aquí. Sois tantos que no puedo ni nombraros. Prometo daros las gracias personalmente.

Y para finalizar, por todos esos pequeños campeones y campeonas por luchar y resistir cada día para vencer esta enfermedad. Y miles de gracias a todas las familias por su incondicional apoyo y confianza depositada. Esto va por todos vosotros. Un especial agradecimiento también a las muchas asociaciones y fundaciones que aportan todo lo necesario para hacer esto posible: la Fundación para la Investigación Médica Aplicada (FIMA), la Fundación Síndrome de Dravet, la Asociación Desafía Dravet, la Asociación Apoyo Dravet, el programa E-rare CureDravet y la Fundación Inocente-Inocente.

A todos ¡gracias, gracias y mil gracias!

Abbreviations

Abbreviations

5´UEs	5' untranslated exon
5'UTR	5' untranslated region
˚C	grades centigrade
α	alpha
β	beta
ΔCP_{target}	difference in crossing threshold points of the target gene
µg	microgram
µL	microliter
µm	micrometer

A

AAV	adeno-associated virus
AAV9	AAV serotype 9
ADP	adenovirus death protein
AdV	adenovirus
AEDs	antiepileptic drugs
AISs	axon initial segments
AP	anteroposterior
APS	ammonium persulfate
ASOs	antisense oligonucleotides
ATTC	American type culture collection

B

BBB	blood brain barrier
bp	base pairs
BG	basal ganglia
BLI	bioluminescence imaging
BS	brainstem
BSA	bovine serum albumin
BZ	benzodiazepine

C

CAG	cytomegalovirus early enhancer fused to chicken β-actin promoter/rabbit β-globin splice acceptor site
CAR	coxsackie adenovirus receptor
Cb	cerebellum
Cc	corpus callosum
cDNA	complementary DNA
CMV	cytomegalovirus

cm	centimeter
CNRs	conserved non-coding regions
CNS	central nervous system
CPE	cytopathic effect
CRISPR/Cas	clustered regulatory interspaced short palindromic repeats-associated protein 9
Ctx	cortex

D

D	domain
DAPI	4´,6-diamidino-2-phenylindole
dCas9	endonuclease-dead Cas9
dCAS9-VPR	dCas9 protein fused to a VPR transcription activation domain
DEE	developmental and epileptic encephalopathy
DEPC	diethyl pyrocarbonate
DG	dentate gyrus
dH_2O	distilled water
DI	discrimination index
DMEM	Dulbecco´s modified eagle medium
DNA	deoxyribonucleic acid
dNTPs	deoxynucleotides triphosphates
DOX	doxycycline
DS	Dravet syndrome
DSF	Dravet Syndrome Fundation
DTT	dithiothreitol
DV	dorsoventral

E

ED	effector domain
EDTA	ethylenediaminetetraacetic acid
EEG	electroencephalogram
EF1α	human elongation factor-1α
EGTA	ethylene glycol tetraacetic acid
EFMR	epilepsy limited to females with mental retardation
E_{ref}	qPCR efficiency of reference gene
E_{target}	qPCR efficiency of target gene
EtOH	ethanol

F

FBS	foetal bovine serum
FGAdV	first generation adenovirus

G

GABA	gamma-aminobutyric acid
$GABA_A$	GABA receptor type A
GCS	generalized clonic seizures
GTCS	generalized tonic-clonic seizures
$GEFS^+$	generalized epilepsy with febrile seizures plus
$GEFS^{+2}$	generalized epilepsy with febrile seizures plus type 2
GFP	green fluorescent protein
GFP-Luc	GFP-luciferase
GP/CP	*globus pallidus/caudate-putamen*
gRNAs	guide RNAs
GT	gene therapy
GTCS	generalized tonic-clonic seizures

H

h	hour/s
HAdVs	human adenoviruses
HAdV5	HAdV type 5
HC	hippocampus
HC-AdV	high-capacity adenoviral vector
HDAi	histone deacetylase inhibitor
HD-AdV	helper-dependent adenovirus
HEK293	human embryonic kidney 293 cell line
Het	heterozygous
HiS	heat-induced seizures
Ho	homozygous
HSG	heparan sulphate proteoglycans
HSV	herpes simplex virus
HT	hypothalamus
HV	helper virus
Hz	hertz

I

ICV	intracerebroventricular
IEDs	interictal epileptiform discharges
IF	immunofluorescence assay
ILAE	International Ligue Against Epilepsy
IP	invisible platform
IRES	internal ribosomal entry site
ITRs	inverted terminal repeats
IV	intravenous

K

Kb	kilobases
kDa	kilodaltons

kg	kilogram/s
KI	knock-in
KO	knock-out
Kv	voltage-gated potassium channel

L

L	liter/s
LFP	local field potentials
LGP	lateral globus pallidus
LGS	Lennox-Gastaut syndrome
Li	liver
lncRNA	long non-coding RNA
LTM	long-term memory
Luc	luciferase
LV	lentivirus
LVC	lateral ventricle

M

m	meter/s
mg	milligram/s
MHC	major histocompatibility complex
min	minute/s
mL	milliliter/s
ML	mediolateral
MLP	major late promoter
MOI	multiplicity of infection
MPLA	multiplex ligation-dependent probe amplification
MRI	magnetic resonance imaging
mRNA	messenger RNA
ms	milliseconds
MWM	Morris water maze

N

NAbs	neutralizing antibodies
NAT	natural antisense transcript
Nav	voltage-gated sodium channel
Nav1.1	voltage-gated sodium channel type 1
ng	nanogram/s
NHP	non-human primates
nm	nanometer/s
nM	nanomolar
NMD	nonsense-mediated decay
NMDA	N-methyl-D-aspartate
NOR	novel object recognition

O

OAVs	oncolytic adenoviruses
OCT	optimal cutting temperature compound
OF	open-field

P

P	postnatal day
pA	polyadenylation signal sequence
PFA	paraformaldehyde
PBS	phosphate buffer saline
$PBS^{-/-}$	PBS without calcium and magnesium
$PBS^{+/+}$	PBS with calcium and magnesium
PCDH19	protocadherin 19
PCR	polymerase chain reaction
pCtx	prefrontal cortex
ph	photons
PMSF	phenylmethylsulfonyl fluoride
Ppp1r2	protein phosphatase 1, regulatory subunit 2
ptCtx	parieto-temporo-occipital cortex
PV	parvalbumin
PVDF	polyvinylidene difluoride
PW	postnatal week

Q

qRT-PCR	quantitative reverse transcription PCR
qs	quantum sufficit

R

RLU	relative light unit
RNA	ribonucleic acid
rpm	revolutions per minute
rRS	revised Racine scale
RT	room temperature

S

s	second/s
S	segment
SCN1A	sodium channel neuronal type I alpha
SDS	sodium dodecyl-sulphate
SE	*status epilepticus*
SEM	standard error of the mean
SGAdV	second generation adenovirus
sgRNAs	single guide RNAs
SMEI	severe myoclonic epilepsy of infancy

SS	spontaneous seizures
SST	somatostatin
Str	striatum
SUDEP	sudden unexpected death in epilepsy
SV2A	synaptic vesicle protein 2A
SW	spike waves

T

TANGO	targeted-augmentation of nuclear gene output
TBS	tris buffered saline
TCS	tonic-clonic seizures
TNF-α	tumor necrosis factor alpha
TTBS	tris buffered saline with tween 20
TLR	Toll-like receptor
TSS	transcription start site

V

V	volt
vg	viral genomes
VGAT	vesicular GABA transporter
VP	visible platform

W

WB	Western blotting
WT	wild type
wo	weeks-old

Z

Zp3	*zona prellucida* 3

Index

Index

List of figures

List of tables

Abstract

Abstract

Dravet Syndrome (DS) is a severe encephalopathy with infantile onset, characterized by seizures refractory to conventional antiepileptic drugs, increased risk of sudden unexpected death in epilepsy (SUDEP), as well as cognitive, behavioral and motor comorbidities. The vast majority of DS cases are caused by heterozygous *de novo* mutations in the *SCN1A* gene, which encodes the alpha (α)-subunit of the voltage-gated sodium channel type 1 (Nav1.1). The defect of Nav1.1 channels particularly affects the function of GABAergic inhibitory neurons causing a general hyperexcitability in the brain, accounting for epileptic and neurological comorbidities.

Preclinical development of new therapeutic approaches requires animal models which represent the disease at genotypic and phenotypic levels. Here we describe that a novel knock-in mouse model carrying a clinically relevant *SCN1A* mutation (A1783V) in all body cells in the C57BL/6 background presents a full spectrum of DS manifestations. Additionally, we provide proof of concept that a High-Capacity Adenoviral vector (HC-AdV) expressing an optimized version of the *SCN1A* coding sequence under the control of the ubiquitous promoter CAG (HCA-CAG-SCN1A) is feasible and able to express functional Nav1.1 channels *in vitro* and *in vivo*. Therapeutic evaluation of this prototypic vector was performed according to the best biodistribution observed after stereotaxic injection in prefrontal cortex, basal ganglia, and cerebellum. When adolescent DS mice already suffering most disease manifestations received the HCA-CAG-SCN1A vector they were protected from SUDEP and showed improvement in hyperthermia-induced seizures, electrophysiological activity, interaction with the environment and prevention from motor impairment. Cognitive dysfunction was partially ameliorated, but hyperactive and anxious behavior persisted.

These results indicate that the transfer of the full *SCN1A* coding sequence using HC-AdV vectors is safe and potentially efficacious for the treatment of DS, offering new opportunities for improvement of therapeutic approaches.

Introduction

Introduction

1. Dravet Syndrome

Dravet syndrome (DS) is a severe epileptic encephalopathy that starts in the first year of life characterized by frequent and prolonged febrile seizures, usually clonic or hemiclonic, generalized or unilateral, and refractory to conventional antiepileptic drugs (AEDs). Following the appearance of seizures, DS patients also develop neurological comorbidities including psychomotor delay, cognitive impairment, some features of autism spectrum disorder as well as an elevated risk of sudden unexpected death in epilepsy (SUDEP)[1]. In 90% of cases, DS is caused by mutations in the *sodium channel neuronal type I alpha* (*SCN1A*) gene which encodes the α subunit of a sodium voltage-gated channel type 1 (Nav1.1), essential for the generation and propagation of action potentials[2]. The loss of function of this channel has a deep negative impact on gamma-aminobutyric acid (GABA)ergic inhibitory neurons, resulting in an excitatory/inhibitory imbalance that contributes to a brain hyperexcitability stage and the appearance of clinical manifestations[3].

The incidence of DS is estimated to be 1 in 15,700 births[4] to 1 in 40,000 births[5], slightly affecting males more frequently than females[5], and representing 1.4% of the infantile epilepsies[6]. Although it is considered a rare disease, only 20% of the estimated DS population is genetically diagnosed.

Sometimes DS is also referred as severe myoclonic epilepsy of infancy (SMEI), a term previously described by Charlotte Dravet in 1978 to differentiate it from the Lennox-Gastaut syndrome (LGS). This is another severe epileptic encephalopathy with later onset in children, usually associated to brain lesions, with a different symptomatology and electroencephalogram (EEG) characteristics. However, years after its first description it was noticed that half of the cases reported as SMEI showed some degree of variability, particularly the absence of the myoclonus and the persistence of epilepsy not only during infancy but also in adulthood. For these reasons, the condition received the eponym of DS and was included in the group of “epileptic encephalopathies” by the International Ligue Against Epilepsy (ILAE) in 2001[7].

1.1. Characteristics of DS

1.1.1. Seizure types

According to the ILAE definition, a seizure is "a transient occurrence of signs and/or symptoms due to abnormal excessive or synchronous neuronal activity in the brain"[8]. Each type of seizure depends on its origin site in the brain, its propagation along different structures, the circadian rhythm, and the maturity of the brain, among many other factors. Moreover, seizures can affect at least one of the brain functions including autonomic, sensory, and motor, as well as cognition, emotions, consciousness, memory, and behavior.

During the evolution of DS, multiple types of seizures are commonly observed, although not all of them are present in the same patient. The most common and characteristic seizures during the course of the disease are described below[9]:

» **Convulsive seizures:** the most common seizures observed throughout the disease. They could be generalized clonic seizures (GCS), generalized tonic-clonic seizures (GTCS), unilateral or hemiclonic, and sometimes "unstable", starting in one hemisphere and then asymmetrically spread through one or both hemispheres. These seizures are characterized to be clonic, affecting muscle contraction and relaxation which finally cause convulsions. They usually last a few minutes, but sometimes can be prolonged more than 15 minutes (min) and evolve into *status epilepticus* (SE).

» **SE:** is a life-threatening episode characterized by a unique and long-lasting seizure of more than 30 minutes (min) or two or more continuous seizures without consciousness recovery between them. This seizure supposes a neurological emergency that requires prompt care and rescue medication.

» **Myoclonic seizures:** not always present in all DS patients, these seizures can be massive and violent, involving all muscles in both parts of the body, particularly head and trunk. They usually last between 1 to 3 seconds (s) and could be isolated or grouped in jerks, occurring many times during the day.

» **Atypical absences:** are characterized by loss of consciousness of 3 to 10 s, sometimes also accompanied by myoclonic jerks including head nodding and rapid eyelids movements.

» **Obtundation status:** can occur as a non-convulsive SE, characterized by fluctuating alterations of consciousness associated to erratic myoclonus involving mainly fingers and orobucal muscles. Generally, they can last several hours (h) or even days.

» **Focal seizures:** they are divided in two categories: those involving motor activity, or those including prominent autonomic symptoms. Focal motor seizures, also called simple partial seizures, are clonic jerks which affect a limb or a hemiface. On the contrary, complex partial seizures are characterized by autonomic features such as pallor, cyanosis, drooling, respiratory changes, hypotonia, sweating, and/or distal myoclonic jerks. They last few min and can evolve into a unilateral or secondary motor seizure.

» **Tonic seizures:** barely observed in DS patients, they are more frequent in LGS. These seizures occur usually during sleep, increasing the muscle tone until they are stiff and tense, and sometimes they can only be detected by EEG recordings.

1.1.2. Clinical course

The clinical course of DS is age-dependent, manifesting several types of seizures and developing a wide spectrum of neurological comorbidities since the onset of the disease throughout the life of patients. This clinical evolution has been classified into three different stages with well-described symptomatic features: febrile stage, worsening stage, and stabilization stage[1].

At the **"febrile stage"**, the first seizure occurs in apparently normally developing babies during their first year of life, usually between 4 and 8 months of age, often triggered by thermal episodes like mild fever, vaccination, or a warm bath. This first seizure is usually clonic, with generalized or focal onset and refractory to AEDs. In most cases it could be prolonged more than 15 min and often evolve into SE. Throughout this first stage, the frequency of seizures is moderate with no more than one epileptic episode per month. DS is diagnosed according to the characteristic clinical presentation at onset and if unclear, genetic testing is recommended. However, in case of late diagnosis in older children and adults, symptoms may be similar to other epileptic encephalopathies and epileptic syndromes, sometimes leading to an incorrect diagnose and a wrong treatment management. Interictal EEG characteristics in DS are not specific enough to be a clue in its diagnosis, since EEG changes are age-dependent and

influenced by the frequency and severity of seizures and the different pharmacological treatments. However, in most cases some abnormalities are common throughout the evolution of the disease, providing evidence that support the clinical and genetic diagnosis. Before the first year of life, interictal EEG background activity is usually normal, only showing a diffuse or slight slowing if children are recorder shortly after a prolonged seizure. Sleeping recordings show normal organization, and few cases of frontocentral theta activity (4-5 hertz, Hz) have been reported in wakefulness during the first months, becoming common and constant in most cases from the first year through the follow-up[10,11].

From the first until the fifth year of life, the course of DS develops into the **"worsening stage"** with an increase in the frequency of generalized clonic and focal seizures and the appearance of other types of seizures like myoclonic jerks and atypical absences, although myoclonic seizures are only observed in less than half of the cases. Additionally, the incidence of SE and obtundation status becomes higher, and some patients may also present acute encephalopathy, a catastrophic outcome of the disease characterized by non-inflammatory edema, followed by severe febrile SE and subsequent deep coma. During this period, hyperthermia remains the main triggering factor for seizures although many other stimuli such as physical exercise, emotions, noisy environment, and photosensitivity have been identified. Along the second year of age, when seizure frequency is highest than other stages, general development delay becomes evident and worsens throughout years, resulting in a high prevalence of neurodevelopmental disorders among DS patients[12]. However, it should be noted that there is not a clear loss of abilities but a slower cognitive and motor progression. Walking ability starts at normal age but 60% of cases develop ataxia and unsteady gait, increasing along the years and leading to a peculiar way of walking. Uncoordinated movements and facial muscle hypotonia are also noticed, which can make not only chewing and swallowing difficult, but also can cause a slower progression of language. Lack of attention, hyperkinesia and some features of autistic behavior spectrum are also main factors responsible for this characteristic learning delay. Regarding EEG activity, between the second and the fifth year of life, background activity becomes slower and poorly organized[13]. Moreover, during this period a progressive increase of paroxysmal abnormalities induced by eye closure begins, characterized by focal or generalized spike waves (SW) of 2-3 Hz, isolated or in brief bursts, predominantly present in the frontocentral regions. No correlation has been found between the location of these paroxysms and the origin of seizures, maybe because these SW are an echo of the diffuse discharges along the brain[10]. Photosensitivity is also

reported in almost half of cases, and EGG sleep pattern is usually normal unless several seizures appear during the night.

Finally, from the middle of childhood into adolescence the **"stabilization stage"** begins with a general improvement of seizures. Myoclonic and atypical absence seizures tend to disappear, and febrile clonic seizures become less frequent and shorter, appearing mainly during sleep, although fever sensitivity persists through the life of patients. In the majority of cases SE is also considerably less frequent. Cognitive abilities can slowly improve but some neurological and motor impairments persist, making patients totally dependent on familiars or caregivers to carry out daily activities. Along this period to adulthood, slowness of movements and crouching gait replaces previous hyperkinesia, with several orthopedic signs such as kyphosis and kyphoscoliosis. Moreover, adult patients present moderate to severe intellectual disability and some characteristics of autism disorder, as well as a prominent language impairment. During this phase of the disease, EEG background activity becomes normal in most of the cases, although the theta activity persists and even increases in the central regions and the vertex, particularly in patients with intense motor deterioration. Paroxysmal abnormalities decrease and often are only observed during sleep, and photosensitivity usually disappears, remaining a mild light sensitivity in the most resistant types of DS cases[14].

1.1.3. Neuroimaging

The study of the brain structure by magnetic resonance imaging (MRI) is essential for diagnosis and evaluation of patients with seizures disorders. Nevertheless, the majority of studies performed in DS patients show unspecific changes or normality. After a normal MRI at onset, several cases have been reported to develop hippocampal sclerosis during the course of the disease[15,16]. Furthermore, malformations of cortical development such as temporal lobe dysplasia, periventricular nodular heterotopia, and focal cortical dysplasia have been also observed in patients with *SCN1A* mutations[17]. All these findings suggest that alterations in the brain structure might be the result of seizure damage.

1.1.4. Mortality

DS is associated with a significant mortality rate of 10-18% in industrialized countries[18], which is markedly higher than other types of infant epilepsies. Deaths may occur at any age associated to three main causes: (1) SUDEP in approximately 53% of death causes, with one first peak at 1-3 years of age and a second one at 18 years and older; (2) acute encephalopathy

with SE in 36% of patients, with a higher prevalence between 3 and 8 years; and (3) 10% due accidental deaths like drowning[19]. In order to obtain a decrease of this early deaths, some measures like improved diagnosis and good management of seizures and SE are imperative, as well as the use of anti-suffocation pillows to avoid drowning during sleep.

Nevertheless, from all these causes of mortality, SUDEP remains the most difficult to control and prevent due to its unexpected nature without any apparent cause of injury and drowning, and because its mechanisms are not fully defined. One of the strongest hypothesis for SUDEP mechanism is cardiac dysfunctions since many ion channels are expressed both in the brain and heart. This could lead to cardiac arrythmias during seizures. This case of dual expression has been observed in Nav1.1, the sodium channel which is altered and reduced in the vast majority of DS patients[20]. One study performed in several mouse models of DS with premature death revealed that most of these SUDEP occurred immediately following generalized tonic-clonic or focal seizures, showing restrained interictal resting heart-rate variability and episodes of ictal bradycardia[21]. These results are in accordance with those observed in DS patients, where they presented an abnormal lower regulation of heart rate by the autonomic nervous system[22,23] as well as an increase P wave and QT dispersion[24]. These findings suggest that SUDEP could be the result of bradycardia and electrical dysfunction of the ventricle caused by apparent hyperactivity of the parasympathetic input. Another potential mechanism for SUDEP is respiratory dysfunctions[25], since most patients who suffer SUDEP present ictal hypoxemia and hypercapnia[26]. Finally, SUDEP could be related to a cerebral shutdown after GTCS leading to impairments in arousal activity[19]. Therefore, SUDEP could be considered a consequence of cardiorespiratory and consciousness dysfunction, maybe because seizures can spread to the brainstem (BS) where the modulatory systems of autonomic cardioregulatory reflexes, breathing pathways and regulation of arousal are located[27].

Unfortunately, all these SUDEP mechanisms in humans are already poorly understood and need further research for better management and prevention, although it could be difficult without simultaneous EEG recording. Only few cases of monitored SUDEP have been reported, presenting postictal generalized EEG suppression[28], which could be considered as a possible biomarker for SUDEP.

1.2. Etiology of DS

It was in 2001 when the genetic etiology of DS was firstly discovered in a group of patients diagnosed with SMEI. All these patients presented different heterozygous mutations in the *SCN1A* gene which encodes the α subunit of Nav1.1. However, these *SCN1A* mutations were absent in their parents, providing evidence that genetic basis of the disease is due to *de novo* mutations in *SCN1A*[29]. Nowadays it is well known that in nearly 90% of DS patients the genetic basis of the disease is the haploinsufficiency of *SCN1A,* leading to the impairment of the sodium channel function. This is the reason why this syndrome should be considered as a channelopathy.

Two families with generalized epilepsy with febrile seizures plus type 2 ($GEFS^+2$) presented two different *SCN1A* mutations. Nevertheless, contrary to *de novo* DS cases, this study showed an autosomal dominant inheritance of *SCN1A* in this disease[30,31]. In addition, diverse *SCN1A* mutations are also related with other neurological disorders including familial autism[32], familial hemiplegic migraine[33], and aging-related cognitive decline and dementias[34]. All *SCN1A* variants identified in these familial encephalopathies are missense mutations that probably alter but do not abolish Nav1.1 activity. Additionally, some *SCN1A* mutations causing $GEFS^+$, as is the case of R1648H and W1204R, are considered as gain of function mutations given that they induce a dramatically accelerated recovery from inactivation and shifted the voltage-dependence of activation and inactivation in the negative direction[30]. For these reasons, generalized epilepsy with febrile seizures plus $GEFS^+$ patients present a milder epileptic phenotype compared with DS patients.

1.2.1. Nav1.1 channel: structure and function

As already mentioned, the sodium channel affected in DS is Nav1.1, which consists of a protein complex located in the cellular membrane, formed by an α subunit of 260 kDa linked to auxiliary beta (β) subunits of 36 kDa. The transmembrane α subunit constitutes the ion-conducting pore of the channel, essential for sodium ions flow through cell membrane which leads to the propagation of action potentials. The channel is formed by four homologous domains (DI-DIV). Each one consists of six α-helical transmembrane segments (S1-S6) with the amino and carboxy-terminus facing the cytoplasm. Within this six α-helical structure, the voltage sensor is located in the positively charged amino acids of S4, and a hairpin-like P-loop between segments S5 and S6 delineates the pore of the channel[35]. The inactivation gate is located in the intracellular loop that connects DIII and DIV (Figure 1).

Noncovalently linked to this large α subunit there are two smaller auxiliary β subunits (encoded by *SCN1B* and *SCN2B* genes) which regulate the function of the channel in terms of kinetics and cellular localization. These β subunits consists of a transmembrane protein with intracellular carboxy-terminus, and an extracellular amino-terminus forming an IgG-like loop which interacts with other cell adhesion molecules. These β subunits are multifunctional proteins that modulate the function of the α subunit by enhancing ion flow through the pore, promoting the trafficking of the α subunits from the intracellular pool to the neuronal membrane, and acting as a cell adhesion molecule to improve neurite projection[36].

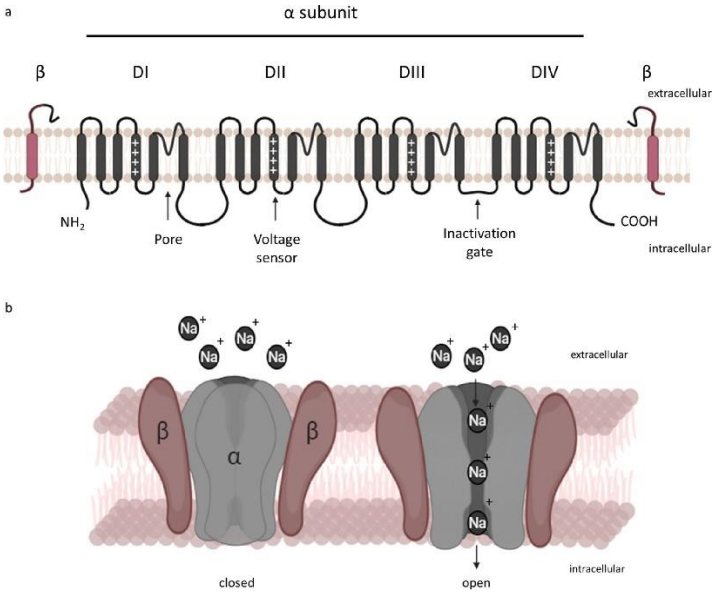

Figure 1. Schematic representation of Nav1.1 voltage-gated sodium channel. (**a**) The α subunit of the channel consists of four domains (DI-DIV), each one formed by six transmembrane segments (S1-S6). (**b**) Folded conformation of the channel. The pore-forming subunit α leads the flux of sodium ions from the extracellular to the intracellular space, whereas the accessory β subunits modulate the subcellular location, the voltage dependence and kinetics of the channel. Figure created with BioRender.com.

Functionally, Nav1.1 channels participate in the maintenance of action potential throughout neuronal membranes. The voltage sensor in the S4 region detects cytosolic potential changes, leading to conformational rearrangements to open the ion-pore for an inward flow of sodium ions when depolarization occurs. Once the action potential reaches the maximum peak, the inactivation gate closes the channel pore within milliseconds, leading to the resting membrane potential state.

Therefore, any alteration of the pore channel that modifies the kinetics of ions flux, either by gain or loss of function of the channel, can affect neuronal excitability and leads to the appearance of seizures.

1.2.2. Nav1.1 distribution and physiopathology

Concerning the brain mapping of Nav1.1 distribution, the expression is higher in the caudal brain, spinal cord[37] and sinoatrial node[20]. From all brain structures, the hippocampus (HC) is specially rich in Nav1.1 with specifically high expression in the soma of dentate granule cells and in GABAergic interneurons of dentate hilus, as well as pyramidal cell somata and proximal dendrites of CA1, CA2, and CA3[38]. Moreover, Nav1.1 was not only localized in soma and dendrites of neurons, but also in axon initial segments (AISs) and axons of parvalbumin (PV) and somatostatin (SST) expressing interneurons which project to the soma and proximal dendrites of excitatory neurons[39,40]. Interestingly, according to the DS mouse model generated by Yu and colleagues, less than 10% of the total sodium channels of pyramidal cells from HC are Nav1.1 channels, whereas the expression of Nav1.2 and Nav1.6 is predominant. The opposite situation is found in GABAergic interneurons, where at least 75% of the sodium current is conducted by Nav1.1[41]. Therefore, Nav1.1 plays an important role in modulating GABAergic inhibition, especially in the dentate gyrus (DG) where the excitatory inputs from the entorhinal and neocortex are filtered[42]. Nav1.1 loss of function in GABAergic interneurons and granule cells in DG greatly impairs the inhibitory activity, reducing the phasic release of GABA, which finally leads to an imbalance between excitation and inhibition in the brain and consequently to the appearance of seizures. Moreover, it has been demonstrated that selective deletion of Nav1.1 in HC, including GABAergic, pyramidal neurons, and glia, not only evoked seizures, but also cognitive deficits as spatial learning deficits[43].

In addition to HC, other brain regions such as striatum (Str) and pyramidal cells in layer V of the cerebral cortex (Ctx) are also rich in Nav1.1 expression and are likely to play a role in seizures and other neurological comorbidities[44]. The same occurs in axons of granule cells and Purkinje cells in the cerebellum (Cb) where, as expected, decreased peak of sodium currents in Purkinje neurons due to Nav1.1 dysfunction causes ataxia and related motor deficits[45]. This channel is highly expressed also in thalamus and cortical inhibitory neurons, two brain areas associated to the initiation and maintenance of seizures[46]. Impairment of Nav1.1 function in suprachiasmatic nucleus of the hypothalamus (HT) had also a negative impact on homeostatic regulation of sleep[47,48], whereas the inhibition/excitation imbalance in Ctx is associated to autism spectrum disorders and cognitive deficits[49,50].

All these findings suggest that loss of function of Nav1.1 in different neuron types, but particularly in GABAergic neurons and Purkinje cells, is the basis not only of seizures, but also the multiple comorbidities observed in DS patients and several animal models.

1.2.3.*SCN1A* gene

SNC1A gene belongs to a family of genes (from *SCN1A* to *SCN11A*) which encodes the functional voltage-gated sodium channel α subunits expressed in different structures of the central and peripheral nervous system as well as muscle and cardiac tissues. Four isoforms are the main sodium channels expressed within central nervous system (CNS): Nav1.1, Nav1.2, Nav1.3 and Nav1.6, encoded by the *SCN1A*, *SCN2A*, *SCN3A*, and *SCN8A* genes, respectively[30]. In mammalian brain, the location and developmental patterns of Nav channels vary depending on the isoform. For instance, in rodents and humans Nav1.3 is highly expressed during embryonic development and declines after birth, just when Nav1.1 and Nav1.2 becomes detectable[37,51]. Conversely, Nav1.7, Nav1.8 and Nav1.9 isoforms are expressed in peripheral nervous system, with lesser importance in the context of epilepsy, and the remaining Nav1.4 and Nav1.5 isoforms are expressed in adult skeletal muscle and embryonic skeletal and heart muscle, respectively[30].

Concerning its structure, *SCN1A* is an 81 kilobase (kb)-spanning gene organized into 26 exons and located in the long arm of chromosome 2 at position 2q24.3[52] (Figure 2a). Unfortunately, the promoter region of this gene is not completely defined, primarily due to its complex 5'-untranslated region (5'UTR). Several spliced untranslated exons (5´UEs) are currently known to be part of the *SCN1A* 5'UTR. Most of them are located in the conserved non-coding regions (CNRs) which are shared by numerous orthologous among several species including mouse, rat, and dog[53]. Within these 5´UEs there are at least five frequently used exons (h1a/h1u, h1b, h1d, h1c/h2u, and h3c), each one carrying multiple transcription factor binding sites and transcription start sites (TSS), distributed over a 75 kb region upstream the *SCN1A* exon 1[54]. Both *SCN1A* human and mouse sequences contain two major 5´exons known as distal exon A and proximal exon B located 75 kb and 54 kb upstream of the coding exon 1, respectively[55] (Figure 2b).

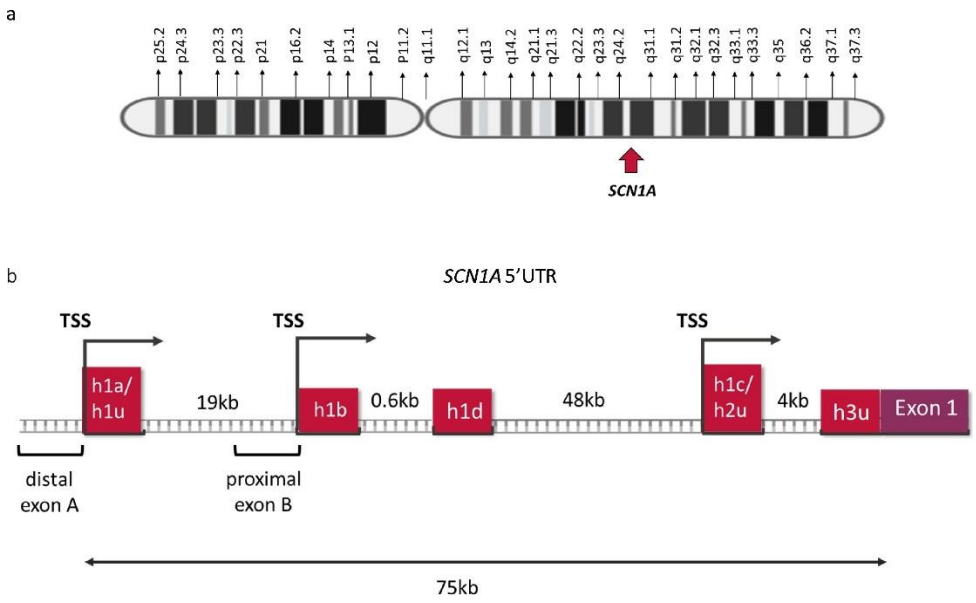

Figure 2. *SCN1A* gene. (**a**) **Cytogenetic location of *SCN1A* gene in chromosome 2q24.3.** (**b**) **Schematic representation of the *SCN1A* 5´UTR promoter region.** The frequently used 5´UEs are represented in pink boxes and TSS are indicated with and arrow. The numbers above the double strand indicate the genomic distance between 5´UE. Figure based on previous publication[54].

1.2.4.*SCN1A* mutations

More than 1,250 different *SCN1A* mutations have been described so far, randomly distributed along the gene, most of them only affecting one to six base pairs (bp) (92%). Approximately half of *de novo SCN1A* mutations are missense and the other half produce truncated Nav1.1 channels. Among them, 19% of cases are due to frameshift mutations, either by deletion or insertion of nucleotides; 17% are produced by premature introduction of one stop codon (nonsense mutations); and barely 9% of cases are due to splicing alterations[52]. More recently, some mutations have been identified in the promoter region[54], increasing the percentage of DS cases due to mutations in the *SCN1A* gene.

It has been described that the nature of *SCN1A* mutations determines the phenotypic variability observed in DS patients and other epilepsies. On one hand, missense mutations seem to be the main cause of GEFS$^+$, whereas deletions, truncations, nonsense, and frameshift mutations are related with classical and severe DS phenotypes[56], although some missense mutations are also responsible for severe DS cases[52,57]. On the other hand, several authors also correlate the grade of severity of the disease with the location of the mutation along the gene. For instance, some studies determined that those mutations affecting the pore-forming region of the channel could be related with DS, and those located outside the pore-forming region are usually associated with the GEFS$^+$ spectrum[58]. Furthermore, the same *SCN1A* mutations have

been observed in both DS and GEFS$^+$ patients, suggesting that the phenotype not only depends on the type of mutation, but also it may be influenced by the genetic background and environmental factors.

The origin of these *de novo* mutations has been demonstrated to be most frequently derived from the paternal chromosome due to the great number of mitoses occurring during spermatogenesis and the acquired mutation susceptibility of methylated deoxyribonucleic acid (DNA) of sperm cells compared with eggs at oogenesis[59].

Familial mutations are observed in a smaller proportion of DS patients (less than 10% of cases) and usually are the result of somatic or gonadal mosaicism from paternal or maternal origin[56,60,61]. Most of these cases are detected because the same missense mutation is present in siblings and the phenotype is milder as compared with full heterozygous mutation, although it could be more severe in the offspring.

Chromosomal rearrangements affecting *SCN1A* and/or contiguous genes are other *de novo* alterations observed in 12.5% of DS patients, usually those who tested negative for *SCN1A* sequence-based mutations[62]. Microdeletions and more unfrequently duplications and amplifications could be identified with multiplex ligation-dependent probe amplification (MPLA) and sometimes could be detected not only in *SCN1A* gene but also in a variable number of contiguous genes clustered in chromosome 2q such as *SCN2A*, *SCN3A*, *SCN7A*, and *SCN9A*[63,64]. These combinations of deletions are associated with a wide spectrum of severity depending on the genes involved. For instance, deletions in *SCN1A* combined with deletions in *SCN2A* or *SCN3A* are related with more severe phenotype whereas combination of *SCN1A* and *SCN9A* deletions are related with milder phenotype.

1.2.5. Other genes related with DS

It is well stablished that pathogenic variants of *SCN1A* gene are the main cause of DS, however in nearly 20% of cases additional genes are implicated or even their genetic etiology still remains unknown. All these cases are found in patients with no detectable mutations in *SCN1A* gene but with phenotypic spectrum identical or similar to classical DS, although there are also significant differences (represented in Figure 3). For this reason, it is important to pay attention to clinical manifestations and the inheritance pattern before accepting any genetic variant as the main cause of DS[65].

On one side, some pathogenic variants of the family of Navs apart from Nav1.1 are associated with DS and other epilepsy syndromes. Mutations in *SCN2A*, encoding for the α2 subunit of Nav1.2 with high expression in HC and Cb, are found both isolated or combined with *SCN1A* variants in few cases of DS as well as other epilepsie syndromes[66]. The same occurs with variants of *SCN9A*, the gene which encodes de Nav1.7 expressed in nociceptive neurons of dorsal root ganglia, neuroendocrine cells, and some types of muscles which in some rare cases have been discovered acting as genetic modifier in DS patients and families affected with inherited febrile seizures[67]. Moreover, it was believed that variations in *SCN8A,* the gene that encodes the Nav1.6 channel which is widely expressed throughout the CNS, especially in excitatory pyramidal neurons and cerebellar Purkinje cells, were also related with DS cases, although this association was finally refused by substantial differences in phenotypes[65]. Finally, few cases of homozygous pathogenic variants of β1 subunit (encoded by the *SCN1B* gene) causing DS-like phenotype have been reported[68,69].

There is also evidence that variations in *CACNA1A*, coding for the α-subunit of the calcium channel Cav2.1, can exacerbate the DS phenotype with an earlier onset and higher incidence and frequency of absence seizures when are combined with mutations in *SCN1A* in comparison with *SCN1A* mutations alone[70].

Beyond ion channels, there are other mutated genes also related with DS-like phenotypes. This is the case of protocadherin 19 (*PCDH19*), a calcium-dependent cell-adhesion molecule which is thought to play a role in neuronal connections and transduction of signals throughout the synaptic membrane in developing brains. Since this gene is located in chromosome Xq22.1, *PCDH19* variants are associated with epilepsy limited to females with mental retardation (EFMR) with an unusual X-linked inheritance pattern in which the disorder is only observed in heterozygous females. Several studies reported familial and *de novo* pathogenic *PCDH19* variants as cause of DS–like phenotype in patients with negative mutations and rearrangements for *SCN1A*, even with one mosaicism case in one male patient[71,72].

Additionally, few genes related to GABA receptors have also been associated with DS etiology. GABA is the main inhibitory neurotransmitter of the CNS, therefore a disruption on its inhibitory synaptic potential leads to a hyperexcited neuronal activity and the appearance of seizures. Variations in two genes coding for the GABA receptor type A ($GABA_A$) subunits have been detected in several studies of generalized epilepsies and epileptic encephalopathies, some of them sharing same clinical pattern with DS. Firstly, *GABRA1*, which encodes the α1 subunit of the $GABA_A$ receptor, being also implicated in juvenile myoclonic epilepsy and other

epileptic encephalopathies such as Ohtahara and West syndromes. *De novo* pathogenic variants *of GABRA1* gene were found in three diagnosed cases of DS[73]. *De novo* mutations in *GABRG2*, the gene for the $GABA_A$ γ2 subunit, were described in patients with epileptic encephalopathies, few of them resembling the phenotypic characteristics of DS[74], as well as mutations in *GABRB3* gene, coding for the β3 subunit of the $GABA_A$ receptor[75].

Finally, several genes coding for completely different proteins are also associated to DS etiology, although the phenotypes observed in these patients usually differ from classical DS. Within these genes we can found: *STXBP1*, coding for syntaxin-binding protein 1 which regulates the release of neurotransmitters[76]; *HCN1*, which encodes a protein that contributes to cationic currents in neurons (the potassium/sodium hyperpolarization-activated cycled nucleotide-gated channel 1)[77]; *CHD2*, coding for chromodomain helicase DNA-binding protein 2, a protein able to regulate gene expression through chromatin remodeling[78]; and *KCNA2*, a gene which encodes the potassium voltage-gated channel subfamily A member 2 with an important role in neuronal repolarization after action potential[79].

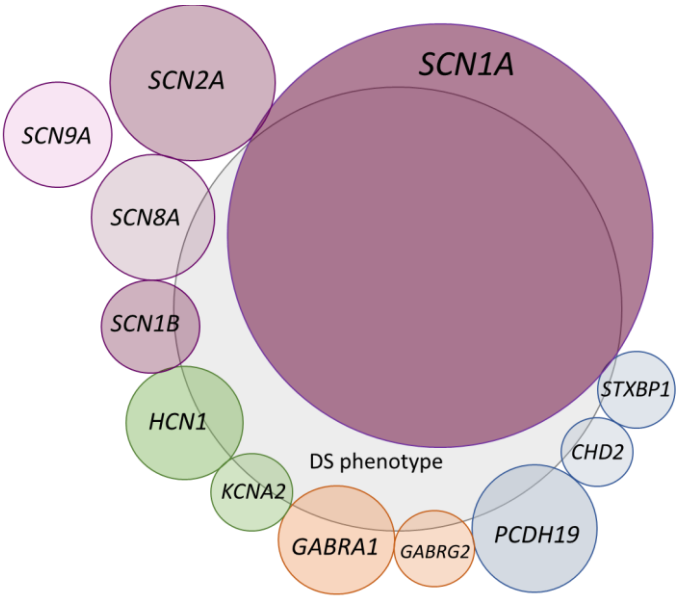

Figure 3. Other genes associated to DS phenotype. Sodium channels (purple), potassium channel (green), chloride channels (red), genes not related with ion channels (blue). Figure adapted from Steel *et al.*[65].

1.3. Animal models of DS

The availability of animal models of DS, with different mutations in the *SCN1A* gene and phenotypic symptoms resembling those observed in patients, provides a good opportunity to gain a deeper insight into the pathophysiology of the disease, as well as their use as an exceptional tool for the development of new and more effective treatments. These two purposes (basic and preclinical research) may dictate the design of specific DS models.

Several transgenic animal models have been developed for the study of DS, from zebrafish (*Danio renio*) to flies (*Drosophila*) although, the most widely used is the murine model.

The first DS mouse model was constructed by Yu and colleagues[41] by a targeted disruption of the last coding exon of *Scn1a* gene in the mouse, generating heterozygous and homozygous knock-out (KO) mice. Decreased firing in GABAergic interneurons, spontaneous seizures (SS), higher sensitivity to suffer heat-induced seizures (HiS), and elevated mortality rate were present in both genotypes, although the onset of these phenotypic manifestations was earlier in homozygotes than in heterozygotes[41,80]. Additionally, homozygous mice exhibited a severe ataxia due to Nav1.1 ablation in Purkinje cells in Cb[45] and also a compensatory increase in Nav1.3 expression[41]. This DS mouse model was also relevant for some neuronal findings that helped to better understand the mechanisms of the disease, such as the reduced action potential number, frequency, and amplitude in GABAergic inhibitory interneurons due to the reduction in Nav1.1 expression. Afterwards, this same mouse model was also studied to determine the importance of genetic background for phenotypic severity[60], revealing that the degree of penetrance of the *Scn1a* mutation seemed to be less severe in 129X1/SvJ than in C57BL/6J background (Table 1).

During the following years, other KO mouse lines were developed with conditional deletion of exon 1 of *Scn1a* gene[81–84] or using, for example, the Cre-*loxP* method in conjunction with the *Dlx1/2* enhancer in a floxed *Scn1a* mouse line to generate a conditional deletion of Nav1.1 in GABAergic neurons, demonstrating that the selective loss of this sodium channel in inhibitory GABAergic interneurons in Ctx and HC is enough to cause SS and premature death[85] (Table 1).

Otherwise, several knock-in (KI) transgenic mouse lines were also created inserting different *Scn1a* mutations in one or both alleles. The first KI mouse model of DS carried the truncated mutation R1407X in exon 21 of the *Scn1a* gene, a premature stop codon found in three human patients[39]. Similar to other DS mouse models, both homozygous and heterozygous mice showed spontaneous GTCS and polyspike-waves with different ages of onset. This model was remarkably relevant for its neurological findings, since it was observed

that Nav1.1 is primarily localized in axons and somata of PV interneurons in the developing neocortex and HC and is implicated in the maintenance but not in the initiation of high-frequency firing.

Later on, more models with different *Scn1a* mutations were created and characterized, exhibiting similar phenotypic characteristics as other DS models (Table 1) as well as providing new insights about Nav1.1 expression and function.

As expected, all homozygous mice generated by the different groups present a severe seizure phenotype and motor symptoms such as ataxia, limb tremors and unstable gait, which start earlier than their heterozygous littermates. But the most remarkable insight is that all homozygous pups die at postnatal day 15 (P15) despite de upregulation of Nav1.3 observed in some models. This data supports that Nav1.1 plays a critical role in CNS physiology and neurotransmission, and its total absence is not compatible with survival, probably resembling the situation in humans. For this reason, only heterozygous *Scn1a* models are really relevant for the study of the disease and the evaluation of novel therapeutic approaches.

There is no doubt that all these genetic mouse models carrying a wide range of *Scn1a* mutations are a useful tool to clarify the physiopathology of DS, however, most of them are based on non-common *SCN1A* mutations[86] or are expressed only in a specific neuron cell population[81,85,87–89]. The primary role of GABAergic interneurons for the epileptic phenotype is indisputable, especially taking into account the total absence of seizures and neurologic signs when *Scn1a* is conditionally deleted only in excitatory neurons[88]. Moreover, it has been demonstrated that the implication of Nav1.1 reduction is not the same for the different GABAergic interneurons, since it has been shown that Nav1.1 deletion in PV expressing inhibitory neurons causes a stronger epileptic and neuropsychiatric phenotype than Nav1.1 deletion in SST inhibitory interneurons[89].

Table 1. Genotypic, phenotypic, and neurologic characteristics of heterozygous transgenic mouse models of DS. Each mouse model was developed carrying a particular *Scn1a* variation, constitutively expressed or affecting specific cell populations in different genetic backgrounds. GFP, green fluorescent protein; Het, heterozygous; Ho, homozygous; IEDs, interictal epileptiform discharges; LTM, long-term memory; P, postnatal day; *Ppp1r2,* protein phosphatase 1, regulatory subunit 2; PW, postnatal week; TCS, tonic-clonic seizures, ZP3, *zona pellucida* 3.

***Scn1a* alteration**	**Final cross-breeding**	**Affected cell population**	**Phenotypic characteristics**
Substitution of region comprising exon 26 by a neomycin cassette (deletion of DIV from the S3 to the C-terminal tail). ***Scn1a*^{tm1Wac}** (Targeted deletion)	*Scn1a*^{tm1Wac} (C57BL/6) (Het) x C57BL/6	All body cells	▪ 80% of mortality by PW13[41,60]. ▪ Frequent SS[41,60]. ▪ Highly susceptible to HiS[60,80]. ▪ IEDs events[80]. ▪ Impaired circadian activity[47]. ▪ Deficits in spatial memory[60]. ▪ Social interaction deficits[60].
	Scn1a^{tm1Wac} (129/SvJ) (Het) x 129SvJ	All body cells	▪ 10% of mortality by PW15[41,60]. ▪ No SS[41,60]. ▪ Susceptible to HiS[60]. ▪ No impaired context-dependent fear memory[60]. ▪ No social interaction deficits[60].
	Scn1a^{tm1Wac} (C57BL/6) (Het) x *Scn1a*^{tm1Wac}-129SvJ (Het)	All body cells	▪ 60% of mortality by PW15[41]. ▪ Frequent SS and IEDs[41]. ▪ Significant ataxia at P21[45].
Replacement of exon 1 by a *loxP*-flanked neomycin cassette	*Scn1a*^{tm1Kea} (129S6/SvEvTac) (Het) x 129S6/SvEvTac	All body cells	▪ 16% of mortality by PW14[82,84]. ▪ No SS by video-EEG monitoring[82,84]. ▪ No overt epileptic phenotype[84].
***Scn1a*^{tm1Kea}** (Targeted deletion)	*Scn1a*^{tm1Kea} (129S6/SvEvTac) (Het) x C57BL/6:129S6/SvEvTac	All body cells	▪ More than 50% of mortality by PW5[82–84]. ▪ SS starting at P18[83,84]. ▪ 50% of TCS by video-EEG monitoring[82]. ▪ Anxiety and hyperactive behavior[83]. ▪ Impaired learning and memory[83].
Insertion of *loxP* sites flanking exon 25	*Scn1a* $^{tm2.1Wac}$ (C57BL/6) (Het) x Tg(I12b-cre)1Jlr (CD-1) (also referred as Dlx-I12-Cre, drives Cre expression under the control of the I12b enhancer element of Dlx1/Dlx2)	GABAergic interneurons in forebrain	▪ 70% mortality at P90[85]. ▪ 33.3% present severe SS[85]. ▪ Susceptible to HiS[85]. ▪ Presence of IEDs preceding seizures[85]. ▪ Exhibited hyperactivity, anxiety, and stereotyped behavior[49]. ▪ Severe impaired spatial learning and memory[49]. ▪ Profound deficits in social interaction[49].
***Scn1a*$^{tm2.1Wac}$** (Conditional deletion)	*Scn1a*$^{tm2.1Wac}$ (C57BL/6) (Ho) injected in both the dorsal medial and lateral HC with the AVV-Cre-GFP vector for scission of exon 25.	Hippocampal neurons	▪ Susceptible to HiS[90]. ▪ Spatial learning deficit and memory[90].

Scn1a alteration	Final cross-breeding	Affected cell population	Phenotypic characteristics
Insertion of *loxP* sites flanking exon 1 ***Scn1a*$^{Flox/+}$** (Conditional deletion)	*Scn1a*$^{Flox/+}$ (C57BL/6J) x C57BL6-Tg(Zp3-cre)93knw/J (Cre controlled by the mouse *zona pellucida* 3 (*Zp3*) promoter)	All body cells	▪ Reduced life span until P33[81]. ▪ 52.3% present SS[81].
	Scn1a$^{Flox/+}$ (C57BL/6J) x C57BL/6N-Tg(Ppp1r2-cre)4127nkza/J (Cre- controlled by the *protein phosphatase 1, regulatory subunit 2 (Ppp1r2)* promoter)	PV+ inhibitory neurons in the forebrain	▪ Normal life span[81]. ▪ Infrequent episodes of SS[81]. ▪ Susceptibility to HiS[81].
Insertion of *loxP* sites flanking exon 7 ***Scn1a*$^{tm2.1Kzy}$** (Conditional deletion)	*Scn1a*$^{tm2.1Kzy}$ (C57BL6/J) (Ho) x *VGAT*-Cre (C57BL/6) [Cre controlled by the v*esicular GABA transporter* (*Vgat*) promoter]	Global inhibitory neurons	▪ 98.5% of mortality before P35[88]. ▪ Spontaneous GCS by P16[88].
	Scn1a$^{tm2.1Kzy}$ (C57BL6/J) (Ho) x *VGAT*-Cre (C57BL/6) + *Emx-1-Cre* (C57BL/6) [Cre controlled by the *Vgat a*nd *Emx-1* promoters]	Pyramidal and inhibitory neurons	▪ 39.5% of mortality before P35[88]. ▪ SS at PW3[88].
	Scn1a$^{tm2.1Kzy}$ (Ho) x *PV*-Cre-TG (C57BL/6J) [Cre controlled by *PV*promoter]	PV+ inhibitory neurons	▪ 10% of mortality at P90[88]. ▪ SS after P16[88]. ▪ Impaired spatial memory[89]. ▪ Hyperactive behavior[89]. ▪ Impaired social novelty preference[89].
	Scn1a$^{tm2.1Kzy}$ (Ho) x *SST*-Cre-KI (C57BL/6J) [Cre controlled by *SST* promoter]	SST+ expressing neurons	▪ Normal lifespan[89]. ▪ No noticeable behavioral seizures[89]. ▪ Susceptibility to HiS[89].

Scn1a alteration	Final cross-breeding	Affected cell population	Phenotypic characteristics
Exon 21 containing the **R1407X** mutation resulting in a stop codon ***Scn1a*$^{tm1.1Kzy}$** (KI, truncation)	*Scn1a*$^{tm1.1Kzy}$(C57BL/6J) (Het) x B6129SF1/J	All body cells	▪ ~25-40% mortality within the first and third months of age[39]. ▪ SS at P18[39]. ▪ Poor spatial learning and memory impairment[91]. ▪ Hyperactivity, anxiety-like behavior[91]. ▪ Impaired sociability[91].
Exon 26 containing the **R1648H** mutation* *Clinically associated with a wide variety of phenotypes ranging from GEFS^{+} to DS ***Scn1a*$^{tm1.1Aesc}$** (KI)	*Scn1a*$^{tm1.1Aesc}$ (C57BL6/J) (Het) x C56BL/6J	All body cells	▪ Normal life span[86]. ▪ Infrequent SS[86]. ▪ Reduced threshold to flurothyl-induced seizures[86]. ▪ Altered sleep regulation[48]. ▪ Induction of repeated seizures transform the milder phenotype into a severe DS-like phenotype: frequent SS, hyperactivity, repetitive movements, social interaction problems and impairment of hippocampal-dependent spatial memory and LTM[92].
Exon 17 containing the **E1099X** mutation resulting in a premature stop codon ***Scn1a*$^{tm1.1Swl}$** (KI, truncation)	*Scn1a*$^{tm1.1Swl}$ (129S2/SvPasCrl) (Het) x C57BL/6JNarl	All body cells	▪ 46.2% of mortality at PW4[93]. ▪ 44.8% of SS at P20-25[93]. ▪ Susceptible to HiS[93].
Exon 26 flanked by *loxP* sites, followed by exon 26 containing the missense **A1783V** mutation ***Scn1a*$^{tm1.1Dsf}$** (Conditional KI)	*Scn1a*$^{tm1.1Dsf}$(C57BL/6J) (Het) x Slc32a1$^{tm2(cre)Lowl}$/J (C57BL/6J) (Cre controlled by the *Vgat* promoter)	VGAT-expressing Inhibitory neurons	▪ 100% mortality by P23[87]. ▪ SS at PW2[87]. ▪ Large amplitude polyspike activity[87]. ▪ Respiratory dysfunction: hypoventilation, apneas and diminished ventilatory response[87].
	Scn1a$^{tm1.1Dsf}$ (C57BL/6J) x B6.CTg(CMV-Cre)1Cgn/J (C57BL/6J) (Cre controlled by the ubiquitous *CMV* promoter)	All body cells	▪ 60-75% mortality by PW5-6[94,95]. ▪ SS[94,95]. ▪ Susceptible to HiS[94]. ▪ Presence of numerous IEDs[94,95]. ▪ Cognitive impairment: learning and visuospatial memory deficits[94,95]. ▪ Behavioral abnormalities: hyperactivity, anxiety, impaired exploratory behavior[94,95]. ▪ No signs of reduced sociability[94]. ▪ Motor dysfunctions[94].

However, preclinical development of new therapies requires mouse models which present all genotypic and phenotypic characteristics in the same manner as human DS patients. For this purpose, the Dravet Syndrome Foundation (DSF) generated in 2015 a new Cre-conditional KI model carrying a heterozygous recurrent missense *SCN1A* mutation found in patients (A1783V) and made it available for the scientific community. This is the first genetic model of epilepsy being incorporated in the National Institutes of Health (NIH) screening program for

new anti-epileptic treatments (https://dravet.eu/novel-open-access-mouse-model-of-dravet-syndrome/). In this case the strain carrying the *Scn1a*-A1783V mutation was crossed with Sox2-Cre mice to incorporate the mutation in all ectodermic-derived tissues (https://www.aesnet.org/meetings_events/annual_meeting_abstracts/view/501949). In our study, in order to mimic all phenotypic and genetic characteristics found in severe DS patients, mice bearing the heterozygous A1783V mutation in all cells have been developed by crossing the *Scn1a*-A1783V strain with cytomegalovirus (CMV)-Cre mice[94]. In the present work we provide a complete phenotypic characterization of this novel DS model.

Recently, the DSF also provided the *Scn1a*^{R613X} model (https://www.jax.org/strain/034129). This mouse model carries a stop codon mutation on nucleotide 1837 in the 129S1/SvlmJ background. Due to its recent development, it remains uncharacterized.

1.4. Current treatment of DS

Current AEDs are typically inefficient in DS. However, the standard treatment consists of pharmacological and non-pharmacological strategies aimed at reducing the severity and frequency of seizures, apart from supportive care in case of SE. These strategies have shown a partial improvement primarily in epileptic symptoms in a variable percentage of patients, although most of them do not respond to conventional therapies or develop secondary resistance to them.

For this reason, it is mandatory to develop more efficacious treatments with a positive impact not only in the management of seizures, but also in the rest of neurological and behavioral manifestations [11,96].

In order to achieve the best possible therapeutic effect, children should start treatment as soon as they are diagnosed. Once the diagnose of DS is suspected, certain AEDs such as carbamazepine, oxcarbazepine, phenytoin, lamotrigine, vigabatrin, phenobarbital, and rufinamide should be generally avoided since they are sodium channel blockers and could exacerbate seizures in DS patients. The pharmacologic treatment currently employed is predominantly based on data obtained in a limited number of small, open-label, and mostly retrospective studies, as well as on experts' opinion. There are three main lines of treatments described below, classified according to its effectiveness in the control of seizures[97].

1.4.1. First-line management

» **Valproic acid**: is a broad-spectrum agent widely used as AED which increases GABAergic function, inhibits voltage-gated ion channels, and acts as an antagonist of N-methyl-D-aspartate (NMDA) receptors. Several retrospective studies evidenced reduction in seizure frequency in 22.2% to 48.0% of patients[98,99]. Valproic acid is usually well-tolerated, although there is a potential risk of hepatotoxicity, particularly in younger patients. Since it has been described a teratogenic effect, probably due to its function as histone deacetylase inhibitor (HDAi)[100], novel derivatives such as valnoctamide have been developed to decrease this risk[101].

» **Clobazam:** it belongs to the family of benzodiazepines (BZ), although it has lower affinity for the $GABA_A$ receptor subunits than the rest of BZ, a property that results in less sedative effects and better tolerability compared with other AEDs. Limited retrospective studies have documented a 28.0% response rate (>50% reduction in seizures)[98].

1.4.2. Second-line management

If first-line treatment is not effective, there is a second option strategy which could be administered as monotherapy or as co-adjuvant for the control of seizures.

» **Stiripentol:** is a positive allosteric modulator of the $GABA_A$ receptor with affinity for both γ-containing $GABA_A$ receptors and δ-containing $GABA_A$ receptors. Therefore, when stiripentol is combined with BZ, the effect on GABAergic neurotransmission is much higher than each compound administered individually[102]. Moreover, stiripentol is an inhibitor of cytochrome P450 in the liver, which causes an increase in plasma concentration of other AEDs, particularly used in co-therapy with clobazam. Stiripentol was approved as adjunctive therapy in DS for pharmacoresistant GTCS combined with valproic acid and/or clobazam and is the only AED that has been shown effect in a randomized, blinded and placebo-controlled study[103].

» **Topiramate:** is a sulfamate derivative of fructose whose main mechanisms of action are: blockade of voltage-gated sodium channels, potentiation of GABA-mediated transmission, antagonism of NMDA receptors, negative modulation of L-type calcium

channels, and inhibition of carbonic anhydrase isoenzymes[104]. Topiramate has been demonstrated to be effective in partial-onset seizures and primary generalized seizures as both monotherapy and combined with other AEDs, with responder rates of 37-78% in reduction of seizure frequency, reaching a 17% of seizure-free patients[105–107].

» **Ketogenic diet:** this non-pharmacological approach has been demonstrated to be a good therapeutic alternative to AEDs for refractory epilepsy. This diet consists of a high fat intake in the context of low carbohydrate and moderate protein consumption. The basis of this ketogenic diet is the oxidation of fats and the production of ketone bodies for its use as the primary source of metabolic energy in the brain instead of glucose. In addition, it leads to acidosis, cellular and extracellular dehydration, the increase of GABA levels, and pH changes that seem to affect ion channels and neurotransmitter receptors[108]. There are several studies supporting the efficacy of ketogenic diet in DS, with an overall of two-thirds of responder patients[109,110]. Obviously, this diet also presents several adverse effects, therefore it should be prescribed and supervised by a dietitian[111].

1.4.3. Third-line management

When all the previous options show no effect there is a third-line of treatment, although it appears to be less effective than combinations of valproic acid/clobazam with stiripentol or ketogenic diet.

» **Levetiracetam:** is a broad-spectrum AED, with no clear mechanism of action. It is only known that levetiracetam binds to the synaptic vesicle protein 2A (SV2A) present in some neuroendocrine cells. This protein acts on exocytosis of synaptic vesicles and regulates the release of neurotransmitters[112]. It has been demonstrated to be effective for convulsive seizures and myoclonus with a responder rate of 64% of patients[113].

» **Bromides:** their mechanism of action remains unknown, but it is believed that bromides cause hyperpolarization by interaction with the chloride channel of the $GABA_A$ receptor. In one study with DS patients, 32% of them became totally free of TCS[114]. In another study 47% of DS patients showed reduced seizure frequency after 12 months of treatment[115]. However, this medication seems inefficacious for focal, absence, and myoclonic seizures.

» **Vagus nerve stimulation:** this surgical approach consists of intermittent electrical stimulation of the left cervical vagus nerve by a device implanted into the chest. The electrical stimulation regulates the brain signaling and reduces the hyperexcitation. The rate of responders is relatively low, around 25-35%[116].

1.4.4. Management of SE

Prolonged seizures and subsequent SE suppose a life-threatening episode and require emergency treatments and protocols by parents, caregivers, and physicians. Firstly, it is important to avoid situations or precipitants that may provoke seizures, such as hot temperatures, high physical exercise, nervousness, and flashing lights. In addition, it is recommended that every patient with DS have a personalized rescue protocol as well as training of parents to administer the medication in cases there is no time to go to the hospital.

When one prolonged seizure occurs, the first step should be the administration of oral, nasal, or rectal diazepam or midazolam, followed by a second dose of intravenous (IV) BZ if the seizure is still ongoing. In case this is not enough to stop the seizure, second-line agents such as valproic acid, levetiracetam, phenytoin, stiripentol, or phenobarbital are also effective in the reduction of SE.

1.5. Novel pharmacological treatments

There are also a few pharmacological therapies which, despite being substances already known and used for other purposes, have demonstrated to be promising alternatives for the control and reduction of seizures.

One of them is fenfluramine, a serotoninergic phenethylamine with high affinity for serotonin receptors type 2A and 2C in the CNS[117]. It was previously used in combination with phentermin as anti-obesity treatment until concerns regarding severe cardiac valvular hypertrophy and pulmonary hypertension were raised, leading to its withdrawal as therapeutic drug in 1997. However, due to its ability to modulate neurotransmission, it was subsequently employed in children with refractory epilepsy[118]. There data available from prospective, double-blind, placebo-controlled trials demonstrate a dose-dependent efficacy and safety of fenfluramine in DS patients, with rates of responders from 41% to 70%[119].

Cannabidiol, a nonpsychoactive component derived from the plant *Cannabis sativa*, has demonstrated to be an effective therapeutic option not only restricted to DS but also to other epileptic encephalopathies such as LGS[120]. This new medicine is formulated as an oil of pure plant-derived cannabidiol under quality-assured pharmaceutical standard and recently approved in U.S. and E.U. as an add-on therapy to clobazam. Cannabidiol was tested on DS patients in a large-scale randomized clinical trial, showing a reduction of seizure frequency of 38.9% from baseline and a responder rate of 43%[121]. Adverse events observed in children were mild or moderate, including mainly vomiting, diarrhea, fatigue, pyrexia, infections in the upper respiratory tract, lethargy, and somnolence. The beneficial effects of cannabidiol have been longer confirmed in several trials carried out in patients with several epileptic encephalopathies[122] and even in mouse models of DS, showing improvement not only in seizure frequency but also in autistic-like behaviors[123].

1.6. Preclinical Nav1.1-targeted novel approaches

Currently there are numerous published and on-going preclinical studies based on the etiological origin of the disease. All these treatments are focused on enhancing Nav1.1 function, either by activation at the protein level or by potentiation of *SCN1A* gene expression.

1.6.1. Channel activators

This strategy relays on the selective potentiation of Nav1.1 function by small molecules or peptides. The proof of concept about the therapeutic potential of this approach was described using the Hm1a, a spider venom peptide which interacts with the inactivation domain of the channel and leads to a persistent current at depolarized potentials[124,125] (Figure 4-(5)). This study confirmed the Hm1a selectivity for Nav1.1 over other Nav or voltage-gated potassium (Kv) channels, especially in GABAergic inhibitory interneurons. DS mice treated with intracerebroventricular (ICV) infusions of Hm1a showed a reduced whole-brain hyperexcitability, a significant decrease or completely abolishment of seizure frequency, and improvement of survival rate[126]. New channel activators are being developed based on homologous recombination of this peptide (rHm1b)[127], being the selectivity for Nav1.1 the main challenge. One drawback of this approach is the need of repeated intrathecal injections to sustain the therapeutic effect.

1.6.2. Gene therapy approaches

Overall, the gene therapy (GT) concept comprises the transference of genetic material into a cell, tissue or entire organ as well as the modification of a defective gene in order to treat or reduce the progression of a genetic disease[128]. Over the last few decades, advances in novel GT strategies, such as the development and improvement of vectors for gene transfer, gene edition, and nucleotide-modulated expression systems have placed this multidisciplinary field in the vanguard of modern medicine. This discipline can be divided in *ex vivo* GT, when isolated cells are *in vitro* modified and autologously transferred to the patient, or *in vivo* GT, in which the genetic material is directly administered into the organism. Despite this *in vivo* therapy could be applied in any kind of tissue, including neuron cells, it is difficult to obtain an acute degree of tissue specificity and the same global efficiency and transference as the *ex vivo* approach.

In order to transfer the therapeutic genetic material into the cells, a vehicle (vector) is usually employed. Vectors can be divided in two categories: non-viral and viral.

» **Non-viral vectors** are a heterogeneous group of vehicles based on chemical or physical structures. In general, they are characterized by its safety profile, with a relatively low immunogenicity which allows repeated administrations. Standardization and high-scale production are usually efficient and affordable. However, they present reduced gene transfer efficiency (especially if nuclear entry is required) and low tissue specificity. The most employed non-viral vectors include lipids and cationic compounds, peptides, and metal particles[129]. Physical methods to deliver naked or minimally coated genetic material include electroporation[130], hydrodynamics injection[131] and bio-ballistic methods[132].

» **Viral vectors.** Taking advantage of the innate ability of viruses to deliver their genetic material into infected cells, viral vectors are an effective GT tool which can be adapted to express therapeutic genetic material without their endogenous pathogenic components. Usually, sequences encoding cytotoxic proteins and others required for viral replication are removed from the viral genome to guarantee safety and increase the cloning capacity of the vector. Depending on their genome´s nature, they can be ribonucleic acid (RNA) or DNA-based viral vectors. They can also be divided in those that have the ability to integrate their genetic material into the cellular genome (integrative vectors) or those that remain in an episomal state (non-integrative vectors). Integrative

vectors are the best choice to maintain the transgene expression in cells with high proliferative index, although it has been found that in some cases the vector genomes can be gradually silenced, leading to the reduction of the transgene expression[133]. Commonly used integrative viral vectors are oncoretroviruses and lentiviruses (LVs). On the contrary, transgene expression with non-integrative vectors is only stable in not actively dividing cells. Within the non-integrative vectors, the most widely-used vectors are adeno-associated virus (AAV), adenovirus (AdV) (described in more detail in section 2), and herpes simplex virus (HSV)[128].

Nowadays, both viral and non-viral vectors are employed in a wide variety of GT strategies for the treatment of DS, including the supplementation of a healthy copy of the *SCN1A* gene (this thesis) and the delivery of gene products able to modulate transcription and translation of the endogenous gene[134–138]. Recently, expression of the Nav1.1 β subunit has shown some therapeutic effect in a DS model[83].

Although crossing the blood brain barrier (BBB) is a key limiting factor, significant improvements in molecular strategies and vectors engineering have been achieved for the delivery of genetic material into the CNS[139,140].

1.6.2.1. Antisense oligonucleotide-based therapeutic strategies

Antisense oligonucleotides (ASOs) are chemically synthesized oligonucleotides, usually 15-30 nucleotides in length, which hybridize by Watson & Crick base-pairing to target messenger RNA (mRNA) and regulate protein expression. ASOs mechanisms include degradation of the target mRNA by ribonuclease H, the prevention of binding of proteins to RNA by steric blockade, and the modulation of alternative splicing. Thus far, ASOs strategy has only been employed in monogenic diseases carrying specific mutations such as β-thalassemia and spinal muscular atrophy, but its application in mutation-independent haploinsufficiencies and neurological disorders is increasing over time[141].

Hsiao and colleagues[134] employed the ASO technology to counteract a natural regulatory mechanism operating on the *SCN1A* gene. They targeted an inhibitory long non-coding RNA (lncRNA) coming from the opposite strand of the coding *SCN1A* gene, also called natural antisense transcript (NAT), in this case known as *SCN1ANAT*. They designed sequences of >70 oligonucleotides called antagoNATs (ASOs) which target different regions of *SCN1ANAT* and block its inhibitory activity, leading to a *SCN1A* upregulation (Figure 4-(1)). Particularly, when

these antagoNATs were intrathecally injected in *Scn1a*$^{tm1.1Swl}$ mice, they observed an improvement in frequency and severity of seizures and a decreased sensitivity to heat-induced seizures compared to untreated DS mice. In addition, it was also observed the presence of antagoNATs inside hippocampal PV+ neurons after a single intrathecal administration in a non-human primate (NHP) model and the increase of *SCN1A* expression in human cells presenting a wide spectrum of *SCN1A* mutations. Taken together, these results demonstrated to be particularly relevant in DS since it is caused by multiple *de novo* mutations which specially affect hippocampal GABAergic inhibitory neurons.

A recently developed approach, known as targeted-augmentation of nuclear gene output (TANGO)[135] (Stoke Therapeutics, Inc.), also employ the ASOs strategy to specifically increase the production of correctly spliced *Scn1a* mRNAs[138]. The selected ASOs target the *SCN1A* gene and increase Nav1.1 expression by decreasing the natural non-productive alternative mRNA splicing, avoiding the degradation of *SCN1A* mRNA by the nonsense-mediated mRNA decay (NMD) pathway (Figure 4-(2)). The feasibility of this approach has been demonstrated *in vivo* in a mouse model by two active ASOs directed against non-productive alternative splicing event in *Scn1a,* leading to the increase of both mRNA and Nav1.1 levels in the mouse brain in a dose-dependent manner. This titratable effect means that the risk of overexpression could be reduced in this ASOs therapy[135,138].

Finally, other approaches not concerning the *SCN1A* gene have proved a potential improvement for the treatment of DS. This is the case for ASOs designed against the *Scn8a* gene, originally employed to treat a developmental and epileptic encephalopathy (DEE) caused by *de novo* mutations in the *SCN8A* gene. This gene encodes the sodium channel Nav1.6 primarily expressed in excitatory neurons which induces a persistent current of Na^+, finally leading to an increased neuronal excitability. Interestingly, the reduction of *Scn8a* expression by a single dose of ASOs in a mouse model of DS increased the survival beyond 5 months of age[142].

1.6.2.2. CRISPR/Cas9-based therapeutic strategies

Supporting the same hypothesis that stimulating the endogenous expression of the healthy allele of *SCN1A* should improve the epileptic phenotype of DS, two recently published works based on clustered regulatory interspaced short palindromic repeats-associated protein 9 (CRISPR-Cas9) technology have shown promising results.

In one of them, the authors employed a modified version of Cas9 by removing its endonuclease activity, called endonuclease-dead Cas9 (dCas9). This dCas9-system associated with single guide RNAs (sgRNAs) is able to bind specifically to sequences of interest in the DNA and modify their function, depending on the functional domains attached to the DNA-binding nucleoprotein. To this aim, Colasante and colleagues selected a sgRNA with optimal binding to the *SCN1A* distal promoter and close to an active TSS. The fusion of dCas9 with a transcriptional activator domain was able to upregulate the expression of *Scn1a* in different interneurons (Figure 4-(3)). In addition, *in vivo* studies demonstrated a significant upregulation of *Scn1a* expression in neonatal DS mice treated with a pair of AAV9 vectors. One vector carried a tetracyclin-inducible TRE-dCas9-VP64 cassette and the second one carried the sgRNA expressed under the control of a GABAergic-specific (mDlx5/6) promoter. Subsequently, mice treated with the *Scn1a*-dCas9 system presented an increase in seizure temperature threshold compared with untreated mice, as well as a reduced severity score of seizures[136].

The second study recently published, carried out by Yamagata and colleagues followed a similar design (Figure 4-(3)). In this case, AAV particles harbored a combination of four guide RNAs (gRNAs) composed by sequences of ~20 nucleotides complementary to the upstream promoter regions (within the distal exon A, see Figure 2b) of both human *SCN1A* and mouse *Scn1a* gene. The mouse model employed was a transgenic DS mice[39] in which a dCas9 protein fused to a VPR transcription activation domain (dCas9-VPR) is expressed under the control of the *Vgat* promoter. The gRNAs-AAV particles were IV administered at P30 to evaluate their effect on heat-induced seizures and behavior features. Results showed an increase of *Scn1a* transcription with the CRISPR-ON treatment, as well as a higher temperature threshold for the heat-induced seizures and an intermediate state between wild type (WT) and *Scn1a*$^{RX/+}$ groups in behavioral test of anxiety and social interaction[137].

1.6.2.3. SINEUPs therapeutic strategies

An ongoing study carried out by the group of Professor Antonello Mallamaci is also based in lncRNA, in this case to enhance translation of Nav1.1 protein (https://dravet.eu/new-research-project-jointly-supported-by-6-european-associations-news/) (not published data available). The activity of these lncRNAs, known as SINEUPs, involves the binding domain of the targeted coding mRNA and an embedded inverted SINEB2 sequence, also referred as effector domain (ED), which increases the protein translation (Figure 4-(4)). Consequently, SINEUPs approach represents an ideal scalable therapy which directly acts on cell cytoplasm to induce a more

physiological increase (2-fold) of Nav1.1 synthesis, compared with other GT approaches, without generating stable genomic changes in the cell DNA[143]. The fact that they function in the cytoplasm may facilitate their delivery to the target cells.

Taken together, all these results indicate that GT approaches based on modulation of cellular functions to enhance the expression of endogenous *SCN1A* gene are reliable and promising therapeutic alternatives for DS. Nevertheless, it is important to mention that these upregulation expression approaches do not distinguish between the healthy and the mutated *SCN1A* allele. This could be problematic in those hypothetical cases in which the mutation causes a gain-of-function of the channel, finally leading to the worsening of the epileptic condition.

1.6.2.4. Gene supplementation strategies

Delivery of a healthy copy of the *SCN1A* gene into the target cells is a straightforward approach for the treatment of DS, which avoids the need for foreign protein expression to achieve an increase of Nav1.1 protein.

One of the most commonly employed vectors is based on AAV[144]. AAVs are small (25 nm) nonenveloped viruses with single stranded DNA genomes of approximately 4.8 kb in length, which belong to the family of parvovirus. In basal conditions, AAV requires the co-infection with other viral vectors, mainly adenoviruses or herpes viruses, to develop an effective infection. As far it is known, there is no severe human pathology associated with AAV infection, making them a safety GT tool, although they induce an innate immune response against the capsid that can reduce the expression of the transgene[145]. Several human AAV serotypes have been identified with different preferential tropism, being the serotype 9 (AAV9) one of the best choices for CNS delivery since its ability to cross the BBB under certain circumstances[146]. Nevertheless, the highest limitation of AAVs is their low cloning capacity, which is unable to accommodate the total coding sequence of the *SCN1A* gene (~6 kb). Based on that, the group of Dr. Rajvinder Karda are developing a novel treatment for DS based on the co-infection of two AAV9 particles containing segments of the *SCN1A* sequence (Figure 4-(8)) (not published data available) (https://cslide-us.ctimeetingtech.com/asgct23/attendee/eposter/poster/424). This strategy is based on the assumption that the two Nav1.1 moieties expressed from each AAV vector will assemble and reconstitute a functional channel.

AAVs have been used to express the small Nav accessory subunit *NaVβ1*, based on the hypothesis that overexpression of *NaVβ1* would increase the expression and function of the entire Nav1.1 channel (Figure 4-(6)). As previously mentioned, β subunits play a modulation role for the ion flow through the pore and for the transmembrane location of the channel. Therefore, based on this assumption, neonatal DS mice were administered with the AAV-*NaVβ1* vector. Treated mice showed an increased survival rate, more noticeable in females, whereas only males showed reduced spontaneous seizures and an improvement of motor activity and anxiety behavior[83].

Another possibility is to employ LVs carrying the entire *SCN1A* coding region. LVs belong to the *Retroviridae* family, characterized by RNA genomes inside a protein capsid, surrounded by a lipid envelope. LVs can infect dividing and non-dividing cells[147]. In principle, they can allocate the entire coding *SCN1A* sequence (cloning capacity up to 10 kb) and transduce cells with high stability transgene expression. Their integrative capacity into the host genome is an insertional mutagenesis risk factor which should be taken into account[148], although the safety of new LVs versions has improved remarkably[149,150]. Another potential concern for the use of LVs to deliver the *SCN1A* coding sequence is the relatively low stability of their RNA genome (Figure 4-(7)).

Finally, adenoviral vectors can also deliver the entire *SCN1A* coding sequence, as described below and in the Results section of the thesis.

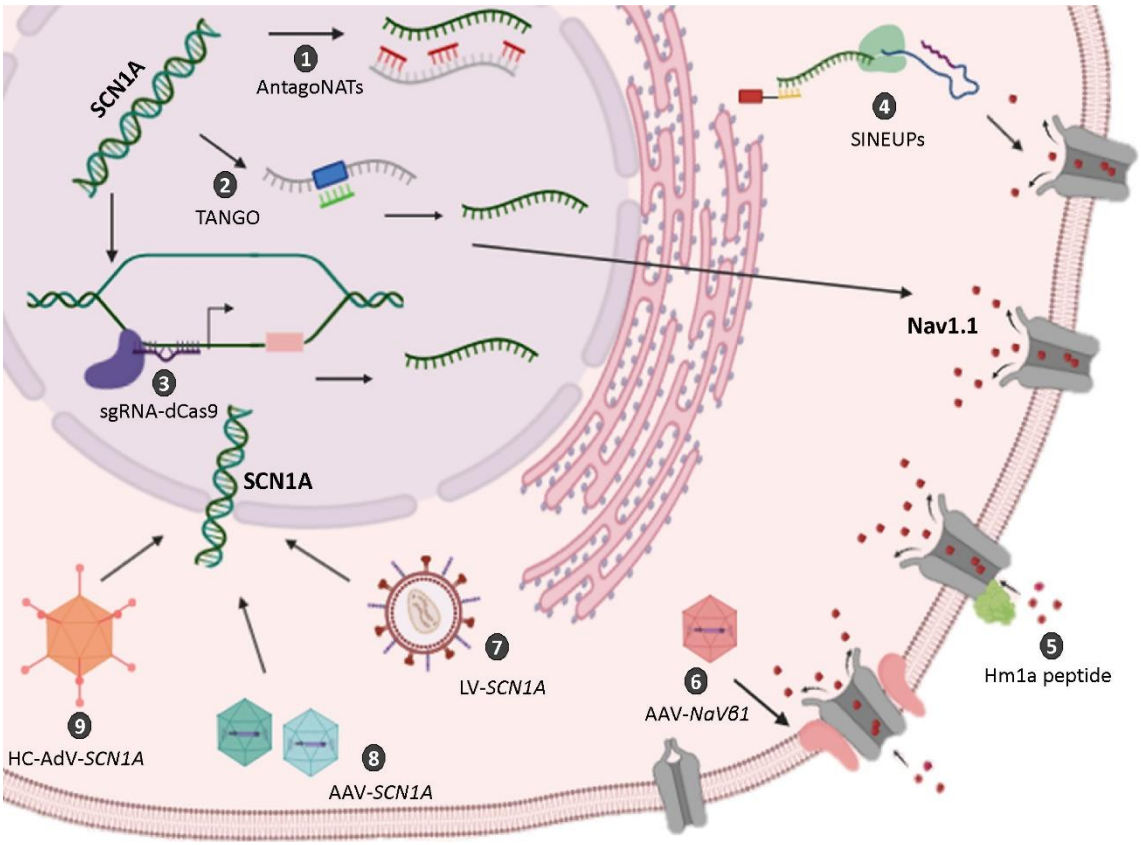

Figure 4. Representation of the different Nav1.1-based therapeutic strategies currently proposed for the treatment of DS. (**1**) Upregulation of *SCN1A* expression by blocking the inhibitory effect of *SCN1ANAT* (grey curved line) with specific antagoNATs (represented in red lines). (**2**) Upregulation of productive *SCN1A* mRNA (green curved line) employing the TANGO system (represented by a light green line). The TANGO-ASO binds within the NMD-exon (blue box) of the non-productive mRNA (grey curved line) to avoid the alternative splicing and further degradation. (**3**) Upregulation of *SCN1A* expression by sgRNA-dCas9 systems recognition of one TSS (angled arrow) in the distal promoter region of *SCN1A* (pink box). (**4**) Cytoplasmatic upregulation of *SCN1A* mRNA translation (green curved line) induced by the SINEUP-lncRNA fused to the ED sequence (represented by a yellow line and a red box, respectively). (**5**) Persistent depolarized current potential of Nav1.1 channel induced by Hm1a peptide (represented in green). (**6**) Modulation of expression and function of Nav1.1 by overexpression of the β1 induced by AAV-*NaVβ1* treatment. (**7-9**) Delivery of the *SCN1A* coding sequence employing LV, a pair of AAVs, and high-capacity adenoviral vectors (HC-AdV), respectively. Figure created with BioRender.com.

2. Adenoviral vectors for the treatment of DS

2.1. General characteristics of adenoviral vectors

Human Adenoviruses (HAdVs) were firstly isolated and characterized from adenoid tissue[151]. They belong to the *Adenoviridae* family, composed by a wide group of mammalian, avian, reptile, fish, and amphibian species sharing numerous characteristics with potential therapeutic profile as viral vectors[152]. HAdVs have been frequently adapted as GT vectors, especially type 5 (HAdV5). In nature, HAdVs are known to be responsible of mild and self-limiting acute respiratory infections, gastroenteritis, and keratoconjunctivitis, primarily affecting pediatric patients[153]. However, clinical manifestations in immune-compromised individuals can cause severe manifestations with high mortality, including hepatitis, pneumonia, nephritis, encephalitis leading to multiorgan failure[154]. AdVs follow a lytic viral cycle and are devoid of oncogenic potential in their permissive hosts.

AdVs are versatile tools for their use as gene delivery vectors since they present numerous advantages, including the easy manipulation of the viral genome, their ability to infect many cell types, and their production at high titers. Their double-stranded DNA genome is very stable and it does not integrate actively in the genome[155], reducing the risk of insertional mutagenesis.

2.2. Virion structure

AdVs are virion particles consisting of a linear double-stranded DNA genome ranging from 26-40 kb in length (36 kb for HAdV5) associated with core proteins and surrounded by a nonenveloped icosahedral capsid of approximately 90 nm in diameter[156].

The protein capsid consists of 20 triangular faces, 30 edges, and 12 vertices; an icosahedral structure primarily composed by 240 hexon protein trimers and 12 complexes of the pentameric penton base protein located in each one of the vertices. Penton capsomers act as an anchor for the trimeric fiber protein projecting from the vertex of the capsid. The fiber is divided in three structural domains: the tail, the shaft, and the knob (Figure 5). The N-terminal tail domain is bound to the penton base; the shaft domain presents different lengths and flexibility among AdV types; and the knob C-terminal portion mediates the binding affinity to the primary host cell receptor. Other minor capsid proteins, including IIIa, VI, VIII, and IX play a

variety of roles from stability of the hexon shell to endosome penetration, transcriptional activation, and nuclear reorganization[157] (Figure 5).

Additionally, the viral core also contains 5 proteins interacting with the DNA: polypeptides V, VII, Mu, terminal protein, and p23 protease (Figure 5). The polypeptides V, VII, and Mu stabilize and condense the viral DNA into the core. The terminal protein is covalently bound to the genome extremes and plays an essential role for the viral replication. The p23 protease is determinant for maturation and assembly of virions particles[158].

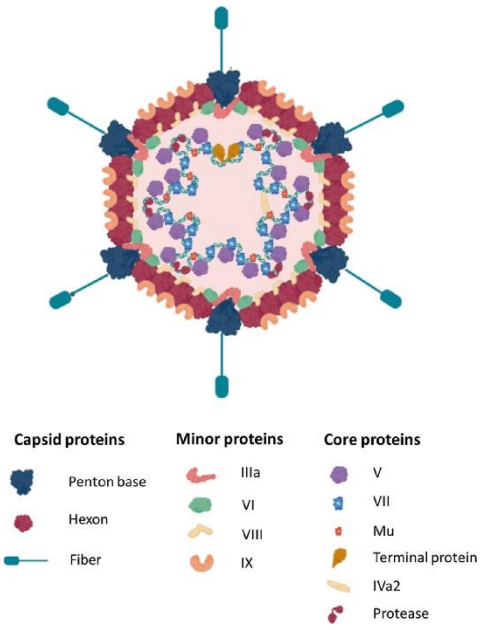

Figure 5. Typical protein structural conformation of an HAdV5 virion. Core and capsid proteins localization are represented in the image. Figure modified from Russell, 2020[158] with BioRender.com

2.3. AdV genome

The AdV genome is a double-stranded, linear DNA which encodes over 50 polypeptides. All AdV share a similar genome organization containing inverted terminal repeats (ITRs), which are conserved motifs acting as origins of viral replication, flanking the 3´and 5´ends[159]. The packaging signal (ψ), located at 5´-end, ensures the correct encapsidation of the viral genome during the particle assembly. Additionally, the AdV genome is divided into five early transcription units (E1A, E1B, E2, E3, and E4), three intermediate transcribed genes (IX, IVa2, and E2 late), and the late transcription region, which generates five families of late mRNAs (L1-L5). All these sequences are transcribed by the RNA polymerase II, resulting in multiple mRNAs by alternative splicing.

The first transcribed gene is E1A, which induces viral transcription and promotes entry into S phase of the host cells, the optimal condition for viral replication. The E1A proteins activate the rest of early gene transcription. E1B products induces blockade of p53-dependent apoptosis[160] to avoid premature cell death of infected cells. The E2 region encodes three proteins essential for viral DNA replication. The E3 transcription unit encodes proteins modulating the host immune response by preventing T cell recognition and tumor necrosis factor alpha (TNF-α) action on the infected cells[161]. The products of E4 unity region are involved in a wide range of functions, including viral DNA replication, exportation of the viral late mRNA, transcription and transduction modulation, and induction of apoptosis of the host cell[162].

Following replication of the viral genome, the activation of intermediate/late transcription units provides two products: the protein IX to be incorporated in the capsid, and the IVa2 protein, involved in the transcriptional control of the viral major late promoter (MLP) for the subsequent expression of late genes[163]. In addition, the IVa2 protein directly interacts with ψ sequence, implicated in the viral DNA encapsidation[164].

Finally, expression of late regions (L1-L5) mediated by MLP provides all building capsid proteins for particle assembly. Then, viral proteases are in charge of virion maturation[164]. Once particles are assembled, MLP activates the expression of a mRNA transcribed from the E3 promoter, encoding the adenovirus death protein (ADP)[163]. The ADP kills the infected cell in the last stage of viral infection and the AdV particles are released outside the cell for their propagation.

2.4. AdV tropism and internalization

The knob domain of the AdV fiber interacts with the primary cell receptor for the initial attachment to the surface of cells. HAdV5 and many other AdVs bind the coxsackie adenovirus receptor (CAR) mainly expressed in epithelial cells, whereas other AdV types preferentially recognize cofactor CD46 or desmoglein-2 as attachment receptors usually found in hematopoietic cells[165]. For this reason, AdV show a wide cellular tropism among different tissues including liver, respiratory tract, heart, gastrointestinal tract, and CNS. Host cells lacking these primary receptors can still be infected by lower affinity interactions between the fiber shaft and the cellular heparan sulphate proteoglycans (HSG)[166].

Subsequently, further internalization of the binding viral particles is mediated by the interaction between the penton base of the capsid and integrins, allowing the entry of the virion through chlatrin-coated vesicles. Once in the endosome, a preliminary pH-mediated disassembly of the viral capsid takes place. The particle is released into the cytoplasm thanks to the pVI protein[167]. Then the virion is transported by microtubules to the pore nucleus where the capsid is completed disrupted, releasing the viral genome intro the nucleus ready to be transcribed[168].

2.5. Immune response to AdV

The immune system induces innate and adaptive responses after AdV vector infection. The humoral immune response can neutralize the vector before host cell infection, and cytotoxic responses can eliminate infected cells[169]. Innate and humoral adaptive responses against viral capsids are common to all AdV-derived vectors, whereas cellular immune responses can be blunted depending on the vector modality, as will be discussed below.

The innate response is triggered by the viral capsid in a dose-dependent manner and is responsible for the acute inflammatory response observed shortly after virus administration. In this inflammatory phase, there is an acute production of pro-inflammatory cytokines and chemokines mediated by Toll-like receptors (TLRs), which activate macrophages and neutrophils infiltration, finally leading to necrosis and tissue damage[170].

The adaptative immune response is consequently activated by antigen presentation of infected cells mediated by major histocompatibility complex (MHC). Cytotoxic T lymphocytes eliminate infected cells presenting viral antigens, and B cells produce neutralizing antibodies (NAbs), mainly against proteins on the virion capsid[169]. Thereof, a second infection of the vector will be blocked by these NAbs and the remaining T memory cells[171].

2.6. AdVs as GT vectors

AdVs offer numerous advantages for their use as viral vectors, including their low human pathogenicity, a broad tissue tropism, and a high nuclear transference efficiency. In addition, AdV´s genome is well characterized, stable and relatively easy to manipulate, allowing high titer production of multiple AdVs adapted for specific therapeutics applications.

Classification of AdV vectors depends on the modifications introduced in the viral genome, each one with specific therapeutic applications.

2.6.1. Oncolytic AdVs

Oncolytic AdVs (OAVs) are employed to destroy cancer cells by modulating their ability to replicate. Cancer-specific replication can be achieved by controlling the early viral genes (mainly E1A) by tumor-specific promoters[172], or by means of selective abrogation of viral functions which can be complemented only by cancer cells[173]. Consequently, OAVs retain most viral genes, but they can incorporate short sequences with the aim of enhancing their antitumoral effects[174,175]. OAVs are highly immunogenic, but this circumstance is usually employed in favor of their therapeutic effect.

2.6.2. First generation AdV vectors

When AdVs are used as gene vehicles, their lytic cycle should be completely avoided. For this aim, **first generation AdVs (FGAdVs)** are obtained by removing the E1 region of the viral genome, releasing up to 5.1 kb in length for the substitution of the therapeutic transgene. *In vitro* vector production therefore requires *in trans* complementation of viral replication E1 sequence, usually provided by packaging cells. The human embryonic kidney 293 cell line (HEK-293) is the most widely used packaging cell line for viral amplification, since these cells contain an integration of approximately 15% of proximal portion of AdV genome[176]. Additionally, further deletion of E3 sequence, dispensable for *in vitro* AdV amplification, increases the cloning capacity of the FGAdV up to 8.2 kb.

Despite few rare cases in which recombination between packaging cells and AdV vectors can result in restored replicative viral function, these FGAdV vectors have demonstrated high transduction efficacy after both *in vitro* and *in vivo* infection[177], without cytopathic effect in the cells. However, residual expression of viral proteins can trigger cytotoxic immune responses resulting in elimination of transduced cells and loss of transgene expression *in vivo*[178,179].

2.6.3. Second generation AdV vectors

Additional deletions of viral genes were supposed to generate safer viral vectors and reduce host immune responses. Based on this hypothesis, **second generation AdV (SGAdV) vectors** include deletions of E2 and/or E4 sequences, increasing also cloning capacity up to 14 kb[180]. However, new packaging cells were required to complement the deleted cells[181,182].

Unfortunately, the remaining viral genome and subsequent production of viral proteins induces a cytotoxic immune response against transduced cells in the same manner as FGAdVs, limiting the stability of transgene expression[178]. Therefore, applications of these early generation AdVs for *in vivo* GT is still re-evaluated, although they are widely used tools for vaccination strategies and pre-clinical *in vitro* and *in vivo* gene transfer[164,183–190].

2.6.4. Third generation AdV vectors

In order to avoid the cytotoxic immune responses after *in vivo* vector administration, a third generation of AdV vectors was developed, also called **high-capacity adenovirus** (**HC-AdV)**, **helper-dependent adenovirus (HD-AdV)** or ***gutless***. This last designation is due to the removal of all coding viral sequences, only maintaining the ITRs and the ψ packaging signal which should be provided *in cis* for the effective viral genome replication and encapsidation, respectively[191]. As expected, HC-AdV infection induces a lower immune response compared with early generation AdV vectors[192,193]. In common with FGAdVs, the innate inflammatory response is induced by capsid proteins, but their rapid degradation and the absence of viral genome reduce the exposure of viral epitopes in cell´s surface. Therefore, a lower adaptative T-cells response is activated after HC-AdV administration, with no signs of elevated transaminases in the liver few days after vector injection, finally resulting in a long-term transgene expression in tissues with slow cellular turnover such as liver or brain. Expression of transgenes after IV administration can last several years after one single administration in NHP[194]. Additionally, the cloning capacity of HC-AdVs is increased up to 37 kb, reason why they received the name of high-capacity AdVs. Only when the length of therapeutic cassettes is shorter than 28 kb, HC-AdVs need to incorporate in their genomes non-coding stuffer DNA to assure the minimal range for stable packaging (75-105% of AdV genome). Since nowadays there are no viable packaging cells able to express all viral genes required for viral genome replication and encapsidation, the *trans*-complementation of deleted sequences is provided by a special E1/E3-deleted FGAdV called **helper virus** (HV). This explains the alternative HD-AdV denomination.

Standard production methods of HC-AdVs rely on co-infection of packaging cells with HV. Since HV contamination of the final product is counterproductive for HC-AdV amplification yield and further immune responses, several strategies have been developed to avoid HV encapsidation. Within these strategies there are some based on deletions or mutations in ψ packaging region[195,196], although the most commonly used strategy consist of recombinase systems which recognize site-specific sequences flanking the ψ sequence[197–199], being the Cre/*loxP* system the most widely employed. In this particular system, Cre-recombinase is constitutively expressed in a special HEK-293 or equivalent cell lines employed as packaging cells. When these cells are co-infected with the HC-AdV and a HV which contains the ψ packaging sequence flanked by *loxP* sites, the ψ is cleaved by Cre-mediated scission. As a result, HV can provide *in trans* all coding sequences required for HC-AdV amplification but is unable to encapsidate its own genome[197]. This strategy is combined with ultracentrifugation in density gradient such as CsCl to separate virions with different genome lengths with final HV contamination ranging from 0.01-1%[200].

Optimized protocols and strategies have been purposed with the aim of reducing the HV contamination for large-scale production and clinical applications of HC-AdVs[198,201]. Expression of Cre-recombinase in packaging cells is decreased due to shut-off of cellular proteins synthesis induced by the HV[202]. This Cre limitation usually occurs in the latest stages of virus amplification, just when the Cre-cleaving function should be most intense to reduce the encapsidation of the growing number of HV genome copies. To circumvent this issue, our group developed a novel approached based on a self-inactivating HV called AdTetCre. This HV expresses a modified Cre recombinase fused with mutated estrogen binding domains under the control of a doxycycline (DOX)-inducible system. This achieves a double level of control of expression (DOX) and nuclear localization (tamoxifen) of the recombinase, allowing the viability of the AdTetCre virus[203]. The use of this HV contributes to reduce vector contamination and makes the system less sensitive to the relative amount of HC-AdV and HV during the amplification process. This approach has been employed for the development of the HC-AdVs in this thesis project.

2.7. HC-AdVs for GT treatment of DS

The numerous advantages offered by HC-AdV vectors make them an optimal tool for the etiological treatment of DS. Firstly, their high cloning capacity allows the insertion not only of long-sized coding sequences, as is the case for *SCN1A*, but also different promoter regions designed to optimize the expression of the transgene in particular target cells. Additionally, the reduced immunogenicity compared with other viral vectors and the long-term expression of the transgene are key points of their therapeutic applications. Several studies support their use with a well-tolerated profile and the absence of immunological response after local administration into the CNS in murine and NHP models, with no signs of damage in peripheral organs[204–206]. Moreover, HC-AdVs administered by intracerebral injection show long-term expression of the transgene, even after their administration in mice pre-exposed to AdV[207,208]. On the other hand, the presence of CAR receptors in neuron projections, presynaptic fractions, and somas[209] allows the infection of HC-AdVs in a wide range of brain cells including neurons, astrocytes, microglia, oligodendrocytes, and ependymal cells. Even so, with the aim of increasing the selectivity of transduced cells, for instance GABAergic inhibitory interneurons, the natural tropism of HC-AdVs can be modified by introducing changes in the fiber domain able to recognize receptors mainly expressed in the target cells. Therefore, considering all these advantages, selection of HC-AdVs as delivery vectors to supply an optimized healthy copy of the *SCN1A* gene seems to be a suitable option for the treatment of DS.

Hypothesis and Objectives

Hypothesis

Since DS is refractory to conventional AEDs, it is mandatory to develop new therapeutic approaches that address not only epilepsy but also the rest of the comorbidities associated with this disease. The availability of animal models resembling the genetic and clinical features of the disease is necessary for preclinical development of these strategies. For this reason, a novel KI mouse model carrying a clinically relevant *Scn1a* mutation in all body cells has been employed in this work.

During the last few years, different GT approaches have obtained important advances to manage DS from its etiological origin. In line with these premises, the hypothesis of this work is based on the potential therapeutic effect of supplementation of a healthy copy of the full *SCN1A* coding sequence employing HC-AdV vectors. This could allow long-term correction of epilepsy and other comorbidities after a single vector administration, avoiding the need of exogenous protein expression. Using an ubiquitous promoter as an initial approach will ensure efficient expression of the transgene and will facilitate the identification of the optimal routes of administration, opening the door for further refinements in the vector.

Objectives

The two major goals of the present work were, on one side, the characterization of a novel murine model for DS. On the other side, to provide a proof of concept about the feasibility and therapeutic utility of transferring a healthy copy of the *SCN1A* gene employing HC-AdV vectors.

To accomplish these goals, specific objectives are formulated as follows:

1. Evaluation of a DS mouse model carrying an ubiquitous heterozygous *SCN1A* mutation (A1783V).

1.1. Determination of survival rate, predisposition to hyperthermia-induced seizures, and electrophysiological analysis.

1.2. Characterization of cognitive, behavioral, and motor functions using a battery of standardized tests.

2. Development of a HC-AdV vector carrying the *SCN1A* coding sequence under the control of the ubiquitous promoter.

2.1. Stabilization of the SCN1A sequence by codon optimization and verification of plasmid functionality.

2.2. Verification of feasibility and functionality of HC-AdVs expressing the *SCN1A* sequence.

2.3. Optimization of the stereotaxic injection protocol to maximize HAdV5 transduction in the brain.

2.4. Evaluation of the therapeutic effect of the HCA-CAG-SCN1A vector administered in adolescent *Scn1a*$^{WT/A1783V}$ mice on survival, epileptic, and neurological manifestations of DS.

Materials & Methods

Materials & Methods

1. *In vitro* studies

1.1. Plasmids and viral vectors construction

All plasmids and viral vectors employed in this work were previously produced by other group members. Plasmids were subcloned by standard molecular biology techniques using restriction endonucleases (New England Biolabs, Ipswich, MA, U.S.) and T4 ligase (Promega, Madison, WI, U.S.). Ligation products were electroporated in One Shot® TOP10 Electrocomp™ *E. coli* (Invitrogen™, Thermo Fisher Scientific, Waltham, MA, U.S.) and spread in LB-Agar plates containing ampicillin or kanamycin (depending on the plasmid, both from Sigma, St. Louis, Missouri, U.S.). Individual colonies were amplified in 2 mL LB medium overnight (plasmids <15 Kb) or during 24 h (plasmids >15 Kb). Plasmid DNA was purified using miniprep kit from Invitrogen™ (Thermo Fisher Scientific, Waltham, MA, U.S.). The correct colonies were identified by restriction enzyme digestion and amplified in 250 mL (plasmids <15 Kb) or 2 L (plasmids >15 Kb) of LB medium. Plasmid DNA was purified using standard and BAC maxiprep kits (Invitrogen™, Thermo Fisher Scientific, Waltham, MA, U.S.) for regular and large plasmids, respectively. For production of FGAdV vectors, the plasmid containing the vector genome was linearized by PacI digestion and transfected into HEK-293 cells. Once the cytopathic effect (CPE) was observed, usually 10-12 days after transfection, cells were harvested and lysed by 3 cycles of freezing/thawing. The viral clones liberated into the supernatant were then isolated by end-limiting dilution. Subsequent clone amplification steps were performed by infections in a growing number of HEK-293 cells, followed by vector purification by double ultracentrifugation in CsCl gradients, as previously described[210]. The Ad-CAG-GFPLuc is an E1/E3-deleted vector encoding a fusion protein green fluorescent protein-luciferase (GFPLuc). Expression of this reporter gene is under the control of a strong and ubiquitous promoter (CAG) consisting of the early cytomegalovirus (CMV) enhancer fused to the chicken β-actin promoter and rabbit β-globin splice acceptor site (Figure 6a).

For HC-AdV construction, the plasmid containing the vector genome was digested with PmeI and transfected in HEK293-Cre cells in the presence of the AdTetCre HV, as previously described[203]. Purification was performed as described for the FGAdV.

A total of four HC-AdV vectors were employed in this project. For longitudinal analysis of transgene expression *in vivo*, the HCA-EF-Luc and HCA-CAG-Luc encoding luciferase under the

control of the human elongation factor-1 α (EF1α) and CAG promoters, respectively were used (Figures 6b and 6c). To facilitate the identification of transduced cells expressing *SCN1A*, the HCA-EF-SCN1A-GFP vector was obtained (Figure 6d). In this vector, expression of *SCN1A* and GFP are linked by an internal ribosomal entry site (IRES) and controlled by the EF1α promoter. Finally, the HCA-CAG-SCN1A expresses the therapeutic gene under the control of the CAG promoter (Figure 6e).

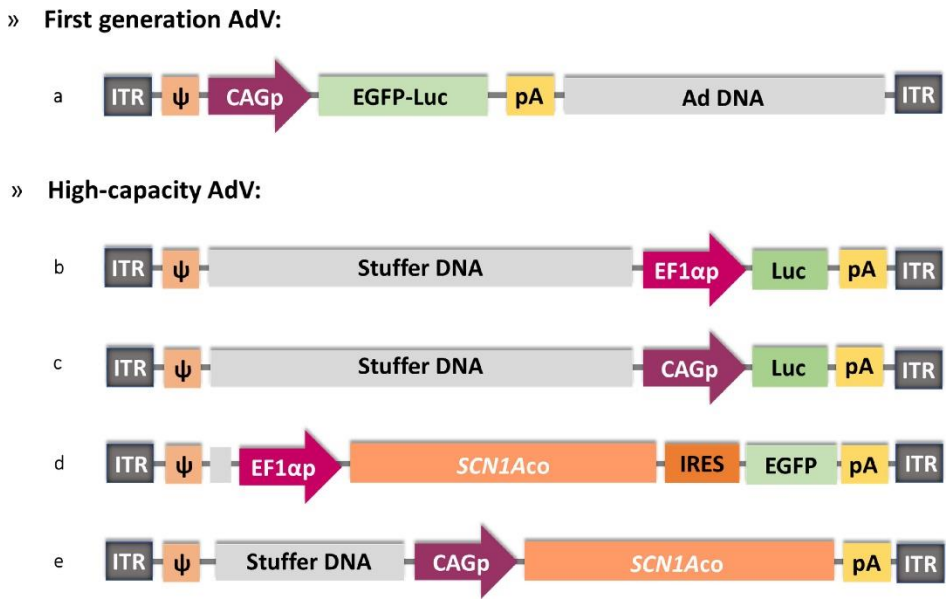

Figure 6: Representation of genomic structure of vectors. a) Schematic representation of Ad-CAG-GPFLuc vector. **b-e)** Schematic representation of the four HC-AdV vectors: HCA-EF-Luc, HCA-CAG-Luc, HCA-EF-SCN1A-GFP, and HCA-CAG-SCN1A. ITR, ψ, packaging signal; and, pA, polyadenylation signal sequence. Not drawn to scale.

Quantification of viral vectors was performed by quantitative reverse transcription polymerase chain reaction (qRT-PCR) to determine the amount of viral genomes (vg). Viral titers obtained are summarized in table 2.

Table 2. List of viral vectors and titers.

Titers of viral vectors	
VECTOR	TITER (vg/µL)
Ad-CAG-GFPLuc	$3.5x10^8$
HCA-EF-Luc	$9.9x10^8$
HCA-CAG-Luc	$2.3x10^9$
HCA-EF-SCN1A-GFP	$1.6X10^9$
HCA-CAG-SCN1A	$8.8x10^7$

1.2. Cell culture

The HEK-293 [American Type Culture Collection (ATCC) CRL-1573] and the SH-SY5Y (ATCC CRL-2266) cell lines were maintained in Dulbecco´s Modified Eagle Medium (DMEM)-high glucose medium (Sigma, St. Louis, Missouri, U.S.) and a 1:1 mixture of Eagle´s Minimum Essential Medium and DMEM/F12 Medium (Gibco™, Thermo Fisher Scientific, Waltham, MA, U.S.), respectively. All culture media were supplemented with 10% foetal bovine serum (FBS), 100 U/mL penicillin, 100 µg/mL streptomycin, 2 mM L-glutamine, and 1% non-essential amino acids (Gibco™, Thermo Fisher Scientific, Waltham, MA, U.S.). Both cell lines were maintained at 37°C and 5% CO_2 in a humidified incubator and tested for mycoplasma contamination.

1.3. Cell transfection

HEK-293 cells were seeded in 24-well, 6-well, and P100 plates at a density of $2.5x10^5$, $1x10^6$, and $6x10^6$ cells per well or plate, respectively. Once the cultures reached 80-90% confluency, usually 24 h later, transfection was performed by addition of a 1:2 mixture of plasmid and Lypofectamine 2000 (Invitrogen™, Thermo Fisher Scientific, Waltham, MA, U.S.). Plasmid DNA concentrations were 0.5, 5, and 30 µg per well in 24-well, 6-well, and P100 plates, respectively. Both plasmid and lypofectamine were diluted in Opti-MEM® medium (Gibco™, Thermo Fisher Scientific, Waltham, MA, U.S.). Transfection mixtures were carefully added to the culture and maintained at 37°C and 5% CO_2 environment for 5 h. Then, the transfection medium was removed and cells were maintained in fresh medium during 48 h until they were collected for the corresponding determinations.

1.4. Cell infections

SH-SY5Y cells were infected with HCA-CAG-SCN1A and HCA-EF-SCN1A-GFP vectors to evaluate the efficacy of *SCN1A* expression. To accomplish this, cells were previously seeded at $2.5x10^5$ and $2.5x10^6$ cells per well densities in 24-well and 6-well plates, respectively. Infections were performed 24 h later, when the culture presented a 80-90% of confluency, by addition of vectors diluted in culture medium supplemented with 2% FBS, 1% streptomycin/penicillin, 1% L-glutamine, and 1% non-essential amino acids (Gibco™, Thermo Fisher Scientific, Waltham, MA, U.S.). Vector concentrations were determined by multiplicity of infection (MOI), calculated as the amount of vg per cell in each well. Cells were incubated with the virus in a volume of 100 or 500 µL of medium, and 1 h later complete growth medium was added up to

0.5 or 2 ml for 24-well or 6-well plates, respectively. Forty-eight h later, cells were processed for qRT-PCR or IF analyses.

2. *In vivo* studies

2.1. Experimental animals

A novel mouse model of DS was used to evaluate the potential therapeutic effect of the prototype vector. This DS mouse model is the result of breading males of the B6(Cg)-*Scn1a*$^{tm1.1Dsf}$/J strain (The Jackson Laboratory, stock no. 026133) with females from the B6.C-Tg(CMV-Cre)1Cgn/J strain (The Jackson Laboratory, stock no. 006054). This latter strain expresses Cre recombinase under the control of the ubiquitous promoter CMV. The B6(Cg)-*Scn1a*$^{tm1.1Dsf}$/J strain contains the WT *Scn1a* exon 26 flanked by *loxP* sites in one of the alleles, followed by another exon 26 harbouring the A1783V mutation. This missense A1783V mutation, one of the most clinically relevant in DS patients, leads to a C to T change at nucleotide 5348 resulting into a substitution from alanine to valine at 1783 position[52,87]. When these heterozygous conditional *Scn1a*-A1783V mice are crossed with homozygous CMV-Cre recombinase mice, the floxed 26 exon suffers scission by Cre-loxP system resulting in approximately 50% of the offspring carrying the two WT alleles (genotype hereinafter referred to as *Scn1a*$^{WT/WT}$) and the other 50% of the offspring presenting one of the mutated allele in all body tissues (genotype hereinafter referred to as *Scn1a*$^{WT/A1783V}$). Experiments were carried out comparing males and females *Scn1a*$^{WT/A1783V}$ to age-matched *Scn1a*$^{WT/WT}$ littermates.

Animals were housed 4-6 per cage, with standard mouse chow and water available *ad libitum* in a 12/12-h light/dark cycle. Breeding and experimental protocols of this study were approved by the Ethical Committee of the Universidad de Navarra, according to the Spanish Royal Decree 53/2013 and corresponding to the registered numbers 058-16 and 059-16.

2.2. Genotyping PCR

Mice were genotyped after weaning (approximately 21 days old) by end-stage PCR. A protocol based on genomic DNA samples isolated from ear punches was employed, which facilitated identification of mice at the same time. Animal biopsies were performed using isoflurane as inhaled anaesthesia (IsoVet, Braun, Melsungen, Germany). DNA extraction and

PCR amplification were performed using the KAPA Mouse Genotyping Kit (Sigma, St. Louis, Missouri, U.S.) in two steps:

» **Genomic DNA extraction**

Each tissue sample was diluted in 44 µL of distilled water (dH_2O), 5 µL of KAPA Express Extract Buffer and 1 µL of KAPA Express Extract Enzyme followed by the next lysis and enzyme inactivation protocol (Figure 7):

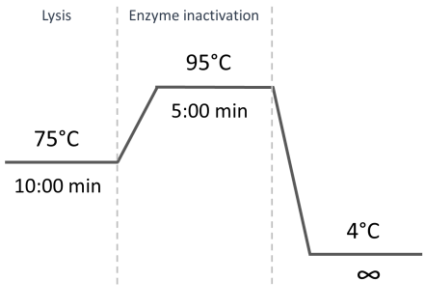

Figure 7. Thermocycling protocol for genomic DNA extraction.

» **PCR Amplification**

One microliter of genomic DNA was diluted in 19 µL of PCR mixture: 9.5 µL of 2X KAPA2G Fast (HotStart) Genotyping Mix with dye, 1 µL of each forward and reverse primers (Sigma, St. Louis, Missouri, U.S.), and dH_2O quantum sufficit (qs) to 19 µL. Primer sequences and their optimal concentration for each mouse strain are described below (Table 3), as well as the optimal five-step cycle PCR protocol for the three different mouse genotypes (Figure 8).

Table 3. List of primers and their sequences used for mice genotyping.

Primers for B6(Cg)-Scn1a$^{tm1.1Dsf}$/J strain genotyping		
PRIMER	TYPE	SEQUENCE (5'- 3')
24472	Forward	GCAACTCTTCACATGGTACTTTCA
24473	Common	GCACCTCTCCTCCTTAGAACA
24489	Mutant Forward	GGAGAAACACGAGCAGGAAG
Primers for B6.C-Tg(CMV-Cre)1Cgn/J strain genotyping		
PRIMER	TYPE	SEQUENCE (5'- 3')
olMR1084	Transgene Forward	GCGGTCTGGCAGTAAAAACTATC
olMR1085	Transgene Reverse	GTGAAACAGCATTGCTGTCACTT
olMR7338	Internal Positive Control Forward	CTAGGCCACAGAATTGAAAGATCT
olMR7339	Internal Positive Control Reverse	GTAGGTGGAAATTCTAGCATCATCC

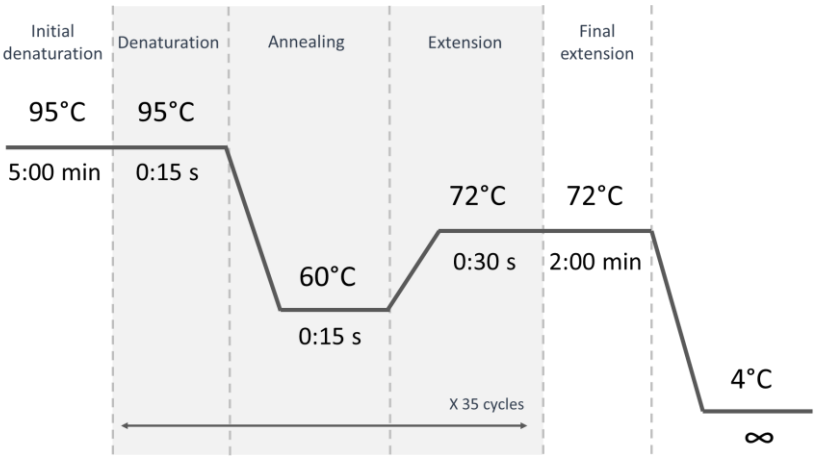

Figure 8. PCR cycling protocol for mice genotyping.

Finally, agarose gel electrophoresis was used to visualize PCR products. In this case, 2% agarose (Sigma, St. Louis, Missouri, U.S.) was diluted in TAE 1x Buffer consisting of Tris-Acetate (Sigma, St. Louis, Missouri, U.S.) 40 mM and 0.1 mM ethylenediaminetetraacetic (EDTA, Sigma, St. Louis, Missouri, U.S.), pH 8. SYBR® safe DNA gel stain (Invitrogen™, Thermo Fisher Scientific, Waltham, MA, U.S.) was added at 1:10,000 dilution to stain DNA. The molecular weight marker (1Kb Plus DNA Ladder, Invitrogen™, Thermo Fisher Scientific, Waltham, MA, U.S.) was mixed with loading buffer containing glycerol (Merk Millipore, MA, U.S.) and a mixture of Xylene Cyanol (Sigma, St. Louis, Missouri, U.S.) and Bromophenol Blue (Sigma, St. Louis, Missouri, U.S.) dissolved in TE buffer (QUIAGEN GmbH, Hilden, Germany). Electrophoresis was carried out at 100 V (power source Bio-rad, Hercules, CA, U.S.).

The expected fragments are:

» **B6(Cg)-*Scn1a*$^{tm1.1Dsf}$/J strain**

- WT (*Scn1a*$^{WT/WT}$): 164 bp
- Heterozygote Pre-Cre (B6(Cg)-*Scn1a*$^{tm1.1Dsf}$/J): 164 bp, 198 bp, and 410 bp
- Heterozygote Post-Cre (*Scn1a*$^{WT/A1783V}$): 164 bp and 198 bp

» **B6.C-Tg(CMV-Cre)1Cgn/J strain** (assay unable to distinguish between homozygous and heterozygous animals)

- WT: 324 bp
- B6.C-Tg(CMV-Cre)1Cgn/J: 100 bp and 324 bp

The hybridization of primers in the genome of mice is represented in figure 9.

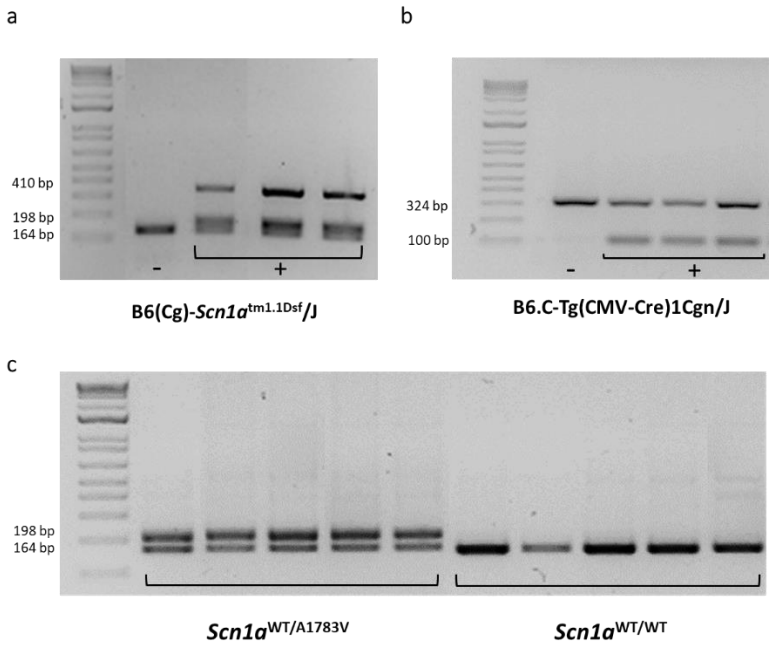

Figure 9. Mouse genotyping. Representative agarose gels of PCR products obtained following the corresponding genotyping reactions (**a**) B6(Cg)-*Scn1a*$^{tm1.1Dsf}$/J (heterozygote pre-Cre) mice present the 164 and 198 bp fragment and the one corresponding to the floxed exon at ~410 bp. (**b**) B6.C-Tg(CMV-Cre)1Cgn/J mice (both homozygotes and heterozygotes) present the transgene at 100 bp and the internal positive control band at 324 bp. (**c**) *Scn1a*$^{WT/A1783V}$ mice present the WT band at 164 bp and the mutant band at 198 bp, whereas the *Scn1a*$^{WT/WT}$ mice only present the 164 bp band.

2.3. Vector administration

Biodistribution studies were carried out in C57BL/6 mice injected with Ad-CAG-GFPLuc vector ($5.2x10^7$ vg/injection in 1.5 µL) by bilateral stereotaxic surgery in different brain locations including HC, Ctx, Cb, in the limit zone of *globus pallidus/caudate-putamen* (GP/CP) (hereinafter referred as basal ganglia, BG), and combinations of some of the last three structures. For the evaluation of the therapeutic efficacy of HCA-CAG-SCN1A, 5 weeks-old (wo) *Scn1a*$^{WT/A1783V}$ mice were bilaterally injected in pCtx, BG, and Cb with both HCA-CAG-SCN1A ($2x10^7$ vg/injection in 1.5 µL) and the same dose of the control vector HCA-CAG-Luc. Animals were previously anesthetized with a ketamine/xylazine (80:10 mg/Kg; Ketamidor 100 mg/mL injectable solution, Richter Pharma AG, Wels, Australia; and Rompun® 20 mg/mL injectable solution, Bayer Animal Health GmbH, Leverkusen, Germany; respectively) combination by intraperitoneal injection and placed in the stereotactic frame. After shaving and disinfecting the head of the animal with ethanol, the skull was exposure by a longitudinal scission using a sterile scalp. Then, periosteum was removed with hydrogen peroxide (H_2O_2) in order to facilitate the visibility of bregma point in the intersection between the coronal and sagittal

cranial sutures. Coordinates for the different brain regions were calculated according to the Paxinos and Watson mouse brain atlas[211] using bregma as the reference point (Table 4 and Figure 10). Once injection locations were defined and drilled with a needle (25G X $^{5}/_{8}$", BD Microlance™ 3, Becton, Dickinson and Company Ltd, Ireland) 1.0-1.5 µL were administered per point using a 10 µL Hamilton Neurons Syringe (Hamilton Company, Nevada, U.S.) and following a 0.4 µL/min infusion rate. Before and after vectors administration, the Hamilton syringe remained inserted for 3 min to allow the adjustment of the brain tissue and the absorption of the vector. Following surgery, animals were individually housed with free access to food and water until their complete recovery.

Table 4. Brain coordinates for stereotaxic injections of vectors. The anteroposterior (AP), mediolateral (ML), and dorsoventral (DV) coordinates for the different brain regions were obtained from the Paxinos and Franklin mouse brain atlas[211], taking bregma as the reference point.

Region	AP (mm)	ML (mm)	DV (mm)
pCtx	+2.58	±1.50	-1.65
HC	-1.94	±1.20	-2.00
BG	-0.58	±2.50	-3.50
Cb	-6.96	±1.00	-2.50

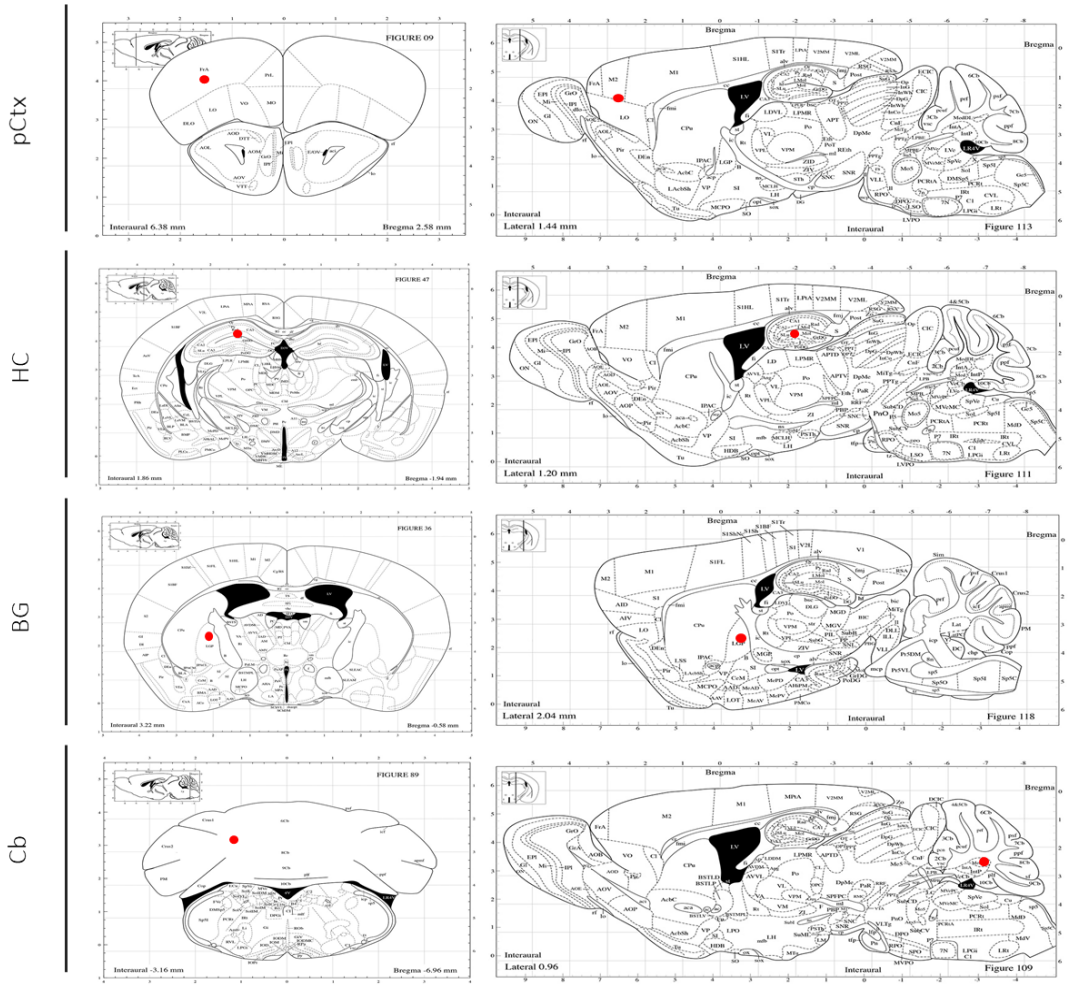

Figure 10. Location of stereotaxic injections in pCtx, HC, BG, and Cb. Left panels represent the coronal sections and right panels the sagittal sections of the corresponding coordinates for each brain region. Images were obtained from the Paxinos and Watson mouse brain atlas (access online via Elsevier, 2001).

2.4. Heat-induced seizures

Epileptogenic thermal threshold of mice was tested by induction of hyperthermia seizures. For the characterization of the DS mouse model, the protocol for thermal induction of seizures was developed and fine-tuned in the laboratory. The setting consisted of a methacrylate cylinder (30 x 20 cm) coupled to a thermal system that gradually increases ambient temperature inside the chamber. Mice body temperature was measured before initiation of heating using a rectal probe RET-4 (Physitemp Instruments LLC, NJ, U.S.) connected to the TCAT-2DF controller (Physitemp Instruments LLC, NJ, U.S.). Animals were introduced into the cylinder prewarmed at 25°C and the environmental temperature was gradually increased 0.5°C every 30 s to a maximum of 45°C or until a GTCS was observed. Body temperature was measured again just after removing the animals from the cylinder and placing them finally into

a cage in contact with a rubber bag filled with cold water to accelerate the recovery. However, this protocol was later improved to a standardized method[60,80] and employed for the evaluation of temperature thresholds in mice treated with the therapeutic vector, as well as their corresponding controls. In this case, mice were body restrained into the methacrylate cylinder with the rectal probe introduced and fixed to their tails, allowing the measurement of the body temperature throughout the test. The temperature probe was connected to the TCAT-2DF controller which was in turn connected to an infrared heat-lamp (HL-1/FS Heat Lamp, 250 watts, 110VAC; Physitemp Instruments LLC, NJ, U.S.). After 10 min of habituation, body temperature was increased 0.5°C every 2 min, controlled by the feedback of the rectal probe to the heat-system. Similarly as previous protocol, body temperatures were increased until the appearance of a GTCS or to a maximum of 42.5°C. Treated *Scn1a*$^{WT/A1783V}$ mice were tested twice: at least 2 days before administration of vectors (pre-surgery) and approximately 30 days after vector administration (post-surgery). Both pre- and post-surgery heat-induced seizures periods were also emulated in untreated *Scn1a*$^{WT/A1783V}$ and *Scn1a*$^{WT/WT}$ littermates to evaluate the therapeutic effect of HCA-CAG-SCN1A vector.

2.5. Behavioural and motor assessment

In order to characterize the neurological comorbidities observed in DS patients in this new *Scn1a*$^{WT/A1783V}$ DS mouse model, mice of different age ranges and both genders were subjected to a complete battery of behavioural and motor test. The same tests were used for the evaluation of therapeutic effect in *Scn1a*$^{WT/A1783V}$ mice, starting two months after vector administration.

All experimental procedures were performed under blind conditions for experimenters.

2.5.1. Open-field test

This test is commonly used for the evaluation of motor activity, hyperactivity and anxiety-like behaviour[212]. Mice were individually introduced in a standardized squared four-compartment open-field (OF) box (LE800SC, 90 x 90 x 40 cm; PanLab Harvard Apparatus, Barcelona, Spain) and were video-recorded in freely moving with soft illumination for 15 min. Video analysis employing a video tracking system (Ethovision XT 5.0, Noldus Information Technology B.V., Wageningen, The Netherlands) provided information about certain parameters such as total distanced moved (cm) for motor evaluation and the mean velocity

(cm/s) for hyperactivity evaluation; and the time spent in the center of the arena (s) used as an anxiety indicator (the more anxious an animal is, the less time it will spent in the center of the arena). Furthermore, stereotypies were manually counted and represented also as an indicator of hyperactivity and anxiety-like behaviour. Animals which explored less than 5% of the total time were excluded from the analysis.

2.5.2. Novel object recognition test

The novel object recognition (NOR) test provides information about learning and visuospatial memory based on mice exploratory behaviour and their preference to interact with a novel object over a familiar one[213]. This test was performed immediately after the OF test, using the same standardized squared four-compartment OF box (LE800SC, 90 x 90 x 40 cm; PanLab Harvard Apparatus, Barcelona, Spain) and the same illumination conditions employed for the open field test. NOR test consists of three different stages:

» **NOR Habituation phase**

Mice were allowed for free exploration into the OF box for 5 min with two identical objects symmetrically separated from each other (Figure 11a).

» **NOR 1 h phase**

One hour after the habituation phase, just one of the objects was removed and changed for a new one placed in a different position of the box. Mice were introduced again into the box for 5 min of exploration (Figure 11b).

» **NOR 24 h phase**

The procedure was the same as described above, changing again the second object for a third new one in a different position 24 h after the habituation phase (Figure 11c).

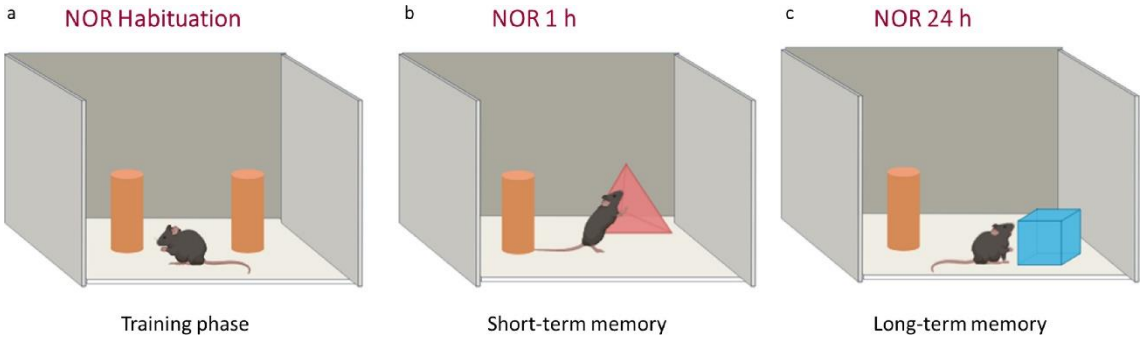

Figure 11. Schematic representation of the NOR test. (**a**) In the NOR habituation phase mice are exposed to two identical objects in an OF arena for 5 min. (**b**) One hour after the habituation phase (NOR 1 h), the same procedure was carried out but changing one of the objects for a new one in a different position. (**c**) The same protocol was followed 24 h after the habituation phase (NOR 24 h), changing again the second object for a novel one in other position of the box. Figure created with BioRender.com.

It is important to note that objects and box were carefully cleaned after each trial to avoid olfactory interferences. All trials were video recorded and manually analysed using a stopwatch to measure the exploration time of each object. Data of NOR 1 h and NOR 24 h were represented as a percentage of exploration calculating the discrimination index (DI) formula:

$$DI = \left[\frac{\text{exploration time of the novel object}}{\text{exploration time of the familial and novel object}} \right] X\ 100$$

According to this equation, a 50% ratio indicates no preferences for both novel and familiar objects; ratios above 50% indicate a preference for the novel object over the familiar one, suggesting a good learning and visuospatial memory retention.

2.5.3. Marble burying test

This test evaluates the interaction of mice with their environment, since digging and burying objects are indicators of normal exploratory behaviour in mice. The marble burying test consists of twelve glass marbles disposed on the surface of the cage bedding, in four rows of three marbles. Mice were individually introduced into the cage and allowed to remain undisturbed for 30 min. Once the animal was removed from the cage, two experimenters quantified the number of uncovered marbles, considering as buried when at least two-thirds

of its surface area was covered by bedding. Data were analysed as the average number of uncovered marbles counted by each experimenter for each mouse.

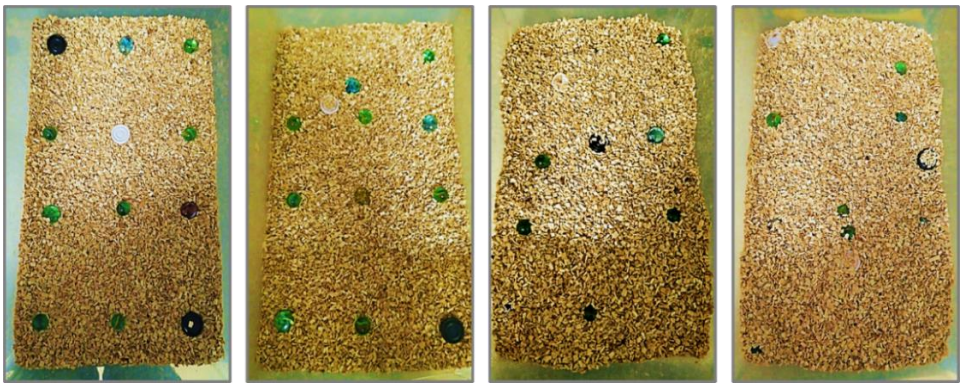

Figure 12. Examples of marble burying test performances. Images from left to right show different performances with higher to fewer amount of uncovered marbles.

2.5.4. Nest building test

Nest building is important for protection, reproduction, and heat conservation; therefore, it can be considered as a clear indicator of animal welfare and constitutes a useful tool for identifying unusual behaviour in mice[214]. Nesting performance can be measured by nest building test, where mice are isolated overnight in a cage with a Mouse Igloo® (Bio-Serv, Flemington, NJ, U.S.) and access to building material (a square of pressed cotton) (Nestlets™ Nesting Material, Ancare, NY, U.S.). The next morning, nesting index was evaluated by two experimenters and classified in three categories according to the bitten state of the cotton nesting material: no nest, partial nest, and complete nest covering the mouse (inside or outside the igloo).

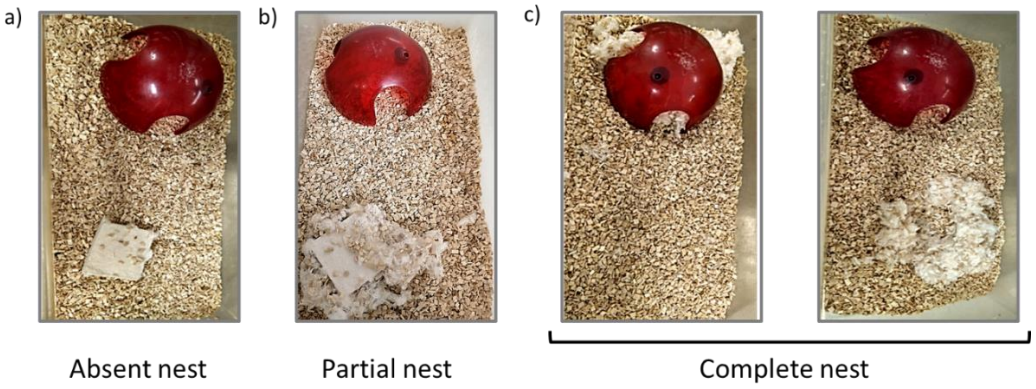

Figure 13. Examples of nest building test performances. (**a**) Image of a score 0: no nest. (**b**) Images of scores 1-2: partial nest. (**c**) Images of score 3: complete nest inside and outside the igloo.

2.5.5. Morris water maze test

The Morris water maze (MWM) is one of the most used tests to assess working memory and hippocampal-dependent spatial learning in mice[215]. MWM consists of a circular pool (1.2 m diameter x 0.6 m heigh. LE820120, PanLab Harvard Apparatus, Barcelona, Spain) filled with white-coloured water and virtually divided into four equal quadrants, in one of which an escape platform is located. Each quadrant is identified by a visual clue that will guide the mouse to the scape platform, which remains covered (invisible) or uncovered (visible) depending on the stage of the test. The tracking system is coupled to a camera placed over the pool that allows to follow in real time the development of the test. The test was carried out as described before with minor modifications[216], and differentiated in three phases: visible platform (VP), invisible platform (IP), and probe tests.

» **Visible platform**

In this visible phase of the test no cues were used, only the platform was visible inside the pool maze raised 1 cm above the level of water. In order to train animals to escape from water, platform was maintained at the same position throughout the learning trials. During 5 consecutive days, one by one mice were released into the water surface, faced to the walls, in one of the three rest quadrants, measuring how long they take to reach the platform (Figure 14a). At first, it is supposed that mice remain more time looking for a way to escape. Eventually, they will learn to directly swim to the platform and climb it up. Each mouse was tested in four trials per day at different starting positions for a maximum of 60 s per trial. If an animal failed to find the platform in this time, it was scored for this trial as 60 s and was gently guided onto it. In order to teach mice that they should stay on the platform to be removed from the pool, all of them were maintained on it for 15 s. All trials were monitored by video recording and escape latency times were analysed with WaterMaze3 program (Actimetrics, Evanston, IL, U.S.).

» **Invisible platform**

Once the training phase was finished, IP phase was performed as a spatial learning task. The basis of this phase is that animals must learn to use distal visual cues to directly swim to the hidden platform starting from different locations around the perimeter of the pool. For this purpose, the platform was located on the opposite quadrant to the one used in the visible phase and hidden 1 cm below the level of coloured water, making it completely invisible. In order to help mice to create a spatial map about where the platform was

hidden, four geometric visual clues were located in the middle of each quadrant surrounding the edges of the pool (Figure 14b). This invisible phase was performed with four trials per day during eight consecutive days, and the procedure was the same as mentioned before: mice were introduced into the water, facing the wall of the pool, and starting from different pseudo-randomly established positions. Animals were video monitored and latency escape times were recorded (WaterMaze3, Actimetrics, Evanston, IL, U.S.) until they reached the platform or after 60 s. Again, if an animal was unable to find the platform in this time, it was guided. In each trial, mice were allowed to remain 15 s over the platform to facilitate the generation of a spatial map to find the platform guided by the surrounding visual clues.

» **Probe test**

During the invisible phase acquisition, on days 4th, 7th and 9th mice were subjected to probe test to determine the rate of memory consolidation. In this case the platform was removed from the pool, leaving only the visual cues as a reference. Mice were allowed to swim freely for 60 s in one single trial (Figure 14c). Commonly, well-trained animals with no memory deficit will swim to the target quadrant where the platform was located before starting to search elsewhere. For this reason, it was measured the time they remain swimming in the target quadrant for the first 15 s of the trial (Probe 15) and in the total 60 s (Probe 60). According to the calculating percentages, values over 25% were considered an indicative of memory retention whereas values below 25% were considered as arbitrary.

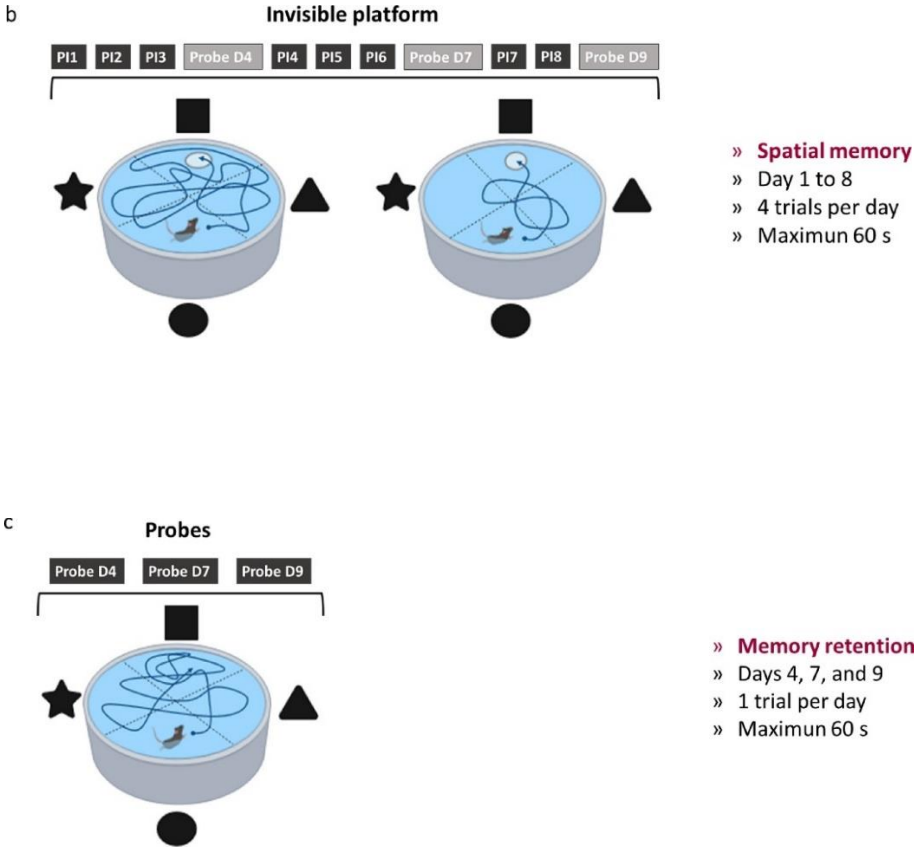

Figure 14. Schematic representation of the MWM test. (**a**) The VP phase constitutes the training task in which mice should learn to reach the platform to escape from water during five consecutive days (PV1-PV5). (**b**) In the IP phase, mice employ the visual cues to find the hidden platform below the level of water. This spatial memory evaluation is carried out during eight consecutive days (IP1-IP8). (**c**) For the probe tests on days 4, 7 and 9 of the IP phase, the platform is removed from the pool in order to assess the memory retention of mice by measuring the time they remain swimming in the target pool. Figure created with BioRender.com.

2.5.6. Social interaction test

In order to evaluate the presence of autism-like behaviour or social abilities impairment in this DS mouse model, each mouse underwent a social interaction test with a mouse of the same gender without any prior contact (no littermates). Pairs formed by the subject and the non-familiar mouse were introduced in each one of the four compartments of the OF box (LE800SC, 90 x 90 x 40 cm; PanLab Harvard Apparatus, Barcelona, Spain) and were allowed to interact between them for 15 min in soft light conditions. Trails were video-recorded and the number of interactions of tested mice were manually measured, as well as the latency time to the first contact.

2.5.7. Rotarod test

Regarding motor assessment of mice, rotarod test was performed in order to evaluate their physical condition, motor coordination and balance[217]. This test is based on a rotating horizontal rod, with controlled speed, supported 30 cm above the base of the apparatus (LE8200 Panlab, Harvard Apparatus, Barcelona, Spain).

First, mice were trained to hold on walking on the rod for 5 consecutive min at a constant speed of 12 revolutions per min (rpm). The next day, the test started placing the animals on the rod with a progressive speed increase from 4 to 40 rpm in a total time of 5 min. Each mouse was tested in three trials, with 60 min resting periods, and two consecutive days. Time remaining on the rod and speed before falling were recorder for each trial, calculating the average per animal.

2.5.8. Inverted Grid test

Using this test, the strength/weight ratio of mice can be evaluated by measuring the ability of the animal to remain clinging to a wire grid for a period of time[218]. Mice were placed on inverted position on a metal cage lid, recording the latency they remain hanging to a maximum of 1 min. Test consisted in three trials per animal with a resting period of 60 min between them, and was repeated in two consecutive days. Average hanging time of each mouse was calculated and represented.

2.5.9. Elevated beam test

Balance and motor coordination were also evaluated with the elevated beam test, a footbridge of 1 m in length and 1 cm of diameter resting 50 cm above the surface[219]. Mice were placed in one edge of the beam and allowed to walk across the entire footbridge from one end to the other for a maximum of 2 min or until they fell down. The test was performed in two trials per mouse waiting 60 min between them and repeated in two consecutive days, calculating average walking time on the beam for each mouse.

2.5.10. Hindlimb clasping test

This test is widely used as a marker of cerebellar ataxia in mouse models of neurodegeneration[220]. Mice were hanged by the base of their tails to evaluate the hindlimb position during 30 s. When hindlimbs were displayed outward, away from abdomen, it was assigned a score of 0. If one of them was retracted toward the abdomen for more than 50% of the hanging time, it received a score of 1. If both hindlimbs were partially or completely retracted for more than 50% of the test, it was assigned with a score 2 and 3, respectively.

2.6. Electrophysiological analysis

The electrophysiological analysis of mice was performed thanks to the collaboration with the team directed by Julio Artieda and Miguel Valencia in the Neuroscience Program at CIMA. All procedures and data analysis were carried out by their group. They performed the characterization of the *Scn1a*$^{WT/A1783V}$ DS model and the evaluation of the therapeutic effect of HCA-CAG-SCN1A vector on local field potentials from different brain structures.

For the electrophysiological characterization of the mouse model, *Scn1a*$^{WT/A1783V}$ and *Scn1a*$^{WT/WT}$ mice (n=5 per group) from two to three months of age were implanted with five equally spaced 50 µm tungsten wires (California Fine Wire, CA 93433, U.S.) across different layers of CA1 and DG of the HC (Figure 15b); and a wire in pCTX. For the electrophysiological analysis of treated mice, two months-old animals (n=6 per group) were implanted with three-four tungsten deep wires in BG, close to the administration area, 15 min after vector or saline injection (protocol described in section 2.3); and an external electrode (screw) was placed over the pCtx (Figure 15c). In all cases, ground and reference screws were placed over the Cb. Coordinates for all electrode placements are described in table 5.

Electrodes were attached to a 3D-printed support (system designed and improved by this laboratory group) and fixed to mice skulls with dental cement (Stoelting, IL, U.S.) (Figure 15a). Animals were left to recover from surgery and one week after implantation they were connected to an acquisition system for electrophysiological recordings (Intan RHD2000 system, IntanTech, CA, U.S.). Recording sessions were simultaneously video recorded to evaluate the behavioural state of the animals and the appearance of clinical seizures. At first, animals were recorded for 30 min of freely moving at RT on an OF box. Then, they were introduced into a heating chamber where temperature was gradually increased from RT to 42°C or until the appearance of a GTCS. Data obtained from electrophysiological analysis and temperature

values were converted by custom-made routines on Matlab (Mathworks, Natick, MA, U.S.) into Spike2 format (Cambridge Electronic Design Limited, UK) to analyse the recordings in order to detect the presence of IEDs, electrical seizures and temperature thresholds at the onset of the seizures. IEDs signals were semi-automatically annotated using Matlab scripts, resampled to 1,000 Hz, band-pass filtered in the 60-80 Hz range and rectificated. IED events were detected when the filtered envelope was > 3 times above baseline and unfiltered envelope was < 3 times above baseline, according to previously described methods[221] and further validated by visual examination. Envelope was computed by estimating the rms value within a 200 ms window. Candidate events were uploaded into the Spike2 file as a marker channel that was further reviewed and curated by two specialists. Examination of video recordings allowed the evaluation of seizures and their semiological description according to a modified Racine score for mice[222].

Finally, location of the electrodes was assessed by histological staining of brain slides. Perfusion and histological processing were carried out as described in Section 3.1. Thirty µm coronal sections of the brains were cut in a microtome and stained with thionine to verify the location of the recording electrodes by microscope. The staining with thionine dye was performed once brain slides were mounted on super frost plus slides (Thermo Fisher Scientific, Carlsbad, CA, U.S.), following the next protocol: Dehydration with diluted series of ethanol (EtOH, Scharlab, S.L. Barcelona, Spain): 100%, 96%, 80%, and 50% of EtOH (2 min per step), followed by two consecutive washes in dH_2O of 2 min each one. Then, slides were dipped into thionine dye diluted in dH_2O (Sigma, St. Louis, Missouri, U.S.) for 1 min. After two washes in dH_2O of 2 min, complete dehydration was carried out again with diluted series of EtOH, maintained 2 min in each solution: 70%, 96% (x2), 100% (x2). Finally, brain slides were introduced in xylol (Scharlab, S.L. Barcelona, Spain) for 2 min and covered with coverslips using DPX (PanReac AppliChem, IL, U.S.).

Table 5. Brain coordinates for electrodes implantation. The AP, ML, and DV coordinates for the different brain regions were obtained from the Paxinos and Franklin mouse brain atlas, taking bregma as the reference point.

Region	AP (mm)	ML (mm)	DV (mm)
pCtx	+2.58	±1.50	-1.50
HC	-1.94	±1.50	-2.00 to -1.00
BG	-0.58	±2.5	-3.75

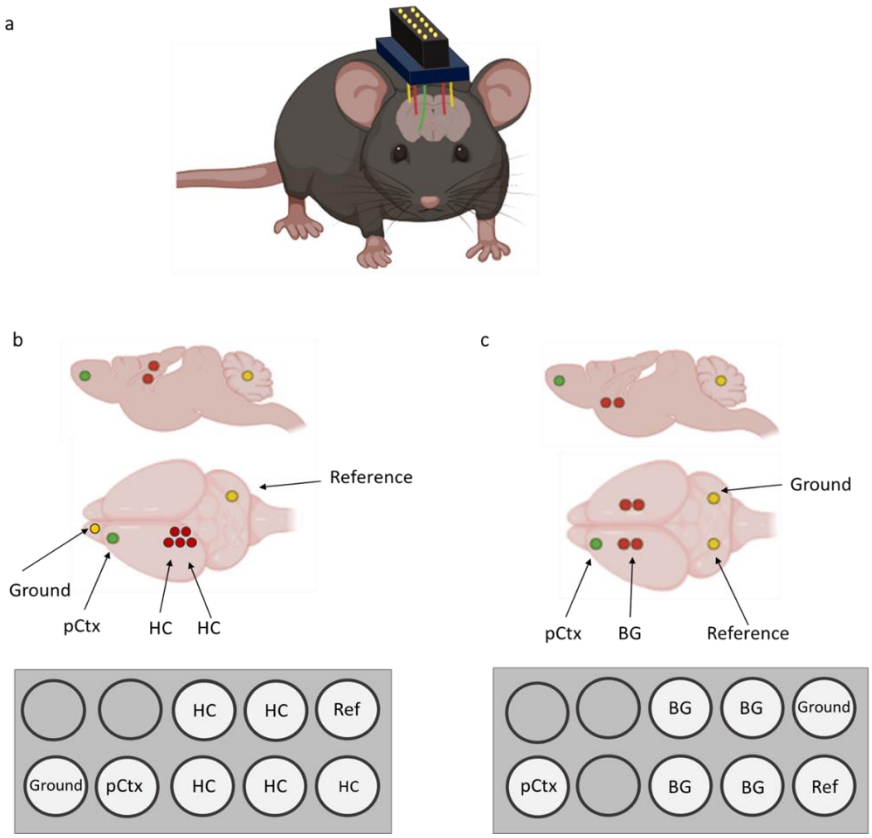

Figure 15. Electrode implantation for electrophysiological analysis. (**a**) Representation of the wires/PRECI-DIP system fixed to mouse´s skull. (**b**) Schematic representation of tungsten wires implanted in mouse´s brains for the electrophysiological characterization of the DS mouse model: pCtx (ground), CA1 and DG (x5), and Cb (reference). (**c**) Schematic representation of tungsten wires implanted in mice brains for the electrophysiological evaluation of treatments: pCtx, BG (x3-4), and Cb (reference and ground). Figure created with BioRender.com.

2.7. *In vivo* bioluminescence imaging (BLI)

Mice previously treated with Ad-CAG-GFPLuc, HCA-CAG-Luc, or HCA-EF-Luc vectors were anesthetized with a ketamine/xylazine (80:10 mg/Kg; Ketamidor 100 mg/mL injectable solution, Richter Pharma AG, Wels, Australia; and Rompun® 20 mg/mL injectable solution, Bayer Animal Health GmbH, Leverkusen, Germany; respectively) mixture by intraperitoneal injection. After shaving their heads with hair removal cream, mice were administered intraperitoneally with 200 µL of the D-luciferin substrate (REGIS Technologies, Inc, IL, U.S.) (30 µg/µL solution in phosphate buffer saline without calcium and magnesium ($PBS^{-/-}$, Gibco™, Thermo Fisher Scientific, Waltham, MA, U.S.). Mice were introduced in the PhotonIMAGER™ Optima apparatus (BioSpace Lab, France) and light emission was measured 5, 10, 15 and 30

min after D-luciferin administration. Luminescence peak values from the head area were analysed using the M3 Vision software (BioSpace Lab, France), acquiring the individual value of each animal. Data were represented as the maximal value obtained for each mouse.

2.8. *Ex vivo* luciferase assay

In the case of mice injected with Ad-CAG-GFPLuc for biodistribution analysis, they were sacrificed 1 h after BLI to obtain several brain structures: pCtx, parieto-temporo-occipital cortex (ptCtx), BG, BS, HT, HC, and Cb. Tissue samples were lysed in 200-500 µL of Passive Lysis Buffer 5X (Promega, Madison, WI, U.S.) using a homogenization pestle (VWR® Pellet Mixer, VWR International, LLC, PA, U.S.) and centrifuged at 13,000 rpm during 5 min at 4°C. Lysate pellets were discarded, employing supernatants for the measurement of luciferase activity with the Luciferase® Reporter Assay System 10-Pack (Promega, Madison, WI, U.S.). Ten µL of each sample was mixed with 50 µL of luciferase, and the luminometer tubes (5 mL, 75 x 12 mm, PS, Sarstedt Inc. Newton, U.S.) were introduced one by one on the Luminat KB 9507 Luminometer (Berthold Technologies, Germany). Results were obtained in relative light unit (RLU) and were normalized by µg of protein loaded, determined by Bradford assay.

2.8.1. Bradford assay

Each sample was tested in triplicate in a 96-wells plate and diluted in $PBS^{-/-}$ with a final volume of 15 µL per well. A standard curve to extrapolate unknown protein values was also carried out in the same plate with serial dilutions (from 0.4 µg/µL to 4.8 µg/µL) of bovine serum albumin (BSA, Heat shock fraction, pH 7, ≥ 98%, Sigma, St. Louis, Missouri, U.S.) diluted in $PBS^{-/-}$. Then, 200 µL of Bio-Rad Protein Assay Solution (Bio-rad, Hercules, CA, U.S.) were added to each well using a 1:5 dilution. Finally, the absorbance was measured at 595 nm in a plate spectrophotometer (Multiskan Ascent, Thermo Fisher Scientific, Waltham, MA, U.S.).

3. Immunofluorescence microscopy

This technique was performed to detect the expression and distribution of transgene products (Nav1.1 channel or GFP) in different cell types.

3.1. Sacrifice and animal perfusion

Brain fixation was performed by transcardial perfusion to ensure tissue preservation. Prior to surgery, ketamine/xylazine mixture (240:30 mg/kg body weight; Ketamidor 100 mg/mL injectable solution, Richter Pharma AG, Wels, Australia; and Rompun® 20 mg/mL injectable solution, Bayer Animal Health GmbH, Leverkusen, Germany; respectively) was intraperitoneally injected. Once the animals were anesthetized, they were cannulated via left ventricle and perfused with 19.5 mL of 0.9% saline solution (B. Braun Medical Inc., Melsungen, Germany) followed by 32.5 mL of 4% paraformaldehyde (PFA, PanReac AppliChem, IL, U.S.) using a peristaltic pump at constant speed (6,5 mL/min). Finally, brains were removed and post-fixed in 4% PAF for 12 h at 4°C; and then cryopreserved in 30% sucrose dissolved in 0.125 M $PBS^{-/-}$ at 4°C for at least a week. After this time, brains were either frozen into optimal cutting temperature compound (OCT) blocks (Scigen, Thermo Fisher Scientific, Carlsbad, CA, U.S.) and then cut in 30 µm sagittal sections using Microm HM550 cryostat (Thermo Fisher Scientific, Carlsbad, CA, U.S.), or directly cut in a freezing microtome in 30 µm sagittal sections. Brain slides were preserved at -20°C in cryopreservation solution (30% ethylene glycol, 30% glycerol, and 30% 0.4 M phosphate buffer (PBS) pH 7.4) dissolved in dH_2O until processed.

3.2. Immunofluorescence procedures

Brain slides were selected according to the intended area of study. Once two-three brain sections per mice were selected, they were firstly washed three times in $PBS^{-/-}$ at RT and incubated with blocking buffer (2% normal goat serum (Thermo Fisher Scientific, Carlsbad, CA, U.S.), 0.5% Triton X-100 (Sigma, St. Louis, Missouri, U.S.), and 1% BSA (Sigma, St. Louis, Missouri, U.S.) diluted in $PBS^{-/-}$ for 2 h at RT in constant slow shaking. Then, they were incubated overnight at 4°C with the primary antibody diluted in blocking buffer. For detection of Nav1.1 the rabbit polyclonal anti-Nav1.1 antibody from Alomone Labs (1:500, Cat# ASC-001, Jerusalem, Israel) was used diluted in blocking solution. For GFP staining, a rabbit polyclonal antibody from Abcam was employed (1:5,000, Cat# ab6556, Cambridge, U.K.). In order to differentiate the type of transduced cells we employed the anti-NeuN monoclonal antibody (1:200, Cat# MAB377, clone A60, Merk Millipore, MA, U.S.) and anti-GFAP (GA5) mouse

monoclonal antibody (1:500, Cat#3670, Cell Signaling Technology®, MA, U.S.) for staining of neurons and astroglia, respectively. The day after, slides were washed again three times with $PBS^{-/-}$ at RT and incubated with the secondary antibodies (Donkey anti-Rabbit IgG (H+L) Alexa Fluor 488 Cat# A-21206; Goat anti-mouse IgG (H+L) Alexa Fluor 488 Cat# A-11019; and Goat anti-Rabbit IgG (H+L) Alexa Fluor 546 Cat# A-11010. All of them acquired from ThermoFisher Scientific (Carlsbad, CA, U.S.), diluted 1:400 in blocking buffer for 90 min at RT protected from light. After 3 more washes in $PBS^{-/-}$, slides were incubated 5 min at RT protected from light with the DNA marker 4´,6-diamidino-2-phenylindole (DAPI, 300 nM, Cat# D1306, ThermoFisher Scientific) for nuclei visualization. Finally, they were washed twice in $PBS^{-/-}$, mounted on super frost plus slides (Thermo Fisher Scientific, Carlsbad, CA, U.S.), and let dry for 24 h protected from light. Then they were dehydrated by immersion in toluene and coverslips were placed using Immu-Mount® mounting medium (Thermo Fisher Scientific, Carlsbad, CA, U.S.). For the assessment of non-specific primary and secondary immunostaining, some sections from each experimental group were incubated without primary or secondary antibody. No immunostaining was observed in any case.

IF assay in transfected and infected cells was similar as the previously described with the following exceptions. Firstly, cells were fixed in 4% PFA and 4% sucrose (Sigma, St. Louis, Missouri, U.S.) solution dissolved in PBS with calcium and magnesium ($PBS^{+/+}$, Gibco™, Thermo Fisher Scientific, Waltham, MA, U.S.) for 5 min. Then, cells were permeabilized with 0.1% Triton X-100 during 5 min followed by blocking with 2% BSA and 3% normal donkey serum (Jackson ImmunoResearch Laboratories, Inc, PA, U.S.) diluted in $PBS^{+/+}$ for 30 min at RT. Incubation with the rabbit polyclonal anti-Nav1.1 (1:400, Cat# ASC-001, Alomone Labs, Jerusalem, Israel) primary antibody, diluted in blocking buffer, were performed overnight at 4°C. After three washes with $PBS^{+/+}$, cells were incubated with the goat anti-rabbit IgG (H+L) Alexa Fluor 546 (1:400, Cat# A-11010, ThermoFisher Scientific, Carlsbad, CA, U.S.) secondary antibody for 2 h at RT and protected from light. Finally, cells were washed with $PBS^{+/+}$.

3.3. Images acquisition

Images from brain slides were obtained with the fluorescence microscope Eclipse boom (Nikon) coupled to a super high-pressure mercury lamp (C-SHG1, Nikon, Japan) using a Plan Apo 10 x / 0.45 DIC L objective. Images were acquired with the DS-Ri2 camera (Nikon, Japan) and the NIS-Elements F 4.60.00 64-bit software (Nikon, Japan). Nav1.1-immunostained structures were detected using the B-2A filter (excitation: 450-490 nm, DM: 505, BA: 530) with green-coloured emissions and DAPI-stained nuclei were detected using the UV-2A filter (excitation: 330-380 nm, DM: 400, BA: 420) with blue-coloured emissions. All images were brightened, and contrast adjusted in parallel on ImageJ 1.52p program (NIH, Bethesda, MD).

Brain slides were also visualized by confocal laser microscopy for a better resolution. In this case, Nav1.1-immunostained structures were observed with a confocal laser scanning microscope (Zeiss Axio Observer.Z1/7 LSM800 with Airyscan and ESID 2XGaAsP detector module) and Plan-Apochromat 63 x / 1.40 Oil DIC M27 objective under 488 nm laser excitation (emission wavelength 509 nm, detection wavelength 480-700 nm, pinhole 50 µm). For GFAP and NeuN detection, structures were observed under 546 nm laser excitation (emission wavelength 573 nm, detection wavelength 560-700 nm, pinhole 50 µm). DAPI-staining nuclei were excited at 353 nm laser (emission wavelength 465 nm, detection wavelength 400-480 nm, pinhole 50 µm). Emission colour codes were again green for Nav1.1-immunostainng and blue for DAPI-staining. Images were acquired in ZEN 2 software (Carls Zeiss, Oberkochen, Germany). Acquired fluorescent images were brightened and contrast adjusted in parallel on ImageJ 1.52p program (NIH, Bethesda, MD) and noise was removed using a bright outlier detection filter.

In the case of IF signals of cell cultures, images were obtained with the inverted fluorescence microscope DM IL LED (Leica, Germany) coupled to the EL6000 external light source (Leica, Germany). Fluorescence images were observed using a filter slider cube slider (cube A for DAPI staining: excitation filter (EF) BP 340-380 nm, suppression filter (SP) LP 4225 nm and dichromatic mirror (DM) 400 nm; cube GFP for Alexa 488 staining: EF BP 470/40 nm, SP BP 525/50 nm and DM 500 nm; and cube N2.1 for Alexa 546 staining: EF 515-560 nm, SP 590 nm, DM 580 nm). Images were acquired with the DFC345FX camera (Leica, Germany) employing the HL Plan I 10x/0.22 PH1 or the HCX PL Fluotar L 20x/0.44 CORR objectives. Fluorescence emissions were adjusted to green or red colour for Nav1.1, green for the GFP, and blue for the DAPI staining employing the Leica Application Suite software (Leica, Germany). The ImageJ 1.52p program (NIH, Bethesda, MD) was used to adjust images for

brightness and contrast in parallel, using design panels and improved sharpness (Radius (sigma): 5.0 px, and mask weight: 0.50).

4. Quantitative reverse transcription-PCR

4.1. RNA extraction

In all cases, animals were sacrificed by neck dislocation and brains were divided in two hemispheres and two half Cb. Half brain was used for quantification of *Scn1a* and *SCN1A*co gene expression by qRT-PCR and the other half for determination of Nav1.1 protein level by western blot (WB) (described below). Ctx, HC, BG and Cb structures were dissected from half brain of mice and were treated with the Maxwell® 16 LEV simplyRNA Cells Kit (Promega, Madison, WI, U.S.) for the RNA isolation according to manufacturer's indications. Cell pellets from transfections and infections were also employed for this technique.

4.2. DNAse treatment and reverse transcription

Isolated RNA templates were used to synthesize complementary DNA (cDNA) by reverse transcription. First, RNA samples were submitted to a DNAse treatment to avoid trace amounts of contaminating DNA. The reaction mix contained 2 µg of RNA, 2 µL of DNase I (Invitrogen™, Thermo Fisher Scientific, Waltham, MA, U.S.), 0.8 µL of RNase OUT Recombinant Ribonuclease Inhibitor (Invitrogen™, Thermo Fisher Scientific, Waltham, MA, U.S.), 2 µL of DNase I Buffer 10x (Invitrogen™, Thermo Fisher Scientific, Waltham, MA, U.S.), and 0.1% diethyl pyrocarbonate (DEPC, Sigma, St. Louis, Missouri, U.S.) water to complete a final volume of 20 µL. After a digestion incubation of 20 min at 37°C, 2 µL of 25 mM EDTA (Invitrogen™, Thermo Fisher Scientific, Waltham, MA, U.S.) were added to stop the DNase I activity. Final inactivation of DNase I was carried out following next protocol:

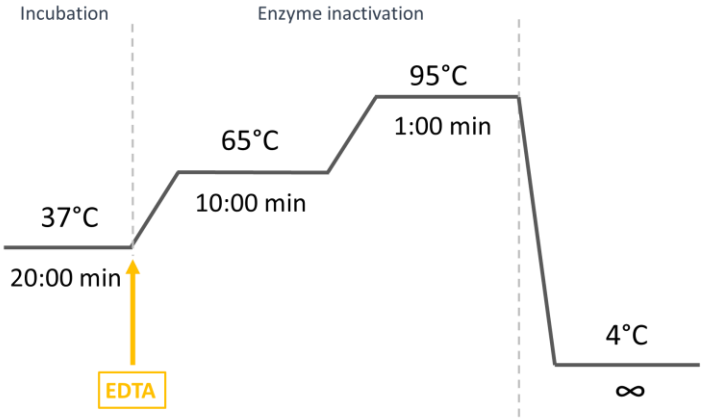

Figure 16. Thermocycling protocol for DNAse treatment. Digestion was carried out at 37ºC for 20 min, followed by two inactivation steps at 65ºC and 95ºC.

Afterwards, RT was performed to obtain the cDNA, adding a retro-transcription mix to each previous reaction. This retro-transcription mix consisted of: 4 µL of 10 mM deoxynucleotides triphosphates (dNTPs), 2 µL of 0.1 M dithiothreitol (DTT, Invitrogen™, Thermo Fisher Scientific, Waltham, MA, U.S.), 1.2 µL RNAse OUT recombinant ribonuclease inhibitor (Invitrogen™, Thermo Fisher Scientific, Waltham, MA, U.S.), 0.13 µL of random primers (3 µg/µL) (Invitrogen™, Thermo Fisher Scientific, Waltham, MA, U.S.), 1.2 µL M-MuLV retro-transcriptase enzyme (Invitrogen™, Thermo Fisher Scientific, Waltham, MA, U.S.), 8 µL of First Strand 5x buffer (Invitrogen™, Thermo Fisher Scientific, Waltham, MA, U.S.) and 6.47 µL of 0.1% DEPC water. Incubation protocol was performed as follows:

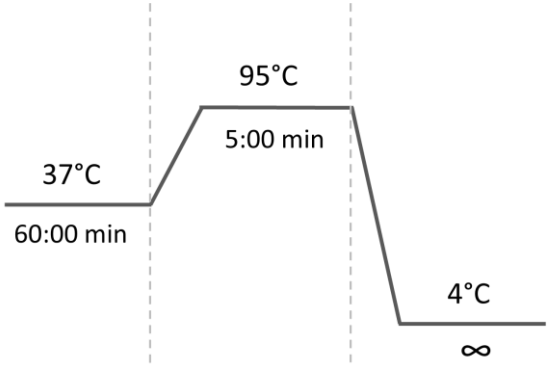

Figure 17. Thermocycling protocol for RT. Reaction was carried out at 37˚C for 1 h, followed by heat-inactivation at 95ºC during 5 min.

4.3. qRT-PCR

*SCN1A*co and *Scn1a* sequences were amplified using primers specifically designed for them and were compared to a reference gene, used to correct sample to sample variations and errors in sample quantification (housekeeping gene).

In order to confirm that qRT-PCR efficiency for target and reference genes was similar, the exponential amplification linearity of each gene was calculated. Date of amplification slopes were generated from serial dilutions of a known concentration cDNA template. Finally, efficiency was calculated using next formula[223]:

$$E\ (\text{efficiency}) = \frac{10}{(-1/\text{slope})}$$

In this case, qRT-PCR reactions consisted of 2 µL of cDNA, 5 µL of iQTM SYBR® Green Supermix reagent (Bio-Rad, Hercules, CA, U.S.), 0.3 µL of both forward and reverse specific primers (table 6) and 2.4 µL of dH_2O. Human *36b4* and mouse *GAPDH* primers were used as housekeeping genes. Each sample was tested by triplicate in 96 well-plates designed for qRT-PCR (Bio-Rad, Hercules, CA, U.S.) and analyzed in CFX96 TouchTM Real-Time PCR Detection System (Bio-Rad, Hercules, CA, U.S.) following the following protocol:

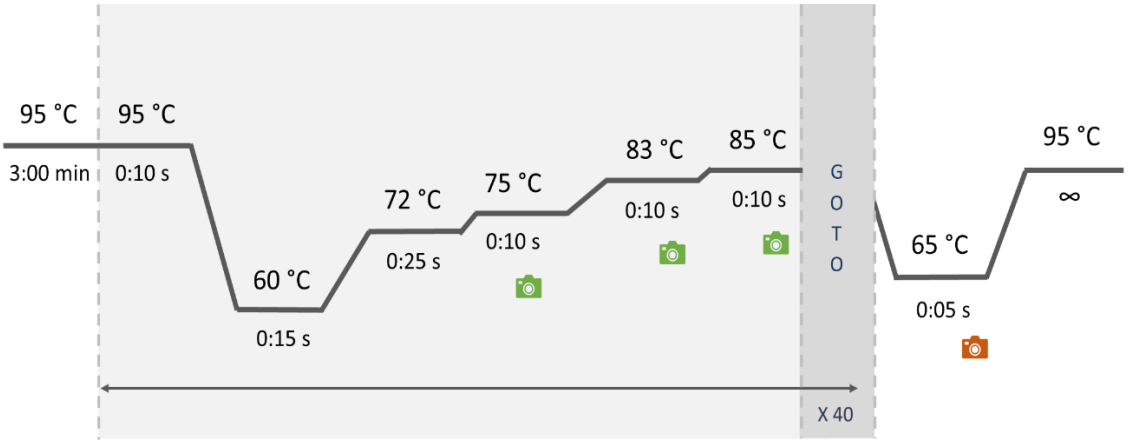

Figure 18. Thermocycling protocol for qRT-PCR. Denaturing was carried out at 95˚C for 3 min, followed by 40 repeated cycles of denaturing (95˚C), hybridization (60˚C), and elongation (72, 75 and 83˚C). Green cameras indicate the cycle of plate readings: *SCN1A*co at 83°C, *Scn1a* at 75°C, m*GAPDH* at 85°C, and m/h*36b4* at 83°C. Melting curve was carried out from 65 to 95˚C. Red camera represent the cycle of melting reading. Time is represented in min:s.

Data were analyzed with CFX Maestro® software (Bio-Rad, Hercules, CA, U.S.), and Cts values were exported to calculate the relative expression of a target gene *vs* a reference gene using a well-established mathematical model[223]. The expression ratio equation is based on qPCR efficiency of target gene (E_{target}) and the difference in crossing threshold points of target (ΔCP_{target}) versus efficiency and CP of the reference gene (E_{ref} and ΔCP_{ref} respectively):

$$\text{Ratio} = \frac{(E_{target})\Delta CP_{target}^{(\text{control-sample})}}{(E_{ref})\Delta CP_{ref}^{(\text{control-sample})}}$$

Primers sequences (Sigma, St. Louis, Missouri, U.S.) used in these qRT-PCR experiments are described below:

Table 6. List of primers and their sequences used for qRT-PCR.

Name	Origin	FP (5´-3)	RP (5´-3´)
Scn1a	Mouse	CATGTATGCTGCAGTTGATTCCA	AACAGGTTCAGGGTAAAGAAGG
SCN1Aco	Human	TCAACATGTACATTGCCGTC	ATCAGCTGCAGTTTGTTGG
GAPDH	Mouse	CCAAGGTCATCCATGACAAC	TGTCATACCAGGAAATGAGC
36b4	Human/Mouse	AACATCTCCCCCTTCTCCTT	GAAGGCCTTGACCTTTTCAG

5. Nav1.1 quantification by Western Blot

5.1. Preparation of membrane-enriched extracts

Since Nav1.1 is a complex transmembrane voltage-gated sodium channel, samples were processed as previously described[216,224] to specifically obtain the denatured membrane-enriched extracts. Briefly, tissue samples were homogenized using a homogenization pestle in ice-cold buffer containing 10 mM Tris-HCl (pH 7.4) (Invitrogen™, Thermo Fisher Scientific, Waltham, MA, U.S.), 320 mM sucrose (Sigma, St. Louis, Missouri, U.S.), phosphatase inhibitors including 5 mM sodium fluoride (NaF, Sigma, St. Louis, Missouri, U.S.) and 0.1 mM sodium orthovanadate (Na_3VO_4, Sigma, St. Louis, Missouri, U.S.), protease inhibitors: Complete™ Protease Inhibitor Cocktail tablets (Roche, Indianapolis, IN, USA) and 0.1 mM phenylmethylsulfonyl fluoride (PMSF, Sigma, St. Louis, Missouri, U.S.), and calcium and magnesium chelating agents such as 5 mM EDTA (Sigma, St. Louis, Missouri, U.S.) and 1 mM

ethylene glycol tetraacetic acid (EGTA, Sigma, St. Louis, Missouri, U.S.) prepared in dH_2O. Homogenates were maintained on ice for 30 min and centrifuged at 700 g for 10 min at 4°C. Nuclei and large tissue debris mainly remained in pellets, which were discarded. Supernatants were centrifuged again at 37,000 g for 40 min at 4°C and removed to resuspend precipitates in a buffer containing 10 mM Tris-HCl (pH 7.4), 0.1 mM Na_3VO_4, 0.1 mM PMSF, 5 mM NaF, 1 mM EGTA, and protease inhibitors mixture tablets dissolved in dH_2O.

Protein content was determined by Bradford assay, and all extracts were adjusted to the same protein concentration and volume in resuspension buffer.

5.2. Protein extracts denaturalization

Each protein extract was solubilized in 0.1 volume of denaturing buffer solution: 20% of sodium dodecyl-sulphate (SDS, Sigma, St. Louis, Missouri, U.S.) and 50 % of β-mercaptoethanol (Sigma, St. Louis, Missouri, U.S.). After 5 min of boiling at 100°C, samples were diluted 1:20 in a second denaturing buffer containing 0.1% of Triton X-100 (Sigma, St. Louis, Missouri, U.S.), 50 mM Tris-HCl (pH 7.4), and dH_2O. Denatured membrane-enriched extracts were centrifuged at 37,000 g at 4°C for 10 min, storing supernatants at -80 °C until use.

5.3. Western blotting

Ten to fifteen µg of denaturalized proteins were mixed with 4x Urea loading buffer [0.2 M Tris-HCl (pH8), 4% of urea, 277 mM of SDS, 0.4 M DTT (Sigma, St. Louis, Missouri, U.S.), 6 mM bromophenol blue (250 µg/Ml, Sigma, St. Louis, Missouri, U.S.) and dH_2O] and were incubated at 60°C for 5 min. Then, mixes were charged and resolved in biphasic 7.5% SDS-polyacrylamide gels. The Amercham™ ECL™ Rainbow™ Marker – Full Range (GE Healthcare Bio-Sciences AB, Sweden) was used as protein molecular weight marker. Protein electrophoresis was performed at 100 V in the Mini-PROTEAN® Tetra Vertical Electrophoresis Cell (Bio-Rad, Hercules, California, U.S.) at 4°C until de higher molecular weight bands of the marker were completely separated. Then, proteins were transferred to a polyvinylidene difluoride (PVDF) membrane (Immobilon®- FL; 0.45 µm pore size; Merck Millipore Ltd., Tullagreenm Carrigtwohill) previously activated in methanol for 5 min. Transference was carried out at 30 V at 4°C overnight in the Trans-Blot™ cell (Bio-Rad, Hercules, California, U.S.). The next day, the membrane and SDS-polyacrylamide gel were stained with Ponceau S solution and brilliant blue

R dye (Sigma, St. Louis, Missouri, U.S.), respectively. After washing the membrane with dH_2O and Tris buffered saline with Tween-20 (TTBS) (0.13 M NaCl, 0.150 M Tris-HCl (pH 7,4), dH_2O and 0.1% Tween-20), it was blocked for 1 h with 5% BSA dissolved in TTBS, in continuous soft shaking. For detection of Nav1.1 and GAPDH proteins, rabbit polyclonal anti-Nav1.1 (1:250; Cat# ASC-001; Alomone Labs, Israel) and rabbit monoclonal (14C10) anti-GAPDH (1:5,000; Cat# 2118S; Cell Signalling Technology, MA, U.S.) primary antibodies were used, respectively, diluted in 2.5% BSA, 0.05% Tween-20 and 0.01% azide in tris buffered saline (TBS). Incubation of membranes was performed overnight at 4°C. After 3 washes with TTBS, membranes were incubated for 1 h at RT with the secondary antibody anti-rabbit IgG HRP conjugate (1:10,000, Cat# NA934, GE Healthcare, IL, U.S.) diluted in 1 % BSA, 0.05 % Tween-20 and 0.01 % azide in TBS. Finally, the membrane was washed twice with TTBS.

The membrane was revealed with a mix of solution A and solution B of chemiluminescent reagents (1:1; Cat# TLA-100, Lumigen ECL Ultra TMA-6, Lumigen, Inc, MI, U.S.). Optical density of signals was obtained with a ChemiDoc™ MP Imaging system (Bio-rad, Hercules, California, U.S.) and quantified with ImageLab™ software (Bio-rad, Hercules, California, U.S.).

6. Statistical analysis

Statistical analysis was performed using GraphPad Prism 6.01 (GraphPad software, San Diego, CA, U.S.). Unless otherwise indicated, results are represented as mean with standard error of mean (SEM). Normality of distributions was evaluated by D'Agostino and Pearson omnibus normality test and statistical comparisons between groups were conducted using the Mann-Whitney test; or the parametric one-way ANOVA with Tukey´s post-test in case of normal distributions, and the non-parametric Kruskal-Wallis with Dunn´s post-test when samples did no present a normal distribution. In the WMM, the Friedman test was applied to test intra-group improvement over trials. The Log-rank test was employed to compare the survival distributions among groups. The significance level was set at $p < 0.05$. Animal and sample size as well as the statistical test employed for each experiment is detailed in the scatter plot graphs.

Results

Results

Part I. Epileptic, cognitive, behavioral, and motor characterization of a novel mouse model of DS

1. Establishment of the colony of the transgenic mouse model of DS

A novel heterozygous KI mouse model of DS carrying the missense A1783V mutation in exon 26 of the *Scn1a* gene was characterized. This mouse line, referred as *Scn1a*$^{WT/A1783V}$, was obtained by breeding males of the B6(Cg)-Scn1a$^{tm1.1Dsf}$/J strain (The Jackson Laboratory, stock no. 026133) with females from the B6.C-Tg(CMV-Cre)1Cgn/J strain (The Jackson Laboratory, stock no. 006054). These strains are referred hereinafter as Scn1a$^{WT/lox}$ and CMV-Cre, respectively. One of the *Scn1a* alleles in the Scn1a$^{WT/lox}$ strain contains exon 26 flanked by *loxP* sites, followed by another exon 26 harbouring the A1783V mutation. When Scn1a$^{WT/lox}$ mice are crossed with CMV-Cre mice, the floxed 26 exon can suffer Cre-mediated scission and the A1783V mutation is incorporated in the mature mRNA expressed from this allele. Since the B6.C-Tg(CMV-Cre)1Cgn/J strain expresses the Cre recombinase under the control of the ubiquitous promoter CMV, the A1783V mutation occurs in one *Scn1a* allele from all body tissues, mimicking the genetic defect observed in most DS patients. The result of this mating protocol is approximately 50% of the offspring with a WT genotype (*Scn1a*$^{WT/WT}$ mice) and the other 50% with one WT and one mutated allele (*Scn1a*$^{WT/A1783V}$ mice), mimicking DS patients. Pups were weaned at 3-4 wo and all experiments were carried out in age-mated males and females of both *Scn1A*$^{WT/A1783V}$ and *Scn1a*$^{WT/WT}$ genotypes.

Body weight of male and female mice was measured weekly from the third to the eighth weeks of age. Results showed a significantly reduced body weight of *Scn1a*$^{WT/A1783V}$ in both genders compared to *Scn1a*$^{WT/WT}$ littermates. Linear regression of body weight curves of *Scn1a*$^{WT/A1783V}$ and *Scn1a*$^{WT/WT}$ controls showed significant differences in elevation ($p<0.001$) but not in slope (Figure 19).

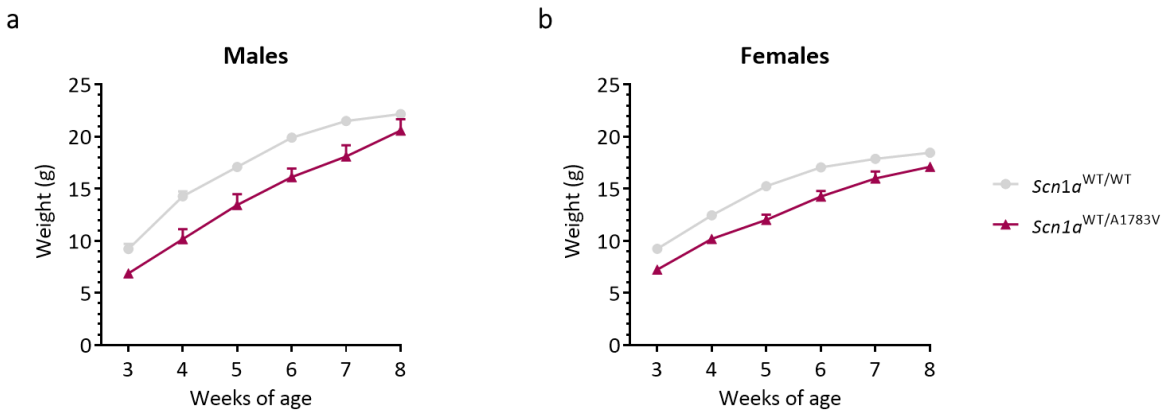

Figure 19. Progression of body weight of *Scn1a*$^{WT/WT}$ and *Scn1a*$^{WT/A1783V}$ mice from the 3rd to the 8th weeks of age. Body weight representation of males (*Scn1a*$^{WT/WT}$ n=40; *Scn1a*$^{WT/A1783V}$ n=15) (**a**) and females (*Scn1a*$^{WT/WT}$ n=30; *Scn1a*$^{WT/A1783V}$ n=20) (**b**). Points represent mean values ± SEM. Significant differences were observed in elevation ($p<0.001$) but not in slope by lineal regression analysis.

2. Survival rate of *Scn1a*$^{WT/A1783V}$ mice

A 24% mortality rate was observed in the Scn1a$^{WT/lox}$ x CMV-Cre offspring. Genotyping of all dead pups confirmed that they corresponded to *Scn1a*$^{WT/A1783V}$ mice in all analyzed cases. Once animals were genotyped at 3 wo, the control of survival rate was more accurately analyzed. Starting from the total percentage of *Scn1a*$^{WT/A1783V}$ survivors at PW3, survival rate of these mice dramatically decreased until the sixth week of age (approximately P40), resulting in 25% long-term survivors. Death rate from PW6 to the end of the study (P120) was lower than 10% (Figure 20). In contrast, the survival rate of *Scn1a*$^{WT/WT}$ littermates was virtually of 100% throughout the study, demonstrating the high mortality rate associated with the *Scn1a* A1783V mutation.

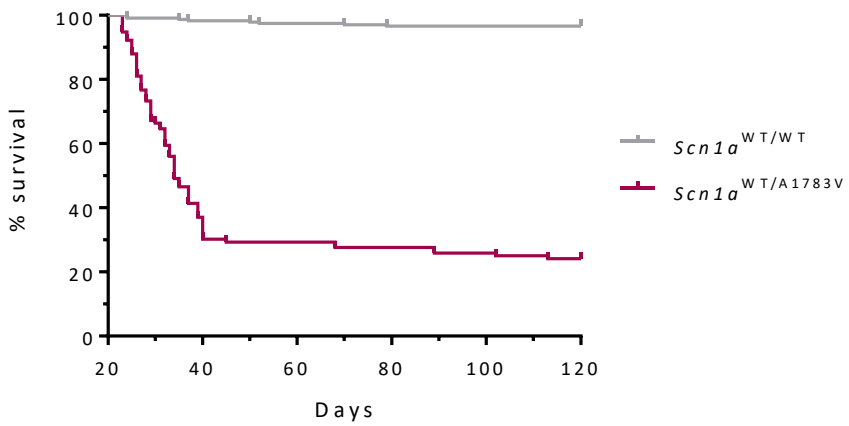

Figure 20. *Scn1a*$^{WT/A1783V}$ mice presents a high mortality rate. Control of mortality was exhaustively analyzed after weaning (P21) to P120. *Scn1a*$^{WT/WT}$ (n=219) and *Scn1a*$^{WT/A1783V}$ (n=116) survival curves were significantly different. $p<0.001$, log-rank test.

As mentioned in the introduction, SUDEP in DS mice can occur as a consequence of bradycardia after a GTCS[21]. Although continuous monitoring of animals is not currently feasible in our facilities, we firstly documented spontaneous seizures in 15% of mice after PW3, although after exhaustive observation of an increased number of mice during longer periods this incidence is around 25%. Despite the limitations of this visual monitoring, this percentage of spontaneous seizures seems too low to explain all cases of SUDEP. Therefore other mechanism including respiratory control could play a key role[25].

3. Analysis of *Scn1a* expression

In order to determine if the *Scn1a*-A1783V mutation induced any change in *Scn1a* expression, *Scn1a*$^{WT/A1783V}$ and *Scn1a*$^{WT/WT}$ mice ranging from 5 to 8 months of age were employed to perform a molecular analysis at mRNA and protein levels in several brain regions.

After sacrifice of animals, one brain hemisphere was used to determine the *Scn1a* mRNA levels by qRT-PCR in Ctx, HC, and Cb. The values were normalized against *GAPDH* mRNA and represented as percentage *vs* *Scn1a*$^{WT/WT}$ controls. *Scn1a*$^{WT/A1783V}$ mice showed no changes in *Scn1a* mRNA levels in Ctx and Cb (*Scn1a*$^{WT/WT}$ *vs* *Scn1a*$^{WT/A1783V}$ 92.7 ± 8.2%, and 91.2 ± 4.2% in Ctx and Cb, respectively), and a reduction in HC (70.9 ± 5.4%) (Figure 21).

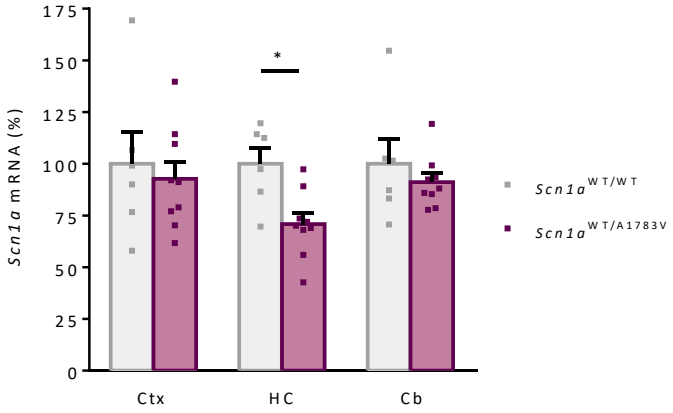

Figure 21. *Scn1a*$^{WT/A1783V}$ mice show a reduction of *Scn1a* mRNA in HC. Mice with the indicated genotypes were sacrificed at 5-8 months of age for analysis of *Scn1a* mRNA by qRT-PCR. Values were normalized against *GAPDH* mRNA levels and calculated as percentage *vs* *Scn1a*$^{WT/WT}$ controls (*Scn1a*$^{WT/WT}$ n=6; *Scn1a*$^{WT/A1783V}$ n=9). Data were analyzed by Kruskal-Wallis with Dunn´s post-test (*p<0.05) and represented as mean ± SEM.

The same structures coming from the other hemisphere were employed to determine the Nav1.1 content in membrane-enriched protein extracts by WB. Representative blots of Nav1.1 and the housekeeping gene GAPDH are shown in figure 22a. Densiometric analysis of Nav1.1 bands normalized to GAPDH shows a slight, non-statistically significant reduction of in *Scn1a*$^{WT/A1783V}$ mice compared with *Scn1a*$^{WT/WT}$ littermates (83.5 ± 7.6%, 90.3 ± 12.2% and 97.2 ± 6.4% in Ctx, HC and Cb, respectively (Figure 22b).

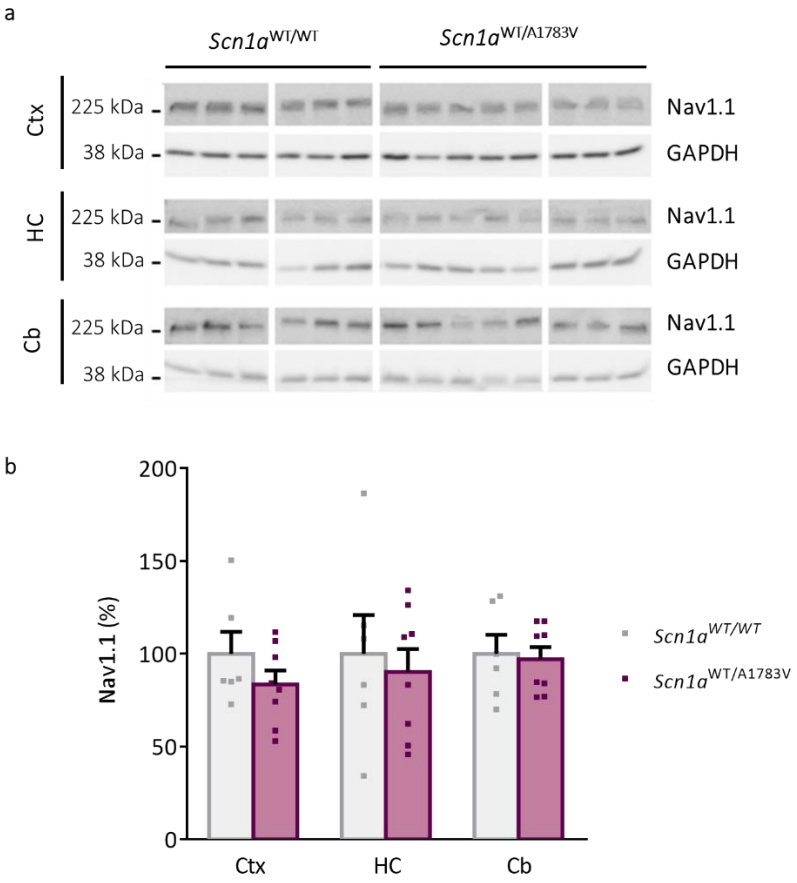

Figure 22. Total Nav1.1 content in the brain is similar between *Scn1a*$^{WT/WT}$ and *Scn1a*$^{WT/A1783V}$ mice. Mice with the indicated genotypes were sacrificed at 5-8 months of age for analysis of Nav1.1 content by WB in the indicated brain structures. (**a**) Representative blots showing Nav1.1 and GAPDH bands. Original blots were cropped and re-arranged to display animals and brain regions grouped. Molecular weights expressed in kDa correspond with the bands of the molecular marker. (**b**) Quantification of Nav1.1 content obtained from densiometric analysis of blots. Individual values were normalized against their corresponding GAPDH levels and represented as mean ± SEM percentages of values *vs* *Scn1a*$^{WT/WT}$ controls (*Scn1a*$^{WT/WT}$ n=6; *Scn1a*$^{WT/A1783V}$ n=8). No statistical differences were detected between *Scn1a*$^{WT/WT}$ and *Scn1a*$^{WT/A1783V}$ mice when data were analyzed by one-way ANOVA with Tukey`s post-test.

The IF assay was used to examine the spatial pattern of Nav1.1 expression in brain samples of *Scn1a*$^{WT/A1783V}$ and *Scn1a*$^{WT/WT}$ mice. Brain slides were stained with a rabbit polyclonal anti-Nav1.1 (green) and DAPI (blue) for nuclei. Images of pCtx, DG, and Cb were taken in a fluorescence microscope, detecting no obvious differences in Nav1.1 content between *Scn1a*$^{WT/A1783V}$ and *Scn1a*$^{WT/WT}$ groups (Figure 23a). Moreover, brain slices were visualized under confocal laser scanning microscope (Figure 23b).

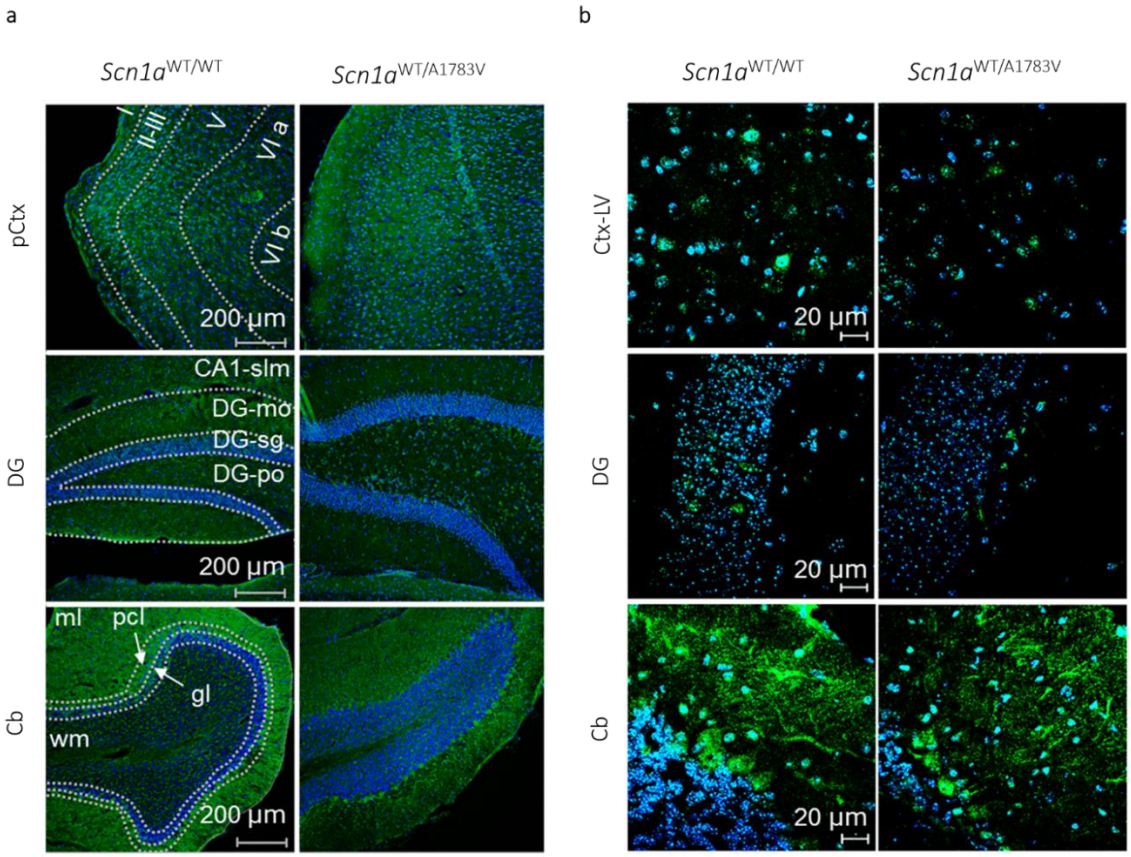

Figure 23. Detection of Nav1.1 by IF. Mice with the indicated genotypes were sacrificed at 5-8 months of age for immunohistological analysis of Nav1.1 expression (green). (**a**) Images acquired by fluorescence microscope in pCtx, DG, and Cb (n=4). The different structures of each brain region were delimited by dotted lines according to the Allen adult mouse brain reference atlas. In pCtx roman numbers indicate the different layers. In DG the lines indicate the stratum lacunosum-moleculare of CA1 (CA1-slm), molecular layer (GD-mo), granule cell layer (DG-sg), and polymorph layer (DG-po) of DG. In Cb the molecular layer (ml), white matter (wm), Purkinje cell layer (pcl), and granule layer (gl) are indicated (**b**) Visualization under confocal laser scanning microscope of cortical layer V (Ctx-LV), DG, and Cb of *Scn1a*$^{WT/WT}$ and *Scn1a*$^{WT/A1783V}$ mice (n=4 for both groups).

4. Hyperthermia-induced seizures in *Scn1a*$^{WT/A1783V}$ mice

Since the first and main triggering factor of seizures in DS patients is hyperthermia episodes (induced by elevated environmental temperatures or fever), the *Scn1a*$^{WT/A1783V}$ mouse model was subjected to elevated temperatures to determine their febrile/hyperthermia-seizure threshold. For this purpose, *Scn1a*$^{WT/A1783V}$ mice and their corresponding *Scn1a*$^{WT/WT}$ littermates were exposed to a gradual increase of environmental temperatures ranging from 25°C to a maximum of 45°C or until the appearance of a GTCS. Both genotypic groups were divided into three different age intervals: 1-2, 2-4 and 4-6 months of age.

All *Scn1a*$^{WT/A1783V}$ mice suffered a behavioral seizure including manifestations corresponding to scores 6-7 of Racine´s scale[222]. Average threshold was 38.4°C for *Scn1a*$^{WT/A1783V}$ mice including all ages (figure 24a). No significant differences were observed among the different age groups (37.9 ± 0.7°C, 38.4 ± 0.6°C, and 37.8 ± 0.7°C for 1-2, 2-4 and 4-6 months, respectively).

In contrast, less than 80% of *Scn1a*$^{WT/WT}$ mice suffered seizures. Among them, the global temperature threshold was 43.0°C, with no differences between age groups (42.7 ± 0.3°C, 43.0 ± 0.3°C, and 43.5 ± 0.4°C for 1-2, 2-4 and 4-6 months, respectively).

In summary, we found a strong reduction of febrile-seizure threshold in *Scn1a*$^{WT/A1783V}$ mice compared with *Scn1a*$^{WT/WT}$ controls in all age groups (***$p<0.001$, One-way ANOVA with Tukey´s post-test), with a difference of more than 4°C. Figure 24b shows the cumulative seizure probability; i.e., the distribution of probability to suffer a seizure at a given temperature for each group at different age intervals. Data showed that the risk to suffer a seizure for *Scn1a*$^{WT/WT}$ mice comprised from 40ºC to 45°C in all ages. In contrast, *Scn1a*$^{WT/A1783V}$ mice presented a range from 31°C to 45°C for the age interval of 1-2 months, and ranges starting from 34°C to 42°C and 36°C to 41°C for age intervals of 2-4 and 4-6 months, respectively.

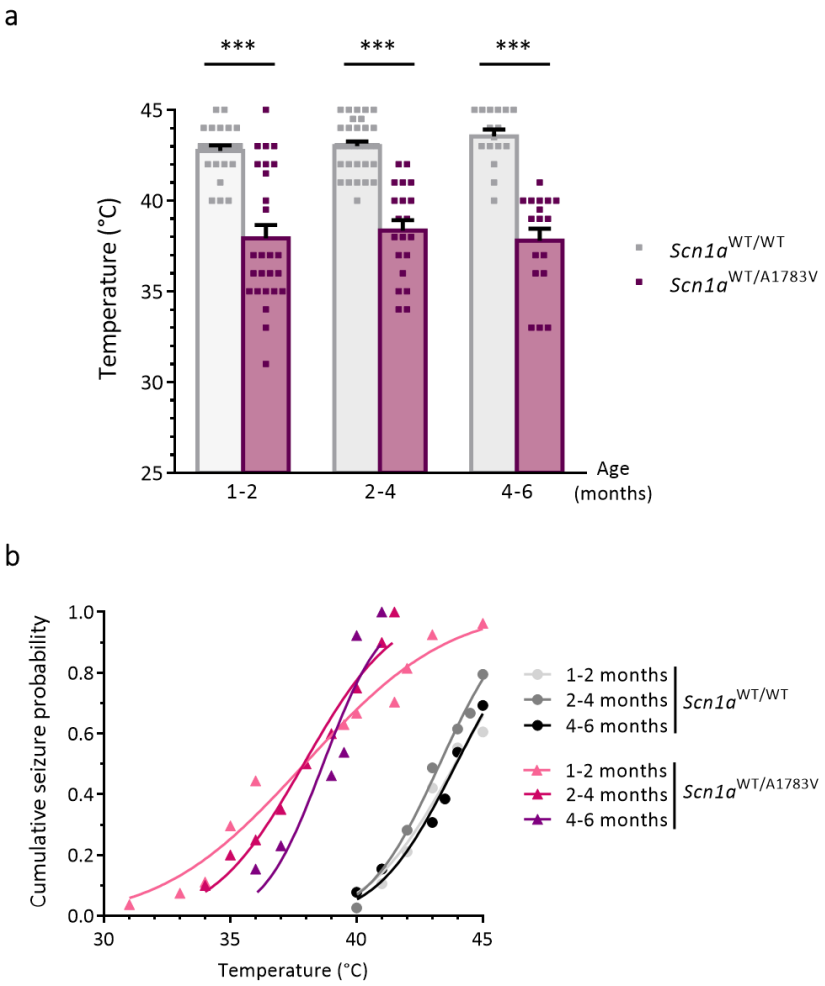

Figure 24. *Scn1a*$^{WT/A1783V}$ show a marked predisposition to hyperthermia-induced seizures. Age-matched *Scn1a*$^{WT/A1783V}$ and control littermates of the indicated age ranges were subjected to controlled increases in ambient temperature up to 45°C. (**a**) The graph shows individual temperatures at the initiation of TCS and the average of each group. Thresholds were significantly lower in *Scn1a*$^{WT/A1783V}$ mice compared to *Scn1a*$^{WT/WT}$ controls in all age intervals tested. *Scn1a*$^{WT/WT}$: 1-2 months n=23, 2-4 months n=31; 4-6 months n=16; *Scn1a*$^{WT/A1783V}$: 1-2 months n=26, 2-4 months n=20; 4-6 months n=17. *** p<0.001, One-way ANOVA with Tukey´s post-test. Data are represented as mean temperature ± SEM. (**b**) Cumulative seizure probability of mice depending on the ambient temperature. The Y axis shows the fraction of mice experiencing seizures below a given temperature (in X axis).

5. Electrophysiological characterization of *Scn1a*$^{WT/A1783V}$ mice

The electrophysiological analysis of the novel *Scn1a*$^{WT/A1783V}$ mouse model was carried out thanks to the specialized contribution of the laboratory directed by Dr Julio Artieda and Dr Miguel Valencia in the Neuroscience Program at CIMA.

These experiments were performed in five *Scn1a*$^{WT/A1783V}$ mice and five *Scn1a*$^{WT/WT}$ littermates from one to three months of age by multisite recordings of electrophysiological activity in pCtx and HC regions. Each mouse was firstly recorded during 30 min in freely moving in an OF arena at RT. During this time local field potentials (LFP) together with simultaneous video recordings were obtained and analyzed, revealing the presence of IEDs in all the *Scn1a*$^{WT/A1783V}$ mice on basal conditions. Both focal (presence of IEDs in a single channel) and generalized (presence of IEDs across several channels simultaneously) distributions were observed in these mice (Figure 25). As expected, no IEDs were detected in any of their *Scn1a*$^{WT/WT}$ littermates.

Next, mice were subjected to a gradual increase of ambient temperatures from 28 to 42°C while brain activity was recorded. None of the *Scn1a*$^{WT/WT}$ mice showed evidence of IEDs during the experiment nor the presence of clinic or subclinic seizures (defined as electrical seizures with and without behavioral manifestations, respectively) (Figure 25a). In contrast, all *Scn1a*$^{WT/A1783V}$ mice showed the presence of numerous IEDs at increasing temperatures that ultimately led to the appearance of clinical (4/5) or subclinical (1/5) heat-induced seizures (Figure 25b). Visualization of video and electrophysiological recordings allowed the correlation of electrophysiological and behavioral findings to the rRS for mice[222]. At first stages of the experiment, IEDs appeared randomly superimposed on the ongoing baseline activity with no behavioral manifestation. At higher temperatures, electrical activity deceleration and intermittent IEDs were accompanied with behavioral manifestations compatible with scores 0-2 of the rRS, following a stabilization of electrical activity (rhythmic) with clear neck jerks, head nodding and clonic tail elevation (score 3). Finally, the electrical activity started to show intermittent clusters of high amplitude polyspikes and spike-wave discharges separated by flat EEG periods, accompanied by behavioral manifestations compatible with rRS 5-6 (TCS lying on belly or side and wild jumping). Seizures usually persisted several minutes after removing the animal from the recording/heating chamber, stopping only when placing mice in a colder environment. In one case, the increase of temperature induced a SE of GTCS leading to death. In two cases electrophysiological recordings allowed detection of a focal origin in the DG of the HC with further generalization to other areas of the HC and pCtx (Figure 25c).

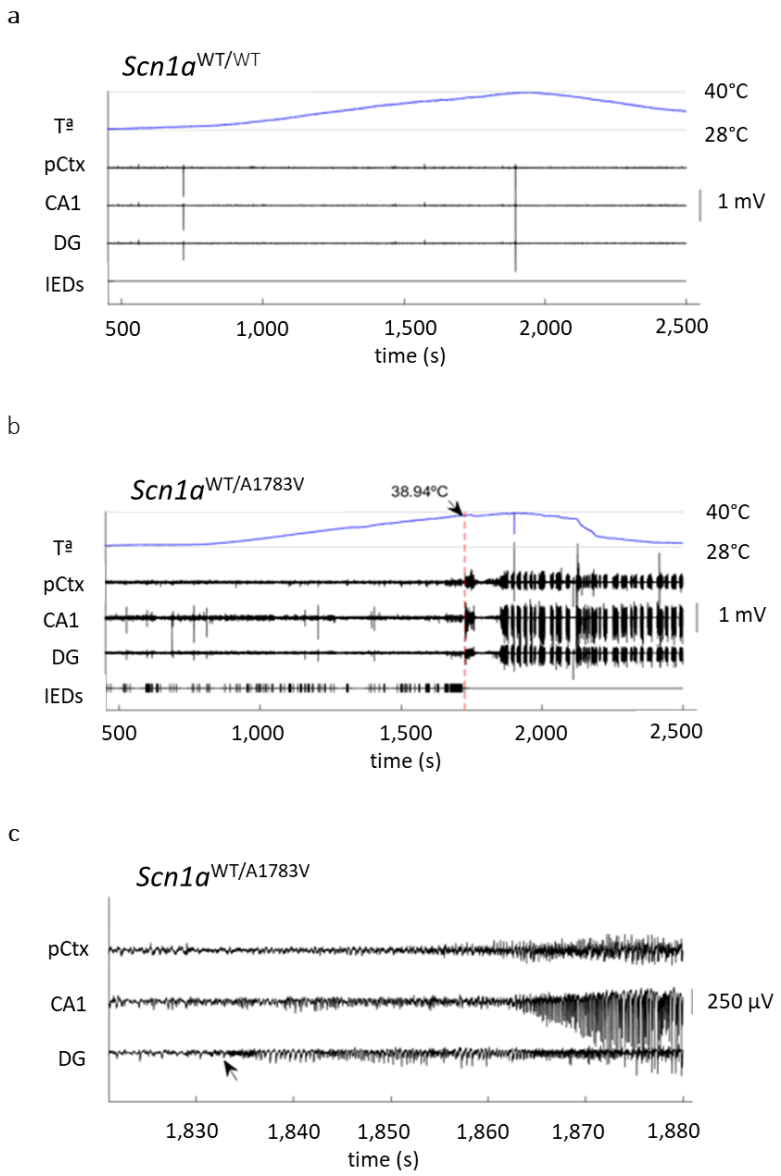

Figure 25. *Scn1a*$^{WT/A1783V}$ mice present an elevated number of IEDs. Electrical activity of *Scn1a*$^{WT/WT}$ and *Scn1a*$^{WT/A1783V}$ mice (n=5 for both groups) was measured during the gradual increase of environmental temperature. Electrodes were placed in the pCtx, CA1 and DG regions of the HC. The heat source was switch on at t=800 s. Representation of the electrical activity recorded in a representative *Scn1a*$^{WT/WT}$ (**a**) and a *Scn1a*$^{WT/A1783V}$ mouse (**b**). Neither IEDs nor seizures were observed in any of the 5 *Scn1a*$^{WT/WT}$ animals. In the *Scn1a*$^{WT/A1783V}$ mouse, the seizure started at 38.94°C around t=1,700 s. Despite the heat source was immediately disconnected, seizures persisted and were organized in clusters, even when the animal was removed from the recording chamber (around t=2,250 s). Of note, IEDs were present at RT (t<1,000 s) and their frequently increased as the temperature raised, reaching a maximum right before the seizure onset. (**c**) Example of a seizure in a *Scn1a*$^{WT/A1783V}$ mouse with focal origin in the DG that is further generalized (pointed by the arrow).

6. Neurological characterization of *Scn1a*$^{WT/A1783V}$ mice

In order to determine if this novel mouse model of DS is a suitable preclinical tool for the development of new treatments for DS, it is mandatory to perform an exhaustive study of all clinical manifestation to correlate them with those observed in DS patients. For this reason, a wide battery of cognitive, behavioral, and motor tests was conducted in the *Scn1a*$^{WT/A1783V}$ mice, which evidenced the presence of neurological comorbidities resembling those suffered by DS patients.

6.1. Assessment of cognitive deficits

The cognitive delay observed in DS patients has been correlated with alterations in task learning and visuo-spatial memory tests in several mouse models of DS[39,60,83,89]. Therefore, *Scn1a*$^{WT/A1783V}$ mice were subjected to the following tests.

6.1.1. Morris water maze

Scn1a$^{WT/A1783V}$ and *Scn1a*$^{WT/WT}$ mice were subjected to the MWM test in order to evaluate their working and spatial learnings. Both groups were tested at 1-3, 3-5 and 5-8 months age ranges.

» **Visible platform phase**

This first phase of the MWM test consists of a training in which mice should learn to escape from water by reaching the VP located in one of the four virtual quadrants of the circular pool. After 5 consecutive days, mice should learn to localize the platform before 60 s, resulting in a reduction of escape latencies throughout the training phase.

As seen in Figure 26, the VP phase of the test revealed that *Scn1a*$^{WT/A1783V}$ mice learned the new task more slowly than the littermate *Scn1a*$^{WT/WT}$ controls. The escape latencies of *Scn1a*$^{WT/A1783V}$ mice were significantly higher at any age interval compared to their age-matched *Scn1a*$^{WT/WT}$ littermates in all steps of the test. Notwithstanding, significant learning was present in both groups throughout the training phase (Friedman test, $p \leq 0.001$ in all groups), indicating that *Scn1a*$^{WT/A1783V}$ mice were able to learn the scape task, although with a slower pace. These data correlate with the cognitive delay (but not regression) observed in DS patients.

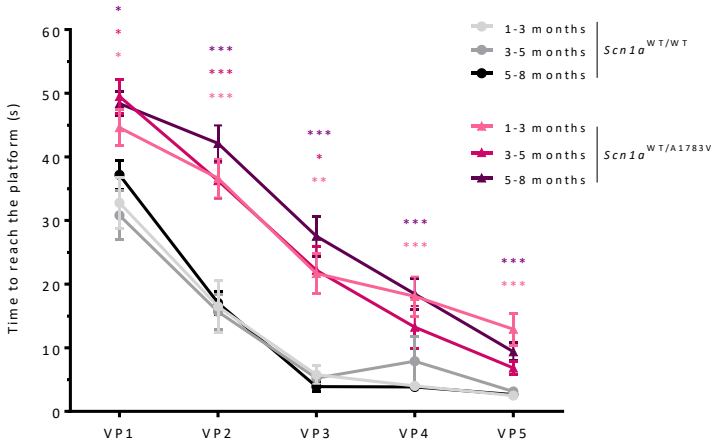

Figure 26. *Scn1a*$^{WT/A1783V}$ mice show a learning delay in the performance of MWM-VP. During 5 consecutive days, mice were trained to find the platform to escape from water. The VP phase carried out in different age intervals showed an increased time to reach the platform in the *Scn1a*$^{WT/A1783V}$ mice compared with their *Scn1a*$^{WT/WT}$ controls. *Scn1a*$^{WT/WT}$: 1-3 months n=11; 3-5 months n=12; 5-8 months n=20; and *Scn1a*$^{WT/A1783V}$: 1-3 months n=17; 3-5 months n=10; 5-8 months n=22. *p<0.05, **p<0.01, ***p<0.001 (one-way ANOVA with Tukey´s post-test for VP1-2 and Kruskal-Wallis with Dunn´s post-test for VP3-VP5). Even so, Friedman test revealed significant learning in both *Scn1a*$^{WT/A1783V}$ and *Scn1a*$^{WT/WT}$ groups (p<0.001). Points represent the average time to reach the platform for each group.

» **Invisible platform phase**

Once all animals passed the training phase, they were subjected to the spatial memory task of the test. In the IP phase, mice should create a spatial map using the surrounding visual cues to localize the hidden platform below the level of colored water. In case of mice suffering a cognitive impairment, they will not be able to find the platform guided by the external cues, and they will show increased escape latencies compared to healthy animals.

Dramatic differences in escape latencies were observed between *Scn1a*$^{WT/A1783V}$ and *Scn1a*$^{WT/WT}$ groups (Figure 27). *Scn1a*$^{WT/A1783V}$ mice were unable to create a spatial map using the visual cues, exhibiting higher escape times than *Scn1a*$^{WT/WT}$ controls with virtually no improvement over the training. In contrast, *Scn1a*$^{WT/WT}$ mice reduced their latency times as training progressed (p<0.001, Friedman test). Statistical differences between *Scn1a*$^{WT/A1783V}$ and *Scn1a*$^{WT/WT}$ groups at any age interval were evident from the IP2 until the end of the invisible phase.

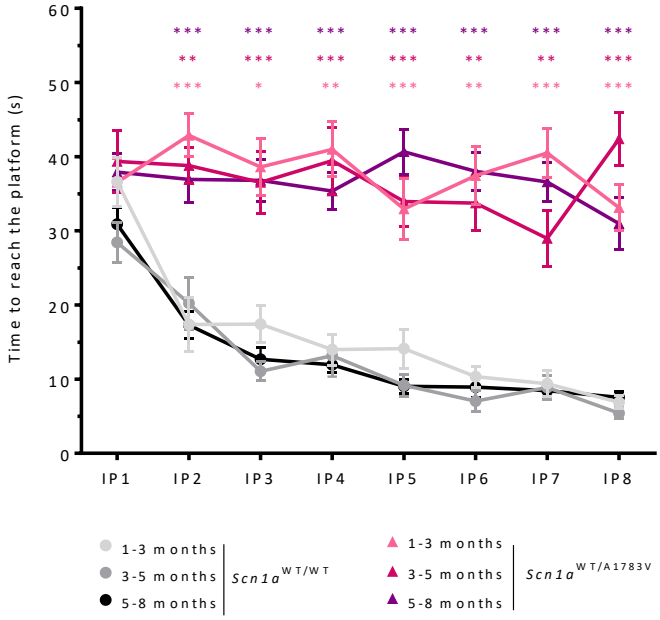

Figure 27. *Scn1a*$^{WT/A1783V}$ mice suffer a spatial learning delay in the MWM-IP. During 8 consecutive days, mice were challenged to find the hidden platform helped by visual cues. *Scn1a*$^{WT/WT}$: 1-3 months n=11; 3-5 months n=12; 5-8 months n=26; and *Scn1a*$^{WT/A1783V}$: 1-3 months n=17; 3-5 months n=10; 5-8 months n=23. Friedman test was used for the analysis of learning curves ($p<0.001$ for *Scn1a*$^{WT/WT}$ and $p>0.05$ for *Scn1a*$^{WT/A1783V}$ mice), indicating lack of learning in *Scn1a*$^{WT/A1783V}$ mice. *$p<0.05$, **$p<0.01$, ***$p<0.001$ (one-way ANOVA with Tukey´s post-test for IP5 and IP8; and Kruskal-Wallis with Dunn´s post-test for IP1-4, IP6-7). Points represents the average time to reach the platform for each group.

» **Probe test**

In order to determine the rate of memory consolidation, on days 4th, 7th and 9th of the IP mice were subjected to the probe test, which measures the time spent searching in the right quadrant of the pool in the absence of the platform, during a period of 15 and 60 s.

In agreement with the lack of spatial learning, *Scn1a*$^{WT/A1783V}$ mice showed no clear preference for any quadrant (~25% time of permanence in the target one), demonstrating a defect in memory retention in both Probe 15 (Figure 28a) and Probe 60 (Figure 28b). Although *Scn1a*$^{WT/A1783V}$ mice spent up to 35% of the time in the right quadrant in the last probe 15, this was lower than age-related *Scn1a*$^{WT/WT}$ mice ($p<0.001$ Kruskal-Wallis test).

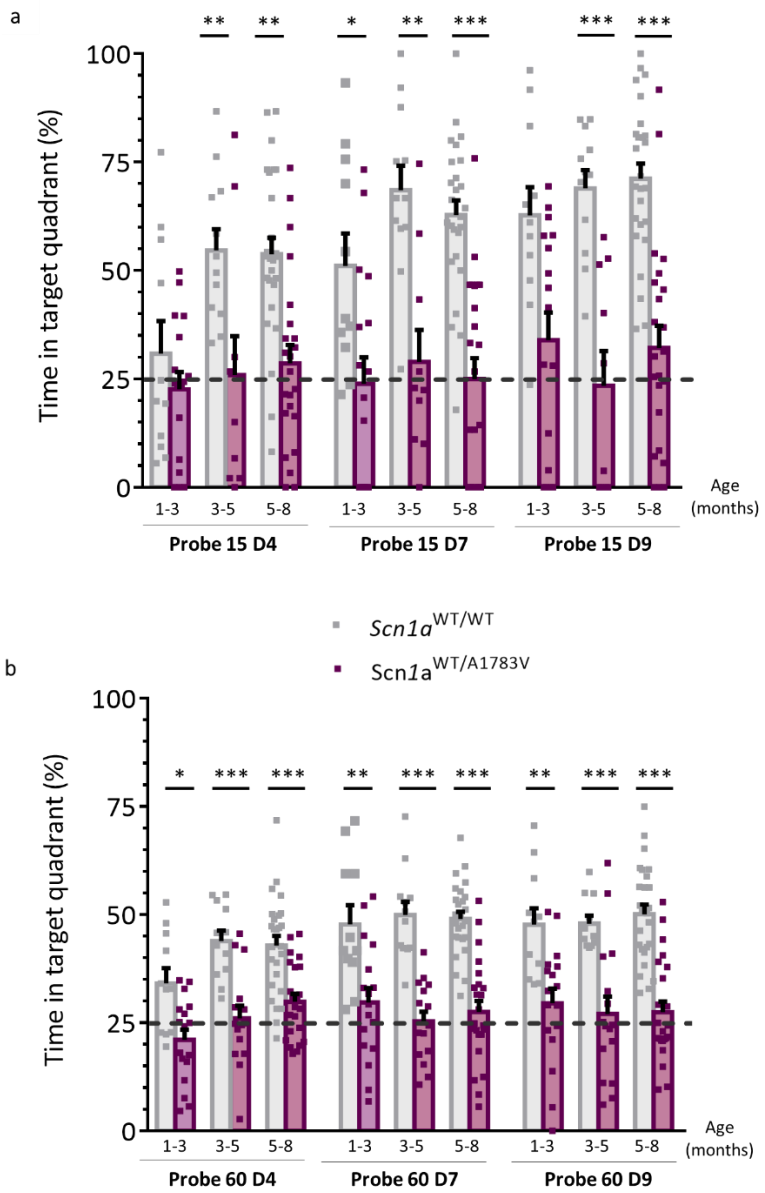

Figure 28. *Scn1a*$^{WT/A1783V}$ mice present memory retention defects in the MWM-Probes tests. On days 4, 7 and 9, memory retention was evaluated by the probe test at the first 15 s **(a)** and in 60 s **(b)**. The graphs represent the percentage of time spent in the right (target) quadrant of the pool at each age interval. *Scn1a*$^{WT/WT}$: 1-3 months n=11; 3-5 months n=12; 5-8 months n=26; and *Scn1a*$^{WT/A1783V}$: 1-3 months n=17; 3-5 months n=10; 5-8 months n=23. Values are represented as mean percentage of time in the target quadrant ± SEM. Squares indicate individual values. *p<0.005, **p<0.01, ***p<0.001 (one-way ANOVA with Tukey´s post-test for Probe 15 day 4 and Probe 15 day 7 and all Probes 60, and Kruskal-Wallis with Dunn´s post-test for Probe 15 day 9).

6.1.2. Novel object recognition test

Supporting the cognitive assessment performed by learning and memory retention of MWM, visuospatial memory was also evaluated through the NOR test, as described in the Methods section.

Age ranges of evaluated mice were the same as in the MWM test. In this case, *Scn1a*$^{WT/A1783V}$ mice retained their ability to remember a familiar object 1 h after the training phase (NOR 1 h), showing values above 50% of exploration in all cases (*Scn1a*$^{WT/WT}$ *vs* *Scn1a*$^{WT/A1783V}$ 68.5 ± 2.9 *vs* 63.5 ± 3.7% at 1-3 months; 68.6 ± 4.1 *vs* 61.4 ± 5.0% at 3-5 months; and 66.4 ± 3.6 *vs* 59.8 ± 3.9% at 5-8 months) (Figure 29).

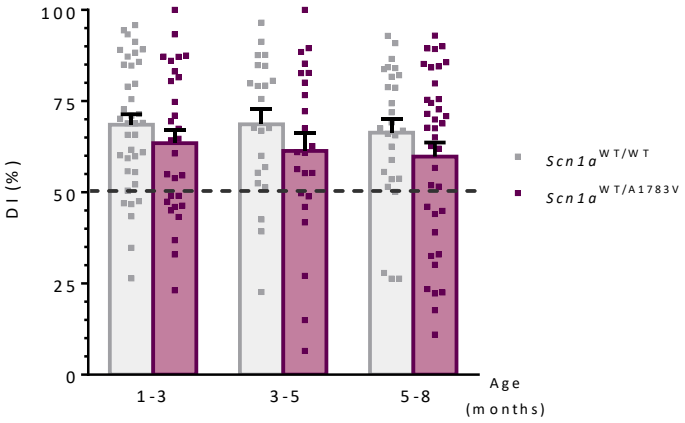

Figure 29. *Scn1a*$^{WT/WT}$ and *Scn1a*$^{WT/A1783V}$ mice exhibit similar short-term visuospatial memory in the NOR 1 h. Mice from the indicated age intervals were exposed to familiar and novel objects 1 h after training. The graphs show the percentage of time spent exploring the novel object over the total exploration time (DI). *Scn1a*$^{WT/WT}$: 1-3 months n=38; 3-5 months n=22; 5-8 months n=27; *Scn1a*$^{WT/A1783V}$: 1-3 months n=29; 3-5 months n=23; 5-8 months n=37. No statistically significant differences were observed (one-way ANOVA with Tukey´s post-test). Data are represented as the mean ± SEM. Squares indicate individual values.

In contrast, an impairment of long-term visuospatial memory was detected in the NOR 24 h in *Scn1a*$^{WT/A1783V}$ mice. The reduced exploratory preference towards the novel object was significantly marked in the 3-5 and 5-8 age ranges, showing values around 50% (*Scn1a*$^{WT/A1783V}$ *vs* *Scn1a*$^{WT/WT}$ 1-3 months: 70.2 ± 3.1% *vs* 58.6 ± 3.9%, 3-5 months: 66.4 ± 4.6% *vs* 47.1 ± 4.1% and 5-8 months: 65.3 ± 3.1% *vs* 47.5 ± 3.8%) (Figure 30). These results indicate a defect in LTM in this *Scn1a*$^{WT/A1783V}$ mouse model, supporting the deficit in learning and spatial memory retention observed in the MWM.

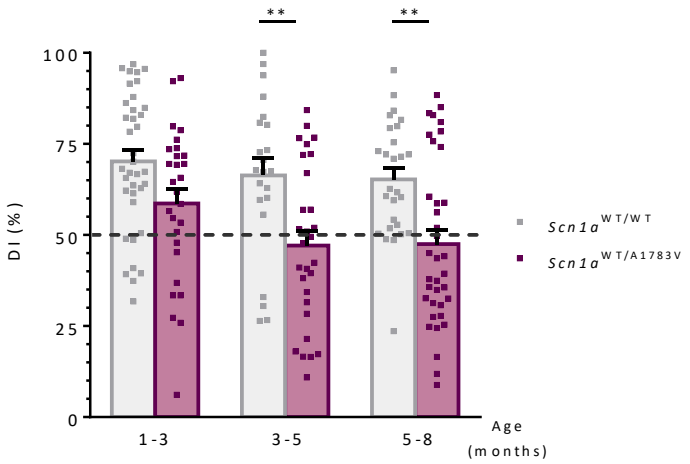

Figure 30. *Scn1a*$^{WT/A1783V}$ mice present a reduced long-term visuospatial memory in the NOR 24 h performance. Mice from the indicated age intervals were exposed to familiar and novel objects 24 h after training. The graphs show the percentage of time spent exploring the novel object over the total exploration time (DI) *Scn1a*$^{WT/WT}$: 1-3 months n=37; 3-5 months n=22; 5-8 months n=27; and *Scn1a*$^{WT/A1783V}$: 1-3 months n=28; 3-5 months n=29; 5-8 months n=36. Values are represented as mean ± SEM. Squares indicate individual values. **p<0.01 one-way ANOVA with Tukey´s post-test.

6.2. Characterization of behavioral manifestations

Several authors have evidenced the presence of behavioral abnormalities in previous mouse models of DS, usually influenced by the genetic background[60] and the specific *Scn1a* mutation[85,89]. *Scn1a*$^{WT/A1783V}$ mice were also subjected to a battery of behavioral tests, including the OF, marble burying, nesting building, and social interaction tests.

6.2.1. Open-field test

The first parameter analyzed was the time spent in the center of the arena as an anxiety indicator. Compared to *Scn1a*$^{WT/WT}$ controls, *Scn1a*$^{WT/A1783V}$ mice presented a dramatic reduction in this parameter, suggesting a strong anxiety behavior in them, which prioritized the safety of the cage corners over their natural exploratory behavior (*Scn1a*$^{WT/WT}$ *vs* *Scn1a*$^{WT/A1783V}$ 1-3 months: 149.6 ± 7.4 s *vs* 84.2 ± 11.0 s; 3-5 months: 143.5 ± 11.5 s *vs* 60.1 ± 6.3 s; and 5-8 months: 162.1 ± 14.0 s *vs* 79.5 ± 20.5 s) (Figure 31).

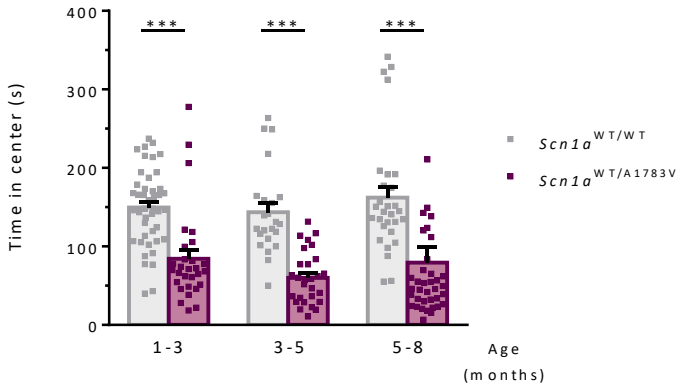

Figure 31. *Scn1a*$^{WT/A1783V}$ mice spent less time in the center of the arena. Mice from the indicated age groups were recorded in the OF arena during 15 min, and the time spent in the center of the space is represented. *Scn1a*$^{WT/WT}$: 1-3 months n=44; 3-5 months n=23; 5-8 months n=29; and *Scn1a*$^{WT/A1783V}$: 1-3 months n=29; 3-5 months n=28; 5-8 months n=37. Values are represented as mean time in the center ± SEM. Squares indicate individual values. ***p<0.001, Kruskal-Wallis with Dunn´s post-test.

Additionally, mean values of peaks velocities in the total arena of *Scn1a*$^{WT/A1783V}$ mice were significantly higher than their *Scn1a*$^{WT/WT}$ controls, indicating hyperactivity/impulsivity (*Scn1a*$^{WT/WT}$ *vs* *Scn1a*$^{WT/A1783V}$: 1-3 months, 8.6 ± 0.3 *vs* 10.3 ± 0.5 cm/s; 3-5 months, 8.4 ± 0.7 *vs* 10.8 ± 0.7 cm/s; 5-8 months, 7.5 ± 0.4 *vs* 9.9 ± 0.4 cm/s) (Figure 32). This hyperactivity is in line with the impulsive reactions observed during routine animal handling.

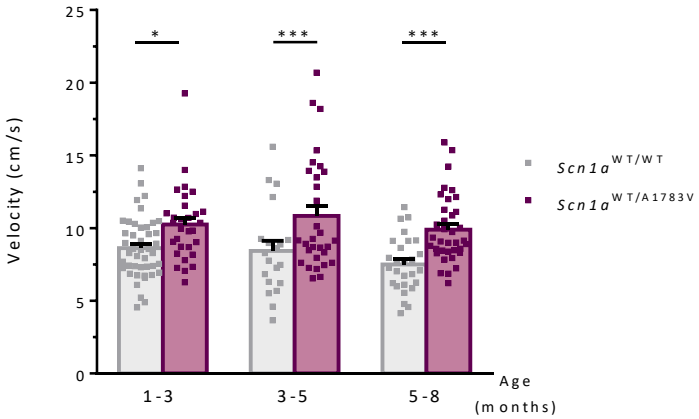

Figure 32. Increased velocity in the total arena of the OF-field in *Scn1a*$^{WT/A1783V}$ mice. Mice from the indicated age groups were recorded in the OF arena during 15 min, and the mean velocity of movements during this period was calculated in cm/s. *Scn1a*$^{WT/WT}$ 1-3 months n=44; 3-5 months n=20; 5-8 months n=27. *Scn1a*$^{WT/A1783V}$ 1-3 months, n=30; 3-5 months, n=30; 5-8 months n=36. Values are represented as mean velocity ± SEM. Squares indicate individual values. *p<0.05, ***p<0.001, Kruskal-Wallis with Dunn´s post-test.

In agreement with these results, an increase in the number of stereotypies was observed in *Scn1a*$^{WT/A1783V}$ mice compared with their *Scn1a*$^{WT/WT}$ littermates, especially frantic and continuous jumps in the walls of the box. This increase started at 3 months of age and become evident in the late stage of the disease (*Scn1a*$^{WT/WT}$ *vs* *Scn1a*$^{WT/A1783V}$ at 1-3 months: 3.0 ± 0.4 *vs* 4.1 ± 0.6; 3-5 months: 3.2 ± 0.6 *vs* 5.2 ± 1.1, and 5-8 months: 2.8 ± 0.5 *vs* 5.4 ± 0.6 stereotypies/min) (Figure 33).

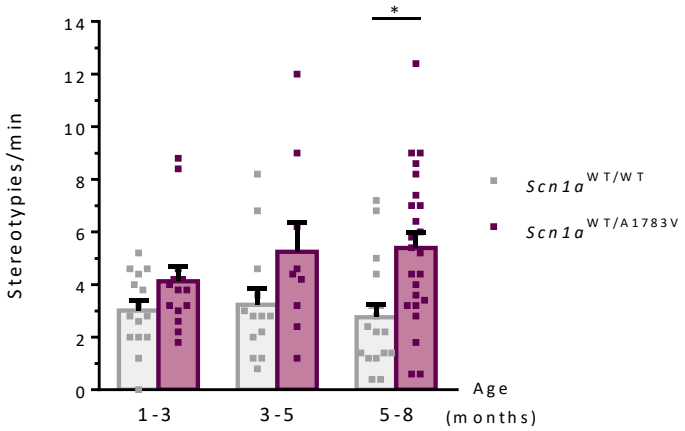

Figure 33. The frequency of stereotypies in *Scn1a*$^{WT/A1783V}$ mice is higher than in *Scn1a*$^{WT/WT}$ controls. Mice from the indicated age groups were recorded in the OF arena during 15 min, and the number of stereotypies per minute was annotated. *Scn1a*$^{WT/WT}$ 1-3 months, n=15; 3-5 months, n=13; 5-8 months, n=17. *Scn1a*$^{WT/A1783V}$ 1-3 months, n=14; 3-5 months, n=9; 5-8 months, n=24. Values are represented as mean ± SEM. Squares indicate individual values. *p<0.05, Kruskal-Wallis with Dunn´s post-test.

6.2.2. Marble burying test

Normal exploratory behavior in mice includes digging and burying objects, suggesting a good interaction with their environment. This behavior parameter could be evaluated by the marble burying test in which each animal is placed in a cage with twelve glass marbles disposed on the surface of the bedding. At the end of the test, quantification of uncovered marbles provides the degree of exploratory behavior: the more uncovered marbles the less interaction with the environment.

The results obtained revealed an increase in the number of uncovered marbles in *Scn1a*$^{WT/A1783V}$ mice at all ages when compared to *Scn1a*$^{WT/WT}$ controls (*Scn1a*$^{WT/WT}$ *vs* *Scn1a*$^{WT/A1783V}$ at 1-3 months: 6.0 ± 0.5 *vs* 10.9 ± 0.3; 3-5 months: 4.5 ± 0.5 *vs* 8.7 ± 0.6; 5-8 months: 4.1 ± 0.5 *vs* 9.6 ± 0.6 uncovered marbles) (Figure 34). Consequently, exploratory behavior was also clearly impaired in this mouse model of DS.

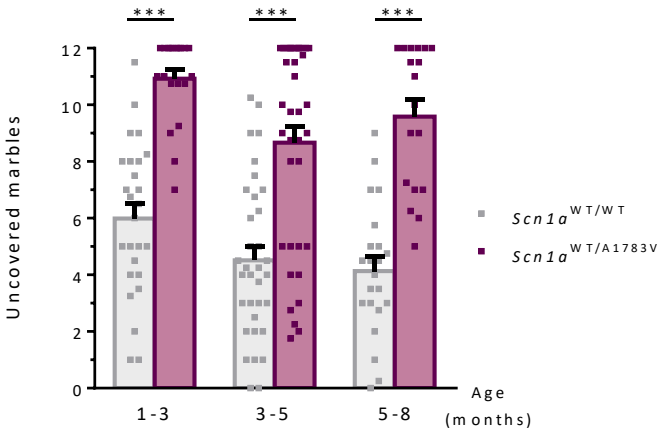

Figure 34. The number of uncovered marbles is higher in *Scn1a*$^{WT/A1783V}$ mice than in control littermates. Mice from the indicated age ranges were placed in a cage with 12 marbles in the surface of the bedding. The amount of buried marbles in 30 min is represented as an indication of exploratory behavior. *Scn1a*$^{WT/WT}$ 1-3 months n=26; 3-5 months, n=34; 5-8 months, n=22. *Scn1a*$^{WT/A1783V}$ 1-3 months, n=20; 3-5 months, n=37; 5-8 months, n=18. Values are represented as mean ± SEM. Squares indicate individual values. ***p<0.001, Kruskal-Wallis with Dunn´s post-test.

6.2.3. Nesting building test

Nest building is considered as a welfare indicator in rodents, which can be altered by illness, injury or other stressors of animals. With the purpose of evaluating this species-adapted behavior and therefore the healthy state of the DS mouse model, mice were provided with nesting material and isolated for one night. The next morning, the presence or the absence of nest and the extent of completion were analyzed.

Data were represented as percentages of mice that built a complete nest, built only a partial nest or hardly touched the nesting material to build a shelter, considered as absent nest. As seen in Figure 35, *Scn1a*$^{WT/WT}$ mice presented higher percentages of complete and partial nests (1-3 months: complete 68%, partial 18% and absent 14%; 3-5 months: complete 67%, partial 25% and absent 8%; 5-8 months: complete 6%, partial 67% and absent 27%), whereas any *Scn1a*$^{WT/A1783V}$ mice barely build nests, with more than 80% of individuals unable to initiate building at all age intervals tested (1-3 months: complete 0%, partial 14% and absent 86%; 3-5 months: complete 5%, partial 11% and absent 84%; 5-8 months: complete 0%, partial 5% and absent 95%).

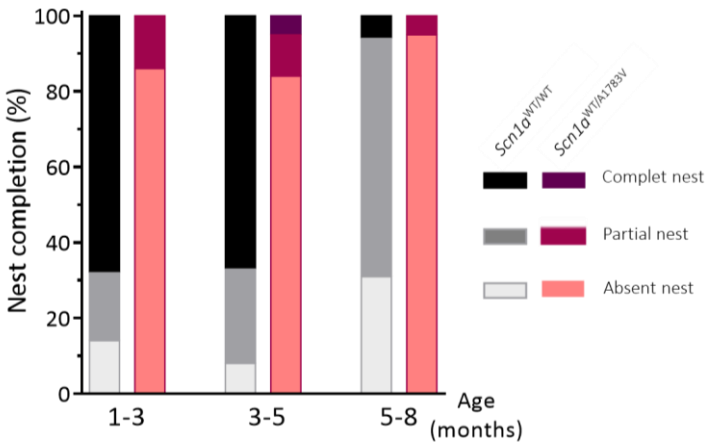

Figure 35. *Scn1a*$^{WT/A1783V}$ mice show a poor performance of nest completion. The intensity of bars indicates the degree of nest building performance for each group and age interval: dark colors represent the building of complete nest, medium colors indicate the presence of an initiated o partial nest, and light colors indicate the total absence of nest. *Scn1a*$^{WT/WT}$ 1-3 months, n=22; 3-5 months, n=12; 5-8 months, n=16. *Scn1a*$^{WT/A1783V}$ 1-3 months, n=14; 3-5 months, n=19; 5-8 months, n=21. Results were calculated as the percentage of *Scn1a*$^{WT/WT}$ and *Scn1a*$^{WT/A1783V}$ animals for each of the three nest building scores.

6.2.4. Social interaction

Several studies have supported de presence of clinical features of autism-like not only in DS patients[225,226] but also in some mouse models of the disease[60,89,91]. To determine if the novel *Scn1a*$^{WT/A1783V}$ mouse model also presented an autism-like behaviour or impairment in social disabilities, each animal was exposed to a non-familial mouse to measure the number of contacts and the latency to the first interaction between them.

In contrast with the previous behavioural alterations, *Scn1a*$^{WT/A1783V}$ mice only showed mild signs of impaired sociability when compared with *Scn1a*$^{WT/WT}$ controls. In fact, only *Scn1a*$^{WT/A1783V}$ mice in the intermediate age group exhibited a moderate reduction in the number of contacts per min (*Scn1a*$^{WT/WT}$ *vs* *Scn1a*$^{WT/A1783V}$ at 1-3 months: 4.7 ± 0.4 *vs* 3.9 ± 0.4; 3-5 months: 5.2 ± 0.4 *vs* 3.7 ± 0.2 and 5-8 months: 4.6 ± 0.4 *vs* 4.1 ± 0.4 contacts/min) (Figure 36a). In agreement with this result, the latency of the first interaction was higher in this age group (*Scn1a*$^{WT/WT}$ *vs* *Scn1a*$^{WT/A1783V}$at 1-3 months: 17.8 ± 4.3 *vs* 19.1 ± 3.2 s; 3-5 months: 8.1 ± 2.0 *vs* 21.1 ± 4.4 s, and 5-8 months: 14.5 ± 3.7 *vs* 18.3 ± 3.3 s) (Figure 36b), suggesting that the main reason for the reduced number of contacts is the delay in the establishment of the first interaction.

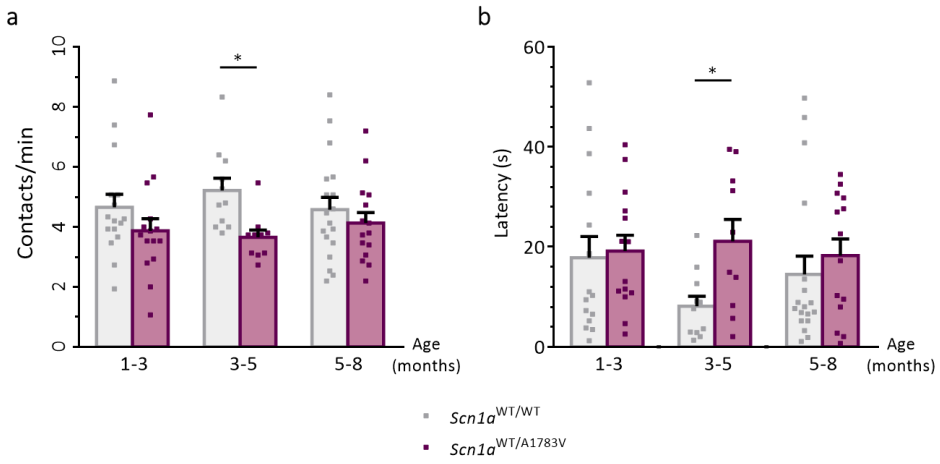

Figure 36. *Scn1a*$^{WT/A1783V}$ mice show mild signs of social impairment. Mice from the indicated age ranges were individually exposed to a non-familial mouse and recorded during 15 min. The number of contacts of the tested mice towards the reference one (**a**) and the latency to the first contact (**b**) are represented. *Scn1a*$^{WT/WT}$ 1-3 months, n=16; 3-5 months, n=11 and 5-8 months, n=18. *Scn1a*$^{WT/A1783V}$ 1-3 months, n=15; 3-5 months, n=10 and 5-8 months, n=15. Values are represented as mean ± SEM. Squares indicate individual values. *p<0.05, Kruskal-Wallis with Dunn´s post-test.

6.3. Evaluation of motor disabilities

In DS patients, motor disabilities become evident during the worsening stage, exhibiting a clear ataxia and unsteady gait[227]. These motor features were also observed in mouse models of DS and were related with the reduction of sodium current and firing action potentials in cerebellar Purkinje neurons[45]. In order to evaluate motor skills of the *Scn1a*$^{WT/A1783V}$ model, mice were subjected to a battery of motor test, including rotarod, inverted grid and elevated beam.

6.3.1. Rotarod

The rotarod test is an optimal tool to evaluate the physical condition of mice, as well as their coordination and balance. After a training period, each mouse was allowed to walk on the rotating rod at increasing velocities, measuring the time they remained walking on it (also referred as latency to fall).

As seen of Figure 37, the ANOVA test showed a reduction in walking ability on the rotarod in *Scn1a*$^{WT/A1783V}$ mice compared with their *Scn1a*$^{WT/WT}$ littermates, especially in the intermediate and older ages (*Scn1a*$^{WT/WT}$ *vs* *Scn1a*$^{WT/A1783V}$ at 1-3 months: 63.0 ± 3.7 *vs* 53.7 ± 8.6 s; 3-5 months: 67.7 ± 9.4 *vs* 45.1 ± 8.0 s, and 5-8 months: 59.2 ± 5.8 *vs* 32.8 ± 4.6 s). These results suggest that motor performance declined over time in this DS mouse model in the same way that happens in DS patients.

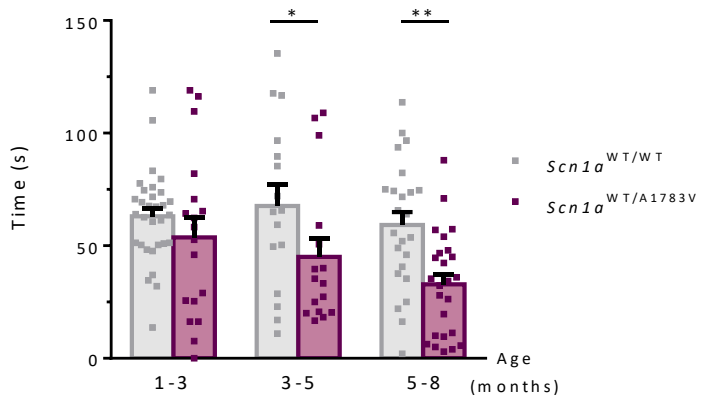

Figure 37. Performance in the rotarod test is reduced in *Scn1a*$^{WT/A1783V}$ mice. Mice from the indicated age ranges were forced to run on the rotary rod after a training period. The graph represents latency to fall. *Scn1a*$^{WT/WT}$ 1-3 months, n=31; 3-5 months, n=16; 5-8 months, n=24. *Scn1a*$^{WT/A1783V}$ 1-3 months, n=18; 3-5 months, n=16; 5-8 months, n=25. Data are represented as mean ± SEM. Squares indicate individual values. *p<0.05, **p<0.01, one-way ANOVA with Tukey´s post-test.

6.3.2. Elevated beam

In addition to the rotarod assessment, the elevated beam test also allowed the evaluation of motor coordination and balance in *Scn1a*$^{WT/A1783V}$ mice. For this purpose, mice were placed in an elevated footbridge, measuring the time they were able to walk through it for a maximum of 2 min. The time they remained in the beam was designated as latency to fall.

In this case, *Scn1a*$^{WT/A1783V}$ mice exhibited lower times walking on the beam compared to *Scn1a*$^{WT/WT}$ mice controls in all of the age intervals tested (*Scn1a*$^{WT/WT}$ *vs* *Scn1a*$^{WT/A1783V}$ at 1-3 months: 119.8 ± 0.2 *vs* 92.1 ± 10.8 s, 3-5 months: 109.7 ± 5.6 *vs* 73.0 ± 10.4 s and 5-8 months: 109.7 ± 5.5 *vs* 65.6 ± 7.0 s) (Figure 38). As observed in the rotarod test, impairment in coordination and balance showed a tendency to worsen over time.

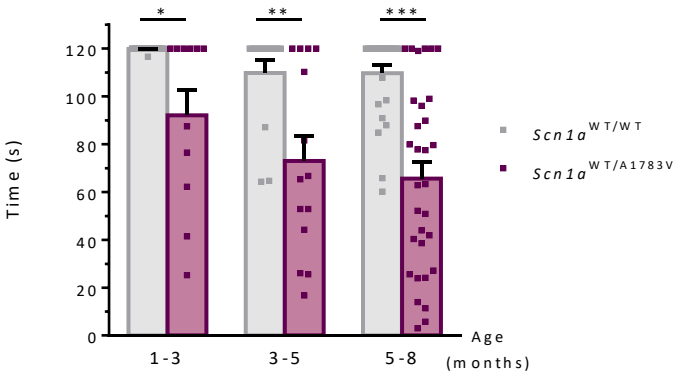

Figure 38. Latency to fall in the elevated beam test is reduced in *Scn1a*$^{WT/A1783V}$ mice. Mice from the indicated age ranges were placed on the elevated footbridge, and the latency to fall is represented. *Scn1a*$^{WT/WT}$ 1-3 months, n=20; 3-5 months, n=14; 5-8 months, n=26. *Scn1a*$^{WT/A1783V}$ 1-3 months, n=11; 3-5 months, n=14; 5-8 months, n=31. Data are represented as mean time ± SEM. Squares indicate individual values. *p<0.05, **p<0.01, ***p<0.001, Kruskal-Wallis with Dunn´s post-test.

6.3.3. Inverted grid

Finally, the performance of the inverted grid test provided information about the strength/weight ratio of the DS mouse model. This test measures how long were mice are able to remain hanging in a grid for a maximum of 60 s.

Statistical differences between *Scn1a*$^{WT/WT}$ and *Scn1a*$^{WT/A1783V}$ groups were observed in all age intervals, with a decreased latency to fall in all *Scn1a*$^{WT/A1783V}$ mice over their corresponding *Scn1a*$^{WT/WT}$ controls (*Scn1a*$^{WT/WT}$ *vs* *Scn1a*$^{WT/A1783V}$ at 1-3 months: 59.60± 0.3 *vs* 44.4 ± 4.4 s; 3-5 months: 55.6 ± 2.3 *vs* 41.5 ± 3.5 s, and 5-8 months: 51.2 ± 3.9 *vs* 33.0 ± 3.7 s) (Figure 39).

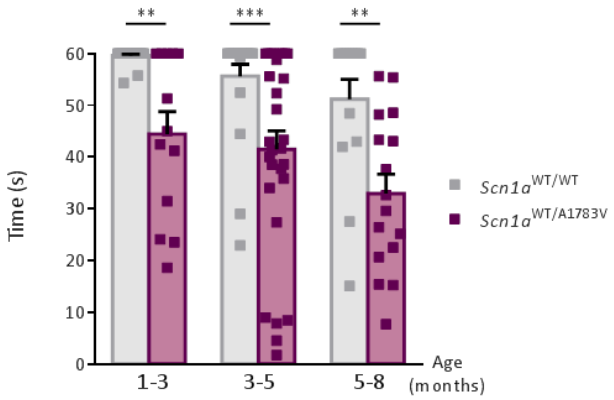

Figure 39. Performance in the inverted grid test is reduced in *Scn1a*$^{WT/A1783V}$ mice. Mice from the indicated age ranges were placed in the inverted grid, and the latency to fall is indicated. *Scn1a*$^{WT/WT}$ 1-3 months, n=25; 3-5 months, n=21; 5-8 months, n=14. *Scn1a*$^{WT/A1783V}$ 1-3 months, n=13; 3-5 months, n=29; 5-8 months, n=16. Data are represented as mean time ± SEM. Squares indicate individual values. **p<0.01, ***p<0.001, Kruskal-Wallis with Dunn´s post-test.

Part II. Proof of concept of *SCN1A* gene supplementation in DS.

7. Validation of plasmids expressing *SCN1A*

The second main aim of this work is to provide a proof of concept about the feasibility of gene supplementation of the entire *SCN1A* coding sequence for the treatment of DS, using the previously characterized mouse model. Our hypothesis is that using HC-AdVs, expression of therapeutic levels of the transgenic Nav1.1 will be maintained for long periods of time after one single administration, avoiding the need for expression of exogenous proteins, and offering the opportunity to treat the disease from its etiological origin.

However, recombinant sodium channels, especially Nav1.1, present particular challenges including their large coding sequence (6 Kb in length in the case of *SCN1A*) and their DNA instability. Alternative splicing of coding exons is the most common mechanism, although RNA editing of specific nucleotide sequences also contributes to the synthesis of different protein variants with changed function and expression patterns[228,229]. To circumvent this issue, it has been proposed a particular cloning protocol including transformation in recombination-free bacteria (for instance Stbl4 competent cells) and growing at low temperatures (27-30°C)[230]. Unfortunately, when the synthesis of the *SCN1A* sequence was ordered to a commercial source, it still contained a substantial fraction of copies with altered pattern (see Appendix Figure 1). It was only by designing a codon-optimized version (hereinafter referred to as *SCN1A*co) when the sequence became stable in *E.Coli*. The codon-optimization is a widely used method to improve recombinant protein expression by accommodating codon bias, which in this case allowed the successful amplification of the *SCN1A* sequence under the recommended conditions.

Once the stable *SCN1A* cDNA was obtained, it was subcloned in several expression cassettes under the control of different ubiquitous regulatory sequences in order to verify the expression and function of the transgene. To this aim, the HEK-293 cell line was chosen due to its low expression of endogenous Nav1.1 levels and its high permissibility for transfection. Cells were transfected with three different plasmids expressing the codon-optimized version of the *SCN1A* sequence: one under the control of the viral CMV early enhancer and promoter, a second one with the hybrid CAG promoter (early CMV enhancer, chicken β-actin promoter with first intron and rabbit β-globin splice acceptor), and the last one with the human EF1α promoter (Figure 40). These promoters have previously shown the ability to mediate effective transgene expression in several neuronal cell

types[231–233]. This last plasmid also co-expressed the reporter gene GFP by virtue of an IRES sequence. The pCDNA3 empty plasmid was used as a negative control.

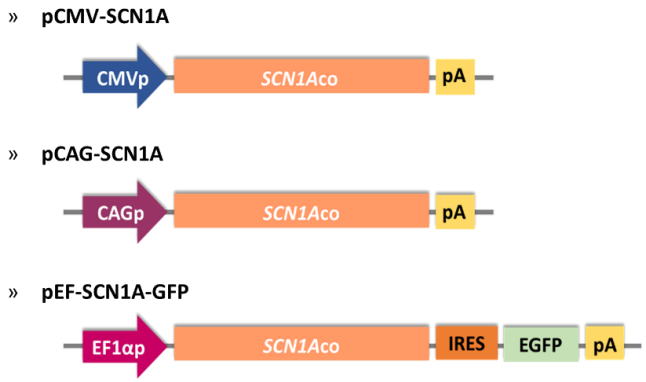

Figure 40. Schematic representation of plasmids carrying the codon-optimized version of *SCN1A*. CMVp, early enhancer and promoter; CAGp, CAG promoter (early CMV enhancer, chicken β-actin promoter with first intron and rabbit β-globin splice acceptor); EF1αp, human elongation factor 1α promoter; IRES, internal ribosomal entry site; EGFP, enhanced green fluorescent protein; pA, poly-adenylation sequence. Not drawn to scale.

Quantification of *SCN1A*co mRNA levels by qRT-PCR 48 h after plasmids transfection confirmed the efficient expression of the transgene under the control of the three promoters. Values were calculated as the number of copies of *SCN1A*co mRNA per cell. (3541.4 ± 1534, 2302.5 ± 246.7 and 565 ± 90.9 copies per cell for pCMV-SCN1A, pCAG-SCN1A, and pEF-SCN1A-GFP, respectively) (Figure 41). Values were compared by the Kruskal-Wallis with Dunn´s multiple comparison test, showing that the EF1α promoter is relatively weaker than CAG (**p<0.01, Kruskal-Wallis with Dunn´s multiple comparison test).

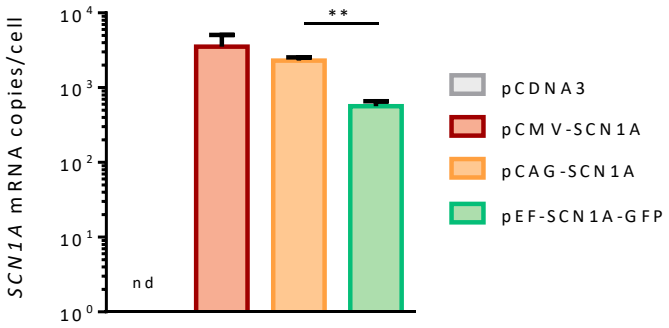

Figure 41. Evaluation of *SCN1Aco* expression plasmids in HEK-293 cells by qRT-PCR. Cells were transfected with the indicated plasmids and mRNA levels were determined 48 h later by qRT-PCR using primers specific for *SCN1Aco*. (pCDNA3 n=7; pCMV-SCN1A n=7, pCAG-SCN1A n=4; pEF-SCN1A-GFP n=4). Values are represented as copies of *SCN1A* mRNA per cell ± SEM. **p<0.01, Kruskal-Wallis with Dunn´s multiple comparison test; nd, not detected.

Next, detection of the Nav1.1 channel was performed by WB analysis in membrane-enriched extracts. Data obtained from the representative blots of Nav1.1 and GAPDH blots (Figure 42a) were

analyzed to obtain the densiometric value of Nav1.1 content for each plasmid. Results were calculated as mean percentage of Nav1.1/GAPDH ratio ± SEM. As expected, the result showed lower Nav1.1 content in cells transfected with pEF-SCN1A-GFP compared with pCAG-SCN1A (Figure 42b).

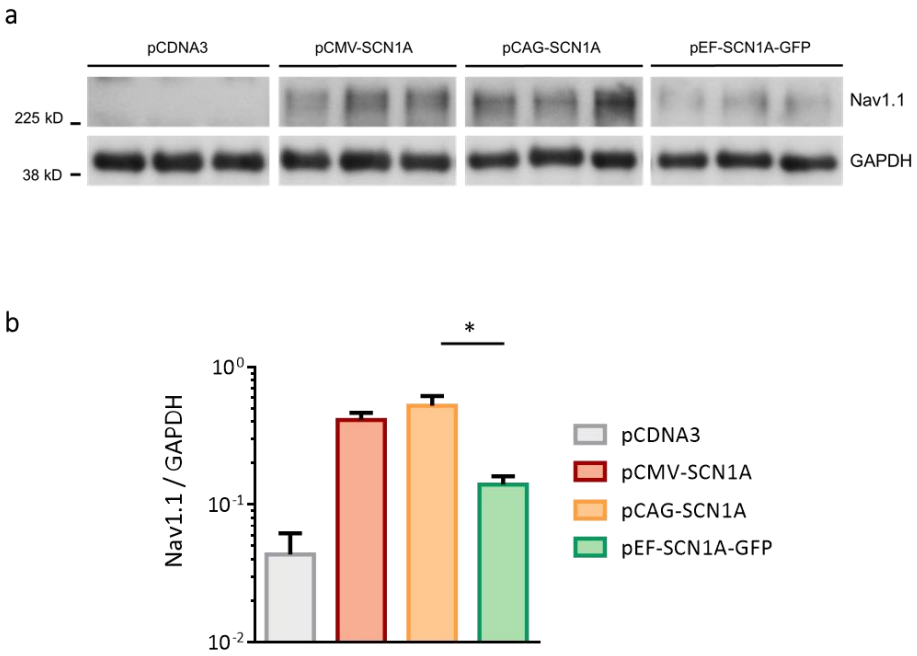

Figure 42. Detection of Nav1.1 content by WB in transfected HEK-293 cells. Cells were transfected with the indicated plasmids, and detection of Nav1.1 content was performed 48 h after cell transfection. (**a**) Representative blots showing Nav1.1 and GAPDH bands. Original blots were cropped and re-arranged. Molecular weights expressed in kDa correspond with the bands of the molecular marker. (**b**) Quantification of Nav1.1 content obtained from densiometric analysis of blots (n=3 for each plasmid). Individual values were normalized against their corresponding GAPDH levels and represented as mean ± SEM. *p<0.05, Kruskal-Wallis with Dunn´s multiple comparison test.

Additionally, Nav1.1 channels were detected by IF assay. As seen in figure 43, Nav1.1 expression is higher in the case of pCMV-SCN1A and pCAG-SCN1A compared with pEF-SCN1A-GFP, following a similar patter as observed by qRT-PCR and WB.

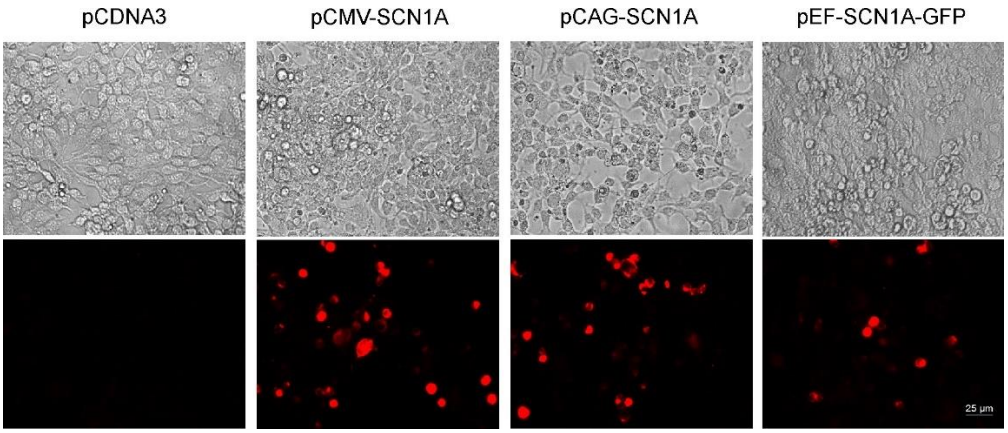

Figure 43. Detection of Nav1.1 by IF assay in transfected HEK-293 cells. Cells were transfected with the indicated plasmids, and 48 h later they were processed for immunostaining. Upper panels correspond to images taken under visible light, whereas lower panels represent the expression of Nav1.1 (red) determined by IF.

The functionality of the Nav1.1 channel expressed from the SCN1Aco transgene was verified by patch-clamp experiments using the pEF-SCN1A-IRES-GFP plasmid, which allows identification of transfected cells under a fluorescence microcopy. These experiments were performed by Jan Tönnesen and Cristina Miguelez in the Achucarro center for neurosciences (Bilbao, Spain) (see Appendix Figure 2).

8. Feasibility of HC-AdVs expressing *SCN1A*

Once it was confirmed the stability and functionality of the *SCN1A*co sequence, a proof of concept of feasibility of vectors expressing *SCN1A* was initiated. Considering the special requirements of cloning capacity and genetic stability, HC-AdVs are suitable candidates. From the repertoire of expression plasmids described above, we discarded pCMV-SCN1Aco because the CMV promoter is prone to silencing *in vivo*[234]. The CAG-SCN1A and EF-SCN1A-IRES-GFP cassettes were introduced in a pro-vector plasmids derived from pDelta28E4[235]. This plasmid contains the AdV´s ITRs and packaging signal as well as non-coding stuffer DNA from human origin. To accommodate these large cassettes, the stuffer DNA in pDelta28E4 was shortened in 5 and 8 Kb to give rise to pD23 and pD20 plasmids, respectively. For initial vector rescue, the resulting pD23-CAG-SCN1A and pD20-EF-SCN1A-GFP plasmids were transfected in the 293-Cre4 packaging cells, which were subsequently infected with the AdTetCre HV, as previously described[203]. We found that both prototypic vectors HCA-CAG-SCN1A and HCA-EF-SCN1A-GFP are feasible and can be produced under standard methods (Figure 44).

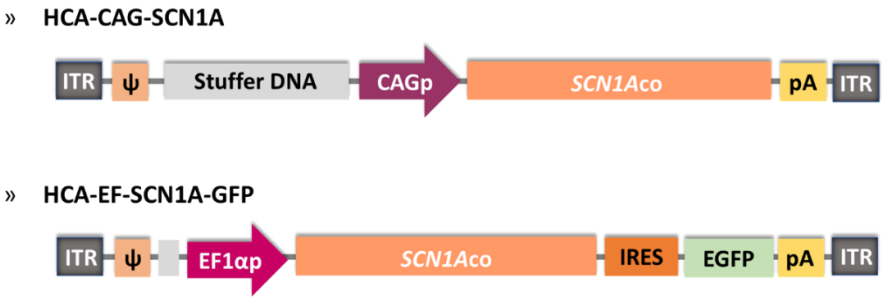

Figure 44. Schematic representation of HC-AdV vectors carrying the codon-optimized version of *SCN1A*. Production of HCA-CAG-SCN1A and HCA-EF-SCN1A-GFP vectors carrying the optimized version of *SCN1A* were feasible using conventional protocols. The genomic structure of vectors are not drawn to scale.

In order to validate the function of these vectors, they were used to infect the SH-SY5Y neuroblastoma-derived cell line at MOIs 10 and 100 (vg/cell). Forty-eight hours later, cells were collected and processed for qRT-PCR and IF assays. Non-infected cells were used as control. The *36b4* gene was employed as housekeeping and results were calculated as $2\Delta CT$[236]. The quantification of *SCN1Aco* mRNA in infected cells demonstrated a dose-dependent effect and a higher expression of HCA-CAG-SCN1A than HCA-EF-SCN1A-GFP (Figure 45) (4567 ± 4210 and 0.2 ± 0.1 2ΔCT for HCA-CAG-SCN1A and HCA-EF-SCN1A-GFP at MOI 100, respectively ($p<0.05$, Kruskal-Wallis with Dunn´s multiple comparison test).

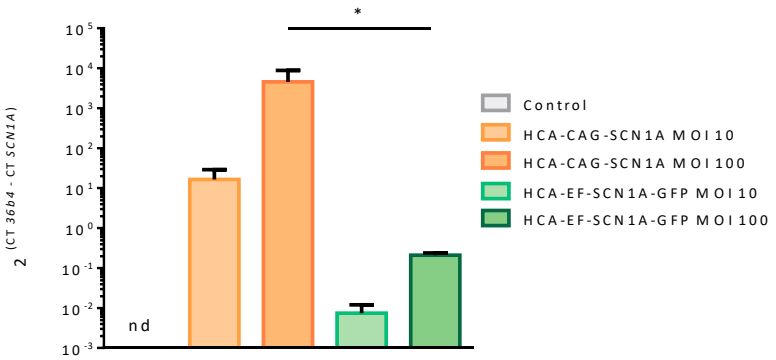

Figure 45. *SCN1A*co mRNA levels of SH-SY5Y cells infected with HCA-CAG-SCN1A are higher than infection with HCA-EF-SCN1A-GFP. Cells were infected with the indicated vectors at MOIs 10 or 100, and cell extracts were obtained 48 h later for quantification of *SCN1A*co mRNA by qRT-PCR. Data are represented as mean 2ΔCT ± SEM. *$p<0.05$, Kruskal-Wallis with Dunn´s multiple comparison test.

These results were confirmed by an IF assay in which higher Nav1.1 content was observed in cells infected with HCA-CAG-SCN1A than HCA-EF-SCN1A-GFP (Figure 46).

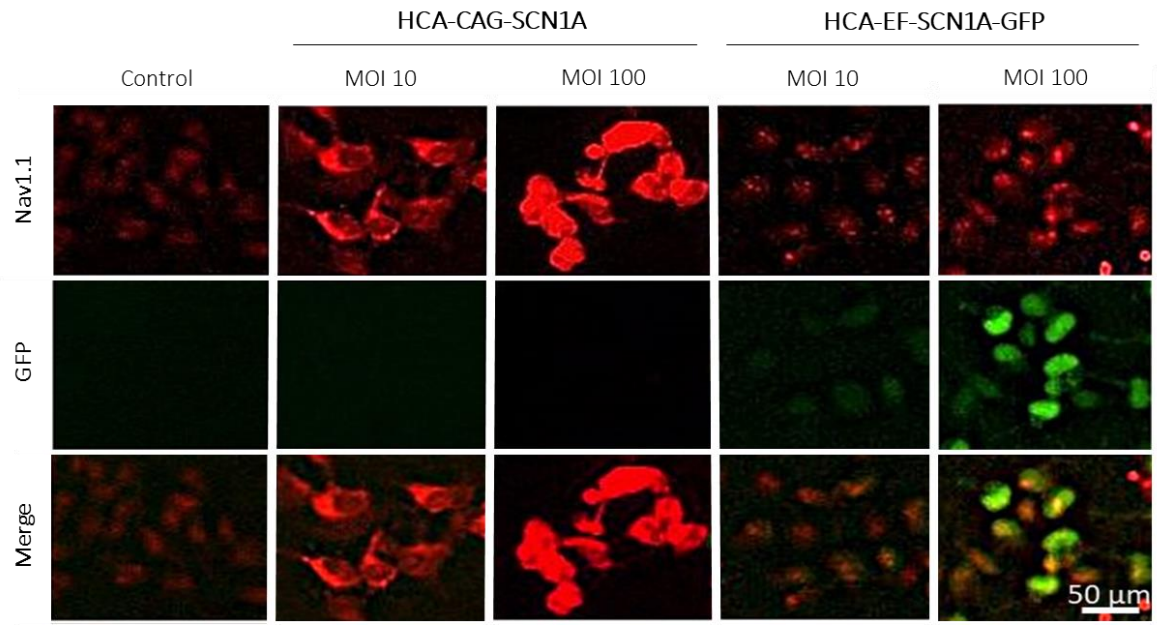

Figure 46. Detection of Nav1.1 by IF in SH-SY5Y cells infected with the vectors. Cells were infected with MOI 10 and 100 of HCA-CAG-SNC1Aco and HCA-EF-SCN1A-GFP vectors and analyzed by IF 48 h later. Upper images correspond to Nav1.1 staining (red), middle images show GFP epifluorescence (green), and lower images are the merge of both staining, with yellow color indicating co-localization of Nav1.1 and GFP.

9. CAG and EF1α promoters: stability of transgene expression in the brain using HC-AdVs

The previous *in vitro* data suggest that the CAG promoter is adequate for transgene expression in neuronal derived cells. However, since this promoter is a synthetic hybrid consisting of viral and eukaryotic sequences, there are some concerns about silencing, as shown in some organs such as the liver[210]. Therefore, to evaluate the *in vivo* stability of transgene expression driven by CAG and EF1α promoters in the brain, HC-AdV vectors expressing the reporter gene luciferase under the control of these promoters were produced. HCA-CAG-Luc and HCA-EF-Luc were bilaterally injected in the brain of C57BL/6 mice (BG and Cb, 2 µL per injection point adjusted to $6.5x10^8$ vg/µL), and luciferase expression was noninvasively monitored by BLI from day 2 post-administration to day 160. In both cases, kinetics of light emission followed a similar pattern in mouse brain, showing an acute decrease during the first 4 weeks and finally a prolonged stabilization stage (Figure 47). This observation is in accordance with expression kinetics obtained in previous studies after intracerebral[208] and systemic[237] administration of HC-AdV vectors. It may reflect the initial transduction of heterogeneous cell populations with different lifespans, or the cessation of inflammatory responses that could inhibit transgene expression. In this case, the result is compatible with long-term expression from neurons, using both promoters.

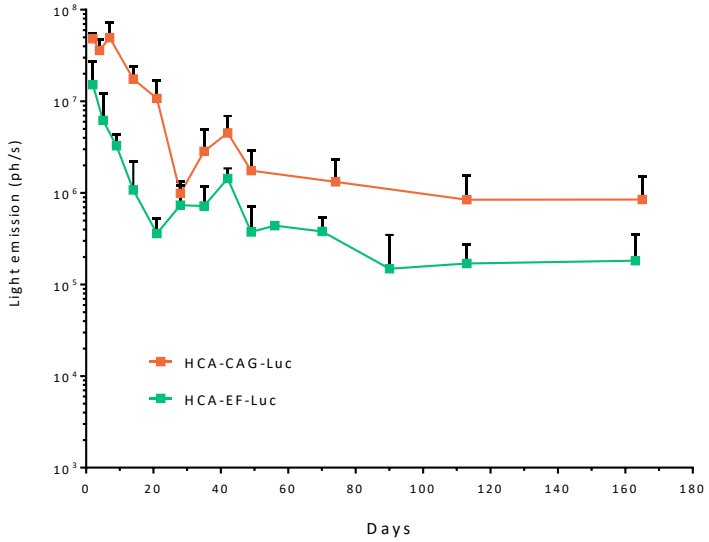

Figure 47. Kinetics of transgene expression in mice treated with HCA-CAG-Luc and HCA-EF-Luc vectors. C57BL/6 mice (n=6) received bilateral injections of the indicated vectors in BG and Cb (2 µL per injection site at $6.5x10^8$ vg/µL), and luciferase activity was monitored by BLI for more than 5 months. The graph shows light emission (in photons (ph)/s) from the head.

Based on the previous results and the antecedents in the literature, we considered the HCA-CAG-SCN1A vector is a suitable tool to perform a proof of concept evaluation of the potential therapeutic effect of *SCN1A*co supplementation.

10. Biodistribution of AdV vectors in the brain

Before evaluating the therapeutic potential of HCA-CAG-SCN1A in the newly characterized DS mouse model we decided to characterize the biodistribution of adenoviral vectors in the brain. DS is a multifocal epilepsy with multiple epileptogenic origins[238,239] and the impairment of Nav1.1 channels in different brain regions[43–45] is associated with other neurological comorbidities. Taking these facts into consideration, a broad *SCN1A* expression throughout the brain would be desirable, although localized expression in critical areas could provide relevant benefits.

Since FGAdV share the same capsid structure as HC-AdV; therefore, these vectors are a cost-efficient way to investigate distribution and tropism throughout the different brain structures. The Ad-CAG-GFPLuc vector is a FGAdV expressing a fusion protein of luciferase and GFP under the control of the CAG promoter. This dual reporter gene allowed global quantification of transduction by luciferase activity and the possibility to identify individual GFP-expressing cells and their specific localization by epifluorescence or microscopy techniques. For this purpose, the Ad-CAG-GFPLuc vector was administered by stereotaxic injection in 5 wo C57BL/6 mice in the following individual

brain structures from both hemispheres: Ctx (including prefrontal, somatosensory, and visual cortex), HC, BG and Cb. Forty-eight hours after surgery, *in vivo* light emission from brains was measured by BLI. Since this type of quantification gives poor spatial resolution because the light is heavily quenched and distorted by the skull (Figure 48), mice were immediately sacrificed, and brains were extracted for detailed analysis. One hemisphere was dissected in several brain structures, including pCtx, ptCtx, HC, Cb, BS, BG and HT to measure their individual luciferase activity expressed as RLU per region for each administration route. Results obtained showed that single administrations in Ctx and BG (Figures 48a and 48c, respectively) presented high values of luciferase activity not only in the injected area but also in other regions including ptCtx, HC, Cb, and HT. Nevertheless, injections in HC and Cb (Figures 48b and 48d) showed good luciferase activity in the injected regions, especially in the case of Cb, but with lower diffusion to other brain areas. These results prompted us to explore some combinations of injections such as BG+Cb and pCtx+BG+Cb. Interestingly, combinations of injected regions were well-tolerated and presented the highest transgene expression in all structures collected, with the exception of pCtx in the case of BG+Cb administration (Figure 48e).

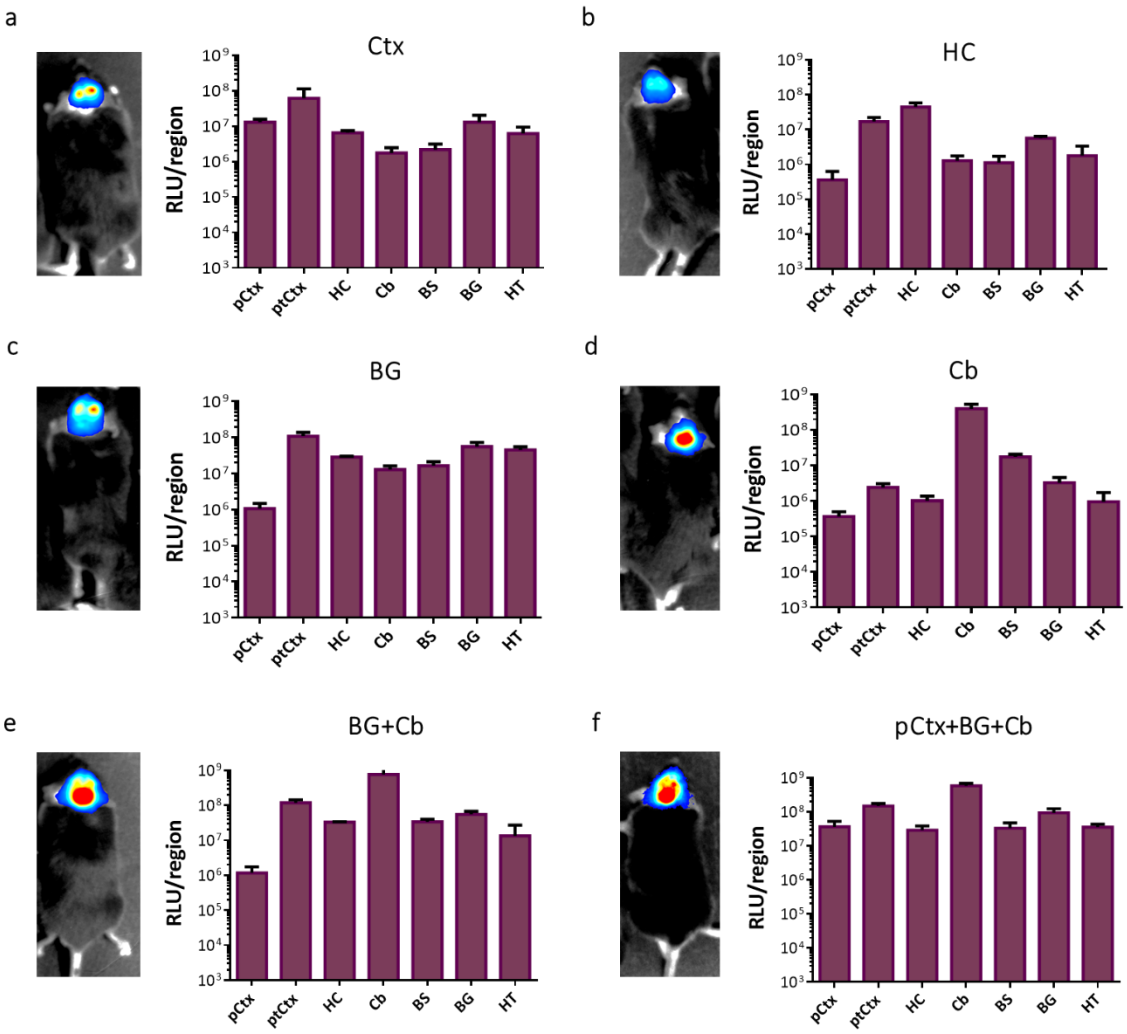

Figure 48. *In vivo* and *ex vivo* luciferase activity in mice injected in different brain regions with the Ad-CAG-GFPLuc vector. The vector was administered to C57BL/6 mice (n=3 for each group and n=7 for the pCtx+BG+Cb group) by bilateral stereotaxic injections in the indicated brain regions (1.5 µL/injection at $3.5x10^7$ vg/µL). Forty-eight hours later, BLI was performed and brains were then dissected in several structures (pCtx, ptCtx, HC, Cb, BS, BG and HT) to quantify the *ex vivo* luciferase activity in tissue extracts using a luminometer (**a**) pCtx, (**b**) HC, (**c**) BG, (**d**) Cb, (**e**) BG+Cb, (**f**) pCtx+BG+Cb. Values correspond to the mean of total luciferase activity (Relative Luciferase Units, RLU) from each brain region ± SEM.

Since the global luciferase activity from each region is influenced by its total tissue mass, in figure 49 we represent the specific luciferase activity relative to the protein content (RLU/µg protein). In agreement with the previous observation, the initial results showed that one single administration in BG was able to achieve a wider distribution of luciferase expression over other brain regions, with relatively lower penetrance in pCtx, Cb, and BS (Figure 49c). Single administration in Ctx showed an intermediate vector diffusion behavior (Figure 49a) between the wide spread of BG and the more restricted expression in the injected area after HC and Cb single administrations (Figures 49b and

49d, respectively). It was only with combinations of injections in different brain structures when the expression was relatively homogeneous, especially with the three-points combination in pCtx+BG+Cb (Figure 49f). Interestingly, HT presented a good transduction, especially after BG and Ctx administrations. The low luciferase activity in the liver in all administration routes indicated that the systemic exposure of the Ad-CAG-GFPLuc vector was marginal, restricting its activity mainly to the brain tissue.

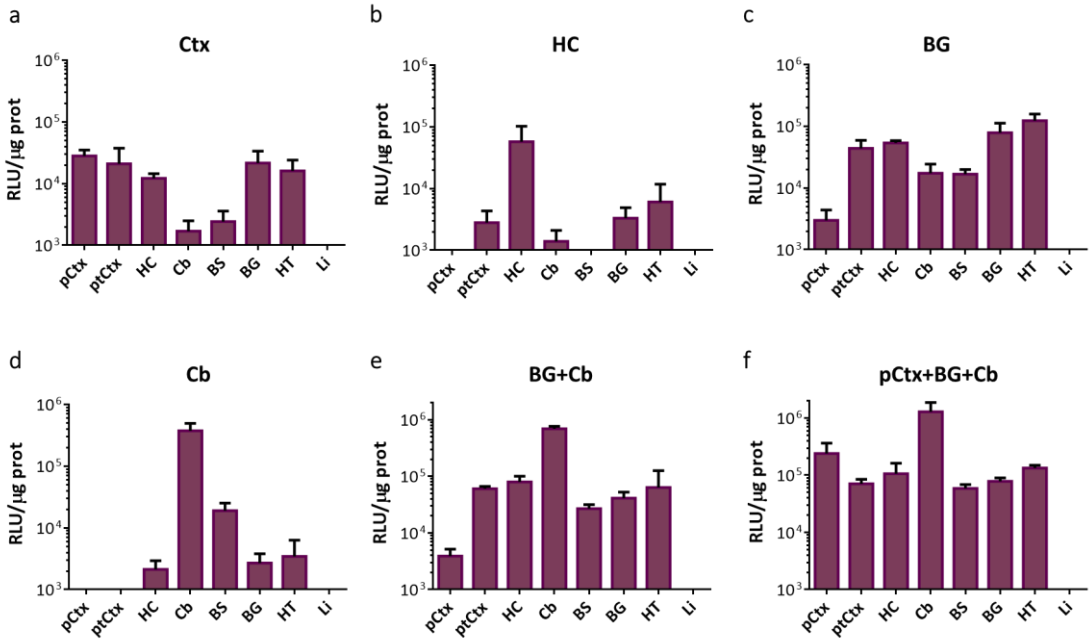

Figure 49. Specific *ex vivo* luciferase activity in mice injected in different brain regions with the Ad-CAG-GFPLuc vector. The vector was administered as described in Figure 48. *Ex vivo* luciferase activity in tissue extracts (pCtx, ptCtx, HC, Cb, BS, BG and HT) is represented as RLU/µg protein. A liver sample (Li) was collected to evaluate extracerebral spread of the vector. (**a**) bilateral administration in pCtx, (**b**) HC, (**c**) BG, (**d**) Cb, (**e**) BG+Cb, (**f**) pCtx+BG+Cb. Values correspond to the mean luciferase activity per µg of protein from each brain region ± SEM.

In order to confirm these quantitative results, the other brain hemispheres were employed to detect the GFP expression by IF. Brain slides were selected according to the coordinates employed for the administration routes, showing a good correlation between the luciferase activity and the GFP expression in most of the injected areas (Figure 50a). Apart from its higher GFP expression, BG continued to be the most suitable area for the vector diffusion among other connected areas, followed by an efficient expression in the Cb after a single local injection in this site. In contrast, IF revealed that GFP detection after injection of vector in the prefrontal, somatosensory, and visual cortical areas was mainly restricted to the injected areas, with other structures such as BG and HC mainly devoid of positive cells (Figure 50a). As expected, HC showed the lowest vector distribution, with most transduced cells located in the corpus callosum (cc). Finally, IF visualization in BG region

using specific antibodies revealed that both neurons and glia were transduced with the Ad-CAG-GFPLuc vector (Figure 50b). This observation is in line with previous studies in which neuronal and glia cells were also transduced employing HC-AdV[208] and the CAG promoter[231].

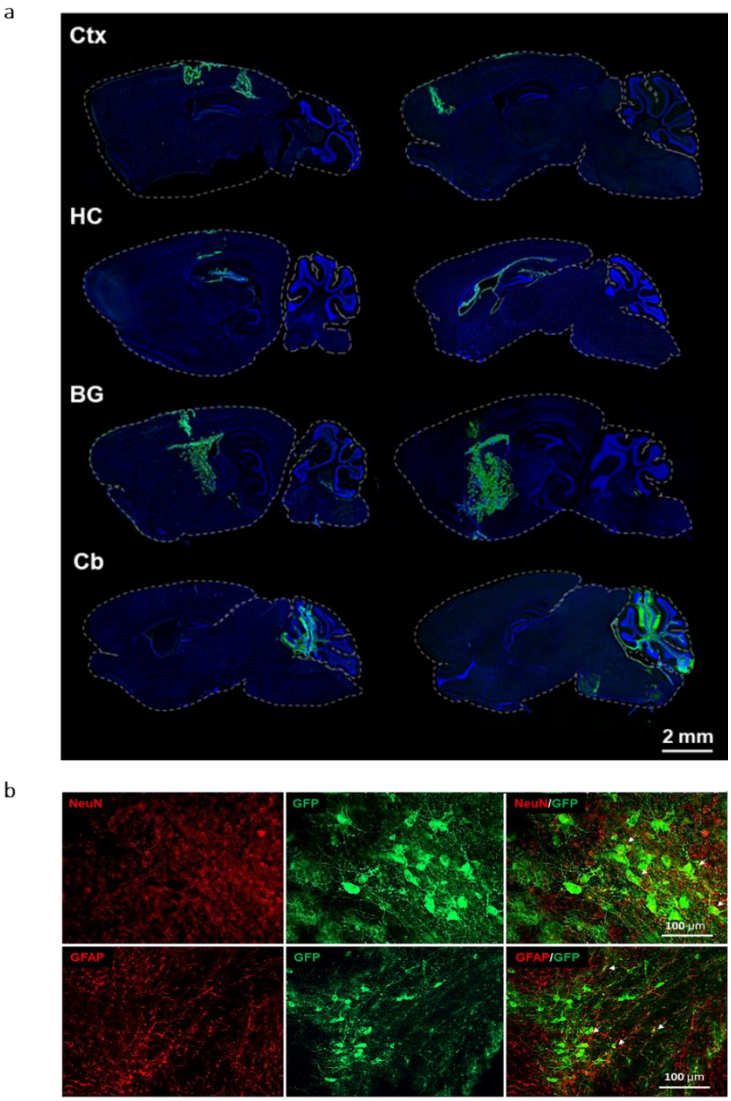

Figure 50. IF analysis revealed that BG and Cb were the areas with more transduced cells, including neurons and astroglia. The Ad-CAG-GFPLuc vector was administered as described in figure 48. Two days later, one brain hemisphere was processed for detection of GFP by IF (**a**) GFP is marked in green. Nuclei were counterstained with DAPI (blue). A dotted line delineates the surface of brains. Pictures show sagittal sections. The location of injections is indicated on the left (Ctx, HC, BG, Cb). (**b**) Co-staining of GFP (green) and NeuN or GFAP (both red) antibodies in BG revealed the transduction of neurons (upper panels) and astroglia (lower panels).

In light with these results, combination of injection in different brain structures seemed to be the best option to obtain a broad transgene expression throughout the brain. Despite there is a certain controversy about these multisite brain surgeries, we found good tolerance in the mouse model. The rate of surgical complications was less than 5%.

11. Therapeutic evaluation of intracerebral administration of HCA-CAG-SCN1A vector in adolescent *Scn1a*$^{WT/A1783V}$ mice

11.1. *In vivo* evaluation of *SCN1A*co transgene expression

In order to evaluate the therapeutic efficacy of the prototypic HCA-CAG-SCN1A vector, it was tested in the novel *Scn1a*$^{WT/A1783V}$ mouse model of DS.

Firstly, to validate the *in vivo* functionality and tolerability of the transgene, 5 wo *Scn1a*$^{WT/A1783V}$ mice were injected with 1.5 µL of HCA-CAG-SCN1A vector (2x10^7 vg/injection) in BG, bilaterally (n=4). As surgery controls, other group received the same volume of saline solution (n=4), whereas untreated *Scn1a*$^{WT/WT}$ mice were used as controls (n=4). One week after vector/saline administration mice were sacrificed and expression of *SCN1A*co in the injected area was evaluated by qRT-PCR. As expected, only *SCN1A*co-treated *Scn1a*$^{WT/A1783V}$ mice presented expression of the transgene, with an average of 7.4x10^5 ± 2.1x10^5 *SCN1A*co copies/µg mRNA (Figure 51). To determine the possible influence of the transgenic *SCN1A*co on the expression of the endogenous gene, mRNA levels of the mouse *Scn1a* were also evaluated using specific primers. The non-parametric Kruskal-Wallis with Dunn´s post-test revealed no significant differences in endogenous *Scn1a* expression between *Scn1a*$^{WT/WT}$ and treated/untreated *Scn1a*$^{WT/A1783V}$ mice (*Scn1a*$^{WT/WT}$: 1.1x10^6 ± 4.3x10^5; *Scn1a*$^{WT/A1783V}$+ saline: 1.2x10^6 ± 8.1x10^4; *Scn1a*$^{WT/A1783V}$+*SCN1A*co: 1.4x10^6 ± 3.8x10^4).

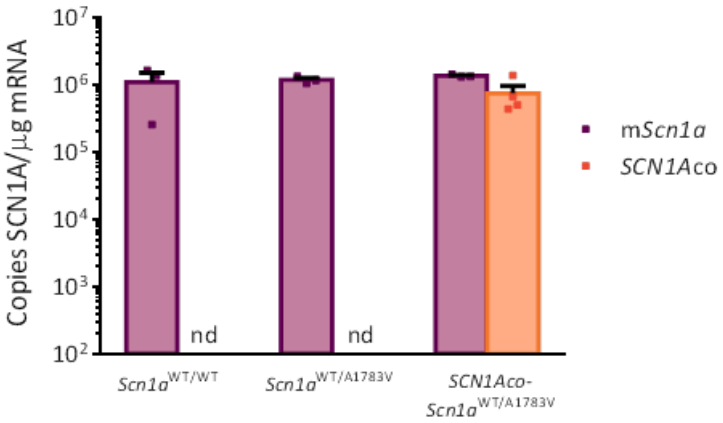

Figure 51. Expression of transgenic *SCN1A*co and endogenous *Scn1a* in *Scn1a*$^{WT/A1783V}$ mice treated with HCA-CAG-SCN1A. The vector was administered by bilateral injection in the BG of Scn1a$^{WT/A1783V}$ mice (n=4, 22x10^7 vg/injection), and one week later they were sacrificed for quantification of *SCN1Aco* and mouse *Scn1a* by qRT-PCR. Untreated (saline-injected) and Scn1a$^{WT/WT}$ mice were included as controls. Data were represented as mean of gene copies per µg of mRNA ± SEM. nd, not detected.

The IF analysis of brain samples revealed a low percentage of cells expressing Nav1.1 above endogenous levels in *Scn1a*$^{WT/A1783V}$ mice injected with the HCA-CAG-SCN1A vector (Figure 52a). However, the number of cells expressing more moderate levels of the channel -and therefore indistinguishable from endogenous expression- could be higher. The Nav1.1 content was also analyzed in membrane-enriched protein extracts obtained from BG of treated mice by WB. No global increase of the channel was observed in these animals (Figure 53b).

Altogether, the analysis of transgene expression is compatible with over-expression of Nav1.1 in a subset of cells in the injected areas, which causes no significant increase the global amount of the channel.

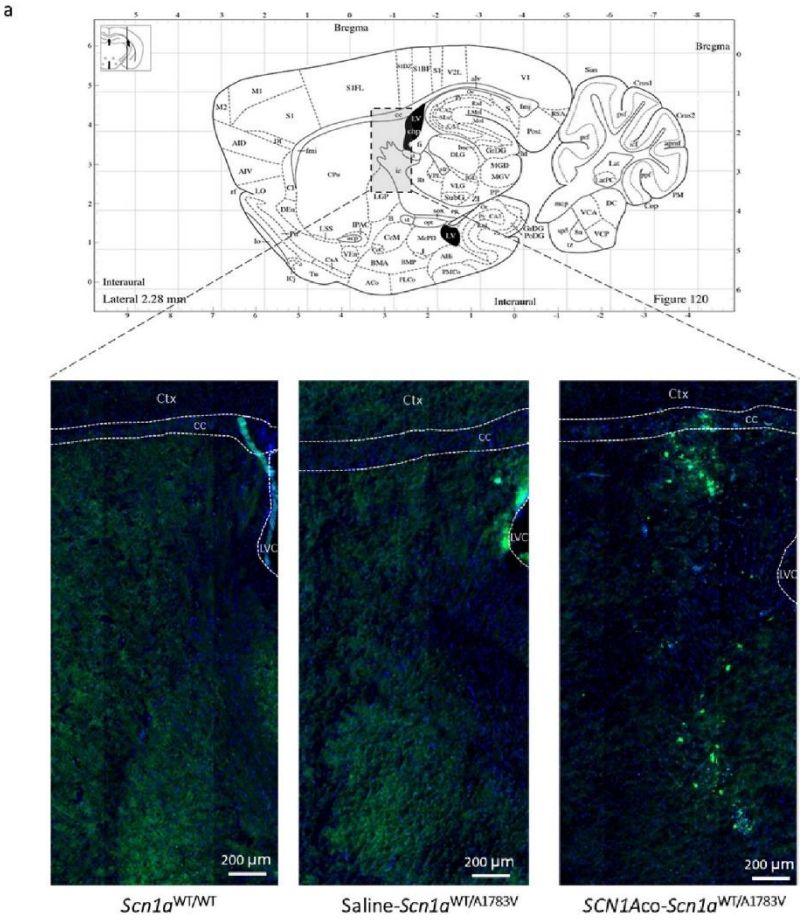

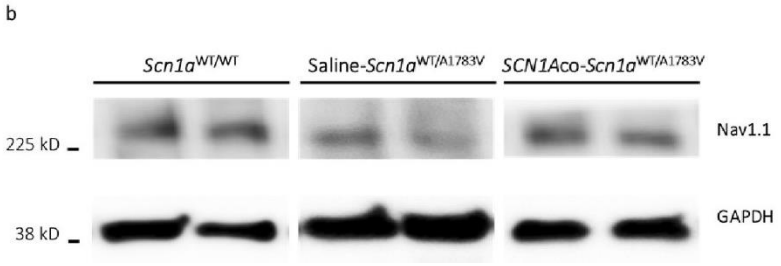

Figure 52. Detection of Nav1.1 in mice treated with HCA-CAG-SCN1A by IF and WB. Mice were treated as described in Figure 51 (n=4). (**a**) Nav1.1 expression was addressed by IF (green), counterstaining the nuclei with DAPI (blue). The region analyzed corresponds to the lateral globus pallidus (LGP) and part of caudate-putamen in the BG region, as indicated by the brain map obtained from the Paxinos´ mouse brain atlas (access online via Elsevier, 2001). Dotted lines delimitate different structures, including Ctx, cc, and the lateral ventricle (LVC). (**b**) Nav1.1 expression was also evaluated by WB in membrane enriched protein extracts prepared from BG. Representative blots show Nav1.1 and GAPDH bands. Original blots were cropped and re-arranged to display animals grouped. Molecular weights expressed in kDa correspond with the bands of the molecular marker.

11.2. Electrophysiological analysis of *SCN1A*co-treated mice

In order to determine if the pattern of expression described above has a functional correlation, treated mice were subjected to electrophysiological analysis. Additional *Scn1a*$^{WT/A1783V}$ mice were bilaterally injected in BG with 1.5 µL of HCA-CAG-SCN1A vector (1.3x10^{8} vg/injection, n=6). As surgery controls, other group received the same volume of saline solution in the same coordinates (n=6). During the surgical procedure, one superficial electrode was located on the pCtx, 3-4 deep electrodes in BG, and two others in the Cb that were used as ground and reference. One week after surgery, both *SCN1A*co-treated and control mice were subjected to electrophysiological recordings. *Scn1a*$^{WT/WT}$ mice were also registered as a healthy control group. Analysis of electrophysiological recordings obtained from the superficial electrodes placed in pCtx, showed a near complete normalization as compared with *Scn1a*$^{WT/WT}$ mice (Figure 53a). Of note, the activity registered in superficial electrodes mimics the EEG evaluation that could be routinely performed in DS patients. Quantification of IEDs demonstrated a significant reduction in in *Scn1a*$^{WT/A1783V}$ mice treated with the HCA-CAG-SCN1A vector (Figure 53b). This amelioration of IEDs was also observed in the recordings obtained from the deep electrodes placed in BG (Figure 53c). These results suggest a good tolerability of the *SCN1A*co transgene and the restoration of EEG activity after one single administration in BG of the therapeutic vector.

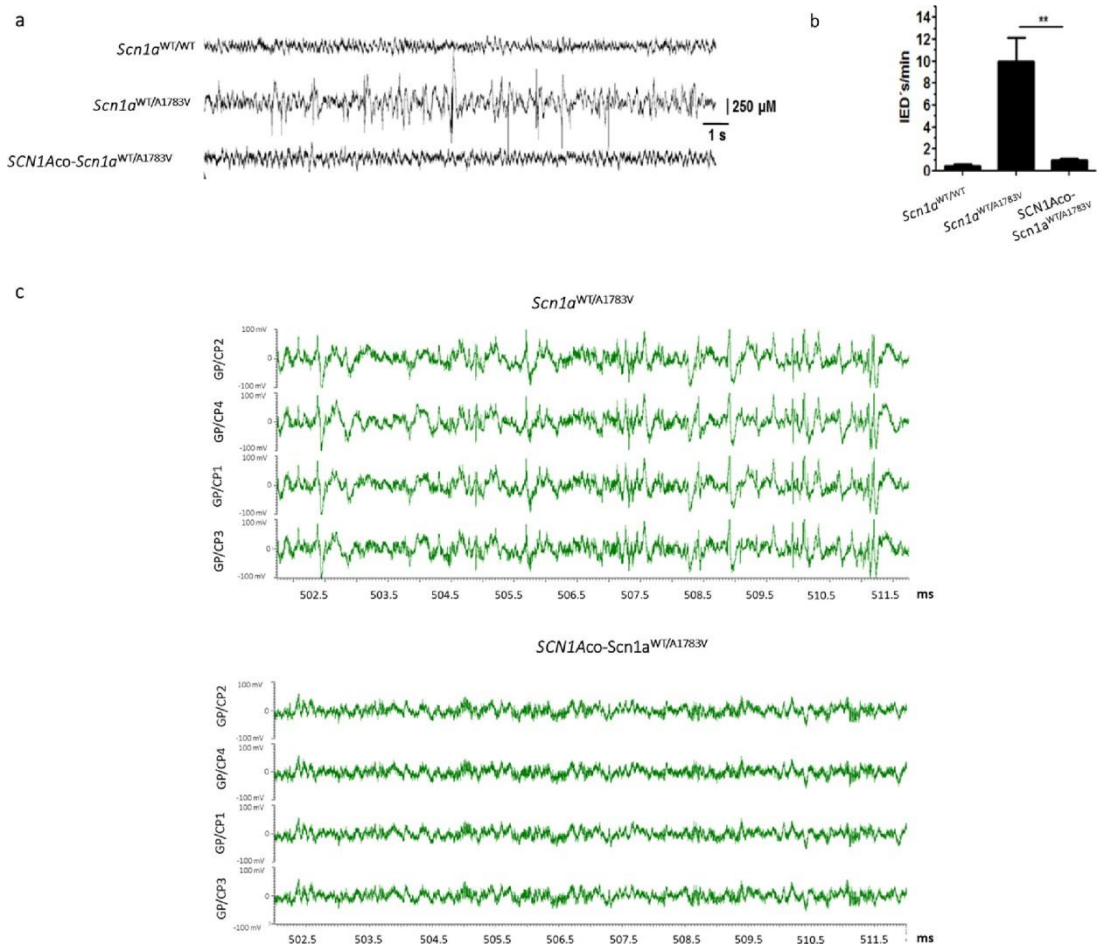

Figure 53. *Scn1a*$^{WT/A1783V}$ mice treated with the HCA-CAG-SCN1A vector show an improvement of brain electrophysiology. *Scn1a*$^{WT/A1783V}$ mice were bilaterally administered in BG with vector (2x10^7 vg/injection, n=6 for both groups) or saline as a control. Fifteen min later, one superficial electrode was placed in pCtx, and four deep electrodes in BG. One week after surgery, mice were subjected to electrophysiological recordings. (**a**) Electrophysiological signals registered by the superficial electrode placed in pCtx in *Scn1a*$^{WT/WT}$ (upper signal), control *Scn1a*$^{WT/A1783V}$ mice (middle signal) and treated *Scn1a*$^{WT/A1783V}$ mice (lower signal). (**b**) *SCN1A*co-*Scn1a*$^{WT/A1783V}$ treated mice presented a significative lower number of IED´s per min than control *Scn1a*$^{WT/A1783V}$ mice in pCtx recording (**p<0.01, Kruskal-Wallis with Dunn´s post-test). (**c**) Electrophysiological signals registered by the deep electrodes placed in BG in *Scn1a*$^{WT/A1783V}$ control mice (upper panel) and *SCN1A*co-*Scn1a*$^{WT/A1783V}$ treated mice (lower panel) faithfully reproduced the effect observed in cortex. Electrodes located in different regions of BG allowed the electrophysiological recording of several channels: GP/CP2, GP/CP4, GP/CP1, and GP/CP3. The time represented corresponds to an interval of 10 s.

11.3. Survival rate and febrile-seizure threshold of HCA-CAG-SCN1A-treated mice

In line with the improvement of electrophysiological activity observed after one administration of HCA-CAG-SCN1A in BG, and based on the previous biodistribution studies, further evaluation of safety and therapeutic potential of this vector was performed in the double injection in BG+Cb and the triple combination in pCtx+BG+Cb. In this respect, a major proportion of brain structures will

express the *SCN1A*co transgene, which could result in a reduction of epileptogenic origins and amelioration of the neurological comorbidities.

To this end, 5 wo *Scn1a*$^{WT/A1783V}$ mice were bilaterally injected with the HCA-CAG-SCN1A vector in both BG+Cb and pCtx+BG+Cb combination routes. A third group of *Scn1a*$^{WT/A1783V}$ mice received the HCA-CAG-Luc reporter vector as a control group in the same brain locations. Finally, *Scn1a*$^{WT/WT}$ and untreated *Scn1a*$^{WT/A1783V}$ mice (ut-*Scn1a*$^{WT/A1783V}$) groups were employed as additional controls.

As observed in the characterization of the *Scn1a*$^{WT/A1783V}$ DS model, the mortality rate was elevated from birth until the 6th week of age (Part I, Section 2 of Results). Despite mortality rate from 5 weeks of age ahead is moderate, an improvement in survival percentage of *SCN1A*co-treated *Scn1a*$^{WT/A1783V}$ mice was observed in both BG+Cb and pCtx+BG+Cb administration routes compared with untreated *Scn1a*$^{WT/A1783V}$ mice (93.8%, 100% and 64.7%, respectively). Actually, the log-Rank test revealed a significance of p<0.02 for pCtx+BG+Cb *vs.* ut-*Scn1a*$^{WT/A1783V}$ mice, and p<0.04 for BG+Cb *vs.* ut-*Scn1a*$^{WT/A1783V}$ mice. In contrast, *Scn1a*$^{WT/A1783V}$ mice treated with the HCA-CAG-Luc vector presented a similar mortality rate as untreated *Scn1a*$^{WT/A1783V}$ mice (Figure 54). Therefore, it could be concluded that treatment with HCA-CAG-SCN1A vector protects *Scn1a*$^{WT/A1783V}$ mice from SUDEP, especially with the triple administration in pCtx+BG+Cb.

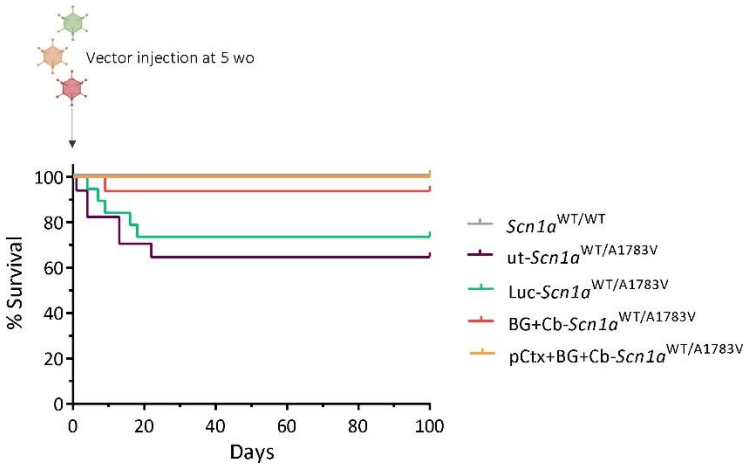

Figure 54. *Scn1a*$^{WT/A1783V}$ mice present an improvement in survival rate after administration of HCA-CAG-SCN1A vector. Five wo *Scn1a*$^{WT/A1783V}$ mice were injected with the HCA-CAG-SCN1A vector in BG+Cb (n=16) or pCtx+BG+Cb (n=12), at 2x10^{7} vg/injection. Additional *Scn1a*$^{WT/A1783V}$ mice (n=19) were treated with the control vector HCA-CAG-Luc. Other controls included untreated *Scn1a*$^{WT/A1783V}$ mice (n=17) and healthy *Scn1a*$^{WT/WT}$ mice (n=20). The graph shows the survival form treatment to day 100. Note that time 0 corresponds to 5 wo mice, in contrast to the full survival curve depicted in Figure 20. Survival curves of BG+Cb-*Scn1a*$^{WT/A1783V}$ and pCtx+BG+Cb-*Scn1a*$^{WT/A1783V}$ were significantly different from ut-*Scn1a*$^{WT/A1783V}$ mice (p=0.04 and p=02, respectively; log-rank test).

In order to evaluate if the HCA-CAG-SCN1A vector had a protective effect on seizures triggered by hyperthermia, temperature thresholds of heat-induced seizures were evaluated one month after vectors administration. For this purpose, mice were subjected to a gradual increase of their bodies temperature (0.5°C every 2 min) until they presented a GTCS or if the body temperature reached 42.5°C. As shown in Figure 55, only *SCN1A*co-treated mice with the bilateral pCtx+BG+Cb injection presented a significant increase of seizure threshold compared with untreated *Scn1a*$^{WT/A1783V}$ mice (40.7 ± 0.2°C and 39.9 ± 0.2°C, respectively). In contrast, no improvement was observed in mice treated with the HCA-CAG-SCN1A vector in BG+Cb (39.5 ± 0.5°C) neither in those who received the HC-CAG-Luc reporter vector (39.4 ± 0.1°C) (Figure 55). The one-way ANOVA with Sidak´s multiple comparison test revealed significant differences between untreated and pCtx+BG+Cb treated mice (**p<0.01) as well as between HCA-CAG-Luc and pCtx+BG+Cb treated mice (***p<0.001).

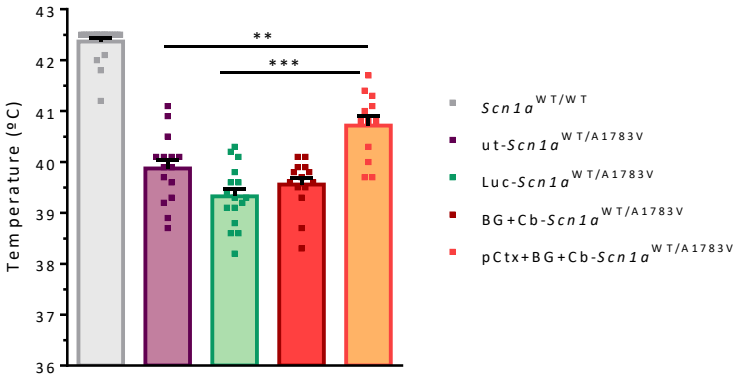

Figure 55. Treatment with HCA-CAG-SCN1A in pCtx+BG+Cb improves the seizure threshold temperature. Mice were treated as described in Figure 54. One month after treatment, mice were subjected to a gradual increase of their bodies' temperature until the appearance of a GTCS or until a maximum of 42.5°C. The graph shows individual (squares) and average seizure threshold temperatures for each treatment group. *Scn1a*$^{WT/WT}$ n=22, ut-*Scn1a*$^{WT/A1783V}$ n=15, Luc-*Scn1a*$^{WT/A1783V}$ n=16, BG+Cb-*Scn1a*$^{WT/A1783V}$ n=14, and *SCN1A*co-*Scn1a*$^{WT/A1783V}$ n=12. **p<0.01, ***p<0.001, one-way ANOVA with Tukey´s post-test.

When the febrile-seizure thresholds were compared before and after treatment, the group treated with the HCA-CAG-SCN1A vector using the triple administration route confirmed and increased in the threshold, in contrast with HCA-CAG-Luc-treated mice. This effect is easily observed by comparison of the cumulative seizure probabilities (Figure 56).

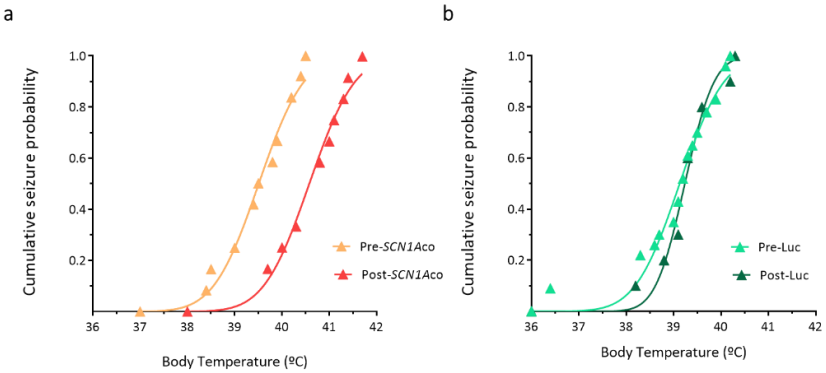

Figure 56. Cumulative seizure probability pre- and post-administration of vectors in *Scn1a*$^{WT/A1783V}$ mice. Mice received the HCA-CAG-SCN1A or HCA-CAG-Luc vectors as described in Figure 54. The graphs show the cumulative seizure probabilities pre-treatment and one month after treatment. Note the shift of the curve in the case of mice treated with the therapeutic vector.

Taken together, these results suggest that the wider distribution of *SCN1A*co expression obtained by the triple pCtx-BG+Cb bilateral administration is required to confer *Scn1a*$^{WT/A1783V}$ mice partial protection from seizures triggered by hyperthermia. As a consequence, this was the selected therapeutic approach to further evaluate the rest of pathophysiological manifestations of DS.

11.4. Behavioral and motor assessment of *Scn1a*$^{WT/A1783V}$ mice after treatment with HCA-CAG-SCN1A vector

Once the most efficient administration route of the HCA-CAG-SCN1A vector was defined, treated and control mice were subjected to a battery of cognitive, behavioral, and motor tests to evaluate the effect on neurological comorbidities associated to the disease. To this end, a group of mice injected in pCtx+BG+Cb with the HCA-CAG-SCN1A vector (*SCN1A*co-*Scn1a*$^{WT/A1783V}$) was evaluated in comparison with a group treated with the control vector HCA-CAG-Luc (Luc-*Scn1a*$^{WT/A1783V}$), untreated *Scn1a*$^{WT/A1783V}$ controls (ut-*Scn1a*$^{WT/A1783V}$), and a group of healthy mice (*Scn1a*$^{WT/WT}$). This neurological evaluation was performed two months after vector administration in order to detect stable improvements caused by the partial restoration of Nav1.1 function. Since stereotaxic surgeries took place at 5 weeks of age, at the time of neurological assessment all groups of mice were approximately 3 months old, a period in which cognitive and behavioral manifestations were already evident in *Scn1a*$^{WT/A1783V}$ mice. Since motor alterations are slightly delayed in this model (Results, Part I), evaluation of this comorbidity took place when mice were 4 months old. Therefore, our experimental setting will determine if treatment of 5 wo mice can revert disease manifestations.

11.4.1. Evaluation of cognitive functions

In order to evaluate if the *SCN1A* supplementation achieved by the HCA-CAG-SCN1A vector was enough to restore the cognitive and memory dysfunction observed in the *Scn1a*$^{WT/A1783V}$ model, the four groups of treated and untreated mice were subjected to the NOR test.

Since ut-*Scn1a*$^{WT/A1783V}$ did not show a short-term visuospatial memory deficit (NOR 1 h) in the characterization of the DS model (Results, Part I, Section 6.1.2.), NOR habituation and NOR 1 h tests were performed following the same protocol as characterization of the model, although visuospatial memory was only evaluated in the LTM test (NOR 24 h). In this case, the result showed a significant improvement of exploration of the novel object in *SCN1A*co-*Scn1a*$^{WT/A1783V}$ over Luc-*Scn1a*$^{WT/A1783V}$ and ut-*Scn1a*$^{WT/A1783V}$ mice (*Scn1a*$^{WT/WT}$: 63.5 ± 2.5%; ut-*Scn1a*$^{WT/A1783V}$: 47.4 ± 4.6%; Luc-*Scn1a*$^{WT/A1783V}$: 47.7 ± 7.7%; *SCN1A*co-*Scn1a*$^{WT/A1783V}$: 64.6 ± 2.7%) (Figure 57).

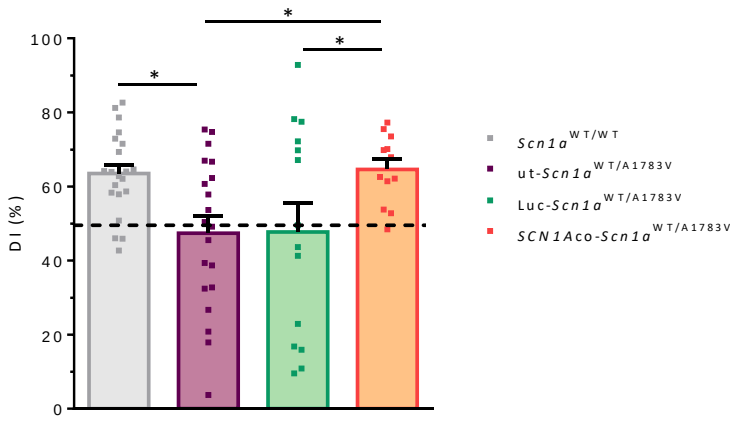

Figure 57. Long-term visuospatial memory improves after treatment with the HCA-CAG-SCN1A vector. Five wo *Scn1a*$^{WT/A1783V}$ mice were injected with the HCA-CAG-SCN1A vector (2x10^7 vg/injection) in pCtx+BG+Cb (SCNA1co-*Scn1a*$^{WT/A1783V}$). Additional *Scn1a*$^{WT/A1783V}$ mice were treated with the control vector HCA-CAG-Luc (Luc-*Scn1a*$^{WT/A1783V}$). Other controls included untreated *Scn1a*$^{WT/A1783V}$ mice (ut-*Scn1a*$^{WT/A1783V}$) and healthy *Scn1a*$^{WT/WT}$ mice. Two months after treatment, all groups were subjected to the NOR 24 h test. The graph shows the average DI ± SEM (%) in the groups as well as individual values (squares). *Scn1a*$^{WT/WT}$ n=21; ut-*Scn1a*$^{WT/A1783V}$ n=20; Luc-*Scn1a*$^{WT/A1783V}$ n=14; and *SCN1A*co-*Scn1a*$^{WT/A1783V}$ n=12. *p<0.05, one-way ANOVA with Sidak´s multiple comparisons test.

In contrast with this result, when learning and visuospatial memory were evaluated using the MWM test, no improvement could be demonstrated in HCA-CAG-SCN1A-treated mice (Figure 58). During the VP phase the delayed learning characteristic of Scn1a$^{WT/A1783V}$ mice was not changed (Figure 58a). At the IP phase of the test all Scn1a$^{WT/A1783V}$ groups showed a deficit in spatial memory compared with their Scn1a$^{WT/WT}$ controls, including the group treated with the HCA-CAG-SCN1A vector (Figure 58b). The probe tests also reflected a significative deficit in memory retention in all

Scn1a$^{WT/A1783V}$ groups, since the percentage of time remaining in the target quadrant presented average values around 25% (Figure 58c-d).

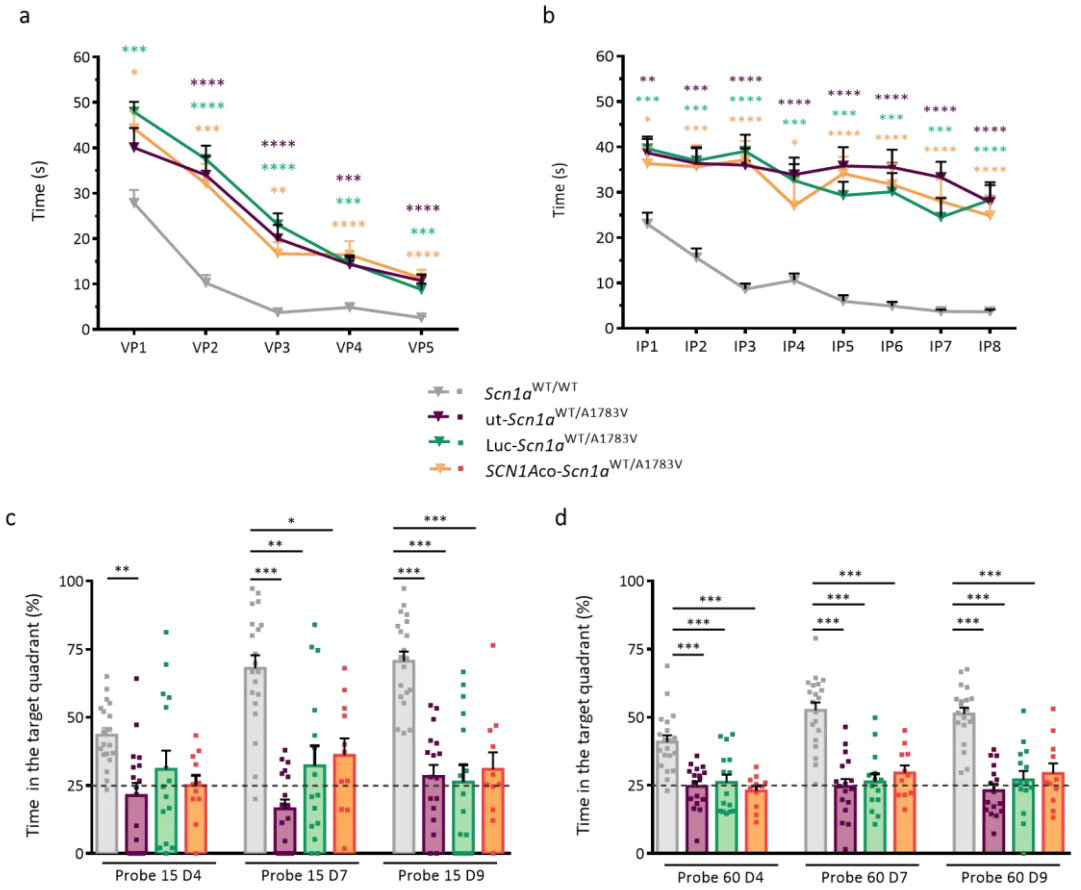

Figure 58. Treatment with the HCA-CAG-SCN1A in the pCtx+BG+Cb does not improve learning delay, visuospatial memory and memory retention in the MWM test. Mice were treated as described in Figure 57. Two months after treatment, all groups were subjected to the MWM test. (**a**) The graph shows the latency to find the VP on the indicated trials (VP1 to VP5). Despite all groups demonstrated the ability to learn the task ($p<0.0001$, Friedman test), all treated and untreated *Scn1a*$^{WT/A1783V}$ mice showed significant higher times to reach the platform than *Scn1a*$^{WT/WT}$ controls. (**b**) During 8 consecutive days, visuospatial memory was evaluated in the IP stage of the MWM test. Only *Scn1a*$^{WT/WT}$ mice demonstrated the ability to learn how to reach the platform ($p<0.0001$, Friedman test). All treated and untreated *Scn1a*$^{WT/A1783V}$ mice showed significant higher times to reach the platform than *Scn1a*$^{WT/WT}$ controls, suggesting a deficit in spatial learning memory. (**c**) On days 4, 7 and 9, memory retention was evaluated in the probe stage of the MWM test. In accordance with the lack of spatial learning, all treated and untreated *Scn1a*$^{WT/A1783V}$ mice showed altered memory retention with no preference for the target quadrant. *Scn1a*$^{WT/WT}$ n=20; ut-*Scn1a*$^{WT/A1783V}$ n=17; Luc-*Scn1a*$^{WT/A1783V}$ n=15, and *SCN1A*co-*Scn1a*$^{WT/A1783V}$ n=12. Values are represented as mean ± SEM. *p<0.005, **p<0.01, ***p<0.001 (one-way ANOVA with Sidak´s multiple comparisons test for VP1-4, IP1-3, IP7-8, and all probes except Probe 15 day 7, which was analyzed with the Kruskal-Wallis with Dunn´s post-test, as well as VP5, IP4-6).

Therefore, our current data do not allow to raise strong conclusions about the correction of cognitive manifestations in adolescent mice treated with HCA-CAG-SCN1A, as it will be discussed.

11.4.2. Evaluation of behavioral manifestations

The effect on hyperactive behavior was evaluated by the OF test. The first parameter to be analyzed was the mean velocity of movements in the total arena. We confirmed an increase in *Scn1a*$^{WT/A1783V}$ mice compared with *Scn1a*$^{WT/WT}$, indicative of hyperactive behavior, with no improvement in animals treated with the therapeutic vector (Figure 59a) (*Scn1a*$^{WT/WT}$: 6.3 ± 0.3 cm/s; ut-*Scn1a*$^{WT/A1783V}$: 9.9 ± 0.5 cm/s; Luc-*Scn1a*$^{WT/A1783V}$: 11.5 ± 0.6 cm/s; *SCN1A*co-*Scn1a*$^{WT/A1783V}$: 9.8 ± 0.5 cm/s). In concordance with this lack of effect, the number of stereotypies in *Scn1a*$^{WT/A1783V}$ mice treated with HCA-CAG-SCN1A was not reduced (Figure 59b) (*Scn1a*$^{WT/WT}$: 3.2 ± 0.3 stereotypies/min; ut-*Scn1a*$^{WT/A1783V}$: 8.3 ± 0.5 stereotypies/min; Luc-*Scn1a*$^{WT/A1783V}$: 7.6 ± 0.3; *SCN1A*co-*Scn1a*$^{WT/A1783V}$: 8.0 ± 0.7 stereotypies/min). Finally, the time spent in the center of the arena as an anxiety indicator, revealed no improvement in HCA-CAG-SCN1A-treated mice (Figure 59c) (*Scn1a*$^{WT/WT}$: 95.2 ± 10.8 s; ut-*Scn1a*$^{WT/A1783V}$: 48.8 ± 6.0 s; Luc-*Scn1a*$^{WT/A1783V}$: 60.9 ± 7.5 s; *SCN1A*co-*Scn1a*$^{WT/A1783V}$: 40.1 ± 8.7 s).

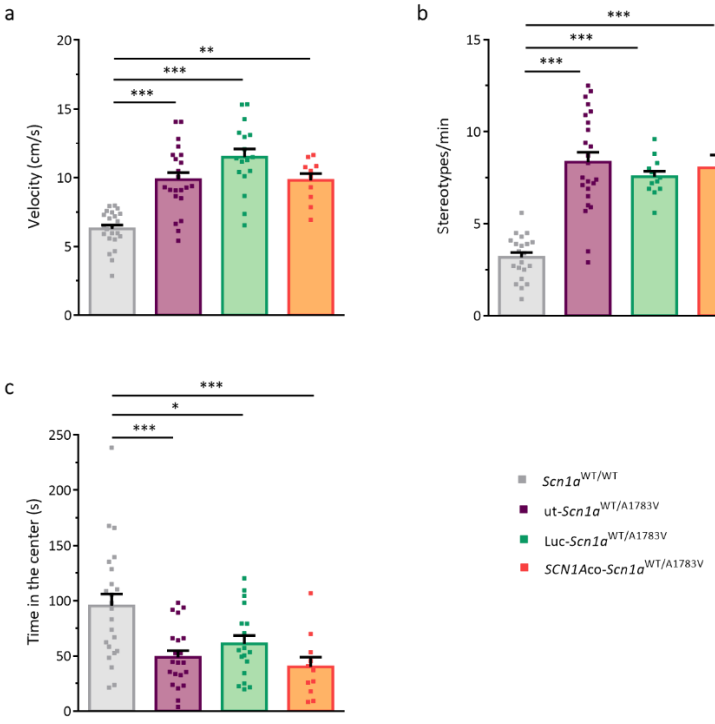

Figure 59. Anxiety and hyperactive behaviors show no amelioration after treatment with the HCA-CAG-SCN1A vector. Mice were treated as described in Figure 57. Two months after treatment, all groups were subjected to the OF test. The analyzed parameters were mean velocity in the total arena (in cm/s) (**a**), number of stereotypies per minute (**b**) and time spent in the center of the arena (**c**). *Scn1a*$^{WT/WT}$ n=23; ut-*Scn1a*$^{WT/A1783V}$ n=24; Luc-*Scn1a*$^{WT/A1783V}$ n=18; and *SCN1A*co-*Scn1a*$^{WT/A1783V}$ n=11. Data were calculated as mean ± SEM. Squares indicate individual values. *p<0.05, **p<0.01, ***p<0.001, one-way ANOVA with Sidak´s multiple comparisons test.

These results indicate that the current treatment cannot ameliorate the hyperactivity in *Scn1a*$^{WT/A1783V}$ mice. In contrast, we observed amelioration of other behavioural parameters related with the interaction with the environment, which are good indicators of the individual´s performance in daily life activities.

On one hand, performance in the marble burying test indicated a significative improvement of the normal exploratory behavior in *Scn1a*$^{WT/A1783V}$ mice treated with HCA-CAG-SCN1A compared with untreated and HCA-CAG-Luc-treated groups. This was documented as a reduced number of uncovered marbles at the end of the test (Figure 60). *Scn1a*$^{WT/WT}$: 2.1 ± 0.3; ut-*Scn1a*$^{WT/A1783V}$: 7.3 ± 0.7; Luc-*Scn1a*$^{WT/A1783V}$: 8.5 ± 0.6; and *SCN1A*co-*Scn1a*$^{WT/A1783V}$: 4.0 ± 0.6 uncovered marbles.

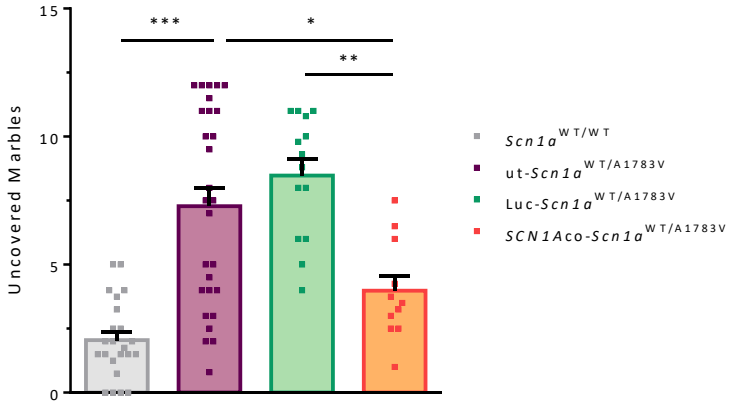

Figure 60. Reduction on uncovered marbles in treated *Scn1a*$^{WT/A1783V}$ mice indicates an improvement of normal exploratory behavior. Mice were treated as described in figure 57. Two months after treatment, all groups were subjected to the marble burying test. The analyzed parameter was the number of uncovered marbles after 30 min of free exploration. *Scn1a*$^{WT/WT}$ n=23; ut-*Scn1a*$^{WT/A1783V}$ n=28; Luc-*Scn1a*$^{WT/A1783V}$ n=14; and *SCN1A*co-*Scn1a*$^{WT/A1783V}$ n=11. Data were calculated as mean ± SEM. Squares indicate individual values.*p>0.05, **p<0.01, ***p<0.001, one-way ANOVA with Sidak´s multiple comparisons test.

In the same line, performance in the nest building test indicated a potential improvement of mice after HCA-CAG-SCN1A treatment, although this amelioration was only partial and some treated mice still failed to build a complete nest (Figure 61) (*Scn1a*$^{WT/WT}$: complete 76%, partial 24% and absent 0%; ut-*Scn1a*$^{WT/A1783V}$: complete 0%, partial 37.5% and absent 62.5%; Luc-*Scn1a*$^{WT/A1783V}$: complete 5.5%, partial 33.4% and absent 61.1%; *SCN1A*co-*Scn1a*$^{WT/A1783V}$: complete 33.3%, partial 33.3% and absent 33.3%).

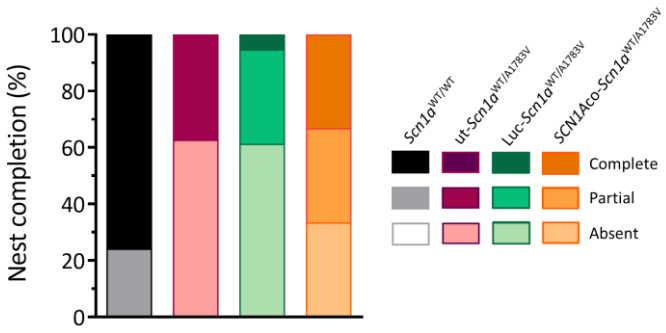

Figure 61. Treatment with HCA-CAG-SCN1A vector potentially improves the nest building performance. Mice were treated as described in figure 57. Two months after treatment, all groups were subjected to the nest building test. The analyzed parameter was the degree of nest completion, indicated by a color code for each group: dark for complete nest; medium for partial building and light colors for absence of nest and no use of materials. The height of bar sections indicates the percentage of mice in each category. *Scn1a*$^{WT/WT}$ n=21; ut-*Scn1a*$^{WT/A1783V}$ n=21; Luc-*Scn1a*$^{WT/A1783V}$ n=10; and *SCN1A*co-*Scn1a*$^{WT/A1783V}$ n=12.

11.4.3. Evaluation of motor impairments

Finally, evaluation of motor function was performed at the end of the second month post-treatment. We choose the rotarod test since this is one of the most robust motor tests for DS at this age. Our results demonstrated a clear improvement of *Scn1a*$^{WT/A1783V}$ mice after treatment with HCA-CAG-SCN1A (Figure 62), in agreement with an efficient transduction of Cb. The latency to fall from the rotating rod was significantly elevated in *Scn1a*$^{WT/A1783V}$ treated with HCA-CAG-SCN1A compared with untreated or HCA-CAG-Luc-treated controls (101 ± 10.1 s vs 63.9 ± 6.2 s and 52.8 ± 7.2 s, respectively, p<0.01 ANOVA).

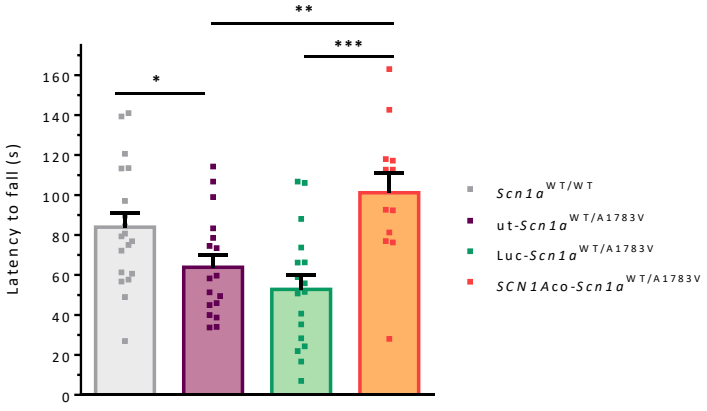

Figure 62. Treatment with HCA-CAG-SCN1A vector shows an improvement of motor function in the rotarod test. Mice were treated as described in figure 57. Two months after treatment, all groups were subjected to the rotarod test. The analyzed parameter was the latency to fall from the rotating rod. *Scn1a*$^{WT/WT}$ n=19; ut-*Scn1a*$^{WT/A1783V}$ n=17; Luc-*Scn1a*$^{WT/A1783V}$ n=17; and *SCN1A*co-*Scn1a*$^{WT/A1783V}$ n=12. Data were calculated as mean ± SEM. Squares indicate individual values. *p>0.05, **p<0.01, ***p<0.001, one-way ANOVA with Sidak´s multiple comparisons test.

In order to confirm these results, we concluded our neurological evaluation with the clasping test, which is usually altered in pathologies associated with ataxia. In fact, we found that untreated *Scn1a*$^{WT/A1783V}$ mice showed a significantly elevated clasping index compared with *Scn1a*$^{WT/WT}$ mice (0.1 ± 0.1 and 2.3 ± 0.2, respectively, p<0.001 ANOVA), which means a marked tendency to retract the forelimbs when they are suspended on their tails (Figure 63). Treatment with HCA-CAG-SCN1A, but not the control HCA-CAG-Luc vector, achieved a partial normalization of the clasping index (1.3 ± 03 and 2.1 ± 0.3, respectively).

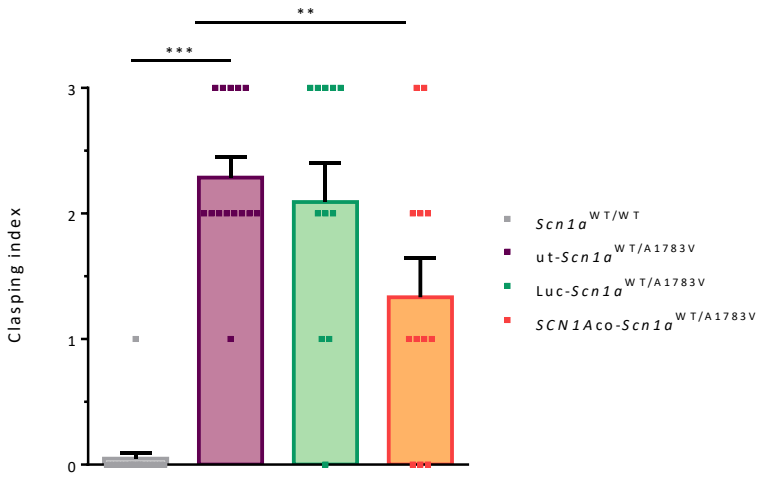

Figure 63. Cerebellar ataxia amelioration after treatment with the HCA-CAG-SCN1A vector. Mice were treated as described in figure 57. Two months after treatment, all groups were subjected to the clasping test. The represented parameter is the clasping index. *Scn1a*$^{WT/WT}$ n=21; ut-*Scn1a*$^{WT/A1783V}$ n=14; Luc-*Scn1a*$^{WT/A1783V}$ n=11; and *SCN1A*co-*Scn1a*$^{WT/A1783V}$ n=12. Data were calculated as mean ± SEM. Squares indicate individual values. *p>0.05, **p<0.01, ***p<0.001, one-way ANOVA with Sidak´s multiple comparisons test.

Discussion

Discussion

DS is a devastating infantile encephalopathy with epileptic and neurological manifestations characterized by its poor response to conventional AEDs. Despite several therapeutic lines are currently available recommended to prevent and reduce seizures, these approaches usually are not enough to slow down the progression and the worsening of the disease. Since the discovery of the etiological origin of DS, numerous efforts have been done to develop new tools and therapeutic strategies for a better management not only of seizures but also for the neurological comorbidities associated with the disease.

Based on this premise, this work had two main objectives. The first one was the characterization of an open-access mouse model of DS to ensure that it resembles the most important clinical manifestations found in DS patients. By choosing an ubiquitous KI model of a clinically relevant mutation in a very sensitive background we aimed to recapitulate the disease at both genetic and phenotypic levels. Our results are in line with this objective.

The second objective was to evaluate the tolerability and efficacy of *SCN1A* supplementation employing a prototypic HC-AdV vector. Interestingly, this proof of concept demonstrated to be a potential therapeutic approach able to reduce mortality and epileptic manifestations in the DS mouse model and to ameliorate several motor and behavioral symptoms associated with the disease.

1. Epileptic, cognitive, behavioral, and motor characterization of a novel mouse model of DS

1.1. Relevance of the novel DS mouse model

Several DS mouse models have been previously developed, all of them expressing different mutations in the *SCN1A* gene. The study of these models revealed important pathophysiological mechanisms involved in the disease, including the impaired activity of GABAergic interneurons due to the reduction of Nav1.1 expression and the preservation of sodium currents in pyramidal cells[41], or the subcellular localization of Nav1.1[39]. Moreover, the variety of clinical manifestations exhibited by all these models, ranging from milder to severe phenotypes, has allowed a better understanding of the relationship between

pathophysiological mechanism and the clinical manifestations of the disease. Most of these DS mouse models exhibited premature dead, especially in those expressing a constitutive *Scn1a* variant[39,41,84,85,88,93], as well as a notable susceptibility to suffer spontaneous and hyperthermia-induced seizures. Additionally, reduced sodium current in cerebellar Purkinje cells has been correlated with ataxia in these mice[45], as well as a wide spectrum of cognitive and behavioral impairments caused by Nav1.1 haploinsufficiency in several brain areas[60,83,85,89]. However, not all these mouse models could be considered optimal tools for preclinical development of new therapies, for several reasons: on one side, many of them present a mild epileptic and neurological DS phenotype, mainly influenced by the type of *SCN1A* mutation and the genetic background employed[60]. On the other side, the majority of them presents the *SCN1A* alteration only in specific type of inhibitory neurons[81,85,87–89]. In addition, the severity of the phenotype is also influenced by the type of GABAergic interneuron affected[89].

It should also be noted that the vast majority of the mentioned animal models have been developed by research groups and are not freely available for the scientific community. For this reason, the Spanish Dravet Syndrome Foundation decided to commission Jackson laboratories to generate a new murine model. This new KI model carries a heterozygous clinically relevant missense *SCN1A* mutation (A1783V)[52,87]. Based on previous data demonstrating the influence of the genetic background for the presence and severity of symptoms, this new model was developed in a pure C57BL/6 background in order to mimic severe cases of DS, which are the patients in urgent need for new therapies. Importantly, during the preparation of this document an independent group has employed the same *Scn1a*$^{WT/A1783V}$ model to characterize early events in DS pathogenesis[95]. Although the periods of study and the methodology employed are different, most of their findings are compatible with our conclusions, as will be discussed below.

1.2. Survival, epileptic, and electrophysiological characteristics of the *Scn1a*$^{WT/A1783V}$ mouse model

One of the first remarkable characteristics of this model is the elevated mortality rate observed from the first days of life. Before weaning, it was observed a mortality rate of approximately 25% of the pups, corresponding all of them with *Scn1a*$^{WT/A1783V}$ mice. Once animals were weaned and genotyped between D21-D28, survival of these mice sharply decreased, showing numerous deaths until the 6th week of age. Then the peak of mortality decreased and survival rate remained relatively stable with approximately a 25% of long-term

survivors, similar to the high mortality reported in previous mouse models[41,84,85,93]. Unfortunately, the mechanisms behind this elevated SUDEP in the majority of cases are still not clarified. On one side it could be due to cardiac and respiratory dysfunctions immediately after a GTCS, as observed in other DS mice. For instance, one previous study revealed that the animals presented a depressed interictal resting heart-rate variability and episodes of ictal bradycardia preceding SUDEP[21]. On the other side, death could be produced by a cerebral shutdown after GTCS[19]. All these SUDEP consequences seem to be related to the BS and thalamus, where the modulatory systems for autonomic cardioregulatory reflexes, respiratory and arousal regulation are located[240]. In fact, the BS is connected with the thalamus, and a marked reduction in the resting-state functional connectivity between them has been described for patients at high risk of suffering SUDEP[241]. Unfortunately, the incidence of SS and their implication on SUDEP could not be properly registered in our laboratory due to the absence of the required equipment. Even so, after several hours of observation from weaning to the end of the experimental period, the manual collection of data estimated that 15-25% of mice suffered visually recognizable SS. Although this value is just an approximation of the real incidence of SS in this model, this frequency seems not high enough to explain the high mortality rate, needing further research to elucidate other possible mechanisms. Fadila *et al.* performed continuous videorecording in *Scn1a*$^{WT/A1783V}$ mice and failed to detect convulsive seizures before P18, suggesting that early mortality cannot be due to GTCS. Similarly with our results, they detected seizures in 30% of mice during the severe stage period (P18-P35) by EEG. Again, this incidence is still too low to account for all the mortality observed in the model[95]. Other studies using DS models with high mortality rate (close to 80%) report only 15 seizures among 21 mice after continuous EEG recording from P22 to P46[138]. Together, these observations suggest that SUDEP may be associated in most cases with subtle, non-convulsive seizures, or it could be dissociated from seizures in some other cases. Other lines of evidence point to the dysregulation of breathing as an important contribution to SUDEP in DS[25,26]. Using a KI model of the A1783V mutation in inhibitory neurons it has been recently described that mice suffer hypoventilation, apnea, and reduced response to CO_2, associated with malfunction of neurons in the retrotrapezoid nucleus[87].

Similarly to human DS patients, these *Scn1a*$^{WT/A1783V}$ mice are susceptible to suffer GTCS triggered by hyperthermia. After increasing environmental temperature above 38.4°C, 50% of *Scn1a*$^{WT/A1783V}$ mice presented a GTCS, and more than 90% experienced seizures at 40°C, in contrast with the threshold above 43°C for *Scn1a*$^{WT/WT}$ controls. In accordance with these results, the electrophysiological activity of this DS model showed an increase of the number of

IEDs when the increase of temperature reached the temperature threshold. These electrical abnormalities are frequently observed in DS patients, especially during the worsening stage, when the background activity is fluctuating and poorly organized[10], equivalent to that observed in the *Scn1a*$^{WT/A1783V}$ mice.

1.3. Cognitive, behavioral, and motor characterization of the *Scn1a*$^{WT/A1783V}$ mouse model

Apart from the genotypic and epileptic similarities, the presence of many neuropsychiatric and motor manifestations observed in DS patients is other important advantage offered by this novel *Scn1a*$^{WT/A1783V}$ mouse model. In order to identify these neurologic comorbidities, mice were subjected to a battery of standardized tests to evaluate their cognitive, behavioral, and motor functions in a quantitative way. This is important for the evaluation of disease-modifying treatments with potential impact on all DS comorbidities.

The MWM test was employed to assess working and spatial memory. During the VP phase, *Scn1a*$^{WT/A1783V}$ mice presented a delay in the learning task. This means that they were progressively improving their ability to find the platform, but they required more time than their *Scn1a*$^{WT/WT}$ littermates. Interestingly, this result is in agreement with observations in DS children, who are capable of acquiring new skills and usually they do not lose them afterwards, although their learning pace is very slow. In some cases these activities include reading writing or riding a bicycle. In contrast, the IP phase and probes of the MWM revealed that *Scn1a*$^{WT/A1783V}$ mice -at all ages tested- were unable to use visual cues to generate a spatial map that allows them to find the hidden platform. Since the MWM test is the golden-standard to evaluate hippocampal function, the deficits observed in *Scn1a*$^{WT/A1783V}$ mice support the relevance of this structure in the physiopathology of DS. In fact, several studies demonstrate that HC also plays a critical role in seizure generation in several mouse models of DS [43,238,242].

In line with the cognitive impairment observed in the MWM, the NOR test revealed a long-term visuospatial impairment (NOR 24 h) in *Scn1a*$^{WT/A1783V}$ mice, especially in the middle and later age intervals tested. However, no differences in short-term visuospatial memory (NOR 1 h) compared with *Scn1a*$^{WT/WT}$ controls were detected. This is in contrast with findings from Fadila *et al*., who detected a reduction of the DI in *Scn1a*$^{WT/A1783V}$ mice in a test similar to the NOR 1 h[95]. The reasons for this discrepancy seem to be due to differences in the used protocols (latency times between training and test phases and spatial localization of the new

object); as well as mice age, in the study of Fadila *et al.* animals were younger (P18-35) than the earliest age group tested in this work (1-3 months).

Behavioral disorders are probably the most variable manifestations among DS patients and pre-clinical mouse models. In these last ones, the presence and severity of abnormalities not only rely on the type of *Scn1a* mutation, but also are influenced by the genetic background[60] and the population of affected cells expressing the *Scn1a* alterations[89]. Even so, there are standardized and robust tests to determine the presence of behavioral disorders such as the OF test, able to evaluate anxious and hyperactive behaviors. In this case, *Scn1a*$^{WT/A1783V}$ mice moved throughout the total open arena at higher velocities than *Scn1a*$^{WT/WT}$ controls, although the total distance recorded was similar between both groups (data not shown). This reflects a pattern of movement in which *Scn1a*$^{WT/A1783V}$ mice presented quick and abrupt movements, in line with the hyper-reactivity observed during animal handling. This is reminiscent of the tendency for elopement characteristic of some DS kids, which greatly complicates the task of their caregivers. Moreover, the time spent in the center of the arena was significantly reduced in all *Scn1a*$^{WT/A1783V}$ mice tested when compared with *Scn1a*$^{WT/WT}$ controls, suggesting the presence of anxiety in this DS mouse model. Finally, during the performance of the open field test it was also noticed the elevated number of stereotypies in *Scn1a*$^{WT/A1783V}$ mice. Although this parameter is usually associated with autistic-like behavior, in this particular case it could be a reflection of the hyperactive behavior since these repetitive movements were mainly frantic jumping in the walls of the arena.

Further evaluation revealed alterations in the exploratory behavior in the marble burying test. Although this test is frequently used to evaluate the anxiety-like behavior of mice[243], it is suspected that the observed poor exploratory efficiency of these *Scn1a*$^{WT/A1783V}$ mice was due to hyperactivity and deficit of attention, a manifestation frequently observed in DS children. In addition, the incomplete nest building performance of these mice suggests an affected welfare and the inability to carry out daily-life routines associated to species-adapted behavior.

In contrast with these behavioral alterations, *Scn1a*$^{WT/A1783V}$ mice did not show clear signs of social impairment, only a moderate delay in the latency to first contact and therefore a reduction in the number of contacts in the middle age interval tested. This non-consistent sociability deficit could be influenced by the C57BL/6 background of this mouse model, which was demonstrated to be relatively resistant to social behavior deficits[244]. Again these results could be in agreement with the reality of DS patients in which their social abilities could be more influenced by other behavioral and motor defects such as dysarthria and oral motor

skills[245] than an intrinsic sociability impairment. In fact, DS patients usually do not avoid personal contact within their familiar environment.

Finally, evaluation of motor abilities revealed that *Scn1a*$^{WT/A1783V}$ mice suffer motor alterations, becoming evident from the third month of age and worsening over time. This trend was especially observed in the rotarod test, in which *Scn1a*$^{WT/A1783V}$ mice showed reduced average times walking on the rotating rod than their *Scn1a*$^{WT/WT}$ littermates. Same results were observed in the inverted grid and in the elevated beam test. Altogether, this battery of test revealed an impairment of motor, balance, and coordination functions in this DS mouse model, resembling the motor delay observed before the two years of age in most of DS patients[246]. Implication of Cb and BG has been reported as two critical structures responsible of ataxia[45,247] and crouching gait[227] in DS, respectively. Alterations in the rotarod were also observed by Fadila *et al.* in the *Scn1a*$^{WT/A1783V}$ model, although they describe it as an early event (before P18) with an amelioration at P18-P35 attributed to a peculiar gait in their mice during this stage. The defect became evident again after P35[95]. In our experience, a standard rotarod apparatus is not suitable for motor evaluation of mice below 13.5 g of body weight (approximately 5 wo in our colony of *Scn1a*$^{WT/A1783V}$ mice).

2. Evaluation of the therapeutic effect of *SCN1A* supplementation employing a prototypic HC-AdV vector in a mouse model of DS

2.1. Relevance of the *SCN1A* supplementation

Current AEDs are largely ineffective for the control of seizures in most DS patients[121,248]. In addition, some evidences indicate that the genetic defect is a key determinant for other comorbidities such as motor, cognitive or behavioral manifestations. Therefore, control of seizures and amelioration of neurological status are two open fronts in DS management. During the last years, numerous pre-clinical studies have focused on the etiological origin of the disease, based on the restoration of Nav1.1 function. In this line, the second main aim of this work was the proof of concept of *SCN1A* gene transfer for the treatment of DS. As a potential advantage against other GT strategies, *SCN1A* cDNA supplementation employing a HC-AdV vector could allow the control of the disease with one single administration, avoiding the need of co-infection with vectors carrying several parts of the *SCN1A* sequence or the expression of exogenous genes such as artificial transcription factors. The downside of this technology is the relatively large size of adenoviral particles, which may compromise the biodistribution inside the brain.

2.2. Feasibility and functionality of HC-AdV vectors carrying the *SCN1A* sequence

For the construction of the therapeutic vector, first it was necessary to solve the problem of *SCN1A* instability, since this sequence is prone to re-arrangements and is difficult to manipulate in plasmids. After trying several cloning protocols, the stabilization of the *SCN1A* cDNA was finally achieved by designing a codon-optimized version of the sequence (*SCN1A*co), which demonstrated an efficient expression activity at mRNA and protein levels in transfected cells. Feasibility and functionality validation of HC-AdV vectors carrying the *SCN1A*co sequence were performed under de control of two different ubiquitous promoters. Further refinement of the therapeutic approach could benefit from promoters specific for inhibitory neurons. However, in our first proof of concept of gene supplementation we decided to avoid the influence of promoter specificity, which needs extensive validation. Our preliminary work on sequences derived from the endogenous *SNC1A* gene indicates very low potency, and variable effects of GABAergic-specific enhancers. Therefore, after *in vitro* and *in vivo* evaluation we opted for the well-characterized CAG promoter[231] for the first therapeutic prototype. It should be taken into account that in most DS patients the genetic defect is present in all the cells, and that *SCN1A* expression is not only found in inhibitory neurons, but also in other cell populations such as pyramidal cells[41,44], astrocytes[249], and myocytes[250]. The use of this promoter allows stringent evaluation of safety. Remarkably, although expression of *SCN1A* was not restricted to inhibitory interneurons but also can take place in excitatory cells and glia, the prototypic HCA-CAG-SCN1A vector has demonstrated to be well-tolerated and able to ameliorate some epileptic and neurological manifestations typical from DS.

In addition, the use of the CAG promoter facilitates the identification of the optimal routes of administration, since the expression of the transgene will largely depend on the vector biodistribution. This is an important issue for the use of adenoviral vectors in the brain.

It is known that seizures in DS have multifocal origins[239,251] and the imbalance of inhibition and excitation is globally spread among the brain, also accounting for the rest of neurological manifestations[44,252]. Assuming the need for a widely distributed expression of the *SCN1A* transgene over the different intracerebral areas, we performed a study of transgene expression by stereotaxic injections of the reporter Ad-CAG-GFPLuc vector in Ctx, HC, BG, and Cb regions. ICV administration was not pursued after our preliminary experiments confirmed the limitation of transgene expression to the ependymal cells (data not shown). As expected, one single intracerebral administration of the AdV vector was not enough to reach a generalized transgene expression among the brain, showing different expression and diffusion efficiencies depending on the injected area. Results obtained from both luciferase emission

quantification and GFP detection indicate that BG was the structure with the wider expression distribution among all single administrations, in line with previous observations[253]. Interestingly, injection in this region showed transgene expression in other areas such as HT and to a lesser extent in HC and the ptCtx, all of them involved in the pathophysiology of DS. Single injection in Ctx (pre-frontal, parietal and occipital) also reached efficient expression with an intermediate spread of the vector to contingent areas, whereas administration in Cb obtained remarkable but restricted expression efficiency in this organ with limited diffusion to BS. Unfortunately, direct injection in HC showed a poor transgene expression in this area.

In light with these results, it was decided to perform stereotaxic injections into combined brain structures in order to obtain the highest possible diffusion of the vector among areas with relevance in DS. Direct injection in Cb was clearly needed because otherwise this structure is not transduced at all. When we combined injection in Cb and BG, we found that pCtx is relatively untargeted. Therefore, the most invasive protocol consisted of bilateral injections in pCtx+BG+Cb. Efficient methods to deliver large particles across the blood-brain or ependymal-brain barriers are possible options for a global vector distribution, however, selective stereotaxic injections are currently the most realistic option mainly supported by its clinical feasibility[254,255]. It should be taken into account that a triple bilateral injection using stereotaxic needles is less invasive than current ablative therapies for epilepsy[256].

2.3. Therapeutic evaluation of the HCA-CAG-SCN1A vector in the *Scn1a*$^{WT/A1783V}$ mouse model

Therapeutic evaluation of the vector was carried out in 5 wo mice, in which the full spectrum of DS manifestations -with the exception of motor disabilities- was already evident, as observed in the appendix figure 3. Although treatment at early ages could obtain better results, we believe this group of patients is clearly in need of new therapies and is more clinically feasible. Therefore, one of the challenges of this work was to determine to what extent pre-existing defects can be reverted by disease-modifying therapies.

The first evidence of safety and biological effect of the HCA-CAG-SCN1A vector came from electrophysiological recordings in animals injected in the BG, using deep and superficial electrodes in BG and pCtx, respectively. Despite non-selective expression of Nav1.1, we observed a reduction in IEDs in treated *Scn1a*$^{WT/A1783V}$ mice, not only in the injected area but also in the Ctx. The data obtained from superficial electrodes are more clinically relevant than deep electrodes, correlating by routinely EEG evaluation performed in DS patients[257]. These

results suggest that the restoration of Nav1.1 function in one brain area such as BG can produce a global amelioration of brain function.

We observed improvement of survival after injection of HCA-CAG-SNC1A in BG+Cb of DS mice. Data from the biodistribution experiments showed that transduction of Cb produced a concomitant expression of the transgene in BS. As previously mentioned, both structures play a central role in autonomic and respiratory regulations and, therefore, in SUDEP[240]. Additionally, some SUDEP victims present an extensive cerebellar volume loss, maybe derived from excitotoxicity in Purkinje cells due to hyperactivation of pontine or long climbing fibers of olivary projections[258]. Damaged Purkinje cells would affect the function of the deep nuclei, leading to alterations of both cardiac and respiratory functions after a GTCS[259]. Altogether, these evidences suggest that restoration of *SCN1A* expression in Cb and BS is a key factor for protection from SUDEP in DS mice, probably improving autonomic and respiratory regulation. Moreover, it cannot be excluded the possibility that *SCN1A* expression in the thalamus could also contribute to control the excitatory stimuli in cortical regions not reached by the vector[260]. The efficient transduction of the HT could exert a positive effect by normalization of circadian rhythms[47,48], although this possibility has not been directly investigated. The potential role of this region in the therapeutic effect of HCA-CAG-SNC1A requires further study to identify the GFP+ cells by IF, since this small structure was entirely collected for luciferase activity analysis.

Despite the improvement of survival observed after administration of the vector in BG+Cb, the addition of a pCtx injection was needed to provide protection from heat-induced seizures in the DS mouse model, suggesting the requirement of wider distribution in order to control de generalization of seizures. Supporting this concept, the relevance of pCtx in the initiation of epileptic activity, following to the BS and then to the thalamus was recently highlighted in patients suffering from LGS[261]. This region is also well-positioned to promote rapid communication with spinal motorneurons involved in tonic seizures. Therefore, the administration route involving pCtx+BG+Cb was selected for further therapeutic evaluation of the vector, not only because of the role of pCtx in the epileptogenic origin, but also for its implication in cognitive functions and memory processes[262]. Apart from HC, some reports also suggest the involvement of pCtx in spatial memory[263,264], in agreement with the improvement in LTM observed in the NOR test in treated *Scn1a*$^{WT/A17833V}$ mice. However, *Scn1a*$^{WT/A17833V}$ mice treated with the HCA-CAG-SCN1A vector showed no improvement in the MWM test, supporting the importance of the HC in these brain functions and the need of vector diffusion among this structure, mainly in hippocampal CA3-region and DG[265,266]. An alternative explanation for the apparent discrepancy between the therapeutic effect in the NOR and

MWM test is the fact that the latter has an aversive component (water). Although ventral HC has been implicated emotional regulations[267] and dorsal HC in spatial memory, ventral HC influence in the functioning of dorsal HC; therefore, the poor performance in the MWM test could be influenced by the anxiety behavior persistent in treated DS mice[268]. Of note, HCA-CAG-SCN1A failed to avoid the hyperactive and anxiety behavior present in the DS model, reinforcing the idea that wider vector distribution is required especially in cortical and hippocampal areas.

In addition to the partial restoration of cognitive functions, HCA-CAG-SCN1A also improved the general welfare of *Scn1a*$^{WT/A17833V}$ mice (evaluated by the marble burying and the nest building tests).

Although motor impairments were not already established at the age of 5 weeks in *Scn1a*$^{WT/A1783V}$ mice, treatment with HCA-CAG-SCN1A seemed to prevent balance and coordination deterioration two months after administration. This improvement was especially observed in the rotarod test, in which treated mice presented latency times equivalent to *Scn1a*$^{WT/WT}$ controls. Amelioration of motor functions are probably due to restoration of Nav1.1 function in Cb and BG[269,270].

These results are in line with a recent work using an AAV vector to deliver gRNAs for a transgenically expressed Cas9-based transcriptional activator specific for the *SCN1A* 5´UTR region[137]. This elegant proof of principle study limits Nav1.1 expression to inhibitory neurons and leverages the efficacy of the AAV-PHP-eB serotype in mouse brain, obtaining a partial therapeutic effect when administered to adolescent (P30) mice.

As final remarks, results obtained in this work demonstrate that the transfer of the full *SCN1A* cDNA using HC-AdVs is feasible and potentially therapeutic for DS. Although widespread distribution of transgene expression is desirable, results obtained in this work indicate that the sub-optimal biodistribution of non-modified HC-AdV vectors is sufficient to obtain a therapeutic effect. Further optimization of vector diffusion in the brain could be accomplished by advanced delivery methods such as convection-enhanced infusion[253,271] or sonoporation[272], or by using vectors derived from alternative adenoviral members with superior neuronal tropism and retrograde transport such as canine AdV[273,274]. The next challenge is to increase the efficacy and selectivity of transgene expression into the brain, in order to assess if there is a threshold for Nav1.1 expression which can influence the therapeutic effect. The HCA-CAG-SCN1A vector will be a useful reference to determine if

physiological expression of *SCN1A* increases the efficacy of this GT approach, maybe avoiding overexpression in excitatory neurons and glia.

We believe the major contribution of this work is the definition of a basic approach with therapeutic potential and the indication of potential ways of improvement for an efficient treatment of DS.

Conclusions

Conclusions

1. A novel knock-in mouse model based on the heterozygous *SCN1A* A1783V mutation in a C57BL/6J genetic background recapitulates most Dravet Syndrome manifestations.

2. Alterations in electrophysiological recordings, survival, motor functions, cognitive functions, interaction with the environment and hyperactivity can be quantified in the new Dravet Syndrome model using standardized tests.

3. Social interaction was relatively preserved in the new Dravet Syndrome model.

4. A High-Capacity Adenoviral vector expressing an optimized version of the human *SCN1A* coding sequence under the control of the CAG promoter is feasible and functional.

5. Intracerebral administration of the HCA-CAG-SCN1A vector in the new Dravet Syndrome model improves brain electrophysiology, survival, motor function and interaction with the environment, and obtains partial protection from hyperthermia-induced seizures and cognitive deterioration.

6. Hyperactivity and anxiety were not improved by the HCA-CAG-SCN1A vector in the Dravet Syndrome mouse model.

7. Supplementation of the *SCN1A* gene using High-Capacity Adenoviral vectors is a feasible strategy for the treatment of Dravet Syndrome, but vector optimization is needed to address all clinical manifestations.

Bibliography

Bibliography

1. Gataullina, S. & Dulac, O. From genotype to phenotype in Dravet disease. *Seizure* **44**, 58–64 (2017).

2. Parihar, R. & Ganesh, S. The *SCN1A* gene variants and epileptic encephalopathies. *J. Hum. Genet.* **58**, 573–580 (2013).

3. Catterall, W. A., Kalume, F. & Oakley, J. C. NaV1.1 channels and epilepsy. *J. Physiol.* **588**, 1849–1859 (2010).

4. Wu, Y. W. *et al.* Incidence of dravet syndrome in a US population. *Pediatrics* **136**, e1310–e1315 (2015).

5. Brunklaus, A., Ellis, R., Reavey, E., Forbes, G. H. & Zuberi, S. M. Prognostic, clinical and demographic features in *SCN1A* mutation-positive Dravet syndrome. *Brain* **135**, 2329–2336 (2012).

6. Durá-Travé, T., Yoldi-Petri, M. E. & Gallinas-Victoriano, F. Epilepsy in children in navarre, Spain: Epileptic seizure types and epileptic syndromes. *J. Child Neurol.* **22**, 823–828 (2007).

7. Engel, J. A proposed diagnostic scheme for people with epileptic seizures and with epilepsy: Report of the ILAE task force on classification and terminology. *Epilepsia* **42**, 796–803 (2001).

8. Fisher, R. S. *et al.* Epileptic seizures and epilepsy: Definitions proposed by the International League Against Epilepsy (ILAE) and the International Bureau for Epilepsy (IBE). *Epilepsia* **46**, 470–472 (2005).

9. Dravet, C. Dravet syndrome history. *Dev. Med. Child Neurol.* **53**, 1–6 (2011).

10. Bureau, M. & Bernardina, B. D. Electroencephalographic characteristics of Dravet syndrome. *Epilepsia* **52**, 13–23 (2011).

11. Wheless, J. W., Fulton, S. P. & Mudigoudar, B. D. Pediatric Neurology Dravet Syndrome : A Review of Current Management. *Pediatr. Neurol.* **107**, 28–40 (2020).

12. Jansson, J. S., Hallböök, T. & Reilly, C. Intellectual functioning and behavior in Dravet syndrome: A systematic review. *Epilepsy Behav.* **108**, (2020).

13. Specchio, N. *et al.* Electroencephalographic features in Dravet syndrome: Five-year follow-up study in 22 patients. *J. Child Neurol.* **27**, 439–444 (2012).

14. Oguni, H., Hayashi, K., Awaya, Y., Fukuyama, Y. & Osawa, M. Severe myoclonic epilepsy in infants - a review based on the Tokyo Women's Medical University series of 84 cases. *Brain Dev.* **23**, 736–748 (2001).

15. Siegler, Z. *et al.* Hippocampal sclerosis in severe myoclonic epilepsy in infancy: a retrospective MRI study. *Epilepsia* **46**, 704–708 (2005).

16. Gaily, E. *et al.* Dravet syndrome: New potential genetic modifiers, imaging abnormalities, and ictal findings. *Epilepsia* **54**, 1577–1585 (2013).

17. Barba, C. *et al.* Co-occurring malformations of cortical development and *SCN1A* gene mutations. *Epilepsia* **55**, 1009–1019 (2014).

18. Sakauchi, M. *et al.* Retrospective multiinstitutional study of the prevalence of early death in Dravet syndrome. *Epilepsia* **52**, 1144–1149 (2011).

19. Devinsky, O., Hesdorffer, D. C., Thurman, D. J., Lhatoo, S. & Richerson, G. Sudden unexpected death in epilepsy: epidemiology, mechanisms, and prevention. *Lancet Neurol.* **15**, 1075–1088 (2016).

20. Maier, S. K. G. *et al.* An unexpected requirement for brain-type sodium channels for control of heart rate in the mouse sinoatrial node. *Proc. Natl. Acad. Sci. U. S. A.* **100**, 3507–3512 (2003).

21. Kalume, F. Sudden unexpected death in Dravet syndrome: Respiratory and other physiological dysfunctions. *Respir. Physiol. Neurobiol.* **189**, 324–328 (2013).

22. Delogu, A. B. *et al.* Electrical and autonomic cardiac function in patients with Dravet syndrome. *Epilepsia* **52**, 55–58 (2011).

23. Baysal-kirac, L. *et al.* Epilepsy & Behavior Analysis of heart rate variability and risk factors for SUDEP in patients with drug-resistant epilepsy. **71**, 60–64 (2017).

24. Ergul, Y., Ekici, B., Tatli, B., Nisli, K. & Ozmen, M. QT and P wave dispersion and heart rate variability in patients with Dravet syndrome. *Acta Neurol. Belg.* **113**, 161–166 (2013).

25. Kim, Y. *et al.* Severe peri-ictal respiratory dysfunction is common in Dravet syndrome. *J. Clin. Invest.* **128**, 1141–1153 (2018).

26. Bateman, L. M., Li, C.-S. & Seyal, M. Ictal hypoxemia in localization-related epilepsy: analysis of incidence, severity and risk factors. *Brain* **131**, 3239–3245 (2008).

27. Friedman, D., Chyou, J. & Devinsky, O. The attending physician Sudden death in epilepsy : of mice and men. **123**, 1415–1416 (2013).

28. Ostrowsky-Coste, K. *et al.* Similar semiology of epileptic and psychogenic nonepileptic seizures recorded during stereo-EEG. *Seizure* **22**, 897–900 (2013).

29. Claes, L. *et al.* De novo mutations in the sodium-channel gene *SCN1A* cause severe myoclonic epilepsy of infancy. *Am. J. Hum. Genet.* **68**, 1327–1332 (2001).

30. Goldin, A. L. & Escayg, A. Sodium channel *SCN1A* and epilepsy: mutations and mechanisms. *Epilepsia* **51**, 16 (2010).

31. Escayg, A. *et al.* Mutations of *SCN1A*, encoding a neuronal sodium channel, in two families with GEFS+2. *Nat. Genet.* **24**, 343–345 (2000).

32. Weiss, L. A. *et al.* Sodium channels *SCN1A*, *SCN2A* and *SCN3A* in familial autism. *Mol. Psychiatry* **8**, 186–194 (2003).

33. Dichgans, M. *et al.* Mutation in the neuronal voltage-gated sodium channel *SCN1A* in familial hemiplegic migraine. *Lancet (London, England)* **366**, 371–377 (2005).

34. Meier, S. *et al. SCN1A* affects brain structure and the neural activity of the aging brain. *Biol. Psychiatry* **72**, 677–683 (2012).

35. Catterall, W. A. From ionic currents to molecular mechanisms: The structure and function of voltage-gated sodium channels. *Neuron* **26**, 13–25 (2000).

36. Calhoun, J. D. & Isom, L. L. The role of non-pore-forming β subunits in physiology and pathophysiology of voltage-gated sodium channels. *Handb. Exp. Pharmacol.* **221**, 51–89 (2014).

37. Beckh, S., Noda, M., Lubbert, H. & Numa, S. Differential regulation of three sodium channel messenger RNAs in the rat central nervous system during development. *EMBO J.* **8**, 3611–3616 (1989).

38. Trimmer, J. S. & Rhodes, K. J. Localization of Voltage-Gated Ion Channels in Mammalian Brain. *Annu. Rev. Physiol.* **66**, 477–519 (2004).

39. Ogiwara, I. *et al.* Nav1.1 localizes to axons of parvalbumin-positive inhibitory interneurons: A circuit basis for epileptic seizures in mice carrying an Scn1a gene mutation. *J. Neurosci.* **27**, 5903–5914 (2007).

40. Duflocq, A., Le Bras, B., Bullier, E., Couraud, F. & Davenne, M. Nav1.1 is predominantly expressed in nodes of Ranvier and axon initial segments. *Mol. Cell. Neurosci.* **39**, 180–192 (2008).

41. Yu, F. H. *et al.* Reduced sodium current in GABAergic interneurons in a mouse model of severe myoclonic epilepsy in infancy. *Nat. Neurosci.* **9**, 1142–1149 (2006).

42. Heinemann, U. *et al.* The dentate gyrus as a regulated gate for the propagation of epileptiform activity. *Epilepsy Res. Suppl.* **7**, 273—280 (1992).

43. Stein, R. E., Kaplan, J. S., Li, J. & Catterall, W. A. Hippocampal deletion of NaV1.1 channels in mice causes thermal seizures and cognitive deficit characteristic of Dravet Syndrome. *Proc. Natl. Acad. Sci. U. S. A.* **116**, 16571–16576 (2019).

44. Tai, C., Abe, Y., Westenbroek, R. E., Scheuer, T. & Catterall, W. A. Impaired excitability of somatostatin- and parvalbumin-expressing cortical interneurons in a mouse model of Dravet syndrome. *Proc. Natl. Acad. Sci. U. S. A.* **111**, 3139–3148 (2014).

45. Kalume, F., Yu, F. H., Westenbroek, R. E., Scheuer, T. & Catterall, W. A. Reduced sodium current in Purkinje neurons from Nav1.1 mutant mice: Implications for ataxia in severe myoclonic epilepsy in infancy. *J. Neurosci.* **27**, 11065–11074 (2007).

46. Blumenfeld, H. Cellular and network mechanisms of spike-wave seizures. *Epilepsia* **46 Suppl 9**, 21–33 (2005).

47. Han, S. *et al.* Na V1.1 channels are critical for intercellular communication in the suprachiasmatic nucleus and for normal circadian rhythms. *Proc. Natl. Acad. Sci. U. S. A.* **109**, (2012).

48. Papale, L. A. *et al.* Altered sleep regulation in a mouse model of *SCN1A*-derived genetic epilepsy with febrile seizures plus (GEFS+). *Epilepsia* **54**, 625–634 (2013).

49. Han, S. *et al.* Autistic-like behaviour in *Scn1a* +- mice and rescue by enhanced GABA-mediated neurotransmission. *Nature* **489**, 385–390 (2012).

50. Yizhar, O. *et al.* Neocortical excitation/inhibition balance in information processing and social dysfunction. *Nature* **477**, 171–178 (2011).

51. Cheah, C. S. *et al.* Correlations in timing of sodium channel expression, epilepsy, and sudden death in Dravet syndrome. *Channels (Austin).* **7**, 468–472 (2013).

52. Lossin, C. A catalog of *SCN1A* variants. *Brain Dev.* **31**, 114–130 (2009).

53. Martin, M. S., Tang, B., Ta, N. & Escayg, A. Characterization of 5' untranslated regions of the voltage-gated sodium channels *SCN1A*, *SCN2A*, and *SCN3A* and identification of cis-conserved noncoding sequences. *Genomics* **90**, 225–235 (2007).

54. de Lange, I. M. *et al.* Influence of common *SCN1A* promoter variants on the severity of SCN1A-related phenotypes. *Mol. Genet. Genomic Med.* **7**, 1–11 (2019).

55. Nakayama, T. *et al.* Deletions of *SCN1A* 5' genomic region with promoter activity in dravet syndrome. *Hum. Mutat.* **31**, 820–829 (2010).

56. Marini, C., Mei, D., Helen Cross, J. & Guerrini, R. Mosaic *SCN1A* mutation in familial severe myoclonic epilepsy of infancy. *Epilepsia* **47**, 1737–1740 (2006).

57. Klassen, T. L. & Bomben, V. C. High resolution molecular genomics autopsy reveals complex SUDEP risk profile. *Epilepsia* **27**, 590–609 (2014).

58. Meisler, M. H. & Kearney, J. A. Sodium channel mutations in epilepsy and other neurological disorders. *J. Clin. Invest.* **115**, 2010–2017 (2005).

59. Heron, S. E. *et al.* De novo *SCN1A* mutations in Dravet syndrome and related epileptic encephalopathies are largely of paternal origin. *J. Med. Genet.* **47**, 137–141 (2010).

60. Rubinstein, M. *et al.* Genetic background modulates impaired excitability of inhibitory neurons in a mouse model of Dravet syndrome. *Neurobiol. Dis.* **73**, 106–117 (2015).

61. Morimoto, M. *et al. SCN1A* mutation mosaicism in a family with severe myoclonic epilepsy in infancy. *Epilepsia* **47**, 1732–1736 (2006).

62. Marini, C. *et al. SCN1A* duplications and deletions detected in Dravet syndrome: Implications for molecular diagnosis. *Epilepsia* **50**, 1670–1678 (2009).

63. Davidsson, J., Collin, A., Olsson, M. E., Lundgren, J. & Soller, M. Deletion of the *SCN* gene cluster on 2q24.4 is associated with severe epilepsy: an array-based genotype-phenotype correlation and a comprehensive review of previously published cases. *Epilepsy Res.* **81**, 69–79 (2008).

64. Wang, J. *et al.* Microchromosomal deletions involving *SCN1A* and adjacent genes in severe myoclonic epilepsy in infancy. *Epilepsia* **49**, 1528–1534 (2008).

65. Steel, D., Symonds, J. D., Zuberi, S. M. & Brunklaus, A. Dravet syndrome and its mimics: Beyond *SCN1A*. *Epilepsia* **58**, 1807–1816 (2017).

66. Shi, X. *et al.* Missense mutation of the sodium channel gene *SCN2A* causes Dravet syndrome. *Brain Dev.* **31**, 758–762 (2009).

67. Mulley, J. C. *et al.* Role of the sodium channel *SCN9A* in genetic epilepsy with febrile seizures plus and Dravet syndrome. *Epilepsia* **54**, 122–126 (2013).

68. Patino, G. A. *et al.* A functional null mutation of *SCN1B* in a patient with Dravet syndrome. *J. Neurosci.* **29**, 10764–10778 (2009).

69. Ogiwara, I. *et al.* A homozygous mutation of voltage-gated sodium channel βi gene *SCN1B* in a patient with Dravet syndrome. *Epilepsia* **53**, 200–203 (2012).

70. Ohmori, I. *et al. CACNA1A* variants may modify the epileptic phenotype of Dravet syndrome. *Neurobiol. Dis.* **50**, 209–217 (2013).

71. Depienne, C. *et al.* Sporadic infantile epileptic encephalopathy caused by mutations in *PCDH19* resembles Dravet syndrome but mainly affects females. *PLoS Genet.* **5**, e1000381 (2009).

72. Marini, C. *et al.* The genetics of Dravet syndrome. *Epilepsia* **52**, 24–29 (2011).

73. Johannesen, K. *et al.* Phenotypic spectrum of *GABRA1*: From generalized epilepsies to severe epileptic encephalopathies. (2016).

74. Shen, D. *et al.* De novo *GABRG2* mutations associated with epileptic encephalopathies. *Brain* **140**, 49–67 (2017).

75. Le, S. V., Le, P. H. T., Le, T. K. Van, Kieu Huynh, T. T. & Hang Do, T. T. A mutation in *GABRB3* associated with Dravet syndrome. *Am. J. Med. Genet. A* **173**, 2126–2131 (2017).

76. Carvill, G. L. *et al. GABRA1* and *STXBP1*: Novel genetic causes of Dravet syndrome. *Neurology* **82**, 1245–1253 (2014).

77. Nava, C. *et al.* De novo mutations in *HCN1* cause early infantile epileptic encephalopathy. *Nat. Genet.* **46**, 640–645 (2014).

78. Suls, A. *et al.* De novo loss-of-function mutations in *CHD2* cause a fever-sensitive myoclonic epileptic encephalopathy sharing features with Dravet syndrome. *Am. J. Hum. Genet.* **93**, 967–975 (2013).

79. Syrbe, S. *et al.* De novo loss- or gain-of-function mutations in *KCNA2* cause epileptic encephalopathy. *Nat. Genet.* **47**, 393–399 (2015).

80. Oakley, J. C., Kalume, F., Yu, F. H., Scheuer, T. & Catterall, W. A. Temperature- and age-dependent seizures in a mouse model of severe myoclonic epilepsy in infancy. *Proc. Natl. Acad. Sci. U. S. A.* **106**, 3994–3999 (2009).

81. Dutton, S. B. *et al.* Preferential inactivation of *SCN1A* in parvalbumin interneurons increases seizure susceptibility. *Neurobiol. Dis.* **49**, 211–220 (2013).

82. Mistry, A. M. *et al.* Strain- and age-dependent hippocampal neuron sodium currents correlate with epilepsy severity in Dravet syndrome mice. *Neurobiol. Dis.* **65**, 1–11 (2014).

83. Niibori, Y., Lee, S. J., Minassian, B. A. & Hampson, D. R. Sexually Divergent Mortality and Partial Phenotypic Rescue After Gene Therapy in a Mouse Model of Dravet Syndrome. *Hum. Gene Ther.* **31**, 339–351 (2020).

84. Miller, A. R., Hawkins, N. A., McCollom, C. E. & Kearney, J. A. Mapping genetic modifiers of survival in a mouse model of Dravet syndrome. *Genes. Brain. Behav.* **13**, 163–172 (2014).

85. Cheah, C. S. *et al.* Specific deletion of NaV1.1 sodium channels in inhibitory interneurons causes seizures and premature death in a mouse model of Dravet syndrome. *Proc. Natl. Acad. Sci. U. S. A.* **109**, 14646–14651 (2012).

86. Martin, M. S. *et al.* Altered function of the *SCN1A* voltage-gated sodium channel leads to γ-aminobutyric acid-ergic (GABAergic) interneuron abnormalities. *J. Biol. Chem.* **285**, 9823–9834 (2010).

87. Kuo, F. S., Cleary, C. M., Loturco, J. J., Chen, X. & Mulkey, D. K. Disordered breathing in a mouse model of Dravet syndrome. *Elife* **8**, (2019).

88. Ogiwara, I. *et al.* Nav1.1 haploinsufficiency in excitatory neurons ameliorates seizure-associated sudden death in a mouse model of dravet syndrome. *Hum. Mol. Genet.* **22**, 4784–4804 (2013).

89. Tatsukawa, T., Ogiwara, I., Mazaki, E., Shimohata, A. & Yamakawa, K. Impairments in social novelty recognition and spatial memory in mice with conditional deletion of Scn1a in parvalbumin-expressing cells. *Neurobiol. Dis.* **112**, 24–34 (2018).

90. Stein, R. E., Kaplan, J. S., Li, J. & Catterall, W. A. Hippocampal deletion of NaV1.1 channels in mice causes thermal seizures and cognitive deficit characteristic of Dravet Syndrome. *Proc. Natl. Acad. Sci. U. S. A.* **116**, 16571–16576 (2019).

91. Ito, S. *et al.* Mouse with Nav1.1 haploinsufficiency, a model for Dravet syndrome, exhibits lowered sociability and learning impairment. *Neurobiol. Dis.* **49**, 29–40 (2013).

92. Salgueiro-Pereira, A. R. *et al.* A two-hit story: Seizures and genetic mutation interaction sets phenotype severity in *SCN1A* epilepsies. *Neurobiol. Dis.* **125**, 31–44 (2019).

93. Tsai, M. S. *et al.* Functional and structural deficits of the dentate gyrus network coincide with emerging spontaneous seizures in an *Scn1a* mutant dravet syndrome model during development. *Neurobiol. Dis.* **77**, 35–48 (2015).

94. Ricobaraza, A. *et al.* Epilepsy and neuropsychiatric comorbidities in mice carrying a recurrent Dravet syndrome *SCN1A* missense mutation. *Sci. Rep.* **9**, 1–15 (2019).

95. Fadila, S. *et al.* Convulsive seizures and some behavioral comorbidities are uncoupled in the *Scn1a*A1783V Dravet syndrome mouse model. *Epilepsia* (2020) doi:10.1111/epi.16662.

96. Strzelczyk, A. & Schubert-Bast, S. Therapeutic advances in Dravet syndrome: a targeted literature review. *Expert Rev. Neurother.* **00**, 1–15 (2020).

97. Wirrell, E. C. Treatment of Dravet Syndrome. *Can. J. Neurol. Sci. Le J. Can. des Sci. Neurol.* **43 Suppl 3**, S13-8 (2016).

98. Dressler, A. *et al.* Efficacy and tolerability of the ketogenic diet in Dravet syndrome - Comparison with various standard antiepileptic drug regimen. *Epilepsy Res.* **109**, 81–89 (2015).

99. Inoue, Y. & Ohtsuka, Y. Long-term safety and efficacy of stiripentol for the treatment of Dravet syndrome: A multicenter, open-label study in Japan. *Epilepsy Res.* **113**, 90–97 (2015).

100. Phiel, C. J. *et al.* Histone Deacetylase is a Direct Target of Valproic Acid, a Potent Anticonvulsant, Mood Stabilizer, and Teratogen. *J. Biol. Chem.* **276**, 36734–36741 (2001).

101. Lin, Y. L., Bialer, M., Cabrera, R. M., Finnell, R. H. & Wlodarczyk, B. J. Teratogenicity of valproic acid and its constitutional isomer, amide derivative valnoctamide in mice. *Birth Defects Res.* **111**, 1013–1023 (2019).

102. Fisher, J. L. Interactions between modulators of the GABA(A) receptor: Stiripentol and benzodiazepines. *Eur. J. Pharmacol.* **654**, 160–165 (2011).

103. Chiron, C. *et al.* Stiripentol in severe myoclonic epilepsy in infancy: a randomised placebo-controlled syndrome-dedicated trial. STICLO study group. *Lancet (London, England)* **356**, 1638–1642 (2000).

104. Mula, M., Cavanna, A. E. & Monaco, F. Psychopharmacology of topiramate: From epilepsy to bipolar disorder. *Neuropsychiatr. Dis. Treat.* **2**, 475–488 (2006).

105. Nieto-Barrera, M. [Idiopathic generalized epileptic syndromes of children]. *Rev. Neurol.* **32**, 650–659 (2001).

106. Coppola, G. *et al.* Topiramate as add-on drug in severe myoclonic epilepsy in infancy: an Italian multicenter open trial. *Epilepsy Res.* **49**, 45–48 (2002).

107. Kröll-Seger, J., Portilla, P., Dulac, O. & Chiron, C. Topiramate in the treatment of highly refractory patients with Dravet syndrome. *Neuropediatrics* **37**, 325–329 (2006).

108. Bough, K. J. & Rho, J. M. Anticonvulsant mechanisms of the ketogenic diet. *Epilepsia* **48**, 43–58 (2007).

109. Caraballo, R. H. *et al.* Ketogenic diet in patients with dravet syndrome. *Epilepsia* **46**, 1539–1544 (2005).

110. Nabbout, R. *et al.* Ketogenic diet also benefits Dravet syndrome patients receiving stiripentol: a prospective pilot study. *Epilepsia* **52**, e54-7 (2011).

111. Groesbeck, D. K., Bluml, R. M. & Kossoff, E. H. Long-term use of the ketogenic diet in the treatment of epilepsy. *Dev. Med. Child Neurol.* **48**, 978–981 (2006).

112. Meehan, A. L., Yang, X., McAdams, B. D., Yuan, L. & Rothman, S. M. A new mechanism for antiepileptic drug action: vesicular entry may mediate the effects of levetiracetam. *J. Neurophysiol.* **106**, 1227–1239 (2011).

113. Striano, P. *et al.* An open-label trial of levetiracetam in severe myoclonic epilepsy of infancy. *Neurology* **69**, 250 LP – 254 (2007).

114. Ernst, J. P., Doose, H. & Baier, W. K. Bromides were effective in intractable epilepsy with generalized tonic-clonic seizures and onset in early childhood. *Brain Dev.* **10**, 385–388 (1988).

115. Lotte, J., Haberlandt, E., Neubauer, B., Staudt, M. & Kluger, G. J. Bromide in patients with SCN1A-mutations manifesting as Dravet syndrome. *Neuropediatrics* **43**, 17–21 (2012).

116. Zamponi, N., Passamonti, C., Cappanera, S. & Petrelli, C. Clinical course of young patients with Dravet syndrome after vagal nerve stimulation. *Eur. J. Paediatr. Neurol. EJPN Off. J. Eur. Paediatr. Neurol. Soc.* **15**, 8–14 (2011).

117. Martin, P. *et al.* Fenfluramine acts as a positive modulator of sigma-1 receptors. *Epilepsy Behav.* **105**, 106989 (2020).

118. Boel, M. & Casaer, P. Add-on therapy of fenfluramine in intractable self-induced epilepsy. *Neuropediatrics* **27**, 171–173 (1996).

119. Cross, J. H. *et al.* Dravet syndrome: Treatment options and management of prolonged seizures. *Epilepsia* **60**, S39–S48 (2019).

120. Devinsky, O. *et al.* Effect of cannabidiol on drop seizures in the lennox–gastaut syndrome. *N. Engl. J. Med.* **378**, 1888–1897 (2018).

121. Devinsky, O. *et al.* Trial of cannabidiol for drug-resistant seizures in the dravet syndrome. *N. Engl. J. Med.* **376**, 2011–2020 (2017).

122. Caraballo, R., Demirdjian, G., Reyes, G., Huaman, M. & Gutierrez, R. Effectiveness of cannabidiol in a prospective cohort of children with drug-resistant epileptic encephalopathy in Argentina. *Seizure* **80**, 75–80 (2020).

123. Kaplan, J. S., Stella, N., Catterall, W. A. & Westenbroek, R. E. Cannabidiol attenuates seizures and social deficits in a mouse model of Dravet syndrome. *Proc. Natl. Acad. Sci.*

U. S. A. **114**, 11229–11234 (2017).

124. Osteen, J. D. *et al.* Selective spider toxins reveal a role for the Nav1.1 channel in mechanical pain. *Nature* **534**, 494–499 (2016).

125. Osteen, J. D., Sampson, K., Iyer, V., Julius, D. & Bosmans, F. Pharmacology of the Na_v1.1 domain IV voltage sensor reveals coupling between inactivation gating processes. *Proc. Natl. Acad. Sci.* **114**, 6836 LP – 6841 (2017).

126. Richards, K. L. *et al.* Selective NaV1.1 activation rescues Dravet syndrome mice from seizures and premature death. *Proc. Natl. Acad. Sci. U. S. A.* **115**, E8077–E8085 (2018).

127. Chow, C. Y. *et al.* A selective NaV1.1 activator with potential for treatment of Dravet syndrome epilepsy. *Biochem. Pharmacol.* 113991 (2020) doi:10.1016/j.bcp.2020.113991.

128. Yazdani, A., Alirezaie, Z., Motamedi, M. J. & Amani, J. Gene Therapy: A New Approach in Modern Medicine. *Int. J. Med. Rev.* **5**, 106–117 (2018).

129. Yin, H. *et al.* Non-viral vectors for gene-based therapy. *Nat. Rev. Genet.* **15**, 541–555 (2014).

130. Wells, D. J. Electroporation and ultrasound enhanced non-viral gene delivery in vitro and in vivo. *Cell Biol. Toxicol.* **26**, 21–28 (2010).

131. Hodges, B. L. & Scheule, R. K. Hydrodynamic delivery of DNA. *Expert Opin. Biol. Ther.* **3**, 911–918 (2003).

132. Lin, M. T., Pulkkinen, L., Uitto, J. & Yoon, K. The gene gun: current applications in cutaneous gene therapy. *Int. J. Dermatol.* **39**, 161–170 (2000).

133. Pannell, D. & Ellis, J. Silencing of gene expression: implications for design of retrovirus vectors. *Rev. Med. Virol.* **11**, 205–217 (2001).

134. Hsiao, J. *et al.* Upregulation of Haploinsufficient Gene Expression in the Brain by Targeting a Long Non-coding RNA Improves Seizure Phenotype in a Model of Dravet Syndrome. *EBioMedicine* **9**, 257–277 (2016).

135. Lim, K. H. *et al.* Antisense oligonucleotide modulation of non-productive alternative splicing upregulates gene expression. *Nat. Commun.* **11**, (2020).

136. Colasante, G. *et al.* dCas9-Based Scn1a Gene Activation Restores Inhibitory Interneuron Excitability and Attenuates Seizures in Dravet Syndrome Mice. *Mol. Ther.* **28**, 235–253 (2020).

137. Yamagata, T. *et al.* CRISPR/dCas9-based *Scn1a* gene activation in inhibitory neurons ameliorates epileptic and behavioral phenotypes of Dravet syndrome model mice. *Neurobiol. Dis.* **141**, 104954 (2020).

138. Han, Z. *et al.* Antisense oligonucleotides increase *Scn1a* expression and reduce seizures and SUDEP incidence in a mouse model of Dravet syndrome. *Sci. Transl. Med.* **12**, (2020).

139. Saraiva, J., Nobre, R. J. & Pereira de Almeida, L. Gene therapy for the CNS using AAVs: The impact of systemic delivery by AAV9. *J. Control. Release* **241**, 94–109 (2016).

140. Stoddard, R. J. & Arielle, L. Mechanisms of microbubble-facilitated sonoporation for drug and gene delivery Therapeutic. *Ther. Deliv* **7**, 117–138 (2016).

141. Bennett Frank, C., Krainer, A. R. & Cleveland, D. W. Antisense Oligonucleotide Therapies for Neurodegenerative Diseases. *Annu. Rev. Neurosci.* **42**, 385–406 (2019).

142. Lenk, G. M. *et al. Scn8a* Antisense Oligonucleotide Is Protective in Mouse Models of SCN8A Encephalopathy and Dravet Syndrome. *Ann. Neurol.* **87**, 339–346 (2020).

143. Zucchelli, S. *et al.* SINEUPs: A new class of natural and synthetic antisense long non-coding RNAs that activate translation. *RNA Biol.* **12**, 771–779 (2015).

144. Naso, M. F., Tomkowicz, B., Perry, W. L. 3rd & Strohl, W. R. Adeno-Associated Virus (AAV) as a Vector for Gene Therapy. *BioDrugs* **31**, 317–334 (2017).

145. Manno, C. S. *et al.* Successful transduction of liver in hemophilia by AAV-Factor IX and limitations imposed by the host immune response. *Nat. Med.* **12**, 342–347 (2006).

146. Dayton, R. D., Wang, D. B. & Klein, R. L. The advent of AAV9 expands applications for brain and spinal cord gene delivery. *Expert Opin. Biol. Ther.* **12**, 757–766 (2012).

147. Sakuma, T., Barry, M. A. & Ikeda, Y. Lentiviral vectors: Basic to translational. *Biochem. J.* **443**, 603–618 (2012).

148. A., H., F., A., M., P. & S., A. Lentiviral Gene Therapy Vectors: Challenges and Future Directions. *Gene Ther. - Tools Potential Appl.* (2013) doi:10.5772/52534.

149. Zufferey, R. *et al.* Self-Inactivating Lentivirus Vector for Safe and Efficient In Vivo Gene Delivery. *J. Virol.* **72**, 9873–9880 (1998).

150. Fang, Y., Gong, X., Xu, M., Zeng, F. & Zhang, J. A self-deletion lentiviral vector to reduce the risk of replication-competent virus formation. *J. Gene Med.* **15**, 102–112 (2013).

151. Rowe, W. P., Huebner, R. J., Gilmore, L. K., Parrott, R. H. & Ward, T. G. Isolation of a Cytopathogenic Agent from Human Adenoids Undergoing Spontaneous Degeneration in Tissue Culture. *Proc. Soc. Exp. Biol. Med.* **84**, 570–573 (1953).

152. Ricobaraza, A., Gonzalez-Aparicio, M., Mora-Jimenez, L., Lumbreras, S. & Hernandez-Alcoceba, R. High-capacity adenoviral vectors: Expanding the scope of gene therapy. *Int. J. Mol. Sci.* **21**, (2020).

153. Khanal, S., Ghimire, P. & Dhamoon, A. S. The repertoire of adenovirus in human disease: The innocuous to the deadly. *Biomedicines* **6**, (2018).

154. Lion, T. Adenovirus infections in immunocompetent and immunocompromised patients. *Clin. Microbiol. Rev.* **27**, 441–462 (2014).

155. Lee, C. S. *et al.* Adenovirus-mediated gene delivery: Potential applications for gene and cell-based therapies in the new era of personalized medicine. *Genes Dis.* **4**, 43–63 (2017).

156. Martín, C. S. Latest insights on adenovirus structure and assembly. *Viruses* **4**, 847–877 (2012).

157. Vellinga, J., Van der Heijdt, S. & Hoeben, R. C. The adenovirus capsid: major progress in minor proteins. *J. Gen. Virol.* **86**, 1581–1588 (2005).

158. Russell, W. C. Adenoviruses: Update on structure and function. *J. Gen. Virol.* **90**, 1–20 (2009).

159. Hearing, P., Samulski, R. J., Wishart, W. L. & Shenk, T. Identification of a repeated sequence element required for efficient encapsidation of the adenovirus type 5 chromosome. *J. Virol.* **61**, 2555–2558 (1987).

160. Nevins, J. R. Regulation of early adenovirus gene expression. *Microbiol. Rev.* **51**, 419–430 (1987).

161. Burgert, H. G. & Kvist, S. The E3/19K protein of adenovirus type 2 binds to the domains of histocompatibility antigens required for CTL recognition. *EMBO J.* **6**, 2019–2026 (1987).

162. Halbert, D. N., Cutt, J. R. & Shenk, T. Adenovirus early region 4 encodes functions required for efficient DNA replication, late gene expression, and host cell shutoff. *J. Virol.* **56**, 250–257 (1985).

163. Shaw, A. R. & Ziff, E. B. Transcripts from the adenovirus-2 major late promoter yield a single early family of 3' coterminal mRNAs and five late families. *Cell* **22**, 905–916 (1980).

164. Ostapchuk, P., Yang, J., Auffarth, E. & Hearing, P. Functional interaction of the adenovirus IVa2 protein with adenovirus type 5 packaging sequences. *J. Virol.* **79**, 2831–2838 (2005).

165. Arnberg, N. Adenovirus receptors: implications for targeting of viral vectors. *Trends Pharmacol. Sci.* **33**, 442–448 (2012).

166. Dechecchi, M. C. *et al.* Heparan Sulfate Glycosaminoglycans Are Receptors Sufficient To Mediate the Initial Binding of Adenovirus Types 2 and 5. *J. Virol.* **75**, 8772–8780 (2001).

167. Greber, U. F., Webster, P., Weber, J. & Helenius, A. The role of the adenovirus protease in virus entry into cells. *EMBO J.* **15**, 1766–1777 (1996).

168. Henaff, D., Salinas, S. & Kremer, E. J. An adenovirus traffic update: From receptor engagement to the nuclear pore. *Future Microbiol.* **6**, 179–192 (2011).

169. Guidotti, L. G. & Chisari, F. V. Noncytolytic control of viral infections by the innate and adaptive immune response. *Annu. Rev. Immunol.* **19**, 65–91 (2001).

170. Muruve, D. A., Barnes, M. J., Stillman, I. E. & Libermann, T. A. Adenoviral gene therapy leads to rapid induction of multiple chemokines and acute neutrophil-dependent hepatic injury in vivo. *Hum. Gene Ther.* **10**, 965–976 (1999).

171. Junt, T. *et al.* Subcapsular sinus macrophages in lymph nodes clear lymph-borne viruses and present them to antiviral B cells. *Nature* **450**, 110–114 (2007).

172. Baker, A. T., Aguirre-Hernández, C., Halldén, G. & Parker, A. L. Designer Oncolytic Adenovirus: Coming of Age. *Cancers (Basel).* **10**, (2018).

173. Bischoff, J. R. *et al.* An adenovirus mutant that replicates selectively in p53-deficient human tumor cells. *Science (80-.).* **274**, 373–376 (1996).

174. Cerullo, V. *et al.* Oncolytic adenovirus coding for granulocyte macrophage colony-stimulating factor induces antitumoral immunity in cancer patients. *Cancer Res.* **70**, 4297–4309 (2010).

175. Pesonen, S. *et al.* Integrin targeted oncolytic adenoviruses Ad5-D24-RGD and Ad5-RGD-D24-GMCSF for treatment of patients with advanced chemotherapy refractory solid tumors. *Int. J. cancer* **130**, 1937–1947 (2012).

176. Graham, F. L., Smiley, J., Russell, W. C. & Nairn, R. Characteristics of a human cell line transformed by DNA from human adenovirus type 5. *J. Gen. Virol.* **36**, 59–74 (1977).

177. Crystal, R. G. Adenovirus: the first effective in vivo gene delivery vector. *Hum. Gene Ther.* **25**, 3–11 (2014).

178. Yang, Y., Ertl, H. C. & Wilson, J. M. MHC class I-restricted cytotoxic T lymphocytes to viral antigens destroy hepatocytes in mice infected with E1-deleted recombinant adenoviruses. *Immunity* **1**, 433–442 (1994).

179. Kass-Eisler, A., Leinwand, L., Gall, J., Bloom, B. & Falck-Pedersen, E. Circumventing the immune response to adenovirus-mediated gene therapy. *Gene Ther.* **3**, 154–162 (1996).

180. Amalfitano, A. *et al.* Production and characterization of improved adenovirus vectors with the E1, E2b, and E3 genes deleted. *J. Virol.* **72**, 926–933 (1998).

181. Amalfitano, A., Begy, C. R. & Chamberlain, J. S. Improved adenovirus packaging cell lines to support the growth of replication-defective gene-delivery vectors. *Proc. Natl. Acad. Sci. U. S. A.* **93**, 3352–3356 (1996).

182. Brough, D. E., Lizonova, A., Hsu, C., Kulesa, V. A. & Kovesdi, I. A gene transfer vector-cell line system for complete functional complementation of adenovirus early regions E1 and E4. *J. Virol.* **70**, 6497–6501 (1996).

183. Zhu, F.-C. *et al.* Safety, tolerability, and immunogenicity of a recombinant adenovirus type-5 vectored COVID-19 vaccine: a dose-escalation, open-label, non-randomised, first-in-human trial. *Lancet (London, England)* **395**, 1845–1854 (2020).

184. van Doremalen, N. *et al.* ChAdOx1 nCoV-19 vaccination prevents SARS-CoV-2 pneumonia in rhesus macaques. *bioRxiv : the preprint server for biology* (2020) doi:10.1101/2020.05.13.093195.

185. Folegatti, P. M. *et al.* Safety and immunogenicity of the ChAdOx1 nCoV-19 vaccine against SARS-CoV-2: a preliminary report of a phase 1/2, single-blind, randomised controlled trial. *Lancet (London, England)* **396**, 467–478 (2020).

186. Mercado, N. B. *et al.* Single-shot Ad26 vaccine protects against SARS-CoV-2 in rhesus macaques. *Nature* (2020) doi:10.1038/s41586-020-2607-z.

187. Wu, S. *et al.* A single dose of an adenovirus-vectored vaccine provides protection against SARS-CoV-2 challenge. *Nat. Commun.* **11**, 4081 (2020).

188. Tostanoski, L. H. *et al.* Ad26 vaccine protects against SARS-CoV-2 severe clinical disease in hamsters. *Nat. Med.* (2020) doi:10.1038/s41591-020-1070-6.

189. Logunov, D. Y. *et al.* Safety and immunogenicity of an rAd26 and rAd5 vector-based heterologous prime-boost COVID-19 vaccine in two formulations: two open, non-randomised phase 1/2 studies from Russia. *Lancet (London, England)* **396**, 887–897 (2020).

190. Hassan, A. O. *et al.* A Single-Dose Intranasal ChAd Vaccine Protects Upper and Lower Respiratory Tracts against SARS-CoV-2. *Cell* 183, 169-184.e13 (2020).

191. Alba, R., Bosch, A. & Chillon, M. Gutless adenovirus: last-generation adenovirus for gene therapy. *Gene Ther.* 12 Suppl 1, S18-27 (2005).

192. Muruve, D. A. *et al.* Helper-dependent adenovirus vectors elicit intact innate but attenuated adaptive host immune responses in vivo. *J. Virol.* **78**, 5966–5972 (2004).

193. Thomas, C. E., Schiedner, G., Kochanek, S., Castro, M. G. & Löwenstein, P. R. Peripheral infection with adenovirus causes unexpected long-term brain inflammation in animals injected intracranially with first-generation, but not with high-capacity, adenovirus vectors: toward realistic long-term neurological gene therapy for chronic. *Proc. Natl. Acad. Sci. U. S. A.* **97**, 7482–7487 (2000).

194. Brunetti-Pierri, N. *et al.* Transgene expression up to 7 years in nonhuman primates following hepatic transduction with helper-dependent adenoviral vectors. *Hum. Gene Ther.* **24**, 761–765 (2013).

195. Kochanek, S. *et al.* A new adenoviral vector: Replacement of all viral coding sequences with 28 kb of DNA independently expressing both full-length dystrophin and beta-galactosidase. *Proc. Natl. Acad. Sci. U. S. A.* 93, 5731–5736 (1996).

196. Alemany, R. *et al.* Complementation of helper-dependent adenoviral vectors: Size effects and titer fluctuations. *J. Virol. Methods* 68, 147–159 (1997).

197. Parks, R. J. *et al.* A helper-dependent adenovirus vector system: removal of helper virus by Cre-mediated excision of the viral packaging signal. *Proc. Natl. Acad. Sci. U. S. A.* **93**, 13565–13570 (1996).

198. Palmer, D. & Ng, P. Improved system for helper-dependent adenoviral vector production. *Mol. Ther.* **8**, 846–852 (2003).

199. Umaña, P. *et al.* Efficient FLPe recombinase enables scalable production of helper-dependent adenoviral vectors with negligible helper-virus contamination. *Nat. Biotechnol.* **19**, 582–585 (2001).

200. Cots, D., Bosch, A. & Chillón, M. Helper dependent adenovirus vectors: progress and future prospects. *Curr. Gene Ther.* **13**, 370–381 (2013).

201. Alba, R., Hearing, P., Bosch, A. & Chillon, M. Differential amplification of adenovirus vectors by flanking the packaging signal with attB / attP - Φ C31 sequences : Implications for helper-dependent adenovirus production. **367**, 51–58 (2007).

202. Ng, P., Evelegh, C., Cummings, D. & Graham, F. L. Cre levels limit packaging signal excision efficiency in the Cre/loxP helper-dependent adenoviral vector system. *J. Virol.* **76**, 4181–4189 (2002).

203. Gonzalez-Aparicio, M. *et al.* Self-inactivating helper virus for the production of high-capacity adenoviral vectors. *Gene Ther.* 18, 1025–1033 (2011).

204. Zou, L., Zhou, H., Pastore, L. & Yang, K. Prolonged transgene expression mediated by a helper-dependent adenoviral vector (hdAd) in the central nervous system. *Mol. Ther.* **2**, 105–113 (2000).

205. Butti, E. *et al.* Absence of an intrathecal immune reaction to a helper-dependent adenoviral vector delivered into the cerebrospinal fluid of non-human primates. *Gene Ther.* **15**, 233–238 (2008).

206. Muhammad, A. K. M. G. *et al.* Safety profile of gutless adenovirus vectors delivered into the normal brain parenchyma: implications for a glioma phase 1 clinical trial. *Hum. Gene Ther. Methods* **23**, 271–284 (2012).

207. Thomas, C. E., Schiedner, G., Kochanek, S., Castro, M. G. & Lowenstein, P. R. Preexisting antiadenoviral immunity is not a barrier to efficient and stable transduction of the brain, mediated by novel high-capacity adenovirus vectors. *Hum. Gene Ther.* **12**, 839–846 (2001).

208. Barcia, C. *et al.* One-year expression from high-capacity adenoviral vectors in the brains of animals with pre-existing anti-adenoviral immunity: clinical implications. *Mol. Ther.* **15**, 2154–2163 (2007).

209. Zussy, C. *et al.* Coxsackievirus Adenovirus Receptor Loss Impairs Adult Neurogenesis, Synapse Content, and Hippocampus Plasticity. *J. Neurosci.* 36, 9558–9571 (2016).

210. Poutou, J. *et al.* Adaptation of vectors and drug-inducible systems for controlled expression of transgenes in the tumor microenvironment. *J. Control. Release* 268, 247–258 (2017).

211. Paxinos, G. & Franklin, K. B. J. The Mouse Brain in Stereotaxic Coordinates, 2nd edition. *Academic Press* 360 p. (2001).

212. Seibenhener, M. L. & Wooten, M. C. Use of the open field maze to measure locomotor and anxiety-like behavior in mice. *J. Vis. Exp.* 1–6 (2015) doi:10.3791/52434.

213. Lueptow, L. M. Novel object recognition test for the investigation of learning and memory in mice. *J. Vis. Exp.* **2017**, 1–9 (2017).

214. Jirkof, P. Burrowing and nest building behavior as indicators of well-being in mice. *J. Neurosci. Methods* **234**, 139–146 (2014).

215. Vorhees, C. V & Williams, M. T. Morris water maze: procedures for assessing spatial and related forms of learning and memory. *Nat. Protoc.* **1**, 848–858 (2006).

216. Ricobaraza, A. *et al.* Phenylbutyrate ameliorates cognitive deficit and reduces tau pathology in an Alzheimer's disease mouse model. *Neuropsychopharmacol. Off. Publ. Am. Coll. Neuropsychopharmacol.* 34, 1721–1732 (2009).

217. Shiotsuki, H. *et al.* A rotarod test for evaluation of motor skill learning. *J. Neurosci. Methods* 189, 180–185 (2010).

218. Deacon, R. M. J. Measuring the strength of mice. *J. Vis. Exp.* (2013) doi:10.3791/2610.

219. Luong, T. N., Carlisle, H. J., Southwell, A. & Patterson, P. H. Assessment of motor balance and coordination in mice using the balance beam. *J. Vis. Exp.* (2011) doi:10.3791/2376.

220. Guyenet, S. J. *et al.* A simple composite phenotype scoring system for evaluating mouse models of cerebellar ataxia. *J. Vis. Exp.* (2010) doi:10.3791/1787.

221. Gelinas, J. N., Khodagholy, D., Thesen, T., Devinsky, O. & Buzsáki, G. Interictal epileptiform discharges induce hippocampal-cortical coupling in temporal lobe epilepsy. *Nat. Med.* 22, 641–648 (2016).

222. Van Erum, J., Van Dam, D. & De Deyn, P. P. PTZ-induced seizures in mice require a revised Racine scale. *Epilepsy Behav.* 95, 51–55 (2019).

223. Pfaffl, M. W. A new mathematical model for relative quantification in real-time RT-PCR. *Nucleic Acids Res.* 29, e45 (2001).

224. Dunah, A. W., Wyszynski, M., Martin, D. M., Sheng, M. & Standaert, D. G. alpha-actinin-2 in rat striatum: localization and interaction with NMDA glutamate receptor subunits. *Brain Res. Mol. Brain Res.* 79, 77–87 (2000).

225. Li, B.-M. *et al.* Autism in Dravet syndrome: prevalence, features, and relationship to the clinical characteristics of epilepsy and mental retardation. *Epilepsy Behav.* 21, 291–295 (2011).

226. Berkvens, J. J. L. *et al.* Autism and behavior in adult patients with Dravet syndrome (DS). *Epilepsy Behav.* 47, 11–16 (2015).

227. Gitiaux, C. *et al.* Motor neuropathy contributes to crouching in patients with Dravet syndrome. *Neurology* 87, 277–281 (2016).

228. Song, W., Liu, Z., Tan, J., Nomura, Y. & Dong, K. RNA editing generates tissue-specific sodium channels with distinct gating properties. *J. Biol. Chem.* 279, 32554–32561 (2004).

229. Zubović, L., Baralle, M. & Baralle, F. E. Mutually exclusive splicing regulates the Nav 1.6 sodium channel function through a combinatorial mechanism that involves three distinct splicing regulatory elements and their ligands. *Nucleic Acids Res.* 40, 6255–6269 (2012).

230. Feldman, D. H. & Lossin, C. The Nav channel bench series: Plasmid preparation. *MethodsX* 1, 6–11 (2014).

231. Yaguchi, M. *et al.* Characterization of the properties of seven promoters in the motor cortex of rats and monkeys after lentiviral vector-mediated gene transfer. *Hum. Gene Ther. Methods* 24, 333–344 (2013).

232. Smith, R. L. *et al.* Characterization of promoter function and cell-type-specific expression from viral vectors in the nervous system. *J. Virol.* 74, 11254–11261 (2000).

233. Gray, S. J. *et al.* Optimizing promoters for recombinant adeno-associated virus-mediated gene expression in the peripheral and central nervous system using self-complementary vectors. *Hum. Gene Ther.* 22, 1143–1153 (2011).

234. Brooks, A. R. *et al.* Transcriptional silencing is associated with extensive methylation of the CMV promoter following adenoviral gene delivery to muscle. *J. Gene Med.* 6, 395–404 (2004).

235. Toietta, G. *et al.* Generation of helper-dependent adenoviral vectors by homologous recombination. *Mol. Ther.* 5, 204–210 (2002).

236. Rao, X., Huang, X., Zhou, Z. & Lin, X. An improvement of the 2ˆ(-delta delta CT) method for quantitative real-time polymerase chain reaction data analysis. *Biostat. Bioinforma. Biomath.* 3, 71–85 (2013).

237. Morral, N. *et al.* Administration of helper-dependent adenoviral vectors and sequential delivery of different vector serotype for long-term liver-directed gene transfer in baboons. *Proc. Natl. Acad. Sci. U. S. A.* 96, 12816–12821 (1999).

238. Liautard, C. *et al.* Hippocampal hyperexcitability and specific epileptiform activity in a mouse model of Dravet syndrome. *Epilepsia* 54, 1251–1261 (2013).

239. Tran, C. H. *et al.* Interneuron desynchronization precedes seizures in a mouse model of Dravet syndrome. *J. Neurosci.* 40, 2764–2775 (2020).

240. Allen, L. A. *et al.* Dysfunctional brain networking among autonomic regulatory structures in temporal lobe epilepsy patients at High Risk of sudden unexpected death in epilepsy. *Front. Neurol.* 8, 1–13 (2017).

241. Tang, Y. *et al.* A resting-state functional connectivity study in patients at high risk for sudden unexpected death in epilepsy. *Epilepsy Behav.* 41, 33–38 (2014).

242. Jansen, N. A., Dehghani, A., Breukel, C., Tolner, E. A. & van den Maagdenberg, A. M. J. M. Focal and generalized seizure activity after local hippocampal or cortical ablation of NaV1.1 channels in mice. *Epilepsia* 61, e30–e36 (2020).

243. Kedia, S. & Chattarji, S. Marble burying as a test of the delayed anxiogenic effects of acute immobilisation stress in mice. *J. Neurosci. Methods* 233, 150–154 (2014).

244. Moy, S. S. *et al.* Mouse behavioral tasks relevant to autism: phenotypes of 10 inbred strains. *Behav. Brain Res.* 176, 4–20 (2007).

245. Turner, S. J. *et al.* Dysarthria and broader motor speech deficits in Dravet syndrome. *Neurology* 88, 743–749 (2017).

246. Verheyen, K. *et al.* Motor development in children with Dravet syndrome. *Dev. Med. Child Neurol.* 61, 950–956 (2019).

247. Nabbout, R. *et al.* Encephalopathy in children with Dravet syndrome is not a pure consequence of epilepsy. *Orphanet J. Rare Dis.* 8, 1–8 (2013).

248. Lagae, L. *et al.* Fenfluramine hydrochloride for the treatment of seizures in Dravet syndrome: a randomised, double-blind, placebo-controlled trial. *Lancet (London, England)* 394, 2243–2254 (2020).

249. Wang, Z. *et al.* Voltage-Gated Sodium Channels Are Involved in Cognitive Impairments in Parkinson's Disease- like Rats. *Neuroscience* 418, 231–243 (2019).

250. Mishra, S. *et al.* Contribution of sodium channel neuronal isoform Nav1.1 to late sodium current in ventricular myocytes from failing hearts. *J. Physiol.* 593, 1409–1427 (2015).

251. Wirrell, E. C. *et al.* Optimizing the Diagnosis and Management of Dravet Syndrome: Recommendations: From a North American Consensus Panel. *Pediatr. Neurol.* 68, 18-34.e3 (2017).

252. Ruffolo, G. *et al.* A novel GABAergic dysfunction in human Dravet syndrome. *Epilepsia* 59, 2106–2117 (2018).

253. Idema, S. *et al.* Anatomical differences determine distribution of adenovirus after convection-enhanced delivery to the rat brain. *PLoS One* 6, (2011).

254. Spencer, D. D. & Spencer, S. S. Surgery for epilepsy. *Neurol. Clin.* 3, 313–330 (1985).

255. Dunoyer, C. *et al.* The use of stereotactic radiosurgery to treat intractable childhood partial epilepsy. *Epilepsia* 43, 292–300 (2002).

256. Catenoix, H., Bourdillon, P., Guénot, M. & Isnard, J. The combination of stereo-EEG and radiofrequency ablation. *Epilepsy Res.* 142, 117–120 (2018).

257. Canafoglia, L. *et al.* Movement-activated cortical myoclonus in Dravet syndrome. *Epilepsy Res.* 130, 47–52 (2017).

258. Allen, L. A. *et al.* Cerebellar, limbic, and midbrain volume alterations in sudden unexpected death in epilepsy. *Epilepsia* 60, 718–729 (2019).

259. Ryvlin, P. *et al.* Incidence and mechanisms of cardiorespiratory arrests in epilepsy monitoring units (MORTEMUS): A retrospective study. *Lancet Neurol.* 12, 966–977 (2013).

260. Ritter-Makinson, S. *et al.* Augmented Reticular Thalamic Bursting and Seizures in Scn1a-Dravet Syndrome. *Cell Rep.* 26, 54-64.e6 (2019).

261. Warren, A. E. L. *et al.* The epileptic network of Lennox-Gastaut syndrome: Cortically driven and reproducible across age. *Neurology* 93, E215–E226 (2019).

262. Barker, G. R. I., Bird, F., Alexander, V. & Warburton, E. C. Recognition memory for objects, place, and temporal order: A disconnection analysis of the role of the medial prefrontal cortex and perirhinal cortex. *J. Neurosci.* 27, 2948–2957 (2007).

263. de Bruin, J. P. C., Sànchez-Santed, F., Heinsbroek, R. P. W., Donker, A. & Postmes, P. A behavioural analysis of rats with damage to the medial prefrontal cortex using the morris water maze: evidence for behavioural flexibility, but not for impaired spatial navigation. *Brain Res.* 652, 323–333 (1994).

264. Sang Jo, Y. *et al.* The medial prefrontal cortex is involved in spatial memory retrieval under partial-cue conditions. *J. Neurosci.* 27, 13567–13578 (2007).

265. Florian, C. & Roullet, P. Hippocampal CA3-region is crucial for acquisition and memory consolidation in Morris water maze task in mice. *Behav. Brain Res.* 154, 365–374 (2004).

266. Hainmueller, T. & Bartos, M. Dentate gyrus circuits for encoding, retrieval and discrimination of episodic memories. *Nat. Rev. Neurosci.* 21, 153–168 (2020).

267. Fanselow, M. S. & Dong, H.-W. Are the dorsal and ventral hippocampus functionally distinct structures? *Neuron* 65, 7–19 (2010).

268. Denninger, J. K., Smith, B. M. & Kirby, E. D. Novel Object Recognition and Object Location Behavioral Testing in Mice on a Budget. *J. Vis. Exp.* (2018) doi:10.3791/58593.

269. Gowen, E. & Miall, R. C. The cerebellum and motor dysfunction in neuropsychiatric disorders. *Cerebellum* 6, 268–279 (2007).

270. Middleton, F. A. & Strick, P. L. Basal ganglia and cerebellar loops: motor and cognitive circuits. *Brain Res. Brain Res. Rev.* 31, 236–250 (2000).

271. Carty, N. *et al.* Convection-enhanced delivery and systemic mannitol increase gene product distribution of AAV vectors 5, 8, and 9 and increase gene product in the adult mouse brain. *J. Neurosci. Methods* 194, 144–153 (2010).

272. Gorick, C. M., Sheybani, N. D., Curley, C. T. & Price, R. J. Listening in on the microbubble crowd: Advanced acoustic monitoring for improved control of blood-brain barrier opening with focused ultrasound. *Theranostics* 8, 2988–2991 (2018).

273. Junyent, F. & Kremer, E. J. CAV-2 - Why a canine virus is a neurobiologist's best friend. *Curr. Opin. Pharmacol.* 24, 86–93 (2015).

274. Salinas, S. *et al.* CAR-associated vesicular transport of an adenovirus in motor neuron axons. *PLoS Pathog.* 5, (2009).

Appendix

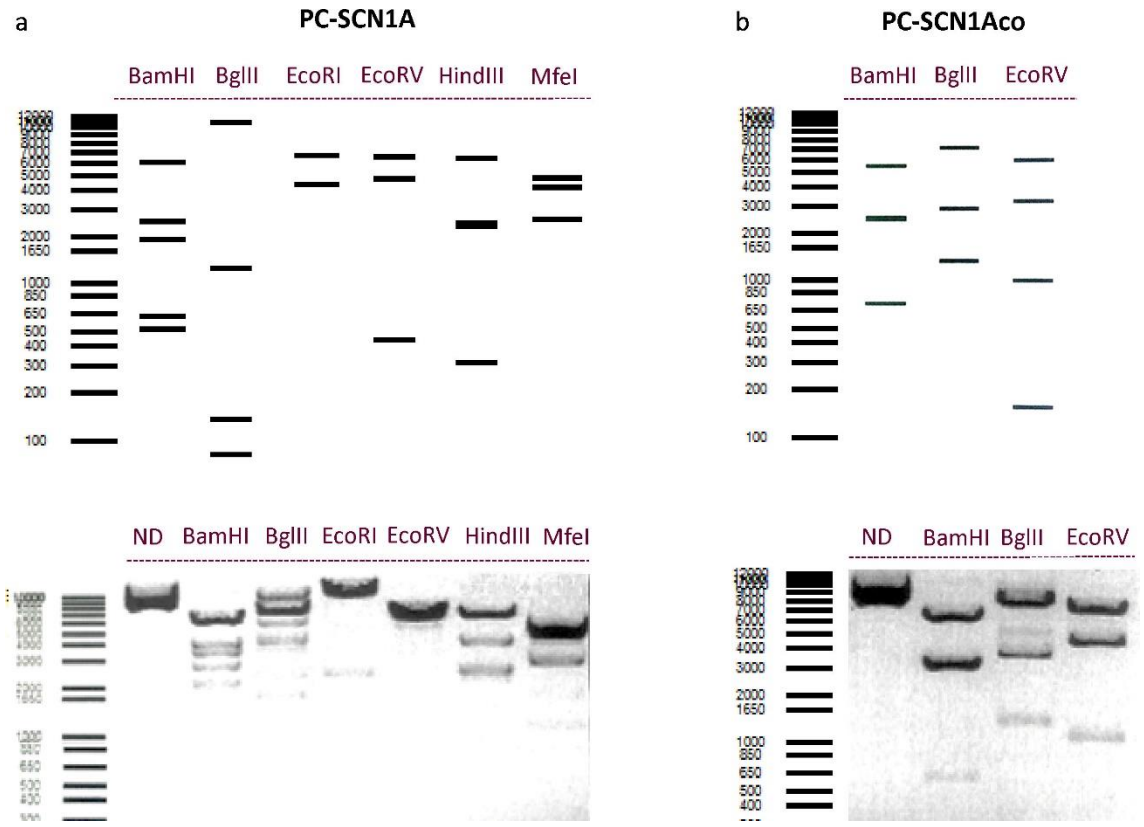

Figure A.1. Restriction maps of pC-SCN1A and pC-SCN1Aco. The standard and the codon-optimized version of the *SCN1A* coding sequence inserted in the corresponding plasmids (pC-SCN1A and pC-SCN1Aco, respectively), were digested with a battery of restriction endonucleases (all from New England Biolabs): BamHI, BglII, EcoRI, EcoRV, HindIII, and MfeI. Expected restriction maps for each individual digestion (Serial Cloner 2.6.1) are represented in the upper panels. Agarose gels with the resulting bands after incubation with the corresponding enzymes are represented in the lower panels. DNA fragments obtained after restriction reaction of the pC-SCN1A plasmid did not correspond to their predicted restriction map (**a**), whereas all enzymatic digestions bands from the pC-SCN1Aco plasmid were correct (**b**). ND, undigested.

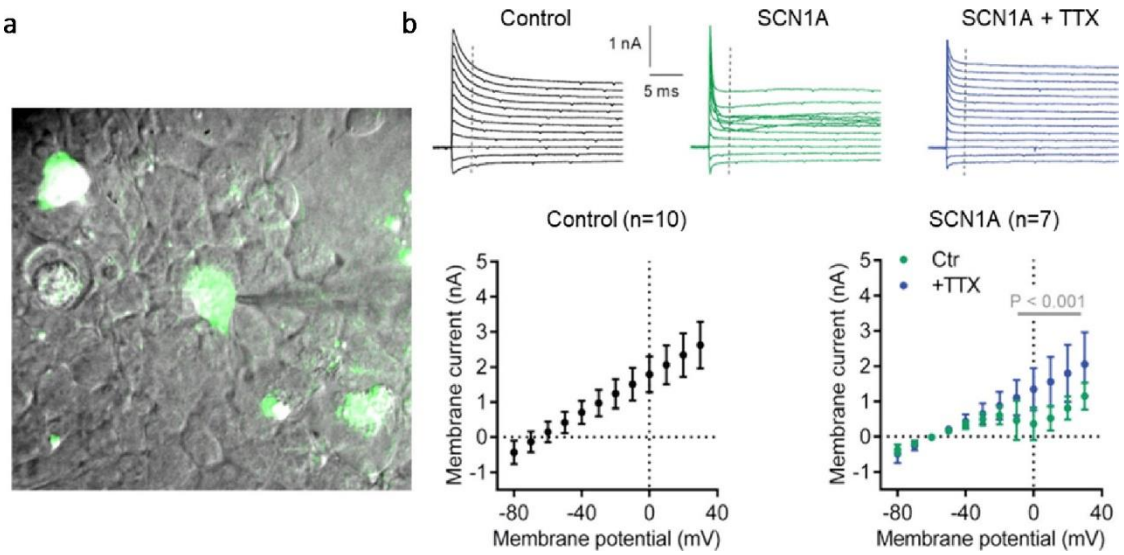

Figure A.2. Functional validation of the *SCN1A* transgene. HEK-293 cells were transfected with the pEF-SCN1A-GFP plasmid, and the function of the Nav1.1 channel was analyzed by patch-clamp 48 h later. (**a**) Representative image of transfected cells under the fluorescence microscope. Note the tip of the micropipette touching the GFP-expressing cell in the center of the image. (**b**) The top graphs show examples of the membrane current response to stepping the membrane potential from -80 mV (bottom) to +30 mV (top) in 10 mV steps in control and transfected cells. The bottom graphs are the corresponding quantifications from the indicated number of cells. Tetrodotoxin (TTX) was added at 2 µM.

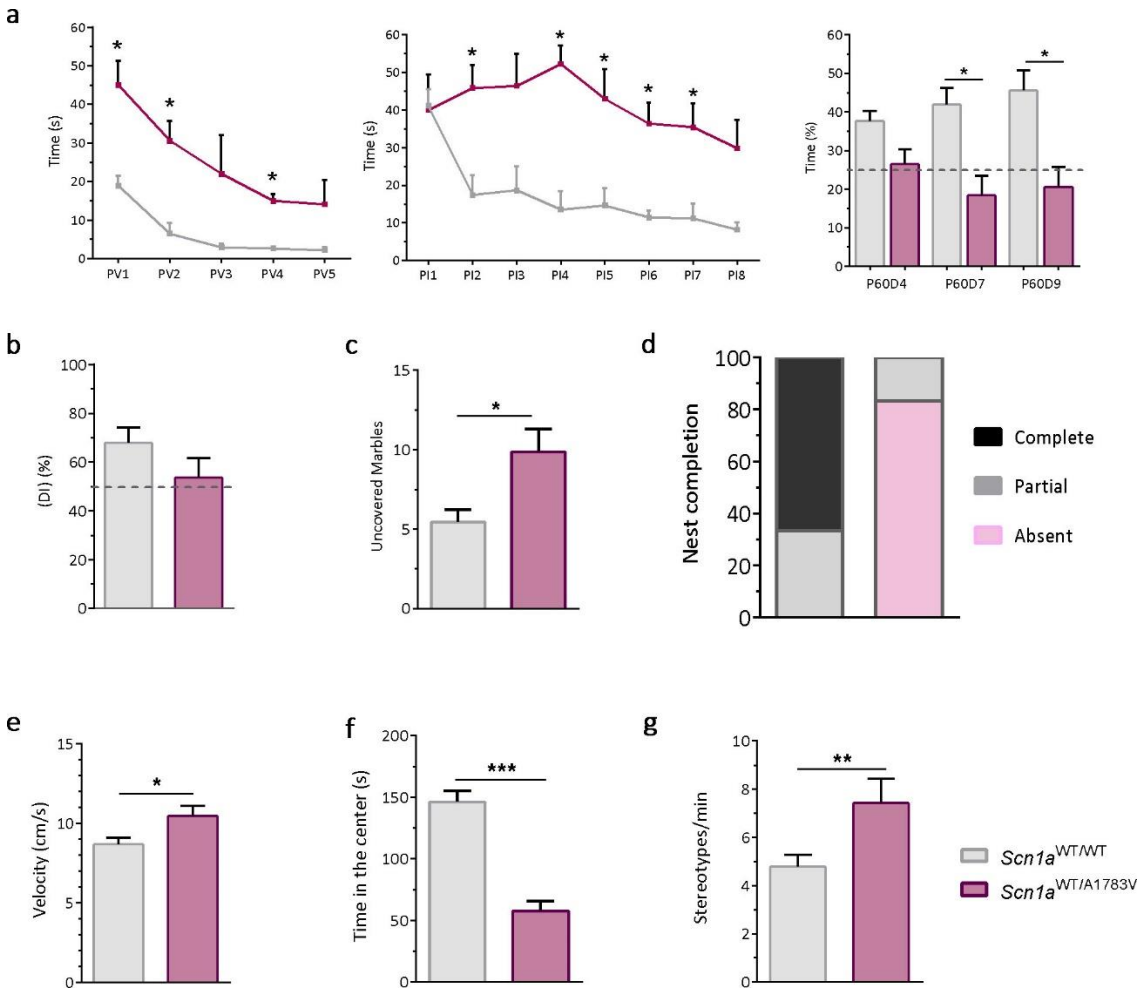

Figure A.3. Adolescent *Scn1a*$^{WT/A1783V}$ mice show cognitive and behavioral alterations. Five to six wo *Scn1a*$^{WT/WT}$ and *Scn1a*$^{WT/A1783V}$ mice were subjected to the indicated tests in order to determine the level of cognitive and behavioral impairment at this age. (**a**) MWM-VP, MWM-IP phases and the Probe 60 of the test are represented in the left, middle and right panels, respectively (n=4 in both groups). (**b**) NOR 24 h (*Scn1a*$^{WT/WT}$ n=13; *Scn1a*$^{WT/A1783V}$ n=5). (**c**) Marble burying test (*Scn1a*$^{WT/WT}$ n=8; *Scn1a*$^{WT/A1783V}$ n=3). (**d**) Nest building test (*Scn1a*$^{WT/WT}$ n=9; *Scn1a*$^{WT/A1783V}$ n=6). **(e-g)** OF (*Scn1a*$^{WT/WT}$ n=16; *Scn1a*$^{WT/A1783V}$ n=9) including velocity (**e**), time spent in the center of the arena (**f**), and number of stereotypies/min (**g**). *p<0.05; **p<0.01; ***p<0.001, Mann-Whitney test.

Published articles

» "**Epilepsy and neuropsychiatric comorbidities in mice carrying a recurrent Dravet syndrome *SCN1A* missense mutation".** Ricobaraza A, Mora-Jimenez L, Puerta E, Sanchez-Carpintero R, Mingorance A, Artieda J, Nicolas MJ, Besne G, Buñuales M, Gonzañez-Aparicio M, Sola-Sevilla N, Valencia M & Hernandez-Alcoceba R. **Scientific Reports, 2019.**
https://www.nature.com/articles/s41598-019-50627-

» **High-Capacity Adenoviral Vectors: Expanding the Scope of Gene Therapy".** Ricobaraza A, Gonzalez-Aparicio M, Mora-Jimenez L, Lumbreras S, Hernandez-Alcoceba R. **International Journal of Molecular Sciences, 2020.**
https://www.mdpi.com/1422-0067/21/10/3643

SCIENTIFIC REPORTS
nature research

OPEN

Epilepsy and neuropsychiatric comorbidities in mice carrying a recurrent Dravet syndrome *SCN1A* missense mutation

Received: 8 May 2019
Accepted: 11 September 2019
Published online: 02 October 2019

Ana Ricobaraza[1], Lucia Mora-Jimenez[1], Elena Puerta[2], Rocio Sanchez-Carpintero[3], Ana Mingorance[4], Julio Artieda[5], Maria Jesus Nicolas[6], Guillermo Besne[6], Maria Bunuales[1], Manuela Gonzalez-Aparicio[1], Noemi Sola-Sevilla[3], Miguel Valencia[6] & Ruben Hernandez-Alcoceba[1]

Dravet Syndrome (DS) is an encephalopathy with epilepsy associated with multiple neuropsychiatric comorbidities. In up to 90% of cases, it is caused by functional haploinsufficiency of the *SCN1A* gene, which encodes the alpha subunit of a voltage-dependent sodium channel (Nav1.1). Preclinical development of new targeted therapies requires accessible animal models which recapitulate the disease at the genetic and clinical levels. Here we describe that a C57BL/6 J knock-in mouse strain carrying a heterozygous, clinically relevant *SCN1A* mutation (A1783V) presents a full spectrum of DS manifestations. This includes 70% mortality rate during the first 8 weeks of age, reduced threshold for heat-induced seizures (4.7 °C lower compared with control littermates), cognitive impairment, motor disturbances, anxiety, hyperactive behavior and defects in the interaction with the environment. In contrast, sociability was relatively preserved. Electrophysiological studies showed spontaneous interictal epileptiform discharges, which increased in a temperature-dependent manner. Seizures were multifocal, with different origins within and across individuals. They showed intra/inter-hemispheric propagation and often resulted in generalized tonic-clonic seizures. ^{18}F-labelled flourodeoxyglucose positron emission tomography (FDG-PET) revealed a global increase in glucose uptake in the brain of Scn1a$^{WT/A1783V}$ mice. We conclude that the Scn1a$^{WT/A1783V}$ model is a robust research platform for the evaluation of new therapies against DS.

Dravet syndrome (DS) is a severe early onset encephalopathy (OMIM 607208) with an average incidence of 1:20,000 births. Although it is also known as severe myoclonic epilepsy of infancy (SMEI), accounting for 1.4% of children with epilepsy[1], seizures are not the only manifestations of the disease[2]. The first symptoms start at 4–8 months of age, in a previously normal infant, as clonic or hemiclonic febrile seizures, usually prolonged and refractory to conventional antiepileptic drugs. The frequency of life-threatening status epilepticus (SE) in these patients can reach 80% during the first year of life. After this "febrile stage" of the disease, a "worsening stage" extends up to the fifth year of life, in which afebrile myoclonic, focal or generalized seizures are frequent, as well as atypical absences[3]. During this period a variety of neurological disturbances appear, including psychomotor delay leading to cognitive disability, motor disturbances as well as hyperkinesia and some features of autism spectrum disorder. During the "stabilization stage" these invalidating problems persist and crouching gait as well

[1]University of Navarra, Gene Therapy Program CIMA, IdiSNA, Navarra institute for health research, Pamplona, Spain. [2]University of Navarra, Department of Pharmacology and Toxicology, IdiSNA, Navarra institute for health research, Pamplona, Spain. [3]University Clinic of Navarra, Dravet Syndrome Unit, Pediatric Neurology Unit, IdiSNA, Navarra institute for health research, Pamplona, Spain. [4]Dracaena Consulting, Madrid, Spain. [5]University of Navarra, Neuroscience Program CIMA, IdiSNA, Navarra institute for health research, Neurophysiology Service, Clinica Universidad de Navarra, University of Navarra, Pamplona, Spain. [6]University of Navarra, Neuroscience Program CIMA, IdiSNA, Navarra institute for health research, Pamplona, Spain. Miguel Valencia and Ruben Hernandez–Alcoceba jointly supervised this work. Correspondence and requests for materials should be addressed to A.R. (email: aricobaraza@unav.es)

as parkinsonian features appear, but epileptic episodes are less frequent. However, the risk of sudden unexpected death in epilepsy (SUDEP) is always present. Overall, mortality rate in DS is estimated at 15% in industrialized countries[4], with approximately 50% of cases due to SUDEP and 35% due to SE.

In nearly 90% of DS patients, the genetic basis of the disease involves the *SCN1A* gene[5,6], which encodes the alpha subunit of a voltage-dependent sodium channel (Nav1.1). This membrane transporter is crucial for the function of GABAergic inhibitory interneurons expressing parvalbumin or somatostatin (PV and ST cells, respectively)[7,8]. Insufficient Nav1.1 activity causes alteration in the excitatory/inhibitory balance of the brain, which is the basis for most clinical manifestations.

Homozygous deletions or loss of function mutations of *SCN1A* are extremely rare in humans, probably because of embryonic lethality. DS patients usually present heterozygous mutations resulting in functional inactivation of one *SCN1A* allele[9]. In approximately half of the cases, the mutated allele produces a truncated Nav1.1 channel due to nonsense, frameshift or splice defect mutations (17%, 19% and 9%, respectively)[10]. The other half presents missense mutations or in-frame deletions, with variable impact on channel function. In the lower spectrum of severity, missense mutations causing moderate impairment have been associated with milder diseases such as genetic epilepsy with febrile seizures plus ($GEFS^{+}$)[11]. In addition, diverse functional alterations of Nav1.1 may contribute to other neurological disorders such as autism[12], familial hemiplegic migraine[13], and aging-related cerebral impairment[14].

Advances in the understanding of DS pathophysiology and the development of new therapies require relevant animal models. This is especially important for the evaluation of novel approaches aimed at restoring Nav1.1 expression or function, which offer the opportunity to control not only seizures, but also the rest of invalidating comorbidities.

A variety of genetic mouse models based on *Scn1a* alterations have been described. Most of them rely on deletions of the gene, either globally or affecting specific cell populations. Mice harboring homozygous deletions in the C57BL/6 background inexorably die two weeks after birth[15–17], whereas haploinsufficient mice show spontaneous seizures and elevated mortality from 3 to 12 weeks of age, resulting in 20% long-term survival[16]. In contrast, clinical manifestations are very mild in the 129 Sv background[18]. Conditional deletion of *Scn1a* in different cell populations has been obtained by crossing mice carrying one floxed *Scn1a* allele with those expressing Cre recombinase under the control of specific promoters[7,19–21]. The prominent role of GABAergic inhibitory interneurons is in line with the drastic epileptic phenotype observed in the VGAT-Cre strain, which is more severely affected than the global *Scn1a* deficient mice. In contrast, deletion of *Scn1a* in excitatory neurons (Emx1-Cre strain) showed no epileptic phenotype[19]. Supporting this concept, a recent work demonstrates that 100% of mice carrying the *Scn1a* A1783V mutation in VGAT-expressing cells die before postnatal day 25[22]. To narrow down the implication of different interneuron populations, Nav1.1 was deleted in PV *vs* ST cells. The results showed that defects in ST cells caused only a mild phenotype. In contrast, mice with defects in PV cells suffered a marked reduction in the threshold temperature for hyperthermia-induced seizures, together with behavioral abnormalities[20]. However, the implication of ST cells in the phenotype of DS mice has been demonstrated in other reports[7]. Apart from the specific alteration introduced in the *Scn1a* gene of each mouse model (deletions, frameshift or missense mutations), the genetic background is an important modifier factor[16,18]. This may explain discrepancies between different studies regarding the role of ST and PV cells on specific manifestations such as hyperactivity and autistic-like behaviors[7,20]. Although these tools are helping to elucidate the physiopathology of DS, preclinical development of new therapies requires a widely available mouse model with the ability to recapitulate the human disease at the genetic and phenotypic levels.

To this end, we have employed conditional knock-in mice with a heterozygous *Scn1a* A1783V mutation in all cells, maintained in a C57BL/6J background. This is a pathogenic missense mutation in exon 26, previously described in DS patients[10,23], which is expected to affect the inactivation gate receptor of Nav1.1 located in the S6 segment of domain 4[22,24]. In this report we describe a remarkable reproduction of DS manifestations in all aspects of the disease such as epileptic activity, motor, behavioral and cognitive alterations. Of note, a knock-in model harboring the same mutation (B6(Cg)-Scn1atm1.1Dsf/J strain crossed with Cox2-Cre expressing mice) has been recently adopted by the US National Institute of Neurological disorders and Stroke (NINDS) in the panel of animal models of the Epilepsy Therapy Screening Program (ETSP). This is the first model of genetic epilepsy to be included in the panel (https://dravet.eu/projects-item/mouse-model/).

Results

$Scn1a^{WT/A1783V}$ mice have a high mortality rate. The B6(Cg)-*Scn1a*$^{tm1.1Dsf}$/J strain contains *Scn1a* exon 26 flanked by loxP sites in one of the alleles, followed by a humanized exon 26 with a C to T change at nucleotide 5348 (https://www.jax.org/strain/026133). Mice from the B6.C-Tg(CMV-Cre)1Cgn/J strain express Cre under the control of the ubiquitous CMV promoter. When these strains are crossed, the floxed exon can suffer Cre-mediated scission and the mutated exon 26 is incorporated in the mature mRNA expressed from this allele. This happens in approximately half of the offspring (genotype hereinafter referred to as $Scn1a^{WT/A1783V}$). In these mice, 50% of the Nav1.1 channels expressed in every cell contain the A1783V amino acid change. Litters of these crosses showed a 24% mortality rate before weaning. In all cases analyzed, dead pups corresponded to $Scn1a^{WT/A1783V}$ mice. The weight of $Scn1a^{WT/A1783V}$ mice surviving after weaning was lower than their $Scn1a^{WT/WT}$ littermates until the 8th week of age (Fig. 1a). Survival of $Scn1a^{WT/A1783V}$ mice dropped sharply from weaning to the 6th weeks of age, and then it remained relatively stable, resulting in approximately 25% long-term survivors (Fig. 1b). Although the main cause of death in these animals needs further study, our results point to SUDEP, since the frequency of spontaneous generalized tonic clonic seizures (15% of mice, starting from week 3 of age) cannot account for the high mortality rate observed.

Analysis of *Scn1a* expression quantified at the mRNA level showed a moderate reduction in hippocampus of $Scn1a^{WT/A1783V}$ mice (Fig. 2a), but no significant changes in Nav1.1 content were observed in membrane-enriched

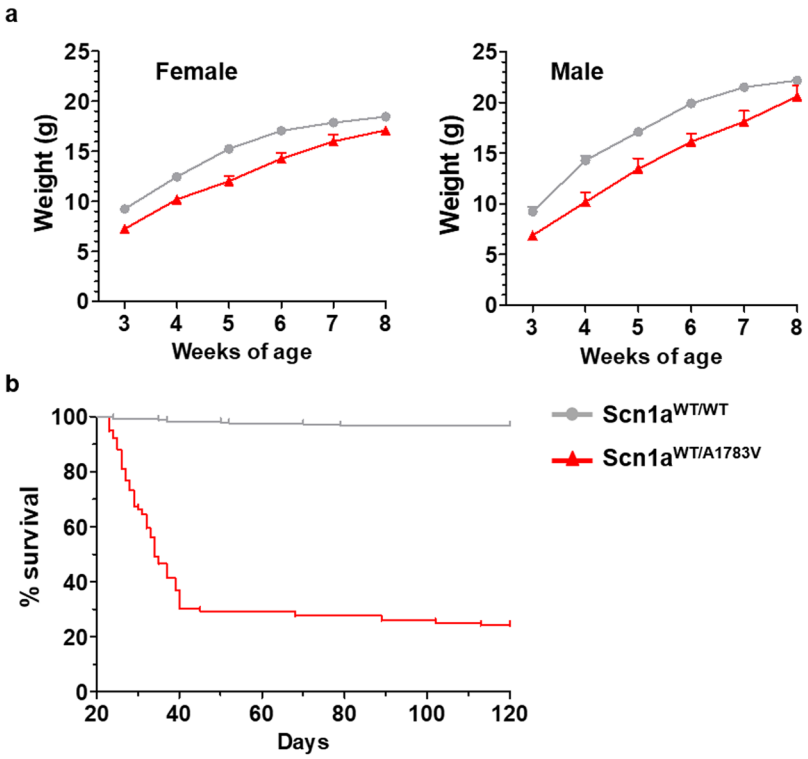

Figure 1. Scn1a$^{WT/A1783V}$ mice present reduced body weight and high mortality during the first 6 weeks of life. (**a**) Animals were weighted once per week since weaning. Points represent mean values ± SEM (females Scn1a$^{WT/WT}$ average n = 30; females Scn1a$^{WT/A1783V}$ n = 20; males Scn1a$^{WT/WT}$ n = 40; males Scn1a$^{WT/A1783V}$ n = 15). Weight curves of Scn1a$^{WT/A1783V}$ and control littermates mice show significant differences in elevation ($p < 0.0001$) but not in slope (linear regression analysis). (**b**) Survival curves of mice after weaning (postnatal day 21) are significantly different ($p < 0.0001$ log-rank test). Of note, Scn1a$^{WT/A1783V}$ mice present a 24% mortality rate before weaning.

extracts by Western blot in any brain structure. If anything, the reduction would be less than 20% (Fig. 2b), and no obvious differences were detected in the immunofluorescence analysis of brain samples (Fig. 2c,d). This is compatible with the expected outcome of a heterozygous missense mutation.

Scn1a$^{WT/A1783V}$ mice present abnormal interictal activity and heat-induced seizures. In order to define the seizure-threshold temperature of this DS model, Scn1a$^{WT/A1783V}$ and their corresponding control littermates were subjected to hyperthermia at different age intervals (1–2, 2–4 and 4–6 months of age). All Scn1a$^{WT/A1783V}$ mice suffered clinically recognizable seizures, with an average threshold of 38.2 ± 2.9 °C (Fig. 3a). In contrast, 80% of Scn1a$^{WT/WT}$ mice experienced seizures only when temperatures increased to a maximum of 45 °C (Fig. 3b), showing an average threshold of 42.9 ± 1.4 °C.

Multisite recordings (hippocampus and prefrontal cortex) were performed in a subgroup of animals from the 1–3 age range to investigate electrophysiological differences between Scn1a$^{WT/A1783V}$ and Scn1a$^{WT/WT}$ littermates (Fig. 4). Thirty minutes of electrophysiological activity together with synchronized digital video recording in awake, freely moving mice in an open-field arena revealed the presence of interictal epileptiform discharges (IEDs) in all of the Scn1a$^{WT/A1783V}$ mice (5 out of 5) at room temperature (RT). IEDs discharges consisted in isolated or grouped spikes (*multispike*) with very short durations (<20 ms) and high amplitudes (>100 µVpp) standing above the background activity (Fig. 4a). Both, focal (i.e. presence of IEDs in a single channel) and generalized (presence of IEDs across several channels simultaneously) distributions were observed. Interestingly, no IEDs were detected in any of their Scn1a$^{WT/WT}$ littermates (5 out of 5). Mice's brain activity was then recorded at increasing temperatures (Fig. 4a). None of the Scn1a$^{WT/WT}$ mice showed evidence of clinic (electrical seizures with behavioral manifestations) or subclinic (electrical seizures without clear behavioral manifestation) seizures nor the presence IEDs within the range of temperatures investigated (28–42 °C). On the contrary, Scn1a$^{WT/A1783V}$ mice showed an increase in the rate of IEDs at increasing temperatures (Fig. 4a) that ultimately led to the appearance of clinical (4/5) or subclinical (1/5) heat-induced seizures in all the animals. Seizures in Scn1a$^{WT/A1783V}$ mice persisted for several minutes. Visual inspection of the simultaneous video and electrophysiological recordings allowed correlation between changes in the electrophysiological activity and behavioral manifestations following a revised Racine scale (rRS) for mice[25]. At RT IEDs appeared randomly superimposed on the ongoing baseline activity with no behavioral manifestation (no jerks, whisker trembling nor behavioral arrest). At increasing temperatures, behavioral manifestation compatible with scores 0–2 of the rRS where accompanied with electrical activity deceleration and in some cases, increases in the rate of IEDs. When approaching to the onset, electrical

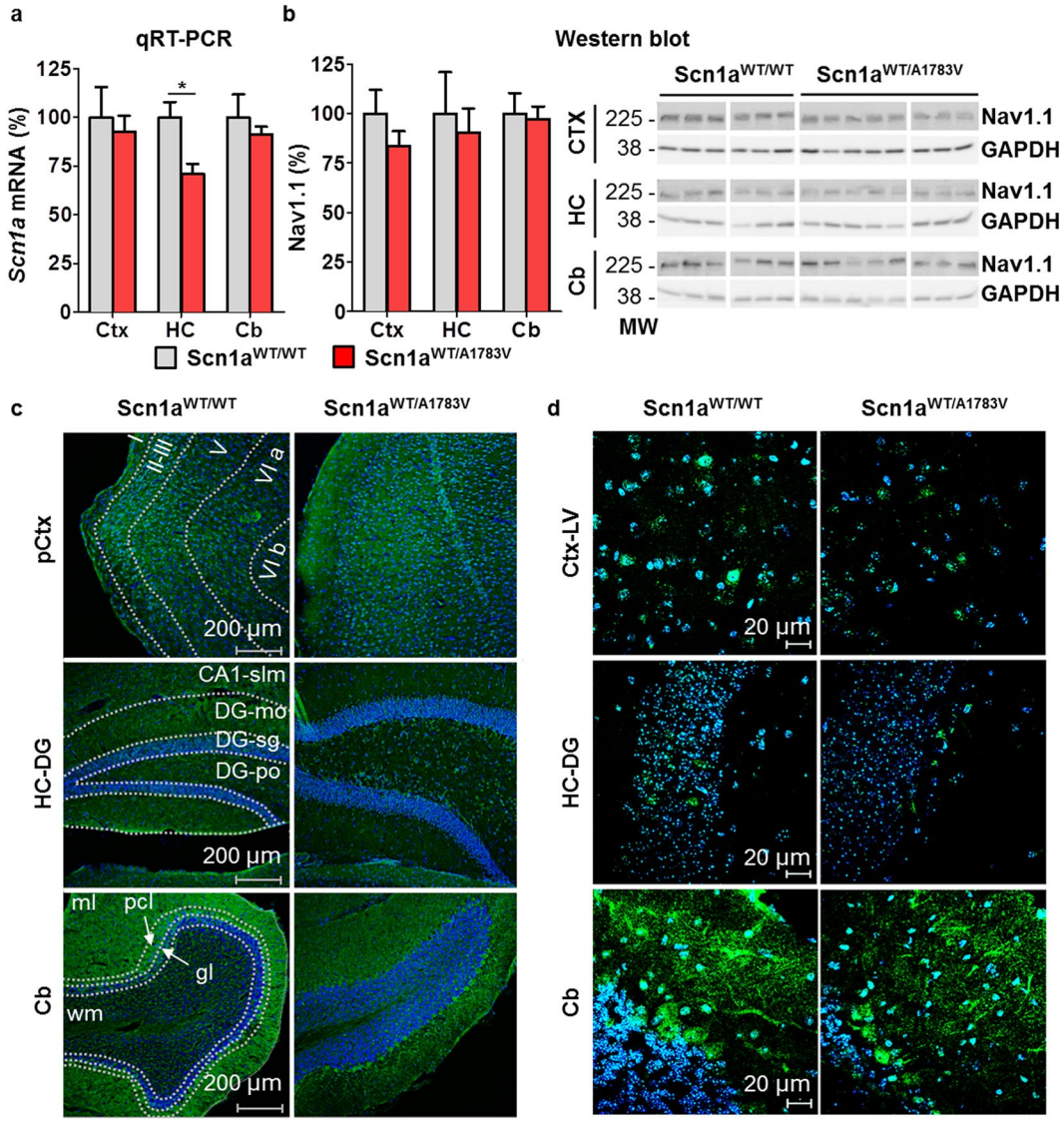

Figure 2. Scn1a$^{WT/A1783V}$ mice present reduced *Scn1a* mRNA in hippocampus, but no significant differences in any brain region at the protein levels. (**a**) mRNA levels of *Scn1a* were determined by qRT-PCR in the cortex (Ctx), hippocampus (HC) and cerebellum (Cb) of Scn1a$^{WT/A1783V}$ and aged-matched littermates (5–8 months). Values (normalized against *GAPDH* mRNA levels) were calculated as percentage *vs* control littermates and data represented as mean ± SEM (n = 6 for Scn1a$^{WT/WT}$ mice and n = 8 for Scn1a$^{WT/A1783V}$ mice). *$p < 0.05$ Kruskal-Wallis with Dunn's post-test. (**b**) Membrane-enriched protein extracts prepared from Ctx, HC and Cb were used to evaluate Nav1.1 protein content by Western blotting. Bars represent the densitometric analysis of individual determinations normalized to GAPDH values. Data are represented as mean percentage ± SEM of values normalized to control mice (n = 6 for Scn1a$^{WT/WT}$ mice and n = 8 for Scn1a$^{WT/A1783V}$ mice). No statistical differences were found between control and Scn1a$^{WT/A1783V}$ mice. The right panel corresponds to representative blots showing Nav1.1 and GAPDH bands. Original blots were cropped and re-arranged to display grouped Scn1a$^{WT/A1783V}$ and control littermates. Full-length blots are available in supplemental material. (**c**) Additional mice were sacrificed for analysis of Nav1.1 by immunofluorescence (green). Nuclei are stained with DAPI (blue). The image shows the indicated brain areas: prefrontal cortex (pCtx); dentate gyrus of the HC (HC-DG); and Cb of representative mice (n = 4 for both groups of animals). The different regions of each structure were delimited by dotted lines based on the Allen adult mouse brain reference atlas. In pCtx roman numbers indicate its different layers. In HC-DG the following regions are included: stratum lacunosum-molecurare of CA1 (CA1-slm); and molecular layer (GD-mo), granule cell layer (DG-sg) and polymorph layer (DG-po) of dentate gyrus. In Cb: molecular layer (ml), white matter (wm), purkinje cell layer (pcl) and granule layer (gl). Scale bar 200 µm. (**d**) In order to study the subcellular localization of Nav1.1 channel, tissue sections were visualized using a confocal laser scanning microscope. The panel shows the labelling observed in cortical later V (Ctx-LV), HC-DG and Cb of representative mice (n = 4 for both groups of animals). Scale bar 20 µm.

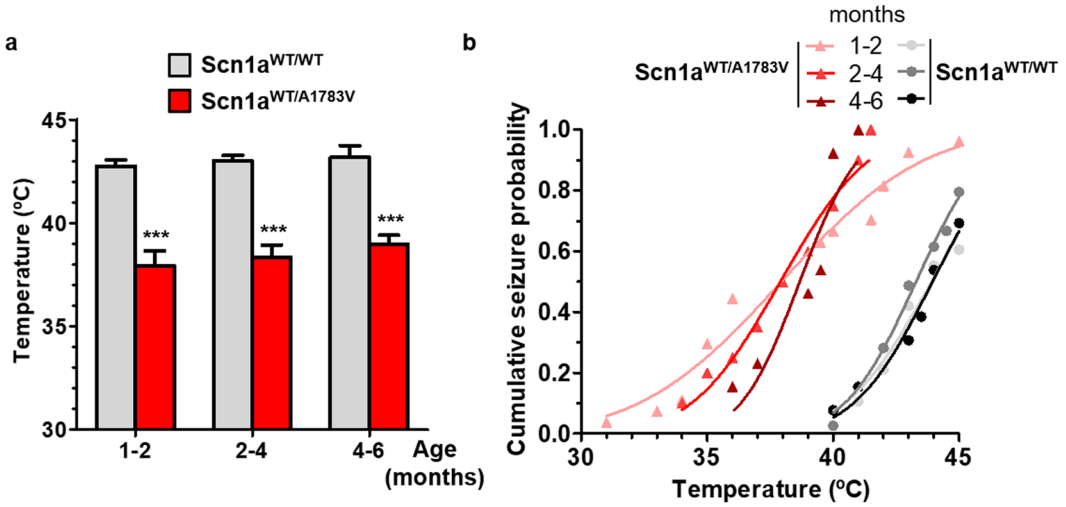

Figure 3. Scn1a$^{WT/A1783V}$ are prone to suffer heat-induced seizures. Mice of the indicated age ranges were exposed to controlled hyperthermia in a chamber with 0.5 °C increments in temperature every 30 s up to 45 °C or until a generalized seizure was reached. (**a**) Thresholds were significantly lower in Scn1a$^{WT/A1783V}$ compared with their control littermates at all age ranges tested. These differences were maintained throughout all the age range tested (Scn1a$^{WT/WT}$: 1–2 mo n = 23, 2–4 mo n = 27 and 4–6 mo n = 9; Scn1a$^{WT/A1783V}$: 1–2 mo n = 26, 2–4 mo n = 20 and 4–6 mo n = 13). ***$p < 0.001$, One-way ANOVA with Tukey's post-test. (**b**) Cumulative seizure probability showing that the risk of seizures is confined between 40–45 °C in all ages in Scn1a$^{WT/WT}$ mice, whereas Scn1a$^{WT/A1783V}$ present a wider temperature range at young ages.

activity became more regular (rhythmic) with slightly smaller amplitude and behavioral manifestations included neck jerks, head nodding and clonic tail elevation (score 3) together with falls of the animal into a sitting position or presence of tonic or clonic contractions in one of the legs (compatible with scores 4–5 of the rRS). Then, electrical activity suddenly changed and showed intermittent clusters of high amplitude polyspikes and spike-wave discharges separeated by periods where EEG traces appeared almost flat (although there was still some electric activity). High amplitude polyspikes and spike-wave periods were accompanied by behavioral manifestations compatible with rRS 5 −6 (i.e clonic and tonic-clonic seizures lying on belly/side or wild jumping). Silent periods were accompanied by episodes of arrest with tonic extension of the muscles corresponding to the maximum score (7). In some cases, seizures persisted after removing the animal from the recording/heating chamber and stopped only when placing mice in a colder environment. In one case, the increase of temperature induced a status epilepticus (SE) of generalized tonic-clonic seizures leading to death.

In two cases electrophysiological recordings allowed detection of a focal origin in the dentate gyrus of the hippocampus with further generalization to other areas of the hippocampus and prefrontal cortex (see Fig. 4b).

Scn1a$^{WT/A1783V}$ mice show cognitive impairment. Spatial learning and memory were evaluated using the Morris water maze (MWM) test at different age intervals (1–3, 3–5 and 5–8 months). The visible platform phase of the test revealed that Scn1a$^{WT/A1783V}$ mice learned new tasks more slowly than their control littermates, which is consistent with the cognitive delay observed in DS patients (Fig. 5a). The difference between both groups was more dramatic in terms of spatial memory, as shown in the invisible platform phase of the test. This indicates that Scn1a$^{WT/A1783V}$ mice are unable to use visual cues to accelerate the location of the hidden platform. In agreement with a defect in retention, the probe test showed significant differences in all age groups.

The novel object recognition tests revealed no differences in short-term visuospatial memory (1 h after training) (NOR 1 h, Fig. 5b). However, long-term visuospatial recognition memory impairment was observed in Scn1a$^{WT/A1783V}$ mice compared to control littermates at mild and late stages of the disease (NOR 24 h, Fig. 5b), indicating a fail of memory consolidation in this animal model that supports the results obtained in the MWM.

Scn1a$^{WT/A1783V}$ mice suffer motor alterations. Gait and movement abnormalities were apparent in Scn1a$^{WT/A1783V}$ mice right after weaning. In order to quantify motor skills, mice were subjected to a battery of tests, including rotarod, inverted grid and elevated beam. Altogether, these tests revealed a significant impairment in coordination and balance, compatible with the clinical observations in DS patients (Fig. 6). In general, motor performance declined over time in Scn1a$^{WT/A1783V}$ mice, although this trend only reached statistical significance in the rotarod test when the early and late age groups were compared (Fig. 6a).

Scn1a$^{WT/A1783V}$ mice present hyperactivity and anxiety. Behavioral manifestations in DS mouse models are heavily influenced by the specific *Scn1a* defects and the genetic background[18–20]. In order to investigate this aspect in Scn1a$^{WT/A1783V}$ mice we employed the open-field test. Whereas total distance moved was not different from their control littermates (not shown) the most dramatic difference observed was the time spent in the center of the arena (Fig. 7a). This is a strong indicator of anxiety behavior in these mice. In addition, Scn1a$^{WT/A1783V}$ showed faster peak velocities than controls (Fig. 7b), suggesting hyperactivity/impulsivity. This result is

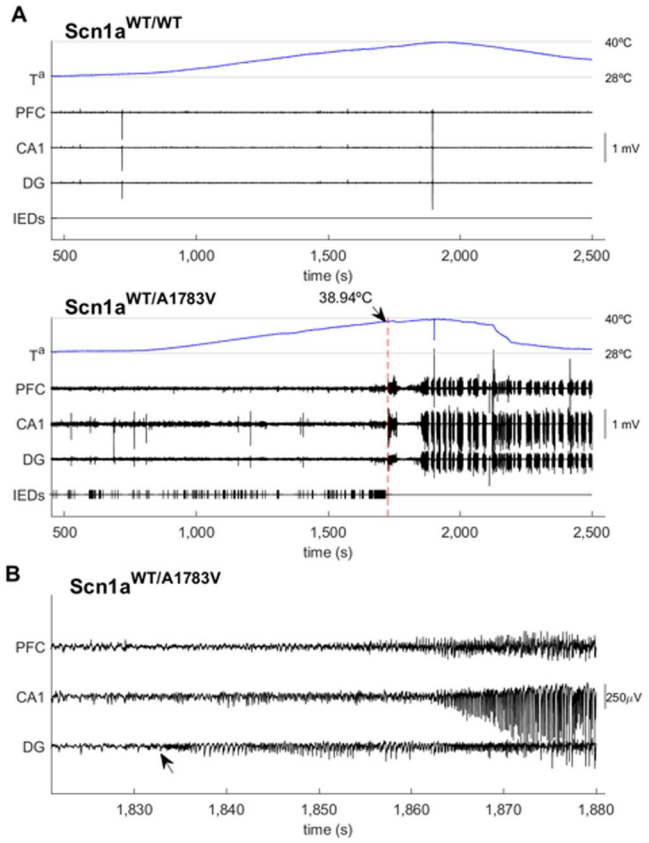

Figure 4. Electrophysiological characterization of freely moving Scn1a$^{WT/A1783V}$ mice. (**a**) Example of the electrical activity recorded in a Scn1a$^{WT/WT}$ (top) and Scn1a$^{WT/A1783V}$ (bottom) mouse during the thermal challenge. Two months-old animals (n = 5) were introduced in the heating chamber, and temperature was increased gradually while electrical activity was recorded in the prefrontal cortex/frontal associative cortex (PFC), CA1 and dentate gyrus (DG) regions. The heat source was switched on at t = 800 s. In the case of the Scn1a$^{WT/A1783V}$ mouse the seizure starts around t = 1,700 s, at T = 38.94 °C. Despite the heat source was immediately disconnected, seizures persisted and were organized in clusters, even when the animal was removed from the recording chamber (around t = 2,250 s). Note the presence of IEDs at RT (t < 1,000 s) and how they increase in frequency as the temperature rises, reaching a maximum right before the seizure (bottom). In contrast, neither IEDs nor seizures were observed in the case of the Scn1a$^{WT/WT}$ mouse (top). (**b**) Example of a seizure with focal origin in the DG that is further generalized (see arrow).

in agreement with the behavior observed during animal handling. In support to the hyperactive behavior, we observed an increase in the number of repetitive movements (stereotypies), starting at 3 months of age (Fig. 7c). In parallel with these signs of hyperactivity, exploratory behavior was severely impaired, as revealed by the marble burying test. Scn1a$^{WT/A1783V}$ mice showed a marked reduction in the normal tendency of rodents to cover objects found in their cages (Fig. 7d). With the aim of studying a complex, species-adapted behavior that could evaluate the individual's performance in daily life activities, we carried out the nest building test. A dramatic reduction in nest assembly was observed in Scn1a$^{WT/A1783V}$ mice, with more than 80% of individuals unable to initiate building at all age intervals tested (Fig. 7e). In contrast with these behavioral alterations, we could only find mild signs of impaired sociability when mice were subjected to the social interaction test[26]. Scn1a$^{WT/A1783V}$ mice in the intermediate age group showed a moderate reduction in contacts during the 15 min period of co-habitation, which was concomitant to an increase in the latency to first contact (Fig. 7f). Therefore, it seems that the main reason for the reduced number of contacts is the delay in the establishment of the first interaction, which could be influenced by the other motor and behavioral defects. This finding is in line with the clinical features of DS patients, whose social abilities are more preserved than the communication skills due to their cognitive impairment[27].

Scn1a$^{WT/A1783V}$ mice show increased glucose uptake in the brain. It has been recently described that DS patients develop abnormal brain glucose uptake starting at 6 years of age[28,29]. In particular, reduced glucose uptake was reported in the fronto-temporo-parietal cortices. Although studies are still very limited, this indicator of cellular metabolism could become a prognostic factor for brain function and/or a marker for therapeutic response in these patients. Therefore, we performed[18] FDG-PET in young and middle-aged Scn1a$^{WT/A1783V}$ mice and age-matched controls that were not subjected to any thermally-induced seizure. In contrast with current clinical reports, we observed a global increase in glucose uptake specifically in the brain of Scn1a$^{WT/A1783V}$ mice. A net increase in brain emission was demonstrated, using the liver as a reference organ (Fig. 8a). Mice were then

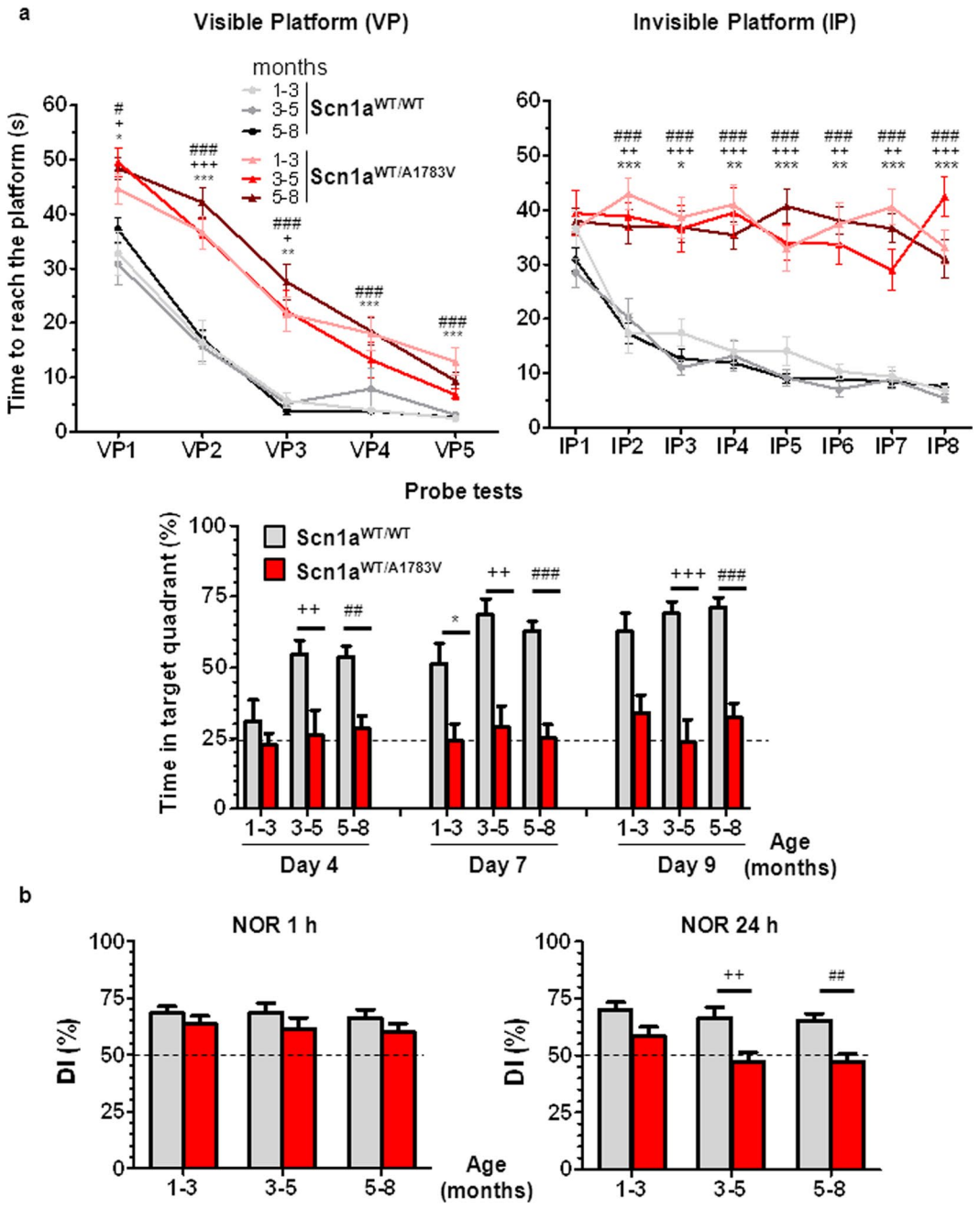

Figure 5. Scn1a$^{WT/A1783V}$ mice show cognitive alterations involving task learning and visuospatial memory. (**a**) The MWM test performed at different ages showed increased escape latency in the visible platform (VP) in the Scn1a$^{WT/A1783V}$ mice compared with their littermate controls, although significant learning was present in both groups of mice ($p < 0.001$ Friedman test). In contrast, the performance in the invisible platform (IP) showed differences both in absolute latencies and the slope of curves, indicating that Scn1a$^{WT/A1783V}$ mice are unable to improve their escape latency throughout the training ($p > 0.05$ and $p < 0.001$ for Scn1a$^{WT/A1783V}$ and Scn1a$^{WT/WT}$ mice, respectively, Friedman). In concordance with the lack of spatial learning, Scn1a$^{WT/A1783V}$ mice showed no preference for the target quadrant in the probe test, consistent with altered retention. Values are represented as mean ± SEM (Scn1a$^{WT/WT}$: 1–3 mo n = 11, 3–5 mo n = 12 and 5–8 mo n = 27; and Scn1a$^{WT/A1783V}$: 1–3 mo n = 17, 3–5 mo n = 10 and 5–8 mo n = 24). (**b**) The NOR test was applied to mice in the same age groups. Although no differences were observed 1 h after training (left panel), a significant reduction in long-term memory was noted in Scn1a$^{WT/A1783V}$ mice (NOR 24 h), revealing a defect in memory consolidation. Values are represented as mean ± SEM (Scn1a$^{WT/WT}$: 1–3 mo n = 37, 3–5 mo n = 26 and 5–8 mo n = 27; Scn1a$^{WT/A1783V}$: 1–3 mo n = 28, 3–5 mo n = 30 and 5–8 mo n = 37). Statistical relevance was assessed applying one-way ANOVA with Tukey's post-test for VP1–2, IP5, IP8, Probe 15 day 4, Probe 15 day 7, NOR 1 h and NOR 24 h or Kruskal-Wallis with Dunn's post-test for VP3–5, IP1–4, IP6–7 and Probe 15 day 9. *$p < 0.05$, **$p < 0.01$, ***$p < 0.001$ for comparison of Scn1a$^{WT/A1783V}$ and Scn1a$^{WT/WT}$ mice. Symbols *, $^{+}$ and $^{\#}$ correspond to the 1–3, 3–5 and 5–8 months age ranges, respectively.

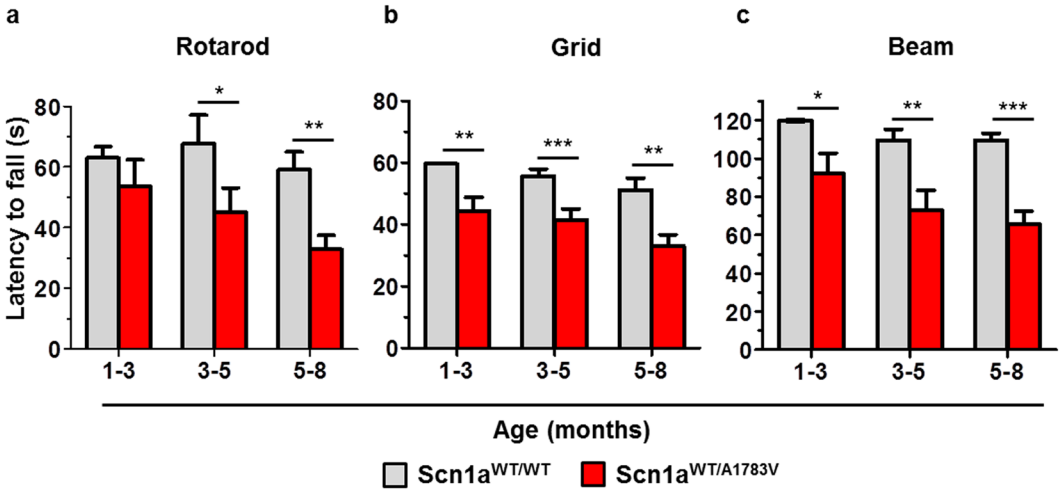

Figure 6. Scn1A$^{WT/A1783V}$ mice show motor impairment. (**a**–**c**) Mice of the indicated age ranges were subjected to the rotarod, inverted grid and elevated beam tests, as indicated. The latency to fall from the rotatory rod was decreased in the Scn1A$^{WT/A1783V}$ mice compared with their control littermates, with significant differences observed from 3 months of age. For the other two tests, a significant reduction was observed in all age groups. Each bar represents the mean ± SEM of elapsed time (s) and are the mean of at least two trials (Scn1a$^{WT/WT}$: 1–3 mo n = 31/25/19, 3–5 mo n = 16/19/14 and 5–8 mo n = 24/14/26; Scn1a$^{WT/A1783V}$: 1–3 mo n = 18/13/11, 3–5 mo n = 16/29/14 and 5–8 mo n = 25/16/31; respectively in each of the tests performed). *$p < 0.05$, **$p < 0.01$, and ***$p < 0.001$. One-way ANOVA with Tukey's post-test for (**a**) and Kruskal-Wallis with Dunn's post-test for (**b**,**c**).

sacrificed and different brain structures were isolated for quantification of radionuclide incorporation. Higher uptake was observed in all regions, including cerebellum, basal ganglia, brainstem, cortex, thalamus and hippocampus (Fig. 8b). Potential reasons for the apparent discrepancy between recent clinical reports and our results are discussed below.

Discussion

DS is a complex encephalopathy affecting the inhibition/excitation balance in the brain, which explains the wide repertoire of clinical manifestations. Apart from the epileptic seizures, other comorbidities have a deep impact on the quality of life of the patients and their families. Therefore, addressing SUDEP, motor, cognitive and behavioral alterations are clear objectives for new experimental therapies looking for patient-centered outcomes[30]. In this context, relevant pre-clinical models and robust methods to quantify response to treatments are becoming a priority in the field. In this report we have characterized a mouse model in which a missense *Scn1a* mutation recurrently observed in patients is present in all cells, thus mimicking a clinically relevant situation at the genetic level. Our results indicate that the most relevant DS manifestations are present in Scn1a$^{WT/A1783V}$ mice, and can be readily quantified using standardized tests. These include a marked sensitivity for thermally-induced seizures, EEG alterations, progressive motor impairment, hyperactivity and cognitive deterioration.

Behavioral alterations are probably the most variable manifestations among DS patients, and the same occurs in pre-clinical mouse models. Apart from the inherent difficulty to discriminate different behavior traits using rodent tests, there is a strong influence of the genetic background and the type of cells affected by the *Scn1a* alterations. In the model described here, the open-field test was a robust method to quantify anxiety (time spent in the center of the arena). Although the high frequency of stereotypies observed in the Scn1a$^{WT/A1783V}$ mice could be considered an autistic-like behavior, we believe that in this case it is mainly a reflection of hyperactivity. This is in agreement with the increased velocity in the open-field and the hyper-reactivity experienced during animal handling. We believe the striking reduction in nest building performance observed in Scn1a$^{WT/A1783V}$ mice is a relevant indicator of poor quality of life and a clear parameter to be considered in the evaluation of new therapies. In contrast, evidences for reduced sociability were not consistent, according to the interaction test. This is probably influenced by the C57BL/6 J genetic background, which is relatively resistant to social interaction defects[20,31]. In fact, PV-specific haploinsufficiency of *Scn1a* in this background showed normal social behavior[20], and only the global introduction of a nonsense mutation (Scn1a$^{RX/+}$ mice) caused alterations in sociability tests. On the other hand, reduced social skills in DS patients are better explained by their difficulties in communication and their cognitive impairment rather than by specific deficits in socialization[27]. In addition, the contribution of cerebellar alterations to an internalizing syndrome should be taken into account[32,33].

In comparison with the previously described knock-in model carrying the R1648H mutation associated with GEFS$^+$ (*Scn1a*$^{RH+}$ mice)[34], Scn1a$^{WT/A1783V}$ have in common the hyperactivity and mild social deficits, whereas the DS mutation causes deeper cognitive impairment, anxiety and higher mortality. Interestingly, a recent study indicates that the phenotype of heterozygous *Scn1a*$^{RH+}$ mice can be aggravated by repeated hyperthermia-induced crisis, resembling DS[35]. This finding highlights the interplay between genetic and environmental factors in disease progression.

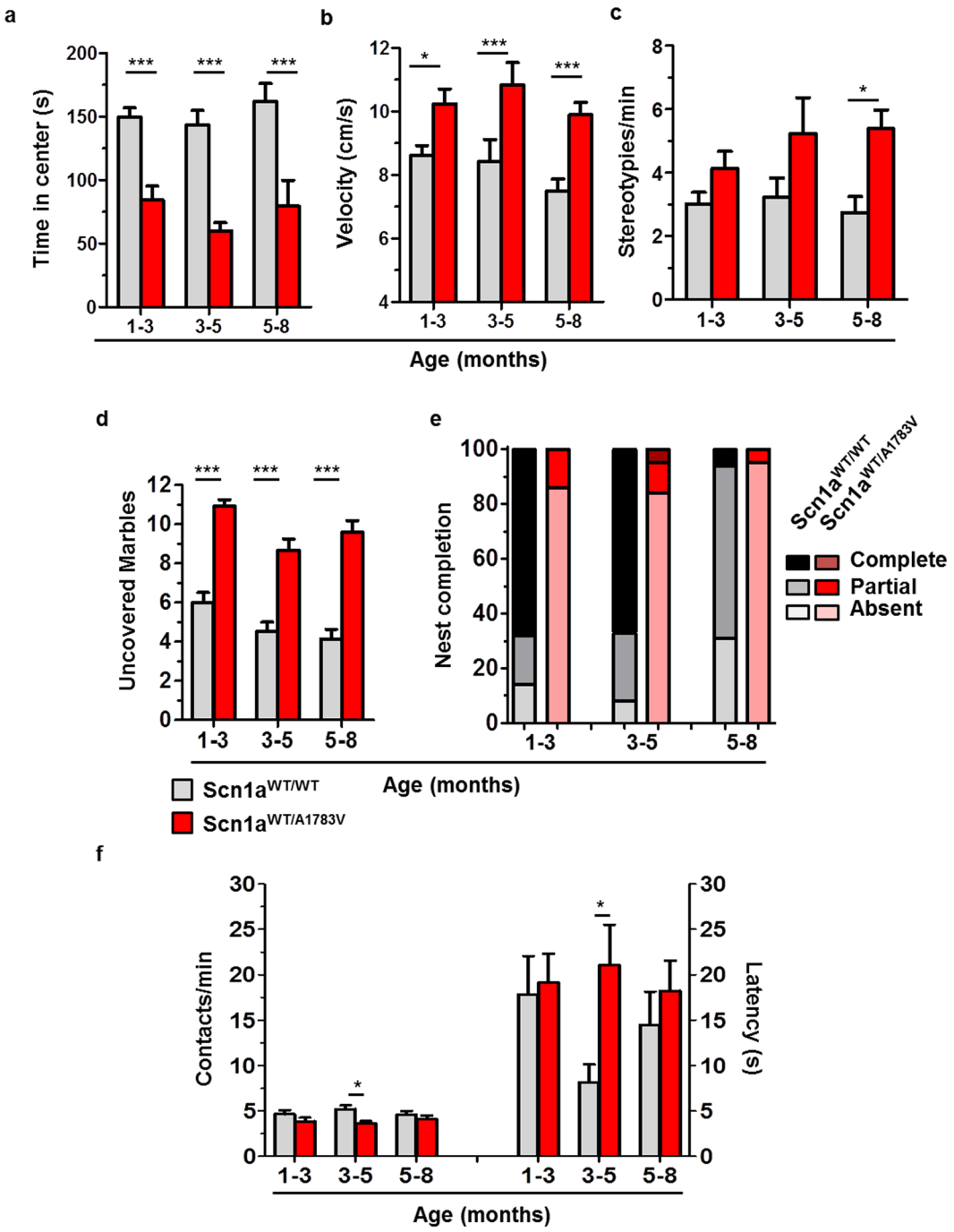

Figure 7. Scn1A$^{WT/A1783V}$ mice show an altered interaction with the environment. Mice of the indicated age ranges were subjected to the open-field test and showed a reduction in the time spent in the center of the arena -indicative of anxiety- (**a**), hyperkinesia (**b**) and an increased number of stereotypies (**c**). No differences in total distance moved were detected in any age-range (data not shown). Other alterations of animal behavior included a reduction in the normal tendency to hide objects in the marble burying test (**d**) and a poor performance in the nest building test (**e**). The graph represents the percentage of mice that complete, initiate or fail to initiate the task during one night (dark, medium and light colors, respectively). In contrast, Scn1A$^{WT/A1783V}$ performed relatively well in the social interaction task (**f**), with a reduction in the number of contacts only observed in the 3–5 months age range (left Y axis), which coincided with a significantly higher latency to approach the unfamiliar mouse for the first time (right Y axis), compared with their control littermates. Values are represented as mean ± SEM (Scn1a$^{WT/WT}$: 1–3 mo n = 44/44/14/26/16/16, 3–5 mo n = 31/30/13/34/6/11, and 5–8 mo n = 29/27/17/8/17/18; Scn1a$^{WT/A1783V}$: 1–3 mo n = 26/29/14/20/6/15, 3–5 mo n = 33/34/9/37/12/11 and 5–8 mo n = 35/36/24/18/20/15; respectively in each of the test performed). *$p < 0.05$; ***$p < 0.001$, Kruskal-Wallis with Dunn's post-test.

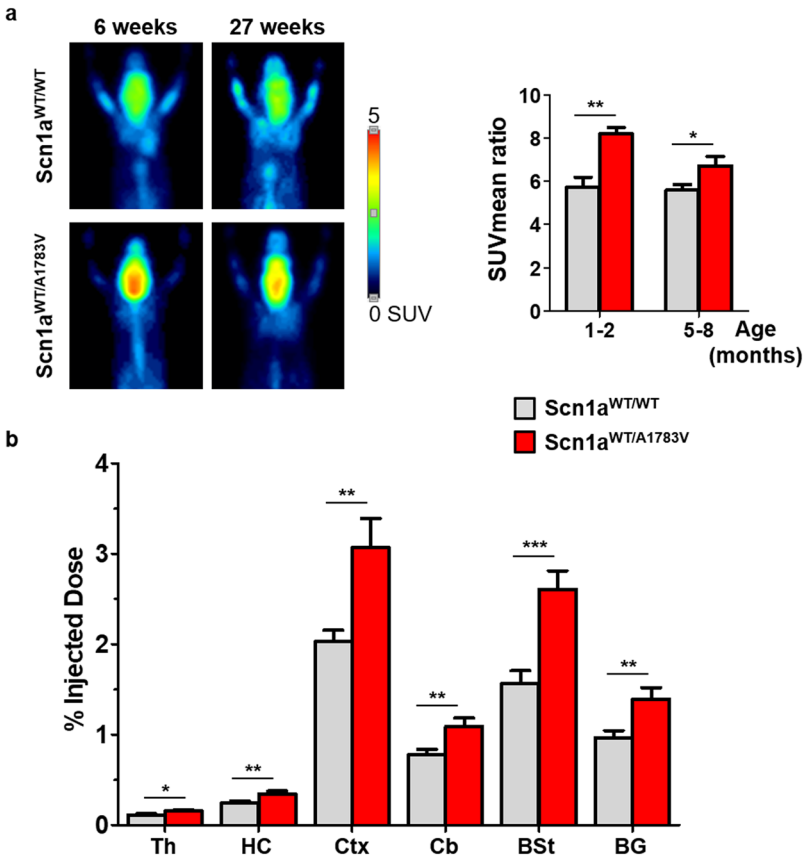

Figure 8. Scn1a$^{WT/A1783V}$ mice show increased glucose uptake in the brain. Mice were subjected to ^{18}F-FDG PET at the indicated ages. (**a**) Left panel correspond to maximum intensity projection PET images of representative mice showing brain ^{18}F-FDG uptake. The quantification of positron emission (mean SUV) is represented in the right panel. (**b**) Mice in the 5–8 age group were sacrificed after PET, and isotope incorporation was quantified in a gamma counter (expressed as % of the injected dose). (1–2 mo n = 7; 5–8 mo n = 14). *p < 0.05; **p < 0.01. Mann Whitney U test.

Finally, we report for the first time an FDG-PET study in a DS murine model, which could be an indirect, but clinically relevant marker for brain function in this disease. In contrast with the pioneering reports in DS patients[28,29], we found an increase in glucose uptake in different brain structures. This is not surprising, taking into account the unbalanced excitatory activity resulting from the insufficient *Scn1a* function. We believe the apparent reduction of glucose uptake observed in the clinical studies can be influenced by the anti-epileptic drugs used in patients[36], and by the normalization method used in these studies. Haginoya *et al.* took cerebellum as a reference[28], whereas Kumar *et al.* used basal ganglia[29]. Our data indicate that both brain regions have elevated uptake positron emission, which complicates the interpretation of results. Brain metabolism is generally reduced in drug-resistant epilepsies[37], especially as a result of prolonged exposure to seizures. However, hypermetabolism has been described in interictal periods when continuous epileptogenic activity is present[38].

To conclude, we present here an "*open access*" DS mouse model based on a clinically relevant genetic alteration, which allows the quantitative evaluation of a wide repertoire of disease manifestations. The selection of methods described in this report cover the most relevant parameters at the clinical, electrophysiological and metabolic levels. We believe this may be a useful tool to test novel therapies and to obtain meaningful data across different research groups.

Materials and Methods

Animals. The conditional *Scn1a*-A1783V mice (B6(Cg)-Scn1atm1.1Dsf/J, The Jackson Laboratory, stock no. 026133) were bred to mice expressing Cre recombinase under the control of the CMV promoter (B6.C-Tg(CMV-Cre)1Cgn/J, The Jackson Laboratory, stock no. 006054[39]). Breeding pairs consisted of heterozygous male *Scn1a*-A1783V and homozygous female CMV-Cre mice. See https://www.jax.org/strain/026133 for details about allele modification and genotyping. Offspring carrying one mutated allele (genotype hereinafter referred to as Scn1a$^{WT/A1783V}$) express the A1783V mutation in the *Scn1a* gene in all body tissues, mimicking what happens in DS. Animals were housed 4–6 per cage with free access to food and water, weighed weekly, and maintained in a temperature and light controlled (12 h/12 h light/dark cycle) environment. The studies were performed by comparing heterozygous transgenic Scn1a$^{WT/A1783V}$ to age-matched negative littermates Scn1a$^{WT/WT}$. Breeding and experimental protocols were approved by the Ethical Committee of the University of Navarra (in accord with the Spanish Royal Decree 53/2013).

Quantitative PCR. In order to minimize the number of animals employed in this part of the study (limited to 6 Scn1a$^{WT/WT}$ and 8 Scn1a$^{WT/A1783V}$), one brain hemisphere and half cerebellum of each animal were dissected and employed to determine mRNA levels of the *Scn1a* gene by quantitative PCR, and the other one for the determination of Nav1.1 protein levels by Western blotting. After dissecting the cerebral cortex, hippocampus and cerebellum, the Maxwell® 16 LEV simplyRNA Cells Kit (Promega, Madison, WI, USA) was used for total RNA isolation following manufacture's indications. Two micrograms of RNA were then treated with DNase I and retro-transcribed into cDNA using M-MLV retro-trasncriptase enzyme (Invitrogen, Thermo Fisher Scientific, Carlsbad, CA, USA) and random primers (Life Technologies, Thermo Fisher Scientific, Carlsbad, CA, USA). These procedures were performed in GeneAmp® PCR System 2400 (Applied Biosystems, Foster City, CA, USA). Quantitative analysis was performed by real-time PCR using iQTM SYBR® Green Supermix reagent (Bio-Rad, Hercules, CA, USA) in CFX96 TouchTM Real-Time PCR Detection System (Bio-Rad, Hercules, CA, USA). Mouse *Scn1a* expression levels were determined using specific primers (FP 5′ CATGTATGCTGCAGTTGATTCCA 3′and RP 5′ AACAGGTTCAGGGTAAAGAAGG 3′)[40] and mouse GAPDH was used as housekeeping gene (FP 5′ CCAAGGTCATCCATGACAAC 3′and RP 5′ TGTCATACCAGGAAATGAGC 3′). All brain samples were tested in triplicate. The relative quantification was carried out using the $2-\Delta Ct$[41]. Data are analysed in percentage *vs* Scn1a$^{WT/WT}$ mice and represented as mean ± SEM.

Preparation of membrane-enriched extracts and western blotting. The cerebral cortex and hippocampus of the other hemisphere and half cerebellum were employed to obtain the membrane-enriched protein fraction (P2) as previously described[42]. Protein concentration was determined by Bradford assay (BioRad Laboratories, Hercules, CA) and part of the preparation was solubilized in denaturing conditions as described before[43]. Protein samples were mixed with 4x Urea-EDTA buffer, resolved onto SDS-polyacrylamide gels and transferred to PVDF membranes. The membranes were blocked with 5% BSA and 0.05% Tween-20 in TBS, followed by overnight incubation at 4 °C with the following primary antibodies: rabbit polyclonal anti-Nav1.1 (Alomone Labs Cat# ASC–001, Cat# 2118S, 1:500) and rabbit moclonal (14C12) anti-GAPDH (Cell Signaling Technology, 1:5,000) diluted in 2,5% BSA, 0.05% Tween–20 and 0,01% azide in TBS. Immunolabeled protein bands were detected by using and anti-rabbit IgG HRP conjugate (GE Healthcare, Cat# NA934V, 1:10,000) and an enhanced chemiluminiscence system (Lumigen ECL Ultra TMA–6, Lumigen, Inc., Cat# TLA–100). Images were acquired with a Chemidoc system (Biorad, Hercules, CA, USA), and Image Lab™ software (Biorad, Hercules, CA, USA) was used for quantification. The employed anti-Nav1.1 antibody is an affinity-purified rabbit polyclonal antisera raised against synthetic peptides corresponding to the intracellular loop between domains I and II of rat Nav 1.1. It has been KO validated[44] and validated for Western blotting immunofluorescence in several publications[45–48] Data are analysed in percentage *vs* Scn1a$^{WT/WT}$ mice and represented as mean ± SEM.

Immunofluorescence procedures, equipment and settings. Additional animals were perfused transcardially with 0.9% saline followed by 4% paraformaldehyde in phosphate buffer (PB) under xylazine/ketamine anesthesia. After perfusion, brains were removed and post-fixed in the same fixative solution for 12 h at 4 °C; and then cryopreserved in 30% sucrose solution in PB at 4 °C until they sank. Microtome sections (thickness: 30 μm) were cut sagitally with a freezing microtome and stored in cryopreserving solution (30% ethylene glycol, 30% glycerol in PB 0.1 M) at −20 °C until processed. To carry out the immunofluorescence, two free-floating tissue sections per animal were processed (n = 4 in each group). Brain sections were washed 3 times with PB at RT and then a blocking step was performed, followed by overnight incubation at 4 °C with the primary antibody (rabbit polyclonal anti-Nav1.1, Alomone Labs Cat# ASC–001, 1:500) diluted in blocking solution (2% donkey normal serum, 0.5% Triton X–100 and 1% BSA in PB). After washing them 3 times with PB, slices were incubated with the secondary antibody (Donkey anti-Rabbit IgG (H + L) Highly Cross-Adsorbed Alexa Fluor 488 Cat# A–21206, 1:400) for 2 h at RT and protected from light. To enable the visualization of nuclei, sections were incubated for 5 min with the DNA marker 4′,6–diamidino–2–phenylindole (DAPI, ThermoFisher Scientific Cat# D1306, 300 nM) protected from light. Finally, slices were washed twice with PB, mounted on super frost plus slides, air dried for 24 h, rinsed in toluene (2 × 5 min), and coverslip was placed with Immu-Mount® mounting medium (ThermoFisher Scientific Cat# 9990402). To ensure comparable immunostaining, sections were processed together under identical conditions. For the assessment of non-specific primary and secondary immunostaining, some sections from each experimental group were incubated without primary or secondary antibody, and no immunostaining was observed in any case. Fluorescence signals displayed in Fig. 2c were acquired with the fluorescence microscope Eclipse Eboom (Nikon) coupled to a super high-pressure mercury lamp (C-SHG1, Nikon, Japan) using a Plan Apo 10 ×/ 0.45 DIC L objective. Images were acquired with the DS-Ri2 camera (Nikon, Japan. Capture quality: 3 × 8–bit, 4908 × 3264) and the program NIS-Elements F 4.60.00 64-bit (Nikon, Japan. Image information: 8 bits, calibration 1,17 μm/px, and dimensions 808 × 808). The B-2A filter (excitation: 450–490 nm, DM: 505, BA: 530) was used to detect Nav1.1–inmunostained structures and the UV-2A one (excitation: 330–380, DM: 400, BA: 420) for DAPI-staining. Emissions were color-coded in green and blue, respectively. Acquired fluorescence images were adjusted in parallel for brightness and contrast in ImageJ 1.52p (NIH, Bethesda, MD), sharpness was improved employing an unsharp mask filter (Radius (sigma): 1.0 px, and mask weight; 0.60). For bigger magnification (Fig. 2d) tissue sections were visualized using a confocal laser scanning microscope (Zeiss Axio Observer.Z1/7 LSM800 with Airyscan and ESID 2XGaAsP detector module) and a Plan-Apochromat 63 ×/ 1.40 Oil DIC M27 objective. Tissue sections were excited using a 488 nm laser for detecting Nav1.1-inmunostained structures (emission wavelength 509 nm, detection wavelength 480–700 nm, pinhole 50 μm) and a 353 nm laser for DAPI-staining (emission wavelength 465 nm, detection wavelength 400–480 nm, pinhole 50 μm). Emissions were color-coded in green and blue, respectively. Images were acquired with the program ZEN 2 (blue edition) (Carl Zeiss. Dimensions: 512 × 512, 16-bit; and image size: 190.16 × 190.16 μm). Acquired fluorescence images

were adjusted in parallel for brightness and contrast in ImageJ 1.52p (NIH, Bethesda, MD), noise was removed applying a bright outlier detection filter (Radius: 0.1 px, and threshold: 90) and sharpness was improved employing an unsharp mask filter (Radius (sigma): 1.0 px, and mask weight: 0.20).

Induction of thermal seizures. In order to evaluate the epileptogenic thermal threshold in our animal model at different ages, a methacrylate cylinder coupled to a thermal system that gradually increased its internal temperature was used. Before introducing the animal into the cylinder, its body temperature was measured employing a rectal probe (RET-4, Physitemp Instruments, LLC) coupled to the TCAT-2LV controller (Physitemp Instruments, LLC). The environmental temperature was gradually increased to a maximum of 45 °C (0.5 °C every 30 s) or until a generalized seizure was reached. After removing the animal from the cylinder and measuring its body temperature as described before, the animal was left in a cool box with free access to water to help it recover.

Electrophysiological recordings. Electrophysiological phenotyping of the DS model was carried out by multisite recordings in 5 Scn1a$^{WT/A1783V}$ and 5 Scn1a$^{WT/WT}$ mice at 2 months of age (71 ± 18 days). Local field potentials (LFP) from the hippocampus CA1 region and prefrontal cortex together with simultaneous video recordings were obtained. To do that, mice were implanted with 5 equally spaced 50 µm tungsten wires (California Fine Wire, CA 93433, USA) across different layers of CA1 and dentate gyrus (DG) and a wire at prefrontal cortex, frontal associative cortex (PFC). Coordinates for electrode placement were selected according to Paxinos and Watson atlas: (AP): −1.94 mm; (ML): 1.5 mm; (DV): −2 to −1 mm for the hippocampal bundles and (AP): 2.58 mm; (ML): 1.5 mm; (DV): −1.5 mm for the PFC. Reference and ground screws were placed over the cerebellum. One week after implantation (time for recovery from surgery and inflammation, as recommended by the ethical committee), animals were connected to an acquisition system for electrophysiological recordings (Intan RHD2000 system, IntanTech). Simultaneous video recordings were used to assess behavioural state of the animals and the presence of (clinical) seizures. Recording session began with 30 min of awake, freely moving recordings of the mice within their cages at RT. Open-field recording was then followed by a thermal challenge where mice were placed into a heating chamber and recorded at increasing temperatures from RT up to 42 °C or the appearance of seizures. Custom-made routines running under Matlab (Mathworks, Natick, MA, USA) were used to convert electrophysiological data and temperature values from Intan format into Spike2 format (Cambridge Electronic Desing Limited, UK). Reviewing features of the Spike2 software were used to visually inspect the recordings in order to assess the presence of abnormal activities (interictal discharges), electrical seizures and temperature values at the onset of the seizures. Interictal epileptiform discharges (IEDs) were semi-automatically annotated by performing an initial detection following previously described methods[49] and further validated by visual inspection. To do that, signals were loaded using Matlab scripts, resampled to 1,000 Hz, band-pass filtered in the 60–80 Hz range and rectified. IED events were detected when the filtered envelope was >3 times above baseline and unfiltered envelope was >3 times above baseline. Envelope was computed by estimating the rms value within a 200 ms window. Then, candidate events were uploaded into the Spike2 file as a marker channel that was further reviewed and curated by two specialists. Video recordings were also reviewed by two different specialist to detect the presence of seizures and to report their semiologycal description according to a modified Racine score for mice[25]. Location of the electrodes was assessed by histological verification. To do that, animals were anaesthetized (ketamine 75 mg/kg and xylacine 11 mg/kg intraperitoneal) and intracardially perfused with a solution of paraformaldehyde (PAF 4%), dissolved in phosphate buffer saline (PBS 0.1 M, pH 7.4). After perfusion, the brain was taken out and post-fixed during 24 h in PAF. Then it was passed to PBS-sacarose for at least 24 h. Brains were cut in coronal axis using a cryotome. Slices of 30 µm were obtained and processed to assess electrodes location. The slides were stained with thionine and then observed in a microscope to verify the location of the recording electrodes.

Behavioural assessment. *Morris water maze test.* The Morris water maze is a hippocampus-dependent learning task that serves to test the working and reference memory function. The test was carried out as described before with minor modifications[43]. The water maze consisted of a circular pool of 1,2 m diameter and 0,6 m height (LE820120, PanLab Harvard Apparatus) filled with water tinted with non-toxic white paint and maintained at 20 °C. During the first part of the test, Visible Platform (VP), mice were trained to find the platform in order to escape from the water. During this phase, the platform was raised above the water surface and mice were trained for 5 consecutive days (four trials per day). In the second part of the test, Invisible Platform (IP), the platform was placed in the opposite quadrant and hidden bellow water level, and visible cues were placed in each of the four quadrants of the maze to allow spatial learning. Mice were trained for 8 consecutive days (four trials per day) to generate a spatial map that allows them to find the platform. In both phases, mice were placed into the maze facing toward the wall of the pool in selected locations pseudo-randomly established. Each trial was finished when the mouse reached the platform (escape latency) or after 60 s; when an animal was unable to find the platform, it was gently guided onto it. After each trial, animals remained on the platform for 15 s. On days 4th, 7th and 9th of the IP phase all mice were subjected to a probe trial in order to evaluate their retention. Platform was removed from the pool and mice allowed to swim during 60 s in the pool, measuring the time spent in the quadrant where the platform was placed during the IP for the first 15 s (Probe 15). All trials were recorded and analysed with the program WaterMaze3 (Actimetrics, Evanston, IL).

Novel object recognition test. Novel object recognition test (NOR) was conducted for the assessment of visuospatial memory. A standard squared four compartment open-field box mildly illuminated was employed (LE800SC, PanLab Harvard Apparatus, $90 \times 90 \times 40$ cm). All trials were recorded and exploration times for each object were analysed manually blindly. Before performing the test, animals were habituated to the box during 15 min, these data were employed to evaluate their motor spontaneous activity as it will be described later. The test consists of

three different stages; the first one is the habituation phase. Two identical objects were placed into the box, symmetrically separated from each other, and each mouse was allowed to explore them for 5 min. After a delay of 1 h or 24 h, the mouse was placed again in the cage and exposed for 5 min to one familiar object in the same position and to a novel object placed in a new location (NOR 1 h and NOR 24 h phases). All trials were video recorded and the total time spent exploring each object was measured manually by using a stopwatch. To avoid the presence of olfactory trails, the apparatus and the objects were thoroughly cleaned after each trial. The discrimination index (DI) was calculated as percentage following this equation: (Exploration time of the novel object/Total exploration time) × 100. Consequently, a ratio of 50% reflects equal exploration of the familiar and the novel object, indicating no learning retention, and ratios above 50% are indicative of visuospatial learning retention.

Rotarod test. Motor coordination, balance and physical condition were tested in a rotarod apparatus (LE8200 Panlab, Harvard Apparatus). The day before the test, animals were trained to walk over the rotating rod for 5 min at a constant speed of 12 rpm. For the test, animals were positioned on a rod programmed to rotate with lineal increasing speed going from 4 to 40 rpm in 5 min. Animals underwent three trials with a resting time of 60 min between them. The time spent in the accelerating cylinder was recorded, representing the mean value. Of note, mice were not subjected to the rotarod test until they weighted at least 10 g, since animals with lower weights showed inconsistent results.

Inverted grid test. Grip strength was tested by evaluating the capability of the mouse to remain clinging to an inverted cage lid for 1 min. Animals underwent three trials with a resting time of 60 min between them. The time spent hanging from the lid was recorded, and the score was estimated by the mean value of the three trials.

Elevated beam test. In order to assess motor coordination the elevated beam test was used. The test was carried out using a cylindrical, narrow and elevated footbridge. The animal must walk on it for a maximum of two minutes and the time of permanence was evaluated. Animals underwent two trials with a resting time of 60 min between them. The time spent over the footbridge was recorded, and the score was estimated by the mean value of both trials.

Open-field test. Motor activity was tested for 15 min in a standardized squared four-compartment open-field box mildly illuminated (LE800SC, PanLab Harvard Apparatus, 90 × 90 × 40 cm). Trials were video recorded and automatically analysed using a video tracking system (Ethovision XT 5.0, Noldus Information Technology B.V., Wageningen, The Netherlands). Parameters as distance moved (cm), mean speed (cm/s) and time spent in the central zone (15 cm apart from the walls) were measured and represented. The last value was employed to evaluate the presence of anxious behaviour. Of note, mice showing very low exploratory activity (less than 5% of the time dedicated to exploration) were excluded from the analysis, since they tend to remain in one corner of the cage and would introduce a bias in the evaluation of anxiety. The presence of stereotypies, indicative of anxiety and hyperactivity, was also evaluated by visual inspection and manually counted.

Marble burying test. Normal exploratory behaviour was assessed with the marble burying test[50]. Twelve glass marbles were put uniformly in a cage, three marbles per line, and mice were placed in the centre of each cage and allowed to interact with them for 30 min. After this period of time, two blind experimenters quantified the number of unburied marbles.

Nest building test. This test is useful for identifying abnormal behaviour in mice[51]. Animals were placed in a box provided with a piece of tightly packed cotton material (Nestlets™ Nesting Material, Ancare) and let to interact with it overnight. The day after, nesting index was evaluated and scored as no nest, partial nest or complete nest covering the mouse.

Social interaction task. In each trial, four pairs of mice were tested simultaneously in a standardized squared four-compartment open-field box mildly illuminated (LE800SC, PanLab Harvard Apparatus, 90 × 90 × 40 cm). Each mouse was introduced in a compartment occupied by a mouse that had never interacted with it (occupant mouse). Both animals could freely interact for 15 min. Trials were video recorded, and the number of social interactions and latency time for the first contact was then manually analysed for each tested mouse.

Measurement of cerebral glucose uptake by positron emission tomography. Cerebral glucose metabolism, reflecting neuronal and synaptic activity, was assessed *in vivo* by positron emission tomography (PET) with the radiotracer 18– fluorodeoxyglucose (^{18}F-FDG). Mice were fasted overnight but allowed to drink water ad libitum. Mice were injected with ^{18}F-FDG dose (9,5 MBq ± 0,6 in 80–100 μL) through the tail vein and placed back in the cage for an uptake period of 50 min. Then, animals were anesthetized with 2% isoflurane in 100% O_2 gas and placed prone to acquire a static 15-min study in a small animal PET tomograph (Mosaic, Philips). Images were reconstructed applying dead time, decay, and random and scattering corrections. For the *ex vivo* studies of radiotracer incorporation, animals were sacrificed at the end of the study by neck dislocation and different parts of brain were dissected. *Ex vivo* counting of radioactivity in the samples was performed in a gamma counter (Hidex Automatic Gamma Counter, Hidex Oy, Turuk, Finland) to calculate the percentage of injected dose (%ID). For the semi-cuantiative analysis of the *in vivo* PET images, studies were analyzed using the PMOD software (PMOD v3.2, PMOD Technologies Ltd., Adliswil, Switzerland). Images were expressed in standardized uptake value (SUV) units, using the formula SUV = [tissue activity concentration (Bq/cm^3)/injected dose (Bq)] × body weight (g). To assess brain uptake of ^{18}F-FDG, two spherical volumes of interest (VOIs) were drawn for each image including the entire brain and liver (reference organ). Then, a semiautomatic delineation tool was

used applying a predefined threshold of 50% of the maximum or minimum voxel value to obtain new VOIs that delimited the brain and liver respectively. Finally, the average SUV of the voxels within the VOIs were calculated (SUV mean) and a SUVmean ratio was calculated dividing brain SUV_{mean}/ liver SUV_{mean} (SUV_{mean} ratio).

Statistical analysis. Data were processed for statistical analysis using the Graphpad Prism software. After identifying outliers by applying the Grubb's test, data normality was assessed with the D'Agostino and Pearson omnibus normality test. In Fig. 1 linear regression analysis was performed to assess statistical significance. In the rest of figures, if data followed normality a one-way analysis of variance (ANOVA) followed by Tukey's multiple post hoc test was applied; otherwise, Mann Whitney U test or Kruskal-Wallis test followed by Dunn's test were used. In the WMM, the Friedman test was applied to test intra-group improvement over trials. The significance level was set at $p < 0.05$.

Data Availability

The datasets generated during and/or analysed during the current study are available from the corresponding author on reasonable request.

References

1. Wu, Y. W. *et al*. Incidence of Dravet Syndrome in a US Population. *Pediatrics* **136**, e1310–e1315 (2015).
2. Dravet, C. Dravet syndrome history. *Dev. Med. Child Neurol.* **53**(Suppl 2), 1–6 (2011).
3. Gataullina, S. & Dulac, O. From genotype to phenotype in Dravet disease. *Seizure* **44**, 58–64 (2017).
4. Sakauchi, M. *et al*. Retrospective multiinstitutional study of the prevalence of early death in Dravet syndrome. *Epilepsia* **52**, 1144–1149 (2011).
5. Claes, L. *et al*. De novo mutations in the sodium–channel gene SCN1A cause severe myoclonic epilepsy of infancy. *Am. J. Hum. Genet.* **68**, 1327–1332 (2001).
6. Marini, C. *et al*. SCN1A duplications and deletions detected in Dravet syndrome: Implications for molecular diagnosis. *Epilepsia* **50**, 1670–1678 (2009).
7. Rubinstein, M. *et al*. Dissecting the phenotypes of Dravet syndrome by gene deletion. *Brain* **138**, 2219–2233 (2015).
8. Yamakawa, K. Molecular and cellular basis: insights from experimental models of Dravet syndrome. *Epilepsia* **52**(Suppl 2), 70–71 (2011).
9. Martin, M. S. *et al*. Altered function of the SCN1A voltage–gated sodium channel leads to gamma–aminobutyric acid–ergic (GABAergic) interneuron abnormalities. *J. Biol. Chem.* **285**, 9823–9834 (2010).
10. Lossin, C. A catalog of SCN1A variants. *Brain Dev.* **31**, 114–130 (2009).
11. Escayg, A. & Goldin, A. L. Sodium channel SCN1A and epilepsy: mutations and mechanisms. *Epilepsia* **51**, 1650–1658 (2010).
12. Weiss, L. A. *et al*. Sodium channels SCN1A, SCN2A and SCN3A in familial autism. *Mol. Psychiatry* **8**, 186–194 (2003).
13. Dichgans, M. *et al*. Mutation in the neuronal voltage–gated sodium channel SCN1A in familial hemiplegic migraine. *Lancet (London, England)* **366**, 371–377 (2005).
14. Meier, S. *et al*. SCN1A affects brain structure and the neural activity of the aging brain. *Biol. Psychiatry* **72**, 677–683 (2012).
15. Kalume, F., Yu, F. H., Westenbroek, R. E., Scheuer, T. & Catterall, W. A. Reduced Sodium Current in Purkinje Neurons from NaV1.1 Mutant Mice: Implications for Ataxia in Severe Myoclonic Epilepsy in Infancy. *J. Neurosci.* **27**, 11065–11074 (2007).
16. Yu, F. H. *et al*. Reduced sodium current in GABAergic interneurons in a mouse model of severe myoclonic epilepsy in infancy. *Nat. Neurosci.* **9**, 1142–1149 (2006).
17. Ogiwara, I. *et al*. Nav1.1 Localizes to Axons of Parvalbumin–Positive Inhibitory Interneurons: A Circuit Basis for Epileptic Seizures in Mice Carrying an Scn1a Gene Mutation. *J. Neurosci.* **27**, 5903–5914 (2007).
18. Rubinstein, M. *et al*. Genetic background modulates impaired excitability of inhibitory neurons in a mouse model of Dravet syndrome. *Neurobiol. Dis.* **73**, 106–117 (2015).
19. Ogiwara, I. *et al*. Nav1.1 haploinsufficiency in excitatory neurons ameliorates seizure–associated sudden death in a mouse model of dravet syndrome. *Hum. Mol. Genet.* **22**, 4784–4804 (2013).
20. Tatsukawa, T., Ogiwara, I., Mazaki, E., Shimohata, A. & Yamakawa, K. Impairments in social novelty recognition and spatial memory in mice with conditional deletion of Scn1a in parvalbumin–expressing cells. *Neurobiol. Dis.* **112**, 24–34 (2018).
21. Cheah, C. S. *et al*. Specific deletion of NaV1.1 sodium channels in inhibitory interneurons causes seizures and premature death in a mouse model of Dravet syndrome. *Proc. Natl. Acad. Sci.* **109**, 14646–14651 (2012).
22. Kuo, F. S., Cleary, C. M., LoTurco, J. J., Chen, X. & Mulkey, D. K. Disordered breathing in a mouse model of Dravet syndrome. *Elife* **8** (2019).
23. Klassen, T. L. *et al*. High–resolution molecular genomic autopsy reveals complex sudden unexpected death in epilepsy risk profile. *Epilepsia* **55**, 6–12 (2014).
24. McPhee, J. C., Ragsdale, D. S., Scheuer, T. & C, W. A critical role of transmembrane segment SVI6 of the Sodium channel α subunit in fast inactivation. *J Biol Chem* **270**, 12025–12034 (1995).
25. Van Erum, J., Van Dam, D. & De Deyn, P. P. PTZ–induced seizures in mice require a revised Racine scale. *Epilepsy Behav.* **95**, 51–55 (2019).
26. Wilson, C. A. & Koenig, J. I. Social interaction and social withdrawal in rodents as readouts for investigating the negative symptoms of schizophrenia. *Eur Neuropsychopharmacol* **24**, 759–773 (2015).
27. Villeneuve, N. *et al*. Cognitive and adaptive evaluation of 21 consecutive patients with Dravet syndrome. *Epilepsy Behav.* **31**, 143–148 (2014).
28. Haginoya, K. *et al*. [18F]fluorodeoxyglucose–positron emission tomography study of genetically confirmed patients with Dravet syndrome. *Epilepsy Res.* **147**, 9–14 (2018).
29. Kumar, A. *et al*. Evolution of Brain Glucose Metabolic Abnormalities in Children With Epilepsy and SCN1A Gene Variants. *J. Child Neurol.* **33**, 832–836 (2018).
30. Nabbout, R. *et al*. Development and content validation of a preliminary core set of patient– and caregiver–relevant outcomes for inclusion in a potential composite endpoint for Dravet Syndrome. *Epilepsy Behav.* **78**, 232–242 (2018).
31. Moy, S. S. *et al*. Mouse behavioral tasks relevant to autism: Phenotypes of 10 inbred strains. *Behav. Brain Res.* **176**, 4–20 (2007).
32. Olivieri, G. *et al*. Cognitive–behavioral profiles in teenagers with Dravet syndrome. *Brain Dev.* **38**, 554–562 (2016).
33. Chieffo, D. *et al*. Cognitive decline in Dravet syndrome: Is there a cerebellar role? *Epilepsy Res.* **106**, 211–221 (2013).
34. Sawyer, N. T. *et al*. Scn1a dysfunction alters behavior but not the effect of stress on seizure response. *Genes, Brain Behav.* **15**, 335–347 (2016).
35. Salgueiro–Pereira, A. R. *et al*. A two–hit story: Seizures and genetic mutation interaction sets phenotype severity in SCN1A epilepsies. *Neurobiol. Dis.* **125**, 31–44 (2019).
36. Theodore, W. Antiepileptic drugs and cerebral glucose metabolism. *Epilepsia* **29**, S48–55 (1988).

37. Govil–Dalela, T., Kumar, A., Behen, M. E., Chugani, H. T. & Juhász, C. Evolution of lobar abnormalities of cerebral glucose metabolism in 41 children with drug–resistant epilepsy. *Epilepsia* **59**, 1307–1315 (2018).
38. Chugani, H., Shewmon, D. A., Khanna, S. & Phelps, M. E. Interictal and postictal focal hypermetabolism on positron emission tomography. *Pediatr. Neurol.* **9**, 10–15 (1993).
39. Schwenk, F., Baron, U. & Rajewsky, K. A cre–transgenic mouse strain for the ubiquitous deletion of loxP–flanked gene segments including deletion in germ cells. *Nucleic Acids Res.* **23**, 5080–5081 (1995).
40. Chen, W. *et al*. Tumor necrosis factor–α enhances voltage–gated Na+ currents in primary culture of mouse cortical neurons. *J. Neuroinflammation* **12**, 1–10 (2015).
41. Livak, K. J. & Schmittgen, T. D. Analysis of relative gene expression data using real–time quantitative PCR and the 2–ΔΔCT method. *Methods* **25**, 402–408 (2001).
42. Dunah, A. W., Wyszynski, M., Martin, D. M., Sheng, M. & Standaert, D. G. α–Actinin–2 in rat striatum: localization and interaction with NMDA glutamate receptor subunits. *Mol. Brain Res.* **79**, 77–87 (2000).
43. Ricobaraza, A. *et al*. Phenylbutyrate ameliorates cognitive deficit and reduces tau pathology in an alzheimer's disease mouse model. *Neuropsychopharmacology* **34**, 1721–1732 (2009).
44. Kalume, F. *et al*. Sleep impairment and reduced interneuron excitability in a mouse model of Dravet Syndrome. *Neurobiol. Dis.* **77**, 141–154 (2015).
45. Alshammari, M. A., Alshammari, T. K. & Laezza, F. Improved Methods for Fluorescence Microscopy Detection of Macromolecules at the Axon Initial Segment. *Front. Cell. Neurosci.* **10**, 1–20 (2016).
46. Hargus, N. J., Nigam, A., Bertram, E. H. & Patel, M. K. Evidence for a role of Na v 1.6 in facilitating increases in neuronal hyperexcitability during epileptogenesis. *J. Neurophysiol.* **110**, 1144–1157 (2013).
47. Martinez–Losa, M. *et al*. Nav1.1–Overexpressing Interneuron Transplants Restore Brain Rhythms and Cognition in a Mouse Model of Alzheimer's Disease. *Neuron* **98**, 75–89.e5 (2018).
48. Verret, L. *et al*. Inhibitory interneuron deficit links altered network activity and cognitive dysfunction in alzheimer model. *Cell* **149**, 708–721 (2012).
49. Gelinas, J. N., Khodagholy, D., Thesen, T., Devinsky, O. & Buzsáki, G. Interictal epileptiform discharges induce hippocampal–cortical coupling in temporal lobe epilepsy. *Nat. Med.* **22**, 641–648 (2016).
50. Deacon, R. Digging and marble burying in mice: simple methods for *in vivo* identification of biological impacts. *Nat. Protoc.* **1**, 122–4 (2006).
51. Deacon, R. Assessing nest building in mice. *Nat Protoc* **1**, 1117–9 (2006).

Acknowledgements

We would like to express our deepest gratitude to the families of DS patients for their unconditional support and inspiration. We thank excellent contributions from the micro-PET core facility of the University of Navarra (Maria Collantes and Marga Ecay), Animal facility and Morpohology core from CIMA. This work has been funded by Foundation for Applied Medical Research (FIMA), CureDravet E-rare project from EU, Inocente-inocente Foundation, Desafía Dravet Association and Apoyo Dravet Association. LM is a recipient of a Pedro Lopez Berastegui fellowship. We thank the Helpify platform and the work from the fundraising department of the University of Navarra for its contribution to the sustainability of this project.

Author Contributions

A.R., R.S., A.M., J.A., M.V. and R.H. conceived the experiments. A.R., L.M., E.P., M.N., G.B., M.B., M.G, and N.S.S. conducted the experiments. A.R., J.A., M.V. and R.H. analyzed the results. A.R., R.H., M.V., and J.A. wrote the manuscript. All authors reviewed the manuscript.

Additional Information

Supplementary information accompanies this paper at https://doi.org/10.1038/s41598-019-50627-w.

Competing Interests: The authors declare no competing interests.

Publisher's note Springer Nature remains neutral with regard to jurisdictional claims in published maps and institutional affiliations.

International Journal of
Molecular Sciences

MDPI

Review

High-Capacity Adenoviral Vectors: Expanding the Scope of Gene Therapy

Ana Ricobaraza, Manuela Gonzalez-Aparicio, Lucia Mora-Jimenez, Sara Lumbreras and Ruben Hernandez-Alcoceba *

Gene Therapy Program. University of Navarra-CIMA. Navarra Institute of Health Research, 31008 Pamplona, Spain; aricobaraza@unav.es (A.R.); gamanuela@unav.es (M.G.-A.); lmora.1@alumni.unav.es (L.M.-J.); slumbreras@alumni.unav.es (S.L.)
* Correspondence: rubenh@unav.es; Tel.: +34-948-194700

Received: 22 April 2020; Accepted: 19 May 2020; Published: 21 May 2020

Abstract: The adaptation of adenoviruses as gene delivery tools has resulted in the development of high-capacity adenoviral vectors (HC-AdVs), also known, helper-dependent or "gutless". Compared with earlier generations (E1/E3-deleted vectors), HC-AdVs retain relevant features such as genetic stability, remarkable efficacy of in vivo transduction, and production at high titers. More importantly, the lack of viral coding sequences in the genomes of HC-AdVs extends the cloning capacity up to 37 Kb, and allows long-term episomal persistence of transgenes in non-dividing cells. These properties open a wide repertoire of therapeutic opportunities in the fields of gene supplementation and gene correction, which have been explored at the preclinical level over the past two decades. During this time, production methods have been optimized to obtain the yield, purity, and reliability required for clinical implementation. Better understanding of inflammatory responses and the implementation of methods to control them have increased the safety of these vectors. We will review the most significant achievements that are turning an interesting research tool into a sound vector platform, which could contribute to overcome current limitations in the gene therapy field.

Keywords: adenovirus; high-capacity adenovirus; helper-dependent; gutless; gene therapy; vector; gene correction

1. Introduction

1.1. General Characteristics of Adenoviruses (AdVs)

The *Adenoviridae* family comprises a wide group of human and animal viruses sharing functional, genetic, and structural characteristics [1]. Traditional classification in serotypes, based on immune cross-reactivity, is being substituted by sequence homology for the identification of new AdV types [2]. Human adenovirus type 5 (HAdV5), belonging to the *Mastadenovirus* genus, is the adenovirus most frequently adapted as gene therapy vector, and we will use it as a paradigm for the description of general characteristics. However, the entire *Adenoviridae* family offers a rich source of members [3] whose peculiarities are being recently exploited for therapeutic purposes (Table 1). In general, the viral particles consist of a linear double-stranded DNA genome ranging from 26 to 46 Kb in length (36 Kb in the case of HAdV5), embedded in core proteins and surrounded by an icosahedral capsid [4]. Each vertex of this outer structure contains five units of a protein called penton, which act as an anchor for the trimeric protein fiber. The most abundant capsid protein is the hexon, which together with other structural proteins forms the facets of the icosahedron. The average size of viral particles is 100 nm in diameter. The C-terminal portion of the fiber (knob) interacts with the primary receptor in cells [5], allowing an initial immobilization of the particle in the cell surface, which facilitates further interaction between the penton

base and integrins [6], as well as binding of fiber shaft to heparan sulphate proteoglycans. These can be considered secondary receptors, which allow infection of cells lacking the primary receptor, albeit at a lower rate. This is the reason why most AdV types present a wide cellular tropism. This fact, together with the possibility of obtaining the virus at high titers, determines that few cells are completely refractory to AdV infection, at least in vitro. However, AdV types using Coxsackie and Adenovirus Receptor (CAR) as primary receptor show preference for epithelial cells, whereas other types such as HAdV35 use CD46 or desmoglein-2, and are able to infect hematopoietic cells (Table 1) [7]. Upon cell attachment, internalization of the virion is activated through chlatrin-mediated endocytosis [8]. A programmed disassembly of the capsid is required for further progression of particles in their journey to the cell nucleus [9]. Of note, this is an active and very efficient process which largely contributes to the high efficacy of transduction [10]. The endocytic vesicles are disrupted owing to the release of protein VI from the capsid, avoiding lysosomal destruction of the virus [11]. The particles are then transported to the nuclear pore using the microtubular complexes, and the DNA together with some core proteins are finally introduced into the nucleus [12]. It is estimated that 40% of internalized particles complete this process in less than 2 h. Importantly, the double-stranded genome is ready to be transcribed once inside the nucleus, which ensures a rapid and efficient expression of vector-encoded proteins. Wild type AdVs follow a lytic cycle in permissive hosts, completing the steps of early viral genes expression, genome replication, late viral genes expression, genome encapsidation, and particle maturation inside the nuclei. At the end, nuclear and cytoplasmic membranes are disrupted and up to 10,000 new virions are released 48–72 h after infection in highly permissive cells. Most wild type AdVs cause self-limited infections in their respective host species, affecting predominantly the respiratory tract, eyes, and digestive tract, depending on the serotypes (Table 1) [13]. However, human AdVs are severe pathogens in immunocompromised individuals such as patients undergoing bone marrow or solid organ transplantation [14]. In these cases, AdV is found in circulation and shows its capacity to infect internal organs such as liver. Interestingly, the origin of these infections is usually the reactivation of viral reservoirs present in the gut [15], which demonstrates the possibility of latency or chronic, sub-clinical persistence of the virus.

1.2. AdVs as Therapeutic Agents: Versions and Evolution

AdVs can be modified to exploit different properties, giving rise to specialized agents (Figure 1). The lytic cycle can be used to destroy cancer cells (oncolytic adenoviruses, OAV). To this end, replication of the virus should be properly modulated by transcriptional control of the early viral genes (particularly E1A) or ablation of viral functions that are dispensable only in cancer cells [17]. OAVs can incorporate transgenes in order to enhance their therapeutic effect, giving rise to the "armed" OAVs, also called replication-competent vectors. In contrast, when the primary objective is to express transgenes in the target cells, the replicative potential of AdV should be abolished in order to prevent the destruction of cells. This is accomplished by removal of the E1 region, which is complemented *in trans* in the packaging cells during vector amplification. The E3 region, which is dispensable for the amplification of AdV in cell culture, is also removed in most cases to increase the cloning capacity up to 8 Kb. These first-generation, E1/E3-deleted AdV vectors (FGAdV) demonstrated high transduction efficacy in cell cultures and animal models, and its clinical translation raised high expectations [18]. Further deletion of viral genes such as E2 and E4, owing to the development of the corresponding trans-complementing cells, increased the cloning capacity of these second generation AdV vectors (Figure 1). However, the presence of a substantial proportion of the wild type genome leads to a residual expression of viral proteins in the transduced cells, and elicits cytotoxic immune responses against them, limiting the duration of transgene expression in immune-competent hosts [19]. Therefore, the current application of these early generation vectors is limited to vaccination strategies [20], apart from their use as research tools for cell culture transduction. It was only when all viral coding sequences were completely removed (3rd generation, "*gutless*" vectors) that cellular immune responses against transduced cells were dampened and long-term transgene expression was achieved in vivo. Seminal studies in non-human primates (NHP) demonstrated that a single intravenous administration can sustain secretion of therapeutic proteins from the liver for several years [21,22]. In these

vectors, only the inverted terminal repeats (ITR), the packaging signal (Ψ), and in some cases a short non-coding region from the right end of the viral genome, are maintained [23]. These small sequences are required for genome replication during vector production, encapsidation of genomes, and maintenance of genome stability, respectively. The cloning capacity of these vectors is extended to 37 Kb, which justifies their denomination as high-capacity adenoviral vectors (HC-AdVs). Since the size of expression cassettes is usually smaller, HC-AdVs need to incorporate stuffer DNA in their genomes in order to reach the minimal size for stable packaging, which is close to 28 Kb in the case of HAdV5 [24]. Of note, packaging cells expressing all viral genes are not viable, as discussed below. Therefore, trans-complementation is usually achieved using a helper virus (HV), which is a specialized E1/E3-deleted AdV vector. This explains the alternative denomination as helper-dependent AdV vectors (HD-AdV). In the next sections, we will summarize and discuss different aspects of HC-AdVs, with special attention to the therapeutic possibilities they offer and the current challenges in the field.

Table 1. Characteristics of all human adenovirus (HAdV) types, and selected examples of animal AdVs adapted as gene therapy vectors.

Genus	Natural Host	AdV Species (Types)	Receptors	Tropism	Genome Size (Kb)
Mastadenovirus	Human (HAdV)	A (12, 18, 31,61)	CAR, INT	Epithelium (respiratory, intestinal)	34–36
		B (**3**, **7**, **11**, 14, 16, 21, 34, **35***, **50**, 55)	CD46, DSG2, CD80, CD86, LPR, INT	Epithelium (respiratory, ocular, urinary); lymphoid, HSC	
		C (**1***,**2***,**5***,**6***, 57)	CAR, HSPG, LPR, MHC-I, SR, VCAM-1, INT	Epithelium (respiratory, ocular, intestinal); liver	
		D (8–10, 13, 15, 17, **19**, 20, 22–25, **26**, 27, **28**, 29, 30, 32, 33, 36–39, 42, **43**, 44–47, **48**, **49**, 51, 53, 54, 60a, 62–65, 67, 69, 71, 81)	SA, CD46, CAR, INT	Epithelium (respiratory, ocular, intestinal)	
		E (**4**)	CAR, INT	Epithelium (respiratory, ocular)	
		F (40, **41**)	CAR	Epithelium (intestinal)	
		G (52)	SA, CAR	Epithelium (intestinal)	
	Canine (CAdV)	A (**2***)	CAR	Epithelium (respiratory); neurons	31
	Simian (SAdV) Chimp.	C (**3**, **Pan3**)	CAR	Epithelium (respiratory, ocular, intestinal); liver	36
		E (**7**, **63**, **68**)	CAR	Epithelium (respiratory, ocular, intestinal); liver	36.5
	Porcine (PAdV)	A (**3***)		Epithelium (respiratory, intestinal)	34
	Murine (MAdV)	A (**1**)	INT, HSPG	Epithelium (respiratory, ocular); brain, spinal cord, spleen	31
	Bovine (BAdV)	A (**1**)		Epithelium (respiratory)	35
		B (**3**)	SA	Epithelium (respiratory, intestinal); liver, kidney, heart	34.4

Table 1. *Cont.*

Genus	Natural Host	AdV Species (Types)	Receptors	Tropism	Genome Size (Kb)
Aviadenovirus	Fowl (FAdV)	A (CELO) (**1**)	CAR	Epithelium (respiratory); liver	43.8
		C (**4**, **10**)	CAR	Epithelium (respiratory); liver	45.6
		D (**9**)		nd	45
		E (**8**)		Epithelium (respiratory); liver	45
Atade-novirus	Ovine (OAdV)	D (**7**)	INT	Epithelium (respiratory, intestinal)	29.6

Viruses adapted as gene therapy vectors are marked in bold, and those with HC-AdV versions are distinguished by an asterisk. The best characterized receptors are described (with primary receptor underlined), but they are not exclusive. Note: for chimpanzee AdV we have used the classification described in [16], but some of them can be included in human *Mastadenovirus* species. CAR, Coxackie and Adenovirus receptor; DSG2, desmoglein 2; HSPG, heparan sulphate proteoglycans; INT, integrins; LPR, low-density lipoprotein receptor related protein; MHC-I, major histocompatibility complex-I; SA, syalic acid; SR, scavenger receptor; VCAM-1, vascular cell adhesion molecule-1.

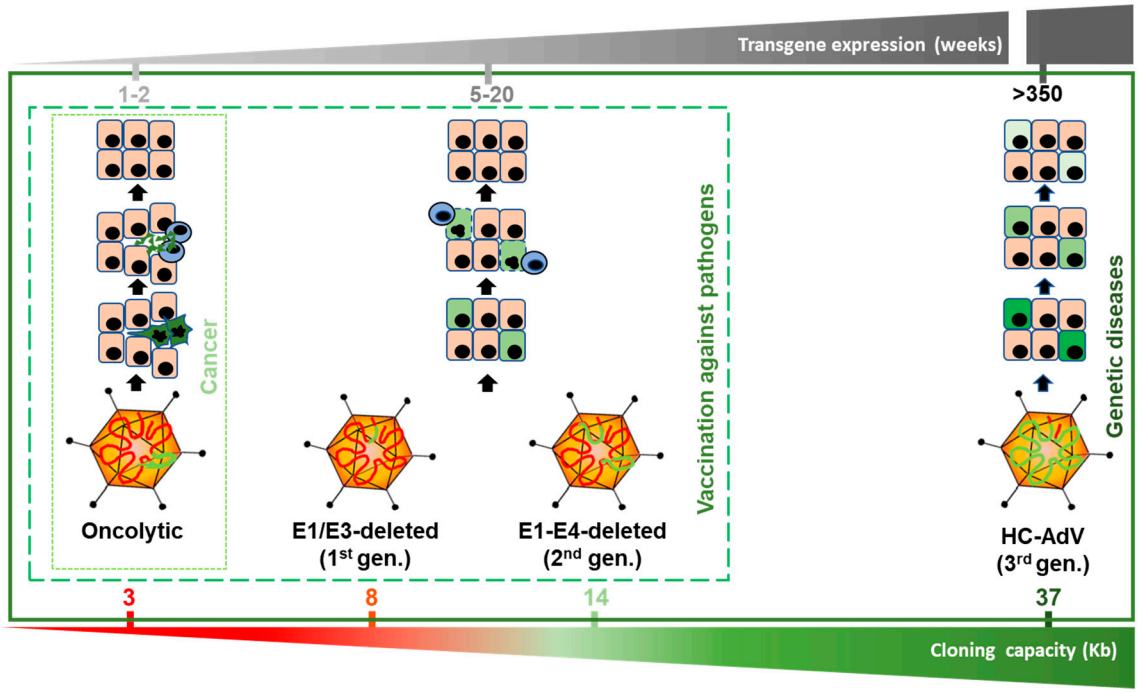

Figure 1. Versions of adenoviral vectors and potential therapeutic applications. The size range allowed for genome packaging is between 28 and 38 Kb. Oncolytic adenoviruses retain most of the viral genome, including the E1 region, which is required for replication. They can accommodate up to 3 Kb of exogenous DNA if the E3 region is partially deleted. Since they replicate their genomes and cause the lysis of infected cells, transgene expression is very intense but transient. Among replication-deficient vectors, E1/E3-deleted (1st generation) versions can harbor up to 8 Kb. This capacity can be extended up to 14 Kb if the E2 and E4 regions are also deleted (second generation). Although these vectors do not cause direct destruction of infected cells, cytotoxic immune responses against them limit the stability of transgene expression. Apart from vaccination strategies, E1/E3-deleted vectors are still a widely used research tool for in vitro and in vivo gene transfer. High-capacity adenoviral vectors (HC-AdVs) (third generation) only retain short non-coding regions from the AdV genome (ITRs and ψ signal), which leaves a cloning capacity of 37 Kb. The lack of viral gene expression in transduced cells reduces cellular immune responses and allows long-term transgene expression, which decreases slowly as the

cells are renewed. HC-AdVs are suitable for all in vivo applications, including gene supplementation and gene correction for monogenic diseases. The indicated duration of transgene expression is based on liver-directed transduction in NHP, but it can be different in other hosts and tissues. In vector genomes, viral DNA is represented in red and exogenous DNA in green (including expression cassettes and/or DNA templates, and stuffer DNA).

2. Production of HC-AdVs

The removal of all viral coding genes dictates the unique properties of HC-AdVs in terms of stability of expression and cloning capacity, which differentiate them from early AdV vector versions. The downside is a greater complexity of the production procedures, because stable expression of all adenoviral genes in packaging cells, in the pattern and amount required for trans-complementation, is not feasible. Therefore, most methods rely on the use of HVs. The main differences among them are the strategies used to avoid HV contamination in the final HC-AdV preparation, as described below.

2.1. Viral Rescue and Amplification

The first method for HC-AdV production dates back to 1996, when Kochanek et al. prepared a plasmid containing 28 Kb of non-viral DNA flanked by AdV ITRs, with the packaging signal in one end [25]. The HV was a FGAdV with a 91 bp deletion in the packaging signal, so it would have a competitive disadvantage for encapsidation. When the plasmid was transfected in HEK293 cells and then cells were infected with the HV, they could rescue a small amount of HC-AdV. After several rounds of co-infection in a growing number of cells, the vector was purified by ultracentrifugation in a density gradient. The final contamination with HV was in the range of 1%, but production of HV was problematic because of the inefficiency of packaging. Later, Parks et al. introduced the concept of Cre-mediated excision of the packaging signal [26]. When this sequence is flanked by loxP sites in the HV and the cells express the recombinase, high yields of HC-AdV with less than 0.1% HV contamination can be routinely obtained. Apart from the efficient removal of the packaging signal, an important advantage of this methods is the easy production of the HV in standard HEK293 cells. Although similar results were obtained when the FLP/frt system was used [27], the Cre/loxP system is currently the gold standard, and it is the basis for most improvements developed since then, as described below. The HV is usually an E1/E3-deleted vector, but restoration of the E3 region has been described to increase its helper efficacy. On the other hand, deletion of the E2 region may increase the safety of HVs, although special packaging cells complementing the E1 and E2 genes are required [28]. During HC-AdV amplification, the shut-off of protein synthesis in the cell, imposed by the virus, limits the availability of the Cre recombinase. This is the moment of highest demand for the removal of packaging signal in a growing number of HV genomes [29]. To avoid this limitation, a self-inactivating HV was developed in which the recombinase is inserted in its own genome [30]. Owing to a drug-inducible system and the use of the MerCreMer fusion protein [31], cleavage of ψ can be modulated and this HV can be produced in HEK293 cells. In contrast, this sequence is efficiently cleaved when the expression of MerCreMer is stimulated by doxycycline, and the addition of 4-hydroxy-tamoxifen allows the access of the protein to the nucleus. Increasing the difference in genome size between HV and HC-AdV facilitates the separation of the particles by density, and inverting the orientation of the packaging signal in the HV reduces the risk of productive recombination with the HC-AdV genomes [32]. Deletion of the pIX gene decreases the packaging capacity of HAdV to 35 Kb. If the size of the HV exceeds this limit and harbors this deletion, it can only be produced in specialized HEK293 cells expressing pIX. This phenomenon can be exploited to reduce HV contamination [33]. Flanking the HV packaging signal by attB/attP sequences produces a delay in encapsidation, which can be used to reduce contamination [34]. Other methods rely on the incorporation of the HV genome in other vectors such as Baculovirus [35] or herpes simplex virus (HSV) [36]. More recently, a HV-free method has been described, in which all trans-complementing genes are provided by transfection of a plasmid devoid of packaging signal, in several steps of amplification [37]. This procedure is

reminiscent of the initial stages of amplification in pioneering protocols [38], but the new method relies on co-transfection of a plasmid encoding the AdV pre-terminal protein (pTP) to enhance vector yield. This result challenges the notion that TP should be covalently fused to both genome ends in order to promote genome replication [39]. The suitability of this procedure for large-scale production awaits confirmation.

2.2. Purification

In principle, HC-AdVs can be purified the same as any other AdV. Ultracentrifugation in CsCl density gradients is the traditional method, followed by desalting by size exclusion chromatography (sepharose columns) or dialysis [40,41]. However, iodixanol may have advantages compared with CsCl. On the one hand, it is more biologically compatible and requires shorter centrifugation times. On the other hand, it can preserve particle infectivity during the purification process, and provides better separation of particles with small differences in genome size. In fact, reduction of HV contamination from 2.5 to 0.03% has been reported after two iodixanol purification steps [42]. In principle, these methods allow to discriminate empty and incomplete viral particles from particles containing full vector genomes, improving (reducing) the total to infectious particle ratio. This is especially relevant for HC-AdVs, since crude lysates often present very high ratios. When the difference in genome sizes between HC-AdV and HV is sufficient, selecting the correct fraction can also reduce HV contamination [27]. Anion exchange columns and density gradients can be used sequentially to improve separation [42]. However, ultracentrifugation is not convenient for high-scale production and good manufacturing practices (GMP) adaptation. A combination of chromatographic methods based on capture antibodies, ionic exchange, size exclusion, hydrophobic interaction, and immobilized metal affinity columns has been described [43,44]. Methods that contribute to the enrichment in full vector particles are especially indicated for HC-AdV [45,46].

2.3. Quantification

Common to all viral vectors, the availability of standardized methods for precise quantification of HC-AdVs is an unmet need. The simplest way to determine the amount of particles (vp) in a purified HC-AdV preparation is based on the absorbance at 260 nm, usually performed after disruption of capsids by detergent (SDS) or enzymatic treatment [47,48]. Similar to other vectors such as those derived from adeno-associated virus (AAV), quantitative PCR can be used to determine the amount of viral genomes (vg) [49], which should provide information equivalent to the spectrophotometer. In both cases, the availability of certified standards could contribute to the reproducibility of results, the comparison of different vector batches, and the uniformity of data across laboratories [50]. In contrast with early generation AdV vectors, HC-AdVs are not replicative even in the packaging cells. Therefore, quantification of plaque forming units (pfu) or infectious units (iu) using end-point dilution methods or commercially available kits is not possible. For determination of iu, permissive cells exposed to the vectors can be lysed a few hours later and viral genomes are quantified by PCR [49,50]. Although this method is more restrictive than direct PCR of particles and provides a closer estimation of transduction potency, it is difficult to standardize, and the values are always relative to the cell line and the culture conditions employed. However, iu quantification can explain apparent inconsistencies in the performance of different vector batches. Only when the production process is perfectly standardized, an equivalent ratio between total and infectious particles can be assumed. This ratio is usually higher in HC-AdVs compared with OAVs or FGAdV vectors, and differences have also been reported among AdV vector platforms. For instance, vectors derived from canine adenovirus type 2 (CAV-2) present ratios of less than 3:1 [51], whereas ratios of 10:1 or higher are common for human vectors, although it can be due to the specific cell lines employed for quantification. Comparing the performance of different vectors such as those derived from AAV and AdV is even more complicated. The few articles taking this challenge usually report the dose of AdV using iu and vp, whereas AAV are quantified in vg [52]. However, a relevant comparison should take into account different parameters such as the balance between safety

and efficacy, feasibility of production, and the amount of vector genomes in the target organ needed for the therapeutic effect.

3. Immune Responses and Other Host–Vector Interactions

All HC-AdV interactions with the extracellular milieu are common to the parental AdV type used to develop the HV, unless specific capsid modifications have been implemented. This means, for instance, that HC-AdVs derived from the prototypic HAdV5 will bind with high affinity to erythrocytes in circulation, through direct binding of fiber to the primary CAR receptor, or via natural antibodies to complement receptor CR1 [53]. It is not entirely clear whether this is a barrier for AdV dissemination or if the virus can use these cells as carriers. Vitamin K-dependent coagulation factors such as FVII, FIX, and FX bind to the hexon of many AdV types (including HAdV5). This is a critical factor for transduction of hepatocytes [54], and it can shield the particles from natural IgM antibodies and from the complement system, favoring the function of intravenously administered vectors [55].

In the same vein, HC-AdVs elicit innate and humoral adaptive immune responses similar to other AdV vectors [56]. Of note, inflammatory responses against AdV are largely responsible for the toxicity observed when these vectors are administered systemically at high doses [57]. A dose-dependent elevation of cytokines such as interleukin-6 (IL-6) has been documented in animal models and patients [58,59], and a similar scenario is expected in the case of HC-AdVs [60]. In the vast majority of cases, this is a self-limited event. However, the death of a patient in a pioneering clinical trial 4 days after receiving 3.8×10^{13} vp of an early generation AdV vector [59] is a constant reminder that cytokines should be monitored. New methods to counteract inflammatory mediators such as IL-6 and tumor necrosis factor alpha (TNFα), including monoclonal antibodies, should be available to guarantee the safety of clinical trials based on systemic administration of these agents [61]. It is reassuring to see that after more than 500 clinical trials involving AdV vectors and OAVs, no more vector-related life-threatening adverse effects have been reported. Although clinical experience in specific populations such as young children and severely immunocompromised patients is limited, an increase in immune-related adverse effects is not expected. In the latter group, the risk of OAV replication in normal tissues should be carefully evaluated.

In contrast with the aforementioned considerations, vector-related cellular immune responses against transduced cells are attenuated in the case of HC-AdVs compared with other AdV vectors [62–64]. The rapid degradation of incoming capsids and the lack of viral genes encoded in the vector genome reduce the possibility of presenting highly immunogenic viral epitopes in the surface of the cells. AdV-specific T-cells responses can be stimulated after intravenous administration of HC-AdVs in different animal models [56,65], but in contrast with early generation AdV vectors [66], a biphasic elevation of liver transaminases is not observed [56,67]. This is consistent with a dose-dependent inflammatory response leading to early and transient liver damage, which is not followed by cytotoxic immune responses against transduced hepatocytes (Figure 1). Importantly, the pre-existing anti-AdV humoral and cellular immune responses do not compromise the stability of transgene expression in mice treated with HC-AdVs [62,64], increasing the prospects for successful application of these vectors in humans. However, AdV-specific CD4 T cells are detected in a high proportion of individuals [68], and the possibility of cytotoxicity against transduced cells harboring incoming viral particles cannot be ruled out. Since the predictive value of animal models toward vector-related immune responses is limited, carefully designed clinical trials should investigate this phenomenon. Experience with AAV vectors suggests that rapid or prophylactic corticoid treatment could overcome immune-related loss of transgene expression [69].

4. Genome Stabilization in Transduced Cells

HC-AdV particles penetrating into mammalian cells are transported through microtubules and introduce their genome in the nucleus, following the highly efficient pathway common to all AdV vectors [8]. During this process, the incoming particle components and the vector DNA can be detected

by pattern recognition receptors (PRRs) such as Toll-like receptors (TLRs) and nucleic acid sensors, triggering cellular antiviral defense mechanisms (type I interferons (IFNs), TNFα and other cytokines, depending on the cell type) [70–72]. Compared with the wild type infectious cycle, the absence of viral replication in HC-AdVs reduces the activation of antiviral defenses, but on the other hand the lack of E3 and E4 genes eliminates the natural mechanisms that AdV has developed to counteract these responses [73–75]. It is difficult to determine to what extent the antiviral pathways reduce the efficacy of transgene expression by DNA degradation, transcriptional repression, or other mechanisms. However, the net balance of these early vector-cell interactions is, in a relevant proportion of cells, the persistence of HC-AdV genomes in an episomal state [76]. The kinetics of transgene expression in vivo, in organs such as the liver, is compatible with permanent presence of transcriptionally active genomes during the entire lifespan of transduced cells, when the appropriate promoters are used [22]. During cell division, HC-AdV genomes are more stable than dsDNA fragments transfected by non-viral methods [77], suggesting specific mechanisms of retention. Although a low proportion of chromosomal integrations have been detected, this is a random process inherent to the presence of linear DNA in the nucleus, and it cannot account for the stability of transgene expression in vivo [78]. AdV genomes enter the nucleus still bound to core proteins, and as soon as 1 h after infection, both protein VII and cellular histones are associated with the viral DNA. In the absence of replication, the predominant histone found in vector genomes is H3.3, which progressively replaces protein VII [79]. The process is dependent on the chaperone HIRA [80], and this chromatinization seems to be important for the stabilization of transgene expression. It is not surprising that sequences contained in the vector genome determine its epigenetic status and exert a strong influence on the expression cassette. The cloning capacity of HC-AdVs allows the incorporation of human genomic fragments partially mimicking the chromosomal regions of interest. Therefore, the so called "stuffer" DNA may play a relevant role as part of the expression cassette [81]. Genome persistence at the cellular level is a critical event, but the interplay between cellular, tissue, and systemic factors has a major impact on the stability of transgene expression in vivo. For instance, an initial period of high expression followed by a decline and then long-term stabilization has been reported in some studies using intravenous administration of HC-AdVs [21,77,82]. This may be due to the initial transduction of several populations of cells in the liver, each one with a different turnover (long-lasting hepatocytes versus Kupffer cells, etc.). The same could apply to glial versus neuronal populations in the brain [62]. Of note, this phenomenon can lead to apparent disappearance of transgene expression if the initial intensity is low, depending on the sensitivity of detection methods [83]. Finally, the influence of the transgene product should be taken into account. These factors may explain some differences observed when the vectors are administered to rodents, dogs, macaques, and baboons at different ages. Importantly, remarkable stability has been observed in adult NHPs when the transgene encodes an endogenous protein, which could be detected in serum more than 7 years after initial vector administration [22].

5. Beyond HAdV5: Expanding the Repertoire of HC-AdVs

HAdV5 is a robust platform for the construction of HC-AdVs. Binding of capsids to the primary receptor CAR, and the interaction with secondary receptors such as integrins and HSPG, allow efficient infection of a variety of cell types, especially those of epithelial origin [8]. In addition, the length of its fiber and the interaction with blood proteins determine a marked liver tropism upon intravenous administration [54,84]. However, other HAdV5 features are not so favorable, such as the high frequency of neutralizing antibodies (NAbs) in adults [85,86] and the massive uptake by resident macrophages in the liver (Kupffer cells), which contributes to inflammation and reduces hepatocyte transduction [87–89]. In addition, HAdV5 is relatively inefficient infecting hematopoietic cells, and some tumors may reduce the expression of CAR [90,91]. Luckily, the *Adenoviridae* family provides a wide repertoire of members with specific properties matching many therapeutic needs (Table 1) [92,93]. Moreover, new capsid variants can be obtained by pseudotyping [94–98], rational design [99–101], or forced genome recombination followed by in vitro or in vivo screening [102]. Of note, in most

cases the same HC-AdV genome can be incorporated in different capsids depending on the HV employed, which means that all the technology developed to target FGAdV and oncolytic vectors can be readily applied to HC-AdVs [103,104]. Producing a collection of antigenically distinct vectors would enable efficient re-administration, if needed, or heterologous prime-boost vaccination regimes. Finally, vectors can be coated with a variety of polymers in order to change their properties (reviewed in [105,106]). This can reduce their immunogenicity and protect particles form NAbs. In many cases, masking AdV epitopes results in loss of infectivity, which can be restored and re-directed to specific cell populations by ligand attachment into the shield [107]. Chemical coating can be facilitated by discrete genetic modification in the capsid. For instance, alanine to cysteine mutation into the hypervariable region 5 (HVR5) of HAdV5 allows efficient attachment of polyethylene glycol (PEI), which modulates hepatocyte transduction and reduces uptake of capsids by Kupffer cells [108].

Members of species B HAdV such as HAdV35 bind to CD46 as a primary receptor instead of CAR, which allows them to infect cells of hematopoietic origin, including hematopoietic stem cells (HSC) [7]. The construction of chimeric HVs displaying the HAdV35 fiber in the context of the standard HAdV5 backbone made it possible the advent of HC-AdVs with this expanded tropism [109]. HAdV35 fiber knob mutants with enhanced affinity for CD46 (35++) have been selected from an *E.Coli* expression library, and vectors displaying the selected variants showed improved transduction of $CD46^+$ cells in vivo, with lower liver sequestration [94]. Coupled with other strategies for genome integration, these vectors are opening unprecedented opportunities in genetic and acquired diseases, as will be discussed in the next sections. Other HAdV types such as HAdV6 show reduced uptake by Kupffer cells. This property can be conferred to HAdV5-based vectors by swapping the hexon hypervariable regions between both types of vectors [95]. The chimeric 5/6 HC-AdV vector showed enhanced liver transduction and lower inflammatory reactions compared with equivalent vectors derived from HAdV5, as expected [96]. Interestingly, it was also superior to those derived from HAdV6, probably because the longer shaft of HAdV5 fiber is favorable for hepatocyte infection. The modularity of AdV components and the compatibility of them among different members of the family allow a vast number of potential combinations.

AdV derived from other host species are being exploited for therapeutic purposes, and some of them have been modified as HC-AdVs (Table 1). Apart from other specific properties, these agents have the advantage of low seroprevalence in humans, which facilitates their clinical application. However, cross-reactivity of NAbs, and especially T cells, have been reported between HAdV5 and certain chimpanzee AdVs, such as type 6 (ChAdV6 or AdC6) and ChAdV7 [110,111]. This unfavorable event seems more unlikely in AdVs isolated from more distant species such as bovine and porcine [112]. The downside is that these viruses usually require the development of dedicated production systems, in particular packaging cells. Regarding safety, it should be taken into account that HC-AdVs present the highest degree of attenuation, thus avoiding the risk of unexpected virulence in humans. The CAV-2 presents a strong dependence for CAR in order to infect cells, which implies that in the brain it shows preferential tropism for neurons versus glial cells [113]. This may reduce inflammatory responses and contribute to the accessibility of the target cells for many genetic diseases affecting the brain. In addition, CAV-2 vectors show an efficient axonal transport from neurites to the soma, because their intracellular trafficking mechanism relies on a vesicular pathway instead of the association of naked particles to the cellular microtubular network [114]. It is believed that this pathway protects the capsid from degradation in their journal through long axons. Therefore, HC-AdVs based on CAV-2 have been developed for the treatment of neurological diseases [115], as recently reviewed [116].

6. Therapeutic Applications of HC-AdVs

6.1. Gene Supplementation in Monogenic Diseases

Since AdV vectors are non-integrative, transgene expression will only be stable if the target cells have a low turnover rate, unless artificial mechanisms are designed to sustain genome replication or

chromosomal integration [117]. In concordance with the natural tropism of the standard HAdV5-based vectors, HC-AdVs have been applied mainly to transduce the liver.

6.1.1. Liver-Directed Gene Supplementation

Gene expression from hepatocytes has therapeutic interest not only for hepatic and metabolic diseases, but also for secretion of proteins into circulation. Hemophilia has been considered a suitable target for liver-directed gene therapy from the beginning of this field, because coagulation factors are naturally produced and secreted from this organ. Transduction of all hepatocytes is not required to obtain a therapeutic effect, as far as the circulating levels of the proteins reach a certain threshold. In general, 5% normal values are needed to convert a severe hemophilia into a mild disease, and 30–50% should be obtained for complete clinical normalization [118]. Hemophilia A was an obvious indication for HC-AdVs because the 7 kb-long coagulation factor VIII cDNA (*F8*) exceeds the cloning capacity of AAVs. Pre-clinical studies in mice showed restoration of circulating FVIII at therapeutic levels using a vector encoding human *F8* under the control of the albumin promoter [119]. Following safety assessment in mice and dogs [120], this strategy moved quickly into the clinic. In 2001, the first patient treated intravenously with 4.3×10^{11} vp/Kg of the vector showed initial signs of efficacy (increase from less than 1% to 3% FVIII levels in serum), according to sponsor´s press releases. However, the appearance of acute thrombocytopenia, increased liver transaminases and elevation of IL-6 prevented the enrollment of more patients in this cohort. Since safer doses of this vector had low therapeutic possibilities, the trial was not continued, and full description of this case is not available in the scientific literature. Although only speculative, one possible explanation for this outcome is a relatively high HV contamination combined with high total to infective particle ratio during mass production of the vector, since the method available at that time was not optimal [25]. In addition, expression of the prokaryotic *LacZ* gene from HV-transduced hepatocytes could contribute to liver damage and immunogenicity. Subsequent pre-clinical developments, including improvements in the production methods, showed therapeutic benefit and moderate, dose-dependent toxicity in stringent models such as hemophilic dogs [67,82,121]. The failure to maintain high levels of FVIII in circulation was mainly attributed to the intrinsic immunogenicity of this protein. In fact, neonatal administration of the vectors achieved tolerance and improved the performance of re-administration in adults, at least in mice [122]. The use of liver-specific promoters also reduces the possibility of transgene expression in antigen-presenting cells [123]. However, no further clinical trials were performed, in part because of the development of efficient AAV vectors carrying shorter versions of the *F8* cDNA [124,125].

Gene therapy approaches for hemophilia B followed a similar pattern. In this case, the relatively small size of the mutated gene (*F9*, cDNA 1.5 Kb) allows the use of AAV vectors without transgene engineering, which has expedited its clinical translation [118]. Other circumstances favoring the success of gene therapy for hemophilia B, irrespective of the choice of vector, include the efficient secretion of the therapeutic protein from the liver and the lower frequency of alloantibody development in patients, compared with hemophilia A [126]. HC-AdVs expressing *F9* under the control of liver-specific promoters have shown excellent preclinical results in murine hemophilia B models [127]. Canine models show higher variability, and some cases of premature transgene expression shutoff have been reported for unknown reasons [128]. However, further work achieved sustained therapeutic levels of clotting FIX in this stringent model [129]. Importantly, studies in NHP confirmed the stability of transgene expression previously observed using other transgenes such as α-1 anti-trypsin (A1AT) and α-fetoprotein [21,58]. In order to enhance liver transduction while reducing systemic exposure to the vector, a HC-AdV encoding human FIX was injected in rhesus macaques through the hepatic artery with transient balloon occlusion of the inferior vena cava. The maximal dose reported (1×10^{12} vp/Kg) was needed to guarantee sustained therapeutic levels of the clotting factor for more than 2 years [130]. No serious adverse effects were observed, but further studies are needed to determine the maximal tolerated dose and therapeutic range of this approach. Of note,

clinical experience indicates that 6×10^{11} vg/Kg of an E1-E4-deleted AdV administered through the portal vein caused a severe inflammatory syndrome in one human subject [59].

Another example in which transgenes expressed from the liver and secreted into circulation can be therapeutic is A1AT deficiency (A1ATD). HC-AdVs encoding A1AT were among the first vectors of this class to be tested in animal models, including NHP [21,131]. In fact, A1AT has been used as a reporter gene in the early evaluation of HC-AdVs [132]. In all cases, efficient and long-lasting expression has been demonstrated. However, the therapeutic potential has not been evaluated in A1AT-deficient models. Since the liver is also affected in this disease because of the aggregation of the mutated protein, full recovery requires simultaneous transgene expression and inhibition/disruption of the endogenous gene. This challenge is now feasible owing to new gene editing tools, and HC-AdVs are a suitable vector platform, as will be discussed in Section 6.2.

Systemic administration HC-AdVs have shown therapeutic effect in different models of dyslipidemia, in which elevated and sustained levels of therapeutic proteins are needed in circulation. A pioneer study demonstrated the lifelong correction of cholesterol levels in Apo E-deficient mice upon a single intravenous administration of HC-AdVs, especially when they incorporate Apo E gene and regulatory sequences in the genomic context [133]. Vectors encoding Apo AI achieved elevation of high-density lipoproteins (HDL) and reduction of low density lipoproteins (LDL), as well as prevention of atherosclerotic lesions in Apo AI-deficient mice [63,134]. Reduction of cardiovascular risk was also demonstrated in Apo E and LDL receptor-deficient mice [135,136]. Apart from liver-directed gene therapy, direct vascular wall transduction is being investigated for reversion of atheromatous plaques. Sustained expression of endothelial cells has been demonstrated upon intra-arterial delivery of HC-AdVs. Using this approach, significant improvement has been observed in high fat diet-fed rabbits [137]. Co-expression of Apo AI and the ATP-binding cassette subfamily A, member 1 (ABCA1) is feasible using HC-AdVs, and this combination can improve the cholesterol efflux from endothelial cells [138]. Reduction of cholesterol and cardiovascular protection was also observed in LDL receptor (LDLR)-deficient mice treated with a vector encoding LDLR. Interestingly, a vector encoding the very low density lipoprotein (VLDL) receptor gene obtained a partial correction of cholesterol levels, probably because it can only restore uptake of Apo E, but not Apo B100-containing lipoproteins [139]. Later on, experiments carried out in rhesus macaques heterozygous for a LDLR mutation highlighted the potential limitations of this approach in the clinical setting, and suggested potential solutions [140]. First, dose-dependent toxicity associated with inflammatory responses was confirmed following intravenous injection of the vector. Taking into account that diseases such as LDLR deficiency require high levels of transgene expression to obtain a therapeutic effect (at least 50% normal values), the therapeutic index of intravenous administration is too narrow. This problem was circumvented by an optimized balloon occlusion method, which decreased the systemic exposure to the vector and reduced 5-fold the therapeutic threshold (1×10^{12} vp/Kg). The second serious concern was an elevation of transaminases (ALT) observed 2 months after treatment. Although the increase was mild and transient, it was followed by a reduction and virtually disappearance of the therapeutic effect (rebound of cholesterol levels to pre-treatment values). In principle, immune responses against the transgene were discarded because the vector expressed the rhesus monkey LDLR cDNA in haploinsufficient animals, and it was under the control of the liver-specific phosphoenol pyruvate carboxykinase (*PEPCK*) promoter. Although no T-cell responses could be detected against adenoviral proteins, this phenomenon is reminiscent of the situation observed in humans treated with AAV vectors [141]. It remains to be tested if the same management (short course of corticoid treatment) will be effective in the case of HC-AdVs, if needed.

Primary hyperoxaluria type 1 (PH1) is caused by defects in alanine:glyoxylate aminotransferase (AGT), resulting in systemic elevation of oxalate and accumulation of calcium oxalate precipitates in the kidney and other organs. This disease is considered a suitable target for liver-directed gene therapy, since there is clinical evidence that liver transplantation (combined with kidney transplantation in most cases) is therapeutic [142]. However, initial preclinical studies indicated that a high percentage

of hepatocytes should be transduced in order to obtain a therapeutic effect. In a mouse model of PH1, a HC-AdV expressing AGT under the control of the liver-specific PEPCK promoter showed a dose-dependent reduction of oxalate in serum [143]. Normal values were only obtained when at least 80% of hepatocytes expressed the transgene (at a dose of 5×10^{12} vp/Kg of vector), suggesting that PH1 is still a challenge for current gene therapy technologies.

An equivalent vector was employed for the treatment of carbamoyl phosphate synthetase 1 deficiency (CPS1D). HC-AdVs are especially indicated for the treatment of this urea cycle disorder, since the size of the *CPS1* cDNA (4.5 Kb) makes it difficult to design efficient AAV vectors. In this case a high dose (5×10^{12} vg/Kg) was also needed for full protection from hyperammonemia in a mouse model [144]. Apart from this, clinical implementation of this approach is further complicated by the need to transduce the immature and rapidly growing liver of newborns. Indirect preclinical evidences generated in a hemophilia A mouse model suggest that HC-AdVs could be efficiently re-administered after a first neonatal dose [122], but this possibility needs confirmation in other animals and in humans.

For diseases requiring high levels of transgene expression, optimization of delivery routes and expression cassettes is crucial, as demonstrated for Crigler-Najjar syndrome type I in the Gunn rat model. The therapeutic dose of a HC-AdV encoding Uridine diphospho-glucuronyl transferase 1A1 (*UGT1A1*) was reduced from 3×10^{12} vp/Kg to 5×10^{10} vp/Kg when an enhancer from the *ApoE* gene was located in the 3'UTR of the transgene, and the vector was delivered by hydrodynamic injection [52]. Clinically compatible methods for enhanced liver transduction are being developed [145].

In acute intermittent porphyria (AIP), mutations in one copy of the porphobilinogen deaminase gene (*PBGD*) cause a reduction in the expression of the enzyme, which is involved in the heme synthesis pathway. Patients suffer attacks of severe abdominal pain and neurovisceral disturbances, which can be life-threatening and provoke progressive irreversible neuropathy [146]. Intravenous administration of a HC-AdV encoding human *PBGD* under the control of a potent liver-specific promoter (albumin enhancer linked to α1 anti-trypsin promoter) achieved correction of neurotoxic intermediate metabolites in a mouse AIP model [147]. Direct intra-hepatic injection obtained the same effect with a 7.5-fold reduction in the vector dose (2×10^{11} vp/Kg). However, experiments performed in macaques (*Macaca fascicularis*) showed that sustained expression of *PBGD* and persistence of vector genomes in the liver required intense immunosuppression [83]. It is not clear if this discrepancy versus previous studies using other HC-AdVs in baboons [22,58] is due to the transgene or the different NHP used.

For lysosomal storage disorders (LSD), transduced hepatocytes can become a stable source of therapeutic enzymes secreted into circulation and internalized by target cells through the mannose-6-phosphate receptor [148]. This is relevant in cases such as Pompe disease (defect of acid α-glucosidase, *GAA*), in which accumulation of glycogen in skeletal muscles, hearth and diaphragm plays a major role in the clinical manifestations. In fact, a HC-AdV expressing GAA under the control of liver-specific sequences (*PEPCK* promoter plus *ApoE* enhancer) achieved long-term correction of glycogen content in skeletal muscles [149]. Importantly, GAA levels in circulation and enzyme uptake in muscles were recapitulated in baboons using the balloon catheter occlusion technique (1×10^{12} vg/Kg) [150]. However, it is possible that simultaneous gene transfer to the brain is required to address all clinical manifestations of Pompe diseases, since there is evidence for accumulation of glycogen in the central nervous system (CNS), and the brain blood barrier (BBB) limits the access of GAA from circulation [151].

6.1.2. Gene Supplementation for Neurological Diseases

The attributes of HC-AdVs, namely the stability of transgene expression and the reduced immunogenicity are particularly important when they are applied in the CNS. In addition, high cloning capacity is often required to allocate large transgenes (such as ion channels), combinations of genes (such as biosynthetic pathways for dopamine production in Parkinson's disease) or complex regulatory regions to restrict expression to specific cell populations. Parenchymal administration of HC-AdV in rodents (up to 2×10^9 vp) was well-tolerated and avoided the generation of NAbs [152–155].

After intrathecal administration in rodents and NHP, none or negligible local immune reaction or systemic toxicity have been observed [101,152,156]. Several studies have carried out a complete neuropathological and cell immune infiltration analysis after vector intracranial administration, showing no long-term major changes apart from those associated to the needle tract [153,155]. No signs of inflammation or toxicity were found in peripheral organs such us liver or kidneys (evaluating both histology and enzymatic activity). Haematological and serum biochemical analysis were normal, in contrast with the systemic administration of vectors. No abnormalities were observed in behavioral testing, and animal growth curves were not affected after treatment [153,154]. However, changes in the transcriptome of human midbrain neuroprogenitor cells (hmNPCs) have been observed after infection with HC-AdVs [157]. In general, mild enrichment score was obtained for four main functional gene categories: (1) Cell cycle or DNA damage response, many of them implied in anti-apoptotic functions; (2) trafficking and neuronal remodelling; (3) immune-response; and (4) biochemistry and metabolism. A stronger enrichment was observed in genes implicated in nervous system development 2 h after infection, and in cellular assembly and organization 5 days post-infection. At the same time, a widespread downregulation of genes involved in neuronal development and cell assembly was observed after HC-AdV infection in concordance with previous reports [158]. It is interesting to note that HC-AdV induced slightly minor transcriptome alterations than CAV-2 or lentiviral vectors (495 transcripts modulated *vs* 592 and 728, respectively) and a weaker immune response, although it could be due to a lower transduction rate [157]. It is worthy to mention that the safety of HC-AdVs can be improved by implementing drug-inducible methods to control expression of transgenes, such as the Tet-on transactivation system. Importantly, the FDA has already approved an administration regimen of doxycycline for this purpose [154]. Controlling the amount and duration of transgene expression can be especially important in the brain, where chronic alteration of proteostasis may lead to neurodegeneration. Gene transfer into the CNS can offer advantages too, since intracerebral administration of HC-AdVs confers partial protection from pre-existing systemic anti-Ad immunity [62,64,159–164], reducing one of the major drawbacks of AdV vectors in humans. The route of administration plays a crucial role in the safety and efficacy of these vectors in the brain. While a careful intraparenchymal administration elicits negligible systemic cellular or humoral responses, other routes such as intraventricular, meningeal or choroid plexus administration can elicit systemic immune responses [165–169].

As previously mentioned, vectors derived from CAV-2 are especially suited for neuronal transduction and axonal transport, owing to their peculiar docking and intracellular trafficking system [114,170–172]. Since a recent review on this subject is available, we will not expand it here [116]. A CAV-2-derived HC-AdV vector encoding the lysosomal enzyme β-glucuronidase was able to improve the neurological status in a mouse model of mucopolysaccharidosis type VII (MPSVII) [115], in which the systemically administered enzyme cannot cross the BBB. Although some discrepancies exist about the percentage of cell populations infected by human HC-AdVs, it is known that they can infect not only astrocytes but also neurons, microglia, oligodendrocytes, and ependymal cells [64,155]. CAR expression is thought to be mainly restricted to neurons in adult mice, *Microcebus murinus* brains and humans [171,173–175], although it has been also detected in astrocytes and astrocytic precursors, microglia, choroid plexus, retinal cells [176–179], and in germinal zones of rodent brains [172,174,178,180,181]. In neurons, CAR can be detected in axons, dendrites, and somas, and in the presynaptic fraction of synaptosome-enriched extracts obtained from adult mouse, *Micronebus murinus*, and human brains [174]. However, it should be taken into account that some studies report little correlation between AdV receptor expression (CAR, integrins or MHCI) and the HC-AdV transduction efficiency or their biological function [182]. Apart from the natural tropism of vectors, re-targeting approaches have led to an increment in transduction of specific cell populations such as the sensory neurons [101,183]. These capsid-modified HC-AdVs showed specificity and efficacy in a moue model of neuropathic pain. Extrapolation of findings obtained in cell culture and animal models to the clinical reality should be done with extreme caution, especially in structures with such

complexity and evolutionary divergence as those forming the CNS. So far, HC-AdVs have not been administered to human patients in the brain, but clinical trials using OAVs predict good tolerance [184].

Apart from therapeutic applications, HC-AdVs are an excellent tool for neurosciences and disease modelling in the CNS. They provide an alternative to traditional ablation/injury methods or chemical labelling of neuronal populations. One example is the TRIO technique that combines CAV-2, AAV, and rabies virus vectors to map input–output connections allowing to delineate the brain information trafficking [185]. A moderate retrograde axonal transport of HAdV5 vectors has been documented, opening the possibility of being used in this type of techniques [113,155,186]. Even if recently implanted, opto- and chemogenetic techniques are considered already essential since they elucidate the function of neurons and the circuits in which they are involved. Both technologies often require the use of Cre knock-in mice [187], but the combination of these techniques with Cre-expressing viral vectors could increase their resolution to the cellular level. HC-AdV vectors have been used for modelling inflammation related to neurodegenerative diseases, by overexpression of a mutated form of leucine-rich repeat kinase 2 (LRRK2) in mice [188] and NHPs [175]; and for developing a chronic in vitro model of Huntington´s disease in primary neuronal cultures [189].

Finally, we should be aware that astrocytes could also be targets for gene therapy in neurological diseases, as they interact with other cell types including neurons, microglia, brain microvascular endothelial cells, and ependymal cells throughout the brain, contributing to the disease and recovery processes [190].

6.1.3. Muscle-Directed Gene Supplementation

Although adenoviral transduction in adult skeletal muscle is not as efficient as in liver, HC-AdVs offer the opportunity to deliver the full cDNAs of genes involved in the most frequent muscular dystrophies, which are often too large to be packaged in other viral vectors. This is the case of *dystrophin* (14 Kb), the gene responsible for the devastating Duchenne Muscular Dystrophy (DMD) [191]. A HC-AdV encoding dystrophin under the control of a strong ubiquitous promoter (CAG) achieved restoration of dystrophin expression [37]. Improvement of motor performance and survival have been observed in mouse models of the disease when the vector is injected in different muscle groups [192,193]. Interestingly, efficient transduction in the diaphragm and subsequent amelioration of respiratory function could be achieved by intraperitoneal injection of the vector [194]. Transduction of muscle-related cells, including myoblasts, can be increased by chimeric fibers harboring the HAdV50 shaft and knob [195]. Fiber knob from HAdV3 (5/3 chimera) also increases infection of muscles and allows sustained expression of dystrophin after local administration in mice [196].

6.1.4. Ex-Vivo Gene Supplementation

For diseases in which therapeutic effects can be obtained by secretion of a therapeutic gene into circulation at moderate levels, the TARGT approach (transduced autologous restorative gene therapy) has been proposed. Patient's dermal fibroblasts are isolated, transduced in vitro with HC-AdVs and implanted subcutaneously. This strategy has been applied for the expression of erythropoietin (Epo) in end-stage renal failure patients. A phase I-II clinical trial demonstrated the feasibility and safety of this treatment. Epo was detected in circulation, and hemoglobin levels were stabilized for at least 5 months after a single cell implantation [197]. In addition, TARGT has been described at the preclinical level for expression of IFN-α [198] and the anti-Her2 monoclonal antibody trastuzumab [199].

6.2. Genome Integration and Gene Editing

Episomal maintenance of vector genomes avoids the risk of insertional mutagenesis, but at the same time it precludes the use of standard HC-AdVs when the target cell has an active turnover. Nevertheless, far from being outside the scope of these vectors, HC-AdVs are suitable platforms for stable modification of this type of cells. One possibility to maintain transgene expression is to synchronize vector and host genome replication, without the need for integration. As a proof of

concept, the Epstein-Barr virus (EBV) nuclear antigen 1 (EBNA-1) was expressed from a HC-AdV, and sequences acting as origins of replication were incorporated (family of repeats from EBV and a 19 Kb fragment from human chromosome 10). The Cre-loxP system was used to circularize the vector genome in transduced cells. The resulting circular double-stranded DNA molecule was replicated in the S phase of the cell cycle and segregated in daughter cells, maintaining transgene expression for several passages [200].

However, most efforts are recently aimed at gene editing or controlled chromosomal integration. HC-AdVs offer safe and efficient vector/host genome interactions owing to the efficacy of gene delivery into the nucleus, the extended cloning capacity, the genome stability, and the blunted cellular immune responses against transduced cells. Random integration can be obtained using *piggyBack* or *Sleeping beauty* (SB) transposon systems [117]. To this end, the expression cassette flanked by *cis*-acting sequences and the transposase are usually contained in separate vectors. In the case of SB, efficient integration requires circularization of DNA. Therefore, a site-specific recombinase is usually expressed together with the transposase. Random integration and the need of co-delivery are compatible with ex vivo approaches, in which high rate of co-infection and further characterization/selection of cells are feasible [201]. For in vivo approaches, integration into defined genome sequences is preferred. To this end, HC-AdV can accommodate site-specific nucleases such as zinc finger nucleases (ZFN), transcription activator-like effector nucleases (TALEN), and clustered regularly interspaced short palindromic repeats-associated protein 9 (CRISPR/Cas9) [202,203]. Generation of double strand breaks in the host genome favors the integration of the therapeutic DNA sequences following the homologous repair (HR) pathways, especially when the donor DNA is present in the same vector [203]. The deleterious effects of high nuclease expression in packaging cells can be mitigated by the incorporation of miRNA target sites into their 3'UTRs [202]. Importantly, DNA templates with large homology arms can be incorporated in HC-AdV, which increases the efficacy and specificity of integration. However, the non-homologous end joining DNA repair process is usually more efficient than the HR, and this can lead to unwanted insertion and deletions, either in target or off-target regions [203]. Therefore, alternative versions of CRISPR/Cas9 with nickase instead of nuclease activity are being developed [204]. Other approaches use the DNA binding domains of ZFN, TALEN, and CRISPR/Cas9 systems fused with other polypeptides to obtain site-specific transcriptional activators or repressors [205,206]. However, they often require persistent expression of the transcriptional modifier to maintain the effect. In contrast, fusion with base editors can obtain permanent correction of pathogenic mutations [207]. So far, in vivo application has relied on pairs of AAVs or non-viral vectors to deliver the 5.2 Kb-long base editor cDNA [207,208], but HC-AdVs are probably on the way.

One potential drawback for in vivo application of all these strategies is the immunogenicity of the transgene products, especially those derived from prokaryotes such as TALEN and CRISPR/Cas9 [209]. Hopefully, when HC-AdVs are used to deliver these genes into rapidly dividing cells, genome modification will occur rapidly and the expression of the foreign protein will be lost before cytotoxic immune responses can eliminate the daughter cells, as recently described for vectors expressing TALENs and CRISPR/Cas9 [210,211]. In any case, avoidance of nucleases and derivatives would eliminate safety concerns regarding genome integrity and immune reactions. Integration of genetic material and substitution of genomic regions containing mutations can be carried out by HR in the absence of nucleases. Since the frequency is low, it requires in vitro enrichment/selection. HC-AdVs can play a major role in these approaches, because the terminal protein (TP) covalently attached to both genome ends reduces the frequency of random integrations [212]. Using a vector carrying fragments of the cystic fibrosis transmembrane conductance (CFTR) locus, infection of 2×10^6 human induced pluripotent stem cells (iPSC) at MOI 350 obtained up to 144 clones harboring integration of the template DNA after positive selection [213]. In 64% of them the integration occurred in the target site, 32% had random integrations, and less than 5% presented aberrant integrations, in which one of the homology arms (interestingly, the right arm) did not recombine with the predicted genomic sequence. This efficacy is compatible with clinical implementation of ex-vivo gene correction,

especially if strategies for negative selection of unintended events are implemented. In this thorough study, a direct correlation between the length of the homology arms and the frequency of site-specific integrations has been reported. Starting from the highest frequency when each homology arm was 11.9 Kb in length, they observed a 30% reduction when one of the arms was 9.5 Kb, and a further 50% reduction with a 5.3 Kb-long arm. Nevertheless, selection of corrected clones was feasible even when the length of the smaller homology arm was 1.3 Kb. These requirements could be influenced by the characteristics of the target region and the genetic defects to be corrected. In a previous study performed in mouse embryonic stem cells (ESC), the minimum homology size to obtain meaningful HR frequencies was 6 Kb, probably because the cells harbored a relatively large insertion (1.6 Kb) rather than point mutations [214]. Based on HR, a promising strategy called GeneRide allows the sustained expression of transgenes under the control of strong endogenous promoters such as the albumin promoter. To this end, the template DNA for integration consists of the sequence preceding the stop codon of the endogenous gene, followed by an autoproteolytic 2A sequence and finally the transgene [215]. Proof of concept for the therapeutic potential of GeneRide has been obtained using AAV vectors, but its efficacy could be enhanced using larger homology regions delivered by HC-AdVs.

Examples with particular clinical relevance for gene integration/editing approaches are the respiratory epithelium and the bone marrow (BM). For sustained amelioration of respiratory manifestations in cystic fibrosis (CF), transduction of basal cells with stem cell properties in the airway epithelium is mandatory. The optimization of delivery routes (intratracheal aerosolization under bronchoscopic guidance), coupled with drugs to open intercellular tight junctions (L-α-lysophosphatidylcholine) has improved the access of HC-AdVs to these cells [216,217]. Once this important barrier has been partially overcome, efforts are now focused on the maintenance of therapeutic gene expression. Al least in vitro, a HC-AdV carrying a TALEN and the CFTR cDNA with 4 Kb homology arms achieved a 5% integration efficiency in the AAVS1 locus in patient-derived cells without positive selection [210]. It is unclear at this moment if this approach could be therapeutic in vivo, but the aforementioned ex-vivo approaches in iPSCs look very promising [213]. Biallelic correction was demonstrated using improved transgenes for selection, but it required sequential infection with different HC-AdV targeting each CFTR allele, and a third step for SB-mediated elimination of the exogenous genes [218].

In the case of BM, the development of HC-AdVs based on HAdV35 has increased the transduction efficacy in HSCs and the feasibility of gene editing approaches for a wide variety of diseases, as described in detail in a recent review [219]. Of note, expression of nucleases in these cells could reduce their repopulation potential. This could be avoided by expressing inhibitory peptides, although it requires an additional transduction step [220]. For the treatment of β-globinopathies such as β-thalasemia and sickle cell anemia, reactivation of the fetal γ-globin gene expression can be therapeutic. To this end, disruption of the recognition sequence for a repressor in the γ-globin gene can be obtained using a chimeric 5/35++ HC-AdV encoding a CRISPR/Cas9, without the need of HR. An increase in γ-globin expression was observed using a standard ex-vivo approach [221]. More importantly, similar results were obtained in this study when a modified vector was administrated intravenously, providing the proof of concept that gene editing is feasible in vivo. Instead of pre-conditioning of the host, HSCs were mobilized by G-CSF/AMD3100 treatment. Selective advantage of gene-modified cells was obtained by incorporating the $mgmt^{P140K}$ transgene, which confers resistance and proliferation stimulus in response to O^6-BG/bis-cloroethyl-nitrosourea (BCNU) treatment. Alternatively, the γ-globin gene has been integrated into the AAVS1 locus by co-administration of a pair of HC-AdVs encoding a CRISPR/Cas9 and the DNA template [222].

The BM can be used as a secretory organ for therapeutic proteins such as coagulation FVIII. In this case, one vector carried the *F8* cDNA together with the $mgmt^{P140K}$ selection gene, and another one expressed the SBx100 transposase to promote integration into the host genome. When these vectors were administered in vivo, the levels of FVIII in circulation reached 5% normal values in a mouse model [223]. Although this level is still lower than that obtained after liver-directed gene therapy [119], permanent transduction of HSCs opens the possibility of local production of therapeutic proteins in

the CNS through migration of glial precursors. This would avoid the need to cross the BBB in LSD and other diseases [224].

In some genetic muscular dystrophies such as DMD, early intervention and stable expression of therapeutic genes in myoblasts is important. Some strategies aimed at dystrophin cDNA integration consist of hybrid AdV-AAV vectors, in which integration occurs at the AAVS1 locus in the presence of the AAV Rep protein, as demonstrated in vitro [225]. An alternative for in vivo gene editing in DMD would be the re-setting of reading frames, the alteration of splicing acceptors or the removal of mutated exons by expression of site-specific nucleases. Proof of concept about the restoration of dystrophin expression has been generated in muscle cell populations in culture using E1-E2-deleted AdVs encoding a combination of CRISPR/Cas9 and TALENs [226]. The use of HC-AdV could improve the in vivo performance of this strategy.

6.3. Cancer

After many disappointing trials, it is clear that current gene therapy technology does not allow transduction of all the cells in a tumor. However, many immunotherapy approaches can benefit from the properties of HC-AdVs, especially when the expression of transgenes should be placed under the control of drug-inducible systems to avoid toxicity, and when a combination of transgenes is needed. The HC-Ad-TK/TetOn-Flt3L vector encodes the suicide gene thymidine kinase (TK) and the dendritic cell chemoattractant FMS-like tyrosine kinase 3 ligand (Flt3L) under the control of a tet-on inducible system [154,164,227]. This vector has demonstrated promising results in rodent models of glioblastoma. A liver-specific, mifepristone-induced expression system [228] has been used to control expression of interleukin-12 for the treatment of colorectal cancer hepatic metastases, showing tumor eradication in synergy with chemotherapy [229]. This vector was safer than an OAV expressing the same transgene [230]. To further reduce systemic exposure to this toxic cytokine, a fully humanized mifepristone-inducible system controlled by the ubiquitous elongation factor 1α (*EF1*α) promoter was developed [231]. The vector carrying this expression cassette can be administered intratumorally, maintaining its antitumor effect in pancreatic cancer models. HC-AdVs can also be employed to express tumor antigens in dendritic cells (DC). The absence of viral genes in the vector preserves the T-cell stimulating capacity of transduced DCs, obtaining better antitumor effects than FGAdVs encoding the same antigen [103].

6.4. Vaccination and Therapy against Infectious Diseases

The strong innate immune responses against AdV particles can be exploited for the design of genetic vaccines. As introduced in the previous sections, some evidences indicate that HC-AdVs outperform FGAdVs when they express the same antigen. This is in part due to the cell cycle arrest caused by FGAdVs in DCs [103,232]. In addition, de novo expression of adenoviral genes, which are usually immunodominant, is detrimental for the generation of multi-specific T-cell responses against the target antigen. This concept was demonstrated when both types of vectors were used for the expression of hepatitis B virus small surface antigen (HBsAg) [233], or the merozoite surface protein 1 (MSP-1) from *Plasmodium falciparum* for vaccination against malaria [234]. Similar results were observed when vectors encoded a model antigen (β-galactosidase) [235]. In this case, the stimulation of both humoral and cellular immune responses was more efficient with the HC-AdV. Interestingly, ex vivo transduction of DCs instead of intraperitoneal administration achieved similar results, while anti-adenoviral responses were reduced. For the clinical translation of these approaches, it should be taken into account the high prevalence of immunity against certain HAdV types in the adult population, including the prototypic HAdV5. This not only compromises the efficacy of transgenic antigen expression, but also boosts immune responses against the adenoviral capsid proteins. In a clinical trial of a HAdV5-based vaccine against HIV, higher risk of infection was observed in a subgroup of vaccinated patients pre-exposed to HAdV5 [236]. Although the mechanism is still controversial [237], one hypothesis is that mucosal homing of anti-HAdV5 immune cells made subjects more susceptible to HIV infection. To overcome these problems, HVs derived from

other human and animal AdVs can be employed to produce the HC-AdVs [103]. The experience gained with FGAdVs and replication-competent AdVs, including clinical trials, indicate that HAdV4, HAdV35, HAdV26, and chimpanzee AdV3, Ad7, AdV63, AdV68, among others, are promising candidates as vector platforms [238–243]. The current Covid-19 pandemic has boosted the interest on genetic vaccines, and some human and simian AdV vectors encoding the SARS-Cov-2 spike protein are advanced candidates (https://cen.acs.org/pharmaceuticals/vaccines/Adenoviral-vectors-new-COVID-19/98/i19). These approaches are based on previous experimental vaccines against MERS-CoV [244,245]. Other anti-viral strategies using HC-AdVs include the controlled expression of cytokines such as IFNα [246] and IL-12 [247] against HCV and HBV, respectively. However, evaluation in stringent animal models for both diseases revealed limited therapeutic effect. Finally, a HC-AdV encoding a CRISPR/Cas9 system with multiple guides against the hepatitis B genome achieved reduction of HBsAg expression and viral copies in liver-derived cell lines [248]. Further work should determine the efficacy of this approach in animal models of HBV infection.

7. Conclusions

During the past two decades, a vast number of preclinical studies have demonstrated the ability of HC-AdVs to transduce relevant target cells in vivo, especially hepatocytes, neurons and endothelial cells. Stable episomal maintenance of genomes in these cells, resulting in sustained expression of transgenes, has been demonstrated not only in rodents but also in larger animal models, including NHPs. Despite clear evidence of therapeutic effect in a large number of disease models, clinical experience with these vectors is virtually absent. This is in part because translational efforts have been focused in other vector platforms, such as AAV. When therapeutic cassettes can fit into the 4.5 Kb size constraint of AAVs, these vectors have shown similar pre-clinical results than HC-AdVs, but they elicit less inflammatory responses and are easier to produce under GMP conditions. However, the field of HC-AdVs is making progress in delivery routes, methods to prevent and manage side effects, and protocols for large-scale production. We believe these vectors will play an important role in the gene therapy arsenal in the near future. Not only as an alternative to AAVs, but more importantly, covering unmet needs in the fields of gene editing and the transfer of large sequences.

Funding: This research was funded by projects RTI2018-097730-B-I00/MCI/AEI/FEDER, UE and AC17/00029 (ISCIII)/FEDER.

Conflicts of Interest: The authors declare no conflict of interest.

Abbreviations

A1AT	Alpha 1 anti-trypsin
A1ATD	Alpha 1 anti-trypsin deficiency
AAV	Adeno-associated virus
AAVS1	Adeno-associated virus integration site 1
ABCA1	ATP-binding cassette subfamily A member 1
AdV	Adenovirus
AGT	Alanine:glyoxylate aminotransferase
AIP	Acute intermittent porphyria
ALT	Alanina aminotrasferasa
BBB	Blood brain barrier
BCNU	Bis-cloroethyl-nitrosourea
BM	Bone marrow
CAR	Coxsackie and adenovirus receptor
CAV-2	Canine adenoviral vector type 2
CF	Cystic fibrosis
CFTR	Cystic fibrosis transmembrane conductance regulator
ChAdV	Chimpanzee adenovirus
CNS	Central nervous system

CPS1D	Carbamoyl phosphate synthetase 1 deficiency
CR1	complement receptor 1
CRISPR/Cas	Clustered regularly interspaced short palindromic repeats-associated protein 9
DC	Dendritic cells
DMD	Duchenne muscular dystrophy
EBNA-1	Epstein-Barr nuclear antigen 1
EBV	Epstein-Barr virus
EF1α	Elongation factor 1 alpha
Epo	Erythropoietin
ESC	Embryonic stem cells
FGAdV	First-generation adenoviral vector
FLP	Flippase
Flt3L	FMS-like tyrosine kinase 2 ligand
FRT	Flippase recognition target
GAA	Acid alpha-glucosidase
GMP	Good manufacturing practices
HAdV	Human adenovirus
HBsAg	Hepatitis B virus small surface antigen
HBV	Hepatitis B virus
HC-AdV	High-Capacity adenoviral vector
HCV	Hepatitis C virus
HD-AdV	Helper-Dependent adenoviral vector
HDL	High-density lipoprotein
hmNPC	Human midbrain neuroprogenitor cells
HR	Homologous recombination
HSC	Hematopoietic stem cells
HSPG	Heparan sulphate proteoglycans
HSV	Herpes simplex virus
HV	Helper virus
HVR5	Hypervariable region V
IFN	Interferon
IgM	Immunoglobulin M
IL-6	Interleukin 6
iPSC	Induced pluripotent stem cells
ITR	Inverted terminal repeats
iu	Infection units
LDL	Low density lipoprotein
LDLR	Low density lipoprotein receptor
LRRK2	Leucine-rich repeat kinase 2
LSD	Lysosomal storage disorders
MERS-CoV	Middle East respiratory syndrome coronavirus
MHCI	Major histocompatibility complex class I
MOI	Multiplicity of infeciton
MPSVII	Mucopolysaccharidosis type VII
MSP-1	Merozoite surface protein 1
NAb	Neutralizing antibody
NHP	Non-human primates
OAV	Oncolytic adenovirus
PBGD	Porphobilinogen deaminase
PEI	Polyethylene glycol
PEPCK	Phosphoenolpyruvate carboxykinase
pfu	Plaque forming units
PH1	Primary hyperoxaluria type 1
PRR	Pattern recognition receptor
pTP	Pre-terminal protein

SAdV	Simian adenovirus
SARS-CoV-2	Severe acute respiratory syndrome coronavirus 2
SB	Sleeping beauty
TALEN	Transcription activator-like effector nucleases
TARGT	Transduced autologous restorative gene therapy
TLR	Toll-like receptor
TNFα	Tumor necrosis factor alpha
TP	Terminal protein
TRIO	Tracing the relationship of inputs and outputs
UGT1A1	Uridine diphospho-glucuronyl transferase 1A1
vg	viral genomes
VLDL	Very low density lipoprotein
vp	viral particles
ZFN	Zinc Finger Nucleases

References

1. Smith, J.G.; Wiethoff, C.M.; Stewart, P.L.; Nemerow, G.R. Adenovirus. *Curr. Top. Microbiol. Immunol.* **2010**, *343*, 195–224.
2. Sarantis, H.; Johnson, G.; Brown, M.; Petric, M.; Tellier, R. Comprehensive Detection and Serotyping of Human Adenoviruses by PCR and Sequencing. *J. Clin. Microbiol.* **2004**, *42*, 3963–3969. [CrossRef]
3. Davison, A.J.; Benkő, M.; Harrach, B. Genetic content and evolution of adenoviruses. *J. Gen. Virol.* **2003**, *84*, 2895–2908. [CrossRef]
4. San Martín, C. Latest Insights on Adenovirus Structure and Assembly. *Viruses* **2012**, *4*, 847–877. [CrossRef]
5. Baker, A.T.; Greenshields-Watson, A.; Coughlan, L.; Davies, J.A.; Uusi-Kerttula, H.; Cole, D.K.; Rizkallah, P.J.; Parker, A.L. Diversity within the adenovirus fiber knob hypervariable loops influences primary receptor interactions. *Nat. Commun.* **2019**, *10*, 741. [CrossRef]
6. Loustalot, F.; Kremer, E.J.; Salinas, S. The Intracellular Domain of the Coxsackievirus and Adenovirus Receptor Differentially Influences Adenovirus Entry. *J. Virol.* **2015**, *89*, 9417–9426. [CrossRef]
7. Murakami, S.; Sakurai, F.; Kawabata, K.; Okada, N.; Fujita, T.; Yamamoto, A.; Hayakawa, T.; Mizuguchi, H. Interaction of penton base Arg-Gly-Asp motifs with integrins is crucial for adenovirus serotype 35 vector transduction in human hematopoietic cells. *Gene Ther.* **2007**, *14*, 1525–1533. [CrossRef]
8. Bilkova, E.; Forstova, J.; Abrahamyan, L. Coat as a Dagger: The Use of Capsid Proteins to Perforate Membranes during Non-Enveloped DNA Viruses Trafficking. *Viruses* **2014**, *6*, 2899–2937. [CrossRef]
9. Burckhardt, C.J.; Suomalainen, M.; Schoenenberger, P.; Boucke, K.; Hemmi, S.; Greber, U.F. Drifting Motions of the Adenovirus Receptor CAR and Immobile Integrins Initiate Virus Uncoating and Membrane Lytic Protein Exposure. *Cell Host Microbe* **2011**, *10*, 105–117. [CrossRef]
10. Chailertvanitkul, V.A.; Pouton, C.W. Adenovirus: A blueprint for non-viral gene delivery. *Curr. Opin. Biotechnol.* **2010**, *21*, 627–632. [CrossRef]
11. Moyer, C.L.; Wiethoff, C.M.; Maier, O.; Smith, J.G.; Nemerow, G.R. Functional Genetic and Biophysical Analyses of Membrane Disruption by Human Adenovirus. *J. Virol.* **2011**, *85*, 2631–2641. [CrossRef] [PubMed]
12. Strunze, S.; Engelke, M.F.; Wang, I.; Puntener, D.; Boucke, K.; Schleich, S.; Way, M.; Schoenenberger, P.; Burckhardt, C.J.; Greber, U.F. Kinesin-1-Mediated Capsid Disassembly and Disruption of the Nuclear Pore Complex Promote Virus Infection. *Cell Host Microbe* **2011**, *10*, 210–223. [CrossRef] [PubMed]
13. Khanal, S.; Ghimire, P.; Dhamoon, A. The Repertoire of Adenovirus in Human Disease: The Innocuous to the Deadly. *Biomedicines* **2018**, *6*, 30. [CrossRef] [PubMed]
14. Ephros, M.; Friedman, B.; Elhasid, R.; Kra-Oz, Z.; Shaked-Mishan, P.; Sattinger, J.; Kassis, I. Incidence and Clinical Manifestations of Adenoviral Infection among Children Undergoing Allogeneic Stem Cell Transplantation. *IMAJ* **2009**, *11*, 744–748. [PubMed]
15. Lion, T. Adenovirus persistence, reactivation, and clinical management. *FEBS Lett.* **2019**, *593*, 3571–3582. [CrossRef] [PubMed]
16. Guo, J.; Mondal, M.; Zhou, D. Development of novel vaccine vectors: Chimpanzee adenoviral vectors. *Hum. Vaccin. Immunother.* **2018**, *14*, 1679–1685. [CrossRef]

17. Baker, A.; Aguirre-Hernández, C.; Halldén, G.; Parker, A. Designer Oncolytic Adenovirus: Coming of Age. *Cancers (Basel)* **2018**, *10*, 201. [CrossRef]
18. Crystal, R.G. Adenovirus: The First Effective in Vivo Gene Delivery Vector. *Hum. Gene Ther.* **2014**, *25*, 3–11. [CrossRef]
19. Yang, Y.; Ertl, H.C.J.; Wilson, J.M. MHC class I-cestricted cytotoxic T lymphocytes to viral antigens destroy hepatocytes in mice infected with E1-deleted recombinant adenoviruses. *Immunity* **1994**, *1*, 433–442. [CrossRef]
20. Ewer, K.; Sebastian, S.; Spencer, A.J.; Gilbert, S.; Hill, A.V.S.; Lambe, T. Chimpanzee adenoviral vectors as vaccines for outbreak pathogens. *Hum. Vaccin. Immunother.* **2017**, *13*, 3020–3032. [CrossRef]
21. Morral, N.; O'Neal, W.; Rice, K.; Leland, M.; Kaplan, J.; Piedra, P.A.; Zhou, H.; Parks, R.J.; Velji, R.; Aguilar-Cordova, E.; et al. Administration of helper-dependent adenoviral vectors and sequential delivery of different vector serotype for long-term liver-directed gene transfer in baboons. *Proc. Natl. Acad. Sci. USA* **1999**, *96*, 12816–12821. [CrossRef] [PubMed]
22. Brunetti-Pierri, N.; Ng, T.; Iannitti, D.; Cioffi, W.; Stapleton, G.; Law, M.; Breinholt, J.; Palmer, D.; Grove, N.; Rice, K.; et al. Transgene Expression up to 7 Years in Nonhuman Primates Following Hepatic Transduction with Helper-Dependent Adenoviral Vectors. *Hum. Gene Ther.* **2013**, *24*, 761–765. [CrossRef] [PubMed]
23. Sandig, V.; Youil, R.; Bett, A.J.; Franlin, L.L.; Oshima, M.; Maione, D.; Wang, F.; Metzker, M.L.; Savino, R.; Caskey, C.T. Optimization of the helper-dependent adenovirus system for production and potency in vivo. *Proc. Natl. Acad. Sci. USA* **2000**, *97*, 1002–1007. [CrossRef] [PubMed]
24. Parks, R.J.; Graham, F.L. A helper-dependent system for adenovirus vector production helps define a lower limit for efficient DNA packaging. *J. Virol.* **1997**, *71*, 3293–3298. [CrossRef]
25. Kochanek, S.; Clemens, P.R.; Mitani, K.; Chen, H.H.; Chan, S.; Caskey, C.T. A new adenoviral vector: Replacement of all viral coding sequences with 28 kb of DNA independently expressing both full-length dystrophin and beta-galactosidase. *Proc. Natl. Acad. Sci. USA* **1996**, *93*, 5731–5736. [CrossRef]
26. Parks, R.J.; Chen, L.; Anton, M.; Sankar, U.; Rudnicki, M.A.; Graham, F.L. A helper-dependent adenovirus vector system: Removal of helper virus by Cre-mediated excision of the viral packaging signal. *Proc. Natl. Acad. Sci. USA* **1996**, *93*, 13565–13570. [CrossRef]
27. Umaña, P.; Gerdes, C.A.; Stone, D.; Davis, J.R.E.; Ward, D.; Castro, M.G.; Lowenstein, P.R. Efficient FLPe recombinase enables scalable production of helper-dependent adenoviral vectors with negligible helper-virus contamination. *Nat. Biotechnol.* **2001**, *19*, 582–585. [CrossRef]
28. Zhou, H.S.; Zhao, T.; Rao, X.M.; Beaudet, A.L. Production of helper-dependent adenovirus vector relies on helper virus structure and complementing. *J. Gene Med.* **2002**, *4*, 498–509. [CrossRef]
29. Ng, P.; Evelegh, C.; Cummings, D.; Graham, F.L. Cre levels limit packaging signal excision efficiency in the Cre/loxP helper-dependent adenoviral vector system. *J. Virol.* **2002**, *76*, 4181–4189. [CrossRef]
30. Gonzalez-Aparicio, M.; Mauleon, I.; Alzuguren, P.; Bunuales, M.; Gonzalez-Aseguinolaza, G.; San Martín, C.; Prieto, J.; Hernandez-Alcoceba, R. Self-inactivating helper virus for the production of high-capacity adenoviral vectors. *Gene Ther.* **2011**, *18*, 1025–1033. [CrossRef]
31. Verrou, C.; Zhang, Y.; Zürn, C.; Schamel, W.W.A.; Reth, M. Comparison of the Tamoxifen Regulated Chimeric Cre Recombinases MerCreMer and CreMer. *Biol. Chem.* **1999**, *380*, 1435–1438. [CrossRef] [PubMed]
32. Palmer, D.; Ng, P. Improved system for helper-dependent adenoviral vector production. *Mol. Ther.* **2003**, *8*, 846–852. [CrossRef]
33. Sargent, K.; Ng, P.; Evelegh, C.; Graham, F.; Parks, R. Development of a size-restricted pIX-deleted helper virus for amplification of helper-dependent adenovirus vectors. *Gene Ther.* **2004**, *11*, 504–511. [CrossRef]
34. Alba, R.; Hearing, P.; Bosch, A.; Chillon, M. Differential amplification of adenovirus vectors by flanking the packaging signal with attB/attP-ΦC31 sequences: Implications for helper-dependent adenovirus production. *Virology* **2007**, *367*, 51–58. [CrossRef] [PubMed]
35. Cheshenko, N.; Krougliak, N.; Eisensmith, R.C.; Krougliak, V.A. A novel system for the production of fully deleted adenovirus vectors that does not require helper adenovirus. *Gene Ther.* **2001**, *8*, 846–854. [CrossRef]
36. Kubo, S.; Saeki, Y.; Antonio Chiocca, E.; Mitani, K. An HSV amplicon-based helper system for helper-dependent adenoviral vectors. *Biochem. Biophys. Res. Commun.* **2003**, *307*, 826–830. [CrossRef]
37. Lee, D.; Liu, J.; Junn, H.J.; Lee, E.; Jeong, K.; Seol, D. No more helper adenovirus: Production of gutless adenovirus (GLAd) free of adenovirus and replication-competent adenovirus (RCA) contaminants. *Exp. Mol. Med.* **2019**, *51*, 1–18. [CrossRef]

38. Alemany, R.; Dai, Y.; Lou, Y.C.; Sethi, E.; Prokopenko, E.; Josephs, S.F.; Zhang, W.W. Complementation of helper-dependent adenoviral vectors: Size effects and titer fluctuations. *J. Virol. Methods* **1997**, *68*, 147–159. [CrossRef]
39. Hartigan-O'Connor, D.; Barjot, C.; Crawford, R.; Chamberlain, J.S. Efficient Rescue of Gutted Adenovirus Genomes Allows Rapid Production of Concentrated Stocks Without Negative Selection. *Hum. Gene Ther.* **2002**, *13*, 519–531. [CrossRef]
40. Peixoto, C.; Ferreira, T.B.; Sousa, M.F.Q.; Carrondo, M.J.T.; Alves, P.M. Towards purification of adenoviral vectors based on membrane technology. *Biotechnol. Prog.* **2008**, *24*, 1290–1296. [CrossRef]
41. Kratzer, R.F.; Kreppel, F. Production, Purification, and Titration of First-Generation Adenovirus Vectors. In *Functional Genomics: Methods in Molecular Biology*; Kaufmann, M., Klinger, C., Savelsbergh, A., Eds.; Springer: New York, NY, USA, 2017; Volume 1654, pp. 377–388. ISBN 978-1-4939-7230-2.
42. Dormond, E.; Chahal, P.; Bernier, A.; Tran, R.; Perrier, M.; Kamen, A. An efficient process for the purification of helper-dependent adenoviral vector and removal of helper virus by iodixanol ultracentrifugation. *J. Virol. Methods* **2010**, *165*, 83–89. [CrossRef] [PubMed]
43. Ma, J.; Su, C.; Wang, X.; Shu, Y.; Hu, S.; Zhao, C.; Kuang, Y.; Chen, Y.; Li, Y.; Wei, Y.; et al. A novel method to purify adenovirus based on increasing salt concentrations in buffer. *Eur. J. Pharm. Sci.* **2020**, *141*, 105090. [CrossRef]
44. Nestola, P.; Silva, R.J.S.; Peixoto, C.; Alves, P.M.; Carrondo, M.J.T.; Mota, J.P.B. Robust design of adenovirus purification by two-column, simulated moving-bed, size-exclusion chromatography. *J. Biotechnol.* **2015**, *213*, 109–119. [CrossRef]
45. Lee, D.; Kim, B.; Seol, D. Improved purification of recombinant adenoviral vector by metal affinity membrane chromatography. *Biochem. Biophys. Res. Commun.* **2009**, *378*, 640–644. [CrossRef]
46. Bo, H.; Chen, J.; Liang, T.; Li, S.; Shao, H.; Huang, S. Chromatographic purification of adenoviral vectors on anion-exchange resins. *Eur. J. Pharm. Sci.* **2015**, *67*, 119–125. [CrossRef] [PubMed]
47. Mittereder, N.; March, K.L.; Trapnell, B.C. Evaluation of the concentration and bioactivity of adenovirus vectors for gene therapy. *J. Virol.* **1996**, *70*, 7498–7509. [CrossRef] [PubMed]
48. Sweeney, J.A.; Hennessey, J.P. Evaluation of Accuracy and Precision of Adenovirus Absorptivity at 260 nm under Conditions of Complete DNA Disruption. *Virology* **2002**, *295*, 284–288. [CrossRef]
49. Puntel, M.; Curtin, J.F.; Zirger, J.M.; Muhammad, A.K.M.; Xiong, W.; Liu, C.; Hu, J.; Kroeger, K.M.; Czer, P.; Sciascia, S.; et al. Quantification of High-Capacity Helper-Dependent Adenoviral Vector Genomes in Vitro and in Vivo, Using Quantitative TaqMan Real-Time Polymerase Chain Reaction. *Hum. Gene Ther.* **2006**, *17*, 531–544. [CrossRef]
50. Palmer, D.J.; Ng, P. Physical and infectious titers of helper-dependent adenoviral vectors: A method of direct comparison to the adenovirus reference material. *Mol. Ther.* **2004**, *10*, 792–798. [CrossRef]
51. Kremer, E.J.; Boutin, S.; Chillon, M.; Danos, O. Canine Adenovirus Vectors: An Alternative for Adenovirus-Mediated Gene Transfer. *J. Virol.* **2000**, *74*, 505–512. [CrossRef]
52. Montenegro-Miranda, P.S.; Pichard, V.; Aubert, D.; Ten Bloemendaal, L.; Duijst, S.; De Waart, D.R.; Ferry, N.; Bosma, P.J. In the rat liver, Adenoviral gene transfer efficiency is comparable to AAV. *Gene Ther.* **2014**, *21*, 168–174. [CrossRef] [PubMed]
53. Carlisle, R.C.; Di, Y.; Cerny, A.M.; Sonnen, A.F.-P.; Sim, R.B.; Green, N.K.; Subr, V.; Ulbrich, K.; Gilbert, R.J.C.; Fisher, K.D.; et al. Human erythrocytes bind and inactivate type 5 adenovirus by presenting Coxsackie virus-adenovirus receptor and complement receptor 1. *Blood* **2009**, *113*, 1909–1918. [CrossRef] [PubMed]
54. Waddington, S.N.; McVey, J.H.; Bhella, D.; Parker, A.L.; Barker, K.; Atoda, H.; Pink, R.; Buckley, S.M.K.; Greig, J.A.; Denby, L.; et al. Adenovirus Serotype 5 Hexon Mediates Liver Gene Transfer. *Cell* **2008**, *132*, 397–409. [CrossRef] [PubMed]
55. Xu, Z.; Qiu, Q.; Tian, J.; Smith, J.S.; Conenello, G.M.; Morita, T.; Byrnes, A.P. Coagulation factor X shields adenovirus type 5 from attack by natural antibodies and complement. *Nat. Med.* **2013**, *19*, 452–457. [CrossRef]
56. Muruve, D.A.; Cotter, M.J.; Zaiss, A.K.; White, L.R.; Liu, Q.; Chan, T.; Clark, S.A.; Ross, P.J.; Meulenbroek, R.A.; Maelandsmo, G.M.; et al. Helper-Dependent Adenovirus Vectors Elicit Intact Innate but Attenuated Adaptive Host Immune Responses in Vivo. *J. Virol.* **2004**, *78*, 5966–5972. [CrossRef]
57. Cotter, M.J. The induction of inflammation by adenovirus vectors used for gene therapy. *Front. Biosci.* **2005**, *10*, 1098. [CrossRef]

58. Brunetti-Pierri, N.; Stapleton, G.E.; Law, M.; Breinholt, J.; Palmer, D.J.; Zuo, Y.; Grove, N.C.; Finegold, M.J.; Rice, K.; Beaudet, A.L.; et al. Efficient, Long-term Hepatic Gene Transfer Using Clinically Relevant HDAd Doses by Balloon Occlusion Catheter Delivery in Nonhuman Primates. *Mol. Ther.* **2009**, *17*, 327–333. [CrossRef]
59. Raper, S.E.; Chirmule, N.; Lee, F.S.; Wivel, N.A.; Bagg, A.; Gao, G.; Wilson, J.M.; Batshaw, M.L. Fatal systemic inflammatory response syndrome in a ornithine transcarbamylase deficient patient following adenoviral gene transfer. *Mol. Genet. Metab.* **2003**, *80*, 148–158. [CrossRef]
60. Brunetti-Pierri, N.; Palmer, D.J.; Beaudet, A.L.; Carey, K.D.; Finegold, M.; Ng, P. Acute toxicity after high-dose systemic injection of helper-dependent adenoviral vectors into nonhuman primates. *Hum. Gene Ther.* **2004**, *15*, 35–46. [CrossRef]
61. Mane, V.P.; Toietta, G.; McCormack, W.M.; Conde, I.; Clarke, C.; Palmer, D.; Finegold, M.J.; Pastore, L.; Ng, P.; Lopez, J.; et al. Modulation of TNFα, a determinant of acute toxicity associated with systemic delivery of first-generation and helper-dependent adenoviral vectors. *Gene Ther.* **2006**, *13*, 1272–1280. [CrossRef]
62. Thomas, C.E.; Schiedner, G.; Kochanek, S.; Castro, M.G.; Lowenstein, P.R. Peripheral infection with adenovirus causes unexpected long-term brain inflammation in animals injected intracranially with first-generation, but not with high-capacity, adenovirus vectors: Toward realistic long-term neurological gene therapy for chronic. *Proc. Natl. Acad. Sci. USA* **2000**, *97*, 7482–7487. [CrossRef] [PubMed]
63. Oka, K.; Belalcazar, L.M.; Dieker, C.; Nour, E.A.; Nuno-Gonzalez, P.; Paul, A.; Cormier, S.; Shin, J.; Finegold, M.; Chan, L. Sustained phenotypic correction in a mouse model of hypoalphalipoproteinemia with a helper-dependent adenovirus vector. *Gene Ther.* **2007**, *14*, 191–202. [CrossRef] [PubMed]
64. Barcia, C.; Jimenez-Dalmaroni, M.; Kroeger, K.M.; Puntel, M.; Rapaport, A.J.; Larocque, D.; King, G.D.; Johnson, S.A.; Liu, C.; Xiong, W.; et al. One-year Expression from High-capacity Adenoviral Vectors in the Brains of Animals with Pre-existing Anti-adenoviral Immunity: Clinical Implications. *Mol. Ther.* **2007**, *15*, 2154–2163. [CrossRef] [PubMed]
65. Kushwah, R.; Cao, H.; Hu, J. Characterization of Pulmonary T Cell Response to Helper-Dependent Adenoviral Vectors following Intranasal Delivery. *J. Immunol.* **2008**, *180*, 4098–4108. [CrossRef] [PubMed]
66. Gallo-Penn, A.M.; Shirley, P.S.; Andrews, J.L.; Tinlin, S.; Webster, S.; Cameron, C.; Hough, C.; Notley, C.; Lillicrap, D.; Kaleko, M.; et al. Systemic delivery of an adenoviral vector encoding canine factor VIII results in short-term phenotypic correction, inhibitor development, and biphasic liver toxicity in hemophilia A dogs. *Blood* **2001**, *97*, 107–113. [CrossRef]
67. Mccormack, W.M.; Seiler, M.P.; Bertin, T.K.; Ubhayakar, K.; Palmer, D.J.; Ng, P.; Nichols, T.C.; Lee, B. Helper-dependent adenoviral gene therapy mediates long-term correction of the clotting defect in the canine hemophilia A model. *J. Thromb. Haemost.* **2006**, *4*, 1218–1225. [CrossRef]
68. Heemskerk, B.; Veltrop-Duits, L.A.; Van Vreeswijk, T.; Ten Dam, M.M.; Heidt, S.; Toes, R.E.M.; Van Tol, M.J.D.; Schilham, M.W. Extensive Cross-Reactivity of CD4+ Adenovirus-Specific T Cells: Implications for Immunotherapy and Gene Therapy. *J. Virol.* **2003**, *77*, 6562–6566. [CrossRef]
69. Nathwani, A.C.; Tuddenham, E.G.D.; Rangarajan, S.; Rosales, C.; McIntosh, J.; Linch, D.C.; Chowdary, P.; Riddell, A.; Pie, A.J.; Harrington, C.; et al. Adenovirus-Associated Virus Vector–Mediated Gene Transfer in Hemophilia B. *N. Engl. J. Med.* **2011**, *365*, 2357–2365. [CrossRef]
70. Suzuki, M.; Cerullo, V.; Bertin, T.K.; Cela, R.; Clarke, C.; Guenther, M.; Brunetti-Pierri, N.; Lee, B. MyD88-Dependent Silencing of Transgene Expression during the Innate and Adaptive Immune Response to Helper-Dependent Adenovirus. *Hum. Gene Ther.* **2010**, *21*, 325–336. [CrossRef]
71. Suzuki, M.; Cela, R.; Bertin, T.K.; Sule, G.; Cerullo, V.; Rodgers, J.R.; Lee, B. NOD2 Signaling Contributes to the Innate Immune Response against Helper-Dependent Adenovirus Vectors Independently of MyD88 in Vivo. *Hum. Gene Ther.* **2011**, *22*, 1071–1082. [CrossRef]
72. Wonganan, P.; Clemens, C.C.; Brasky, K.; Pastore, L.; Croyle, M.A. Species Differences in the Pharmacology and Toxicology of PEGylated Helper-Dependent Adenovirus. *Mol. Pharm.* **2011**, *8*, 78–92. [CrossRef] [PubMed]
73. Gooding, L.R.; Ranheim, T.S.; Tollefson, A.E.; Aquino, L.; Duerksen-Hughes, P.; Horton, T.M.; Wold, W.S. The 10,400- and 14,500-dalton proteins encoded by region E3 of adenovirus function together to protect many but not all mouse cell lines against lysis by tumor necrosis factor. *J. Virol.* **1991**, *65*, 4114–4123. [CrossRef] [PubMed]

74. Lesokhin, A.M.; Delgado-Lopez, F.; Horwitz, M.S. Inhibition of Chemokine Expression by Adenovirus Early Region Three (E3) Genes. *J. Virol.* **2002**, *76*, 8236–8243. [CrossRef] [PubMed]
75. Ullman, A.J.; Reich, N.C.; Hearing, P. Adenovirus E4 ORF3 Protein Inhibits the Interferon-Mediated Antiviral Response. *J. Virol.* **2007**, *81*, 4744–4752. [CrossRef] [PubMed]
76. Jager, L.; Ehrhardt, A. Persistence of High-Capacity Adenoviral Vectors as Replication-Defective Monomeric Genomes in Vitro and in Murine Liver. *Hum. Gene Ther.* **2009**, *20*, 883–896. [CrossRef] [PubMed]
77. Ehrhardt, A.; Xu, H.; Kay, M.A. Episomal Persistence of Recombinant Adenoviral Vector Genomes during the Cell Cycle in Vivo. *J. Virol.* **2003**, *77*, 7689–7695. [CrossRef] [PubMed]
78. Larochelle, N.; Stucka, R.; Rieger, N.; Schermelleh, L.; Schiedner, G.; Kochanek, S.; Wolf, E.; Lochmüller, H. Genomic integration of adenoviral gene transfer vectors following transduction of fertilized mouse oocytes. *Transgenic Res.* **2011**, *20*, 123–135. [CrossRef]
79. Wong, C.; McFall, E.; Burns, J.; Parks, R. The Role of Chromatin in Adenoviral Vector Function. *Viruses* **2013**, *5*, 1500–1515. [CrossRef]
80. Ross, P.J.; Kennedy, M.A.; Christou, C.; Risco Quiroz, M.; Poulin, K.L.; Parks, R.J. Assembly of Helper-Dependent Adenovirus DNA into Chromatin Promotes Efficient Gene Expression. *J. Virol.* **2011**, *85*, 3950–3958. [CrossRef]
81. Ross, P.J.; Kennedy, M.A.; Parks, R.J. Host Cell Detection of Noncoding Stuffer DNA Contained in Helper-Dependent Adenovirus Vectors Leads to Epigenetic Repression of Transgene Expression. *J. Virol.* **2009**, *83*, 8409–8417. [CrossRef]
82. Chuah, M.K.L.; Schiedner, G.; Thorrez, L.; Brown, B.; Johnston, M.; Gillijns, V.; Hertel, S.; Van Rooijen, N.; Lillicrap, D.; Collen, D.; et al. Therapeutic factor VIII levels and negligible toxicity in mouse and dog models of hemophilia A following gene therapy with high-capacity adenoviral vectors. *Blood* **2003**, *101*, 1734–1743. [CrossRef] [PubMed]
83. Unzu, C.; Melero, I.; Hervás-Stubbs, S.; Sampedro, A.; Mancheño, U.; Morales-Kastresana, A.; Serrano-Mendioroz, I.; De Salamanca, R.E.; Benito, A.; Fontanellas, A. Helper-dependent adenovirus achieve more efficient and persistent liver transgene expression in non-human primates under immunosuppression. *Gene Ther.* **2015**, *22*, 856–865. [CrossRef] [PubMed]
84. Vigne, E.; Dedieu, J.; Brie, A.; Gillardeaux, A.; Briot, D.; Benihoud, K.; Latta-Mahieu, M.; Saulnier, P.; Perricaudet, M.; Yeh, P. Genetic manipulations of adenovirus type 5 fiber resulting in liver tropism attenuation. *Gene Ther.* **2003**, *10*, 153–162. [CrossRef] [PubMed]
85. Thorner, A.R.; Vogels, R.; Kaspers, J.; Weverling, G.J.; Holterman, L.; Lemckert, A.A.C.; Dilraj, A.; McNally, L.M.; Jeena, P.M.; Jepsen, S.; et al. Age Dependence of Adenovirus-Specific Neutralizing Antibody Titers in Individuals from Sub-Saharan Africa. *J. Clin. Microbiol.* **2006**, *44*, 3781–3783. [CrossRef]
86. Zhang, S.; Huang, W.; Zhou, X.; Zhao, Q.; Wang, Q.; Jia, B. Seroprevalence of neutralizing antibodies to human adenoviruses type-5 and type-26 and chimpanzee adenovirus type-68 in healthy Chinese adults. *J. Med. Virol.* **2013**, *85*, 1077–1084. [CrossRef] [PubMed]
87. Schiedner, G.; Hertel, S.; Johnston, M.; Dries, V.; Van Rooijen, N.; Kochanek, S. Selective depletion or blockade of Kupffer cells leads to enhanced and prolonged hepatic transgene expression using high-capacity adenoviral vectors. *Mol. Ther.* **2003**, *7*, 35–43. [CrossRef]
88. Piccolo, P.; Vetrini, F.; Mithbaokar, P.; Grove, N.C.; Bertin, T.; Palmer, D.; Ng, P.; Brunetti-Pierri, N. SR-A and SREC-I Are Kupffer and Endothelial Cell Receptors for Helper-dependent Adenoviral Vectors. *Mol. Ther.* **2013**, *21*, 767–774. [CrossRef]
89. Alzuguren, P.; Hervas-Stubbs, S.; Gonzalez-Aseguinolaza, G.; Poutou, J.; Fortes, P.; Mancheno, U.; Bunuales, M.; Olagüe, C.; Razquin, N.; Van Rooijen, N.; et al. Transient depletion of specific immune cell populations to improve adenovirus-mediated transgene expression in the liver. *Liver Int.* **2015**, *35*, 1274–1289. [CrossRef]
90. Küster, K.; Koschel, A.; Rohwer, N.; Fischer, A.; Wiedenmann, B.; Anders, M. Downregulation of the coxsackie and adenovirus receptor in cancer cells by hypoxia depends on HIF-1α. *Cancer Gene Ther.* **2010**, *17*, 141–146. [CrossRef] [PubMed]
91. Lacher, M.D.; Tiirikainen, M.I.; Saunier, E.F.; Christian, C.; Anders, M.; Oft, M.; Balmain, A.; Akhurst, R.J.; Korn, W.M. Transforming Growth Factor-β Receptor Inhibition Enhances Adenoviral Infectability of Carcinoma Cells via Up-Regulation of Coxsackie and Adenovirus Receptor in Conjunction with Reversal of Epithelial-Mesenchymal Transition. *Cancer Res.* **2006**, *66*, 1648–1657. [CrossRef] [PubMed]

92. Stone, D.; Liu, Y.; Li, Z.; Tuve, S.; Strauss, R.; Lieber, A. Comparison of Adenoviruses From Species B, C, E, and F after Intravenous Delivery. *Mol. Ther.* **2007**, *15*, 2146–2153. [CrossRef] [PubMed]
93. Arnberg, N. Adenovirus receptors: Implications for targeting of viral vectors. *Trends Pharmacol. Sci.* **2012**, *33*, 442–448. [CrossRef] [PubMed]
94. Wang, H.; Liu, Y.; Li, Z.; Tuve, S.; Stone, D.; Kalyushniy, O.; Shayakhmetov, D.; Verlinde, C.L.M.; Stehle, T.; McVey, J.; et al. In Vitro and in Vivo Properties of Adenovirus Vectors with Increased Affinity to CD46. *J. Virol.* **2008**, *82*, 10567–10579. [CrossRef]
95. Khare, R.; Hillestad, M.L.; Xu, Z.; Byrnes, A.P.; Barry, M.A. Circulating Antibodies and Macrophages as Modulators of Adenovirus Pharmacology. *J. Virol.* **2013**, *87*, 3678–3686. [CrossRef] [PubMed]
96. Khare, R.; May, S.M.; Vetrini, F.; Weaver, E.A.; Palmer, D.; Rosewell, A.; Grove, N.; Ng, P.; Barry, M.A. Generation of a Kupffer Cell-evading Adenovirus for Systemic and Liver-directed Gene Transfer. *Mol. Ther.* **2011**, *19*, 1254–1262. [CrossRef] [PubMed]
97. Lewis, T.; Glasgow, J.; Harms, A.; Standaert, D.; Curiel, D. Fiber-Modified Adenovirus for Central Nervous System Parkinson's Disease Gene Therapy. *Viruses* **2014**, *6*, 3293–3310. [CrossRef]
98. Stoff-Khalili, M.A.; Stoff, A.; Rivera, A.A.; Mathis, J.M.; Everts, M.; Wang, M.; Kawakami, Y.; Waehler, R.; Matthews, Q.L.; Yamamoto, M.; et al. Gene transfer to carcinoma of the breast with fiber-modified adenoviral vectors in a tissue slice model system. *Cancer Biol. Ther.* **2005**, *4*, 1203–1210. [CrossRef]
99. Yu, D.; Jin, C.; Ramachandran, M.; Xu, J.; Nilsson, B.; Korsgren, O.; Le Blanc, K.; Uhrbom, L.; Forsberg-Nilsson, K.; Westermark, B.; et al. Adenovirus Serotype 5 Vectors with Tat-PTD Modified Hexon and Serotype 35 Fiber Show Greatly Enhanced Transduction Capacity of Primary Cell Cultures. *PLoS ONE* **2013**, *8*, e54952. [CrossRef]
100. Kritz, A.B.; Nicol, C.G.; Dishart, K.L.; Nelson, R.; Holbeck, S.; Von Seggern, D.J.; Work, L.M.; McVey, J.H.; Nicklin, S.A.; Baker, A.H. Adenovirus 5 fibers mutated at the putative HSPG-binding site show restricted retargeting with targeting peptides in the HI loop. *Mol. Ther.* **2007**, *15*, 741–749. [CrossRef]
101. Terashima, T.; Oka, K.; Kritz, A.B.; Kojima, H.; Baker, A.H.; Chan, L. DRG-targeted helper-dependent adenoviruses mediate selective gene delivery for therapeutic rescue of sensory neuronopathies in mice. *J. Clin. Investig.* **2009**, *119*, 2100–2112. [CrossRef]
102. Kuhn, I.; Harden, P.; Bauzon, M.; Chartier, C.; Nye, J.; Thorne, S.; Reid, T.; Ni, S.; Lieber, A.; Fisher, K.; et al. Directed Evolution Generates a Novel Oncolytic Virus for the Treatment of Colon Cancer. *PLoS ONE* **2008**, *3*, e2409. [CrossRef] [PubMed]
103. Weaver, E.A.; Nehete, P.N.; Buchl, S.S.; Senac, J.S.; Palmer, D.; Ng, P.; Sastry, K.J.; Barry, M.A. Comparison of Replication-Competent, First Generation, and Helper-Dependent Adenoviral Vaccines. *PLoS ONE* **2009**, *4*, e5059. [CrossRef]
104. Parks, R.J.; Evelegh, C.M.; Graham, F.L. Use of helper-dependent adenoviral vectors of alternative serotypes permits repeat vector administration. *Gene Ther.* **1999**, *6*, 1565–1573. [CrossRef] [PubMed]
105. Sun, Y.; Lv, X.; Ding, P.; Wang, L.; Sun, Y.; Li, S.; Zhang, H.; Gao, Z. Exploring the functions of polymers in adenovirus-mediated gene delivery: Evading immune response and redirecting tropism. *Acta Biomater.* **2019**, *97*, 93–104. [CrossRef]
106. Fisher, K.D.; Seymour, L.W. HPMA copolymers for masking and retargeting of therapeutic viruses. *Adv. Drug Deliv. Rev.* **2010**, *62*, 240–245. [CrossRef]
107. Morrison, J.; Briggs, S.S.; Green, N.K.; Thoma, C.; Fisher, K.D.; Kehoe, S.; Seymour, L.W. Cetuximab Retargeting of Adenovirus via the Epidermal Growth Factor Receptor for Treatment of Intraperitoneal Ovarian Cancer. *Hum. Gene Ther.* **2009**, *20*, 239–251. [CrossRef]
108. Prill, J.; Espenlaub, S.; Samen, U.; Engler, T.; Schmidt, E.; Vetrini, F.; Rosewell, A.; Grove, N.; Palmer, D.; Ng, P.; et al. Modifications of Adenovirus Hexon Allow for Either Hepatocyte Detargeting or Targeting With Potential Evasion From Kupffer Cells. *Mol. Ther.* **2011**, *19*, 83–92. [CrossRef]
109. Balamotis, M.A.; Huang, K.; Mitani, K. Efficient delivery and stable gene expression in a hematopoietic cell line using a chimeric serotype 35 fiber pseudotyped helper-dependent adenoviral vector. *Virology* **2004**, *324*, 229–237. [CrossRef]
110. Ersching, J.; Hernandez, M.I.M.; Cezarotto, F.S.; Ferreira, J.D.S.; Martins, A.B.; Switzer, W.M.; Xiang, Z.; Ertl, H.C.J.; Zanetti, C.R.; Pinto, A.R. Neutralizing antibodies to human and simian adenoviruses in humans and New-World monkeys. *Virology* **2010**, *407*, 1–6. [CrossRef]

111. Hutnick, N.A.; Carnathan, D.; Demers, K.; Makedonas, G.; Ertl, H.C.J.; Betts, M.R. Adenovirus-specific human T cells are pervasive, polyfunctional, and cross-reactive. *Vaccine* **2010**, *28*, 1932–1941. [CrossRef]
112. Sharma, A.; Tandon, M.; Ahi, Y.S.; Bangari, D.S.; Vemulapalli, R.; Mittal, S.K. Evaluation of cross-reactive cell-mediated immune responses among human, bovine and porcine adenoviruses. *Gene Ther.* **2010**, *17*, 634–642. [CrossRef]
113. Soudais, C.; Laplace-Builhe, C.; Kissa, K.; Kremer, E.J. Preferential transduction of neurons by canine adenovirus vectors and their efficient retrograde transport in vivo. *FASEB J.* **2001**, *15*, 1–23. [CrossRef]
114. Salinas, S.; Bilsland, L.G.; Henaff, D.; Weston, A.E.; Keriel, A.; Schiavo, G.; Kremer, E.J. CAR-Associated Vesicular Transport of an Adenovirus in Motor Neuron Axons. *PLoS Pathog.* **2009**, *5*, e1000442. [CrossRef]
115. Ariza, L.; Giménez-Llort, L.; Cubizolle, A.; Pagès, G.; García-Lareu, B.; Serratrice, N.; Cots, D.; Thwaite, R.; Chillón, M.; Kremer, E.J.; et al. Central Nervous System Delivery of Helper-Dependent Canine Adenovirus Corrects Neuropathology and Behavior in Mucopolysaccharidosis Type VII Mice. *Hum. Gene Ther.* **2014**, *25*, 199–211. [CrossRef] [PubMed]
116. Del Rio, D.; Beucher, B.; Lavigne, M.; Wehbi, A.; Gonzalez Dopeso-Reyes, I.; Saggio, I.; Kremer, E.J. CAV-2 Vector Development and Gene Transfer in the Central and Peripheral Nervous Systems. *Front. Mol. Neurosci.* **2019**, *12*, 71. [CrossRef]
117. Zhang, W.; Muck-Hausl, M.; Wang, J.; Sun, C.; Gebbing, M.; Miskey, C.; Ivics, Z.; Izsvak, Z.; Ehrhardt, A. Integration Profile and Safety of an Adenovirus Hybrid-Vector Utilizing Hyperactive Sleeping Beauty Transposase for Somatic Integration. *PLoS ONE* **2013**, *8*, e75344. [CrossRef] [PubMed]
118. George, L.A. Hemophilia gene therapy comes of age. *Blood Adv.* **2017**, *1*, 2591–2599. [CrossRef] [PubMed]
119. Balagué, C.; Zhou, J.; Dai, Y.; Alemany, R.; Josephs, S.F.; Andreason, G.; Hariharan, M.; Sethi, E.; Prokopenko, E.; Jan, H.Y.; et al. Sustained high-level expression of full-length human factor VIII and restoration of clotting activity in hemophilic mice using a minimal adenovirus vector. *Blood* **2000**, *95*, 820–828. [CrossRef]
120. Zhang, W.W.; Josephs, S.F.; Zhou, J.; Fang, X.; Alemany, R.; Balagué, C.; Dai, Y.; Ayares, D.; Prokopenko, E.; Lou, Y.C.; et al. Development and application of a minimal-adenoviral vector system for gene therapy of hemophilia A. *Thromb. Haemost.* **1999**, *82*, 562–571.
121. Brown, B.D.; Shi, C.X.; Powell, S.; Hurlbut, D.; Graham, F.L.; Lillicrap, D. Helper-dependent adenoviral vectors mediate therapeutic factor VIII expression for several months with minimal accompanying toxicity in a canine model of severe hemophilia A. *Blood* **2004**, *103*, 804–810. [CrossRef]
122. Hu, C.; Cela, R.G.; Suzuki, M.; Lee, B.; Lipshutz, G.S. Neonatal helper-dependent adenoviral vector gene therapy mediates correction of hemophilia A and tolerance to human factor VIII. *Proc. Natl. Acad. Sci. USA* **2011**, *108*, 2082–2087. [CrossRef] [PubMed]
123. Brown, B.D.; Shi, C.X.; Rawle, F.E.M.; Tinlin, S.; Mckinven, A.; Hough, C.; Graham, F.L.; Lillicrap, D. Factors influencing therapeutic efficacy and the host immune response to helper-dependent adenoviral gene therapy in hemophilia A mice. *J. Thromb. Haemost.* **2004**, *2*, 111–118. [CrossRef] [PubMed]
124. McIntosh, J.; Lenting, P.J.; Rosales, C.; Lee, D.; Rabbanian, S.; Raj, D.; Patel, N.; Tuddenham, E.G.D.; Christophe, O.D.; McVey, J.H.; et al. Therapeutic levels of FVIII following a single peripheral vein administration of rAAV vector encoding a novel human factor VIII variant. *Blood* **2013**, *121*, 3335–3344. [CrossRef] [PubMed]
125. Callan, M.B.; Haskins, M.E.; Wang, P.; Zhou, S.; High, K.A.; Arruda, V.R. Successful Phenotype Improvement following Gene Therapy for Severe Hemophilia A in Privately Owned Dogs. *PLoS ONE* **2016**, *11*, e0151800. [CrossRef] [PubMed]
126. Samelson-Jones, B.J.; Arruda, V.R. Protein-Engineered Coagulation Factors for Hemophilia Gene Therapy. *Mol. Ther. Methods Clin. Dev.* **2019**, *12*, 184–201. [CrossRef] [PubMed]
127. Ehrhardt, A.; Kay, M.A. A new adenoviral helper–dependent vector results in long-term therapeutic levels of human coagulation factor IX at low doses in vivo. *Blood* **2002**, *99*, 3923–3930. [CrossRef]
128. Ehrhardt, A.; Xu, H.; Dillow, A.M.; Bellinger, D.A.; Nichols, T.C.; Kay, M.A. A gene-deleted adenoviral vector results in phenotypic correction of canine hemophilia B without liver toxicity or thrombocytopenia. *Blood* **2003**, *102*, 2403–2411. [CrossRef]
129. Brunetti-Pierri, N.; Nichols, T.C.; McCorquodale, S.; Merricks, E.; Palmer, D.J.; Beaudet, A.L.; Ng, P. Sustained Phenotypic Correction of Canine Hemophilia B after Systemic Administration of Helper-Dependent Adenoviral Vector. *Hum. Gene Ther.* **2005**, *16*, 811–820. [CrossRef]

130. Brunetti-Pierri, N.; Liou, A.; Patel, P.; Palmer, D.; Grove, N.; Finegold, M.; Piccolo, P.; Donnachie, E.; Rice, K.; Beaudet, A.; et al. Balloon Catheter Delivery of Helper-dependent Adenoviral Vector Results in Sustained, Therapeutic hFIX Expression in Rhesus Macaques. *Mol. Ther.* **2012**, *20*, 1863–1870. [CrossRef]
131. Morral, N.; Parks, R.J.; Zhou, H.; Langston, C.; Schiedner, G.; Quinones, J.; Graham, F.L.; Kochanek, S.; Beaudet, A.L. High Doses of a Helper-Dependent Adenoviral Vector Yield Supraphysiological Levels of α 1 -Antitrypsin with Negligible Toxicity. *Hum. Gene Ther.* **1998**, *9*, 2709–2716. [CrossRef]
132. O'Neal, W.K.; Zhou, H.; Morral, N.; Langston, C.; Parks, R.J.; Graham, F.L.; Kochanek, S.; Beaudet, A.L. Toxicity Associated with Repeated Administration of First-Generation Adenovirus Vectors Does Not Occur with a Helper-Dependent Vector. *Mol. Med.* **2000**, *6*, 179–195. [CrossRef] [PubMed]
133. Kim, I.-H.; Jozkowicz, A.; Piedra, P.A.; Oka, K.; Chan, L. Lifetime correction of genetic deficiency in mice with a single injection of helper-dependent adenoviral vector. *Proc. Natl. Acad. Sci. USA* **2001**, *98*, 13282–13287. [CrossRef] [PubMed]
134. Leggiero, E.; Astone, D.; Cerullo, V.; Lombardo, B.; Mazzaccara, C.; Labruna, G.; Sacchetti, L.; Salvatore, F.; Croyle, M.; Pastore, L. PEGylated helper-dependent adenoviral vector expressing human Apo A-I for gene therapy in LDLR-deficient mice. *Gene Ther.* **2013**, *20*, 1124–1130. [CrossRef] [PubMed]
135. Pastore, L.; Belalcazar, L.M.; Oka, K.; Cela, R.; Lee, B.; Chan, L.; Beaudet, A.L. Helper-dependent adenoviral vector-mediated long-term expression of human apolipoprotein A-I reduces atherosclerosis in apo E-deficient mice. *Gene* **2004**, *327*, 153–160. [CrossRef]
136. Belalcazar, L.M.; Merched, A.; Carr, B.; Oka, K.; Chen, K.-H.; Pastore, L.; Beaudet, A.; Chan, L. Long-Term Stable Expression of Human Apolipoprotein A-I Mediated by Helper-Dependent Adenovirus Gene Transfer Inhibits Atherosclerosis Progression and Remodels Atherosclerotic Plaques in a Mouse Model of Familial Hypercholesterolemia. *Circulation* **2003**, *107*, 2726–2732. [CrossRef]
137. Wacker, B.K.; Dronadula, N.; Bi, L.; Stamatikos, A.; Dichek, D.A. Apo A-I (Apolipoprotein A-I) Vascular Gene Therapy Provides Durable Protection against Atherosclerosis in Hyperlipidemic Rabbits. *Arterioscler. Thromb. Vasc. Biol.* **2018**, *38*, 206–217. [CrossRef]
138. Stamatikos, A.; Dronadula, N.; Ng, P.; Palmer, D.; Knight, E.; Wacker, B.K.; Tang, C.; Kim, F.; Dichek, D.A. ABCA1 Overexpression in Endothelial Cells in Vitro Enhances ApoAI-Mediated Cholesterol Efflux and Decreases Inflammation. *Hum. Gene Ther.* **2019**, *30*, 236–248. [CrossRef]
139. Nomura, S.; Merched, A.; Nour, E.; Dieker, C.; Oka, K.; Chan, L. Low-density lipoprotein receptor gene therapy using helper-dependent adenovirus produces long-term protection against atherosclerosis in a mouse model of familial hypercholesterolemia. *Gene Ther.* **2004**, *11*, 1540–1548. [CrossRef]
140. Oka, K.; Mullins, C.E.; Kushwaha, R.S.; Leen, A.M.; Chan, L. Gene therapy for rhesus monkeys heterozygous for LDL receptor deficiency by balloon catheter hepatic delivery of helper-dependent adenoviral vector. *Gene Ther.* **2015**, *22*, 87–95. [CrossRef]
141. Mingozzi, F.; High, K.A. Immune responses to AAV vectors: Overcoming barriers to successful gene therapy. *Blood* **2013**, *122*, 23–36. [CrossRef]
142. Brinkert, F.; Ganschow, R.; Helmke, K.; Harps, E.; Fischer, L.; Nashan, B.; Hoppe, B.; Kulke, S.; Müller-Wiefel, D.E.; Kemper, M.J. Transplantation Procedures in Children with Primary Hyperoxaluria Type 1: Outcome and Longitudinal Growth. *Transplantation* **2009**, *87*, 1415–1421. [CrossRef] [PubMed]
143. Castello, R.; Borzone, R.; D'Aria, S.; Annunziata, P.; Piccolo, P.; Brunetti-Pierri, N. Helper-dependent adenoviral vectors for liver-directed gene therapy of primary hyperoxaluria type 1. *Gene Ther.* **2016**, *23*, 129–134. [CrossRef] [PubMed]
144. Khoja, S.; Nitzahn, M.; Hermann, K.; Truong, B.; Borzone, R.; Willis, B.; Rudd, M.; Palmer, D.J.; Ng, P.; Brunetti-Pierri, N.; et al. Conditional disruption of hepatic carbamoyl phosphate synthetase 1 in mice results in hyperammonemia without orotic aciduria and can be corrected by liver-directed gene therapy. *Mol. Genet. Metab.* **2018**, *124*, 243–253. [CrossRef] [PubMed]
145. Brunetti-Pierri, N.; Ng, P. Gene therapy with helper-dependent adenoviral vectors: Lessons from studies in large animal models. *Virus Genes* **2017**, *53*, 684–691. [CrossRef] [PubMed]
146. Fontanellas, A.; Ávila, M.A.; Berraondo, P. Emerging therapies for acute intermittent porphyria. *Expert Rev. Mol. Med.* **2016**, *18*, e17. [CrossRef]
147. Unzu, C.; Sampedro, A.; Mauleón, I.; González-Aparicio, M.; Enríquez de Salamanca, R.; Prieto, J.; Aragón, T.; Fontanellas, A. Helper-dependent adenoviral liver gene therapy protects against induced attacks and corrects protein folding stress in acute intermittent porphyria mice. *Hum. Mol. Genet.* **2013**, *22*, 2929–2940. [CrossRef]

148. Oh, D.-B. Glyco-engineering strategies for the development of therapeutic enzymes with improved efficacy for the treatment of lysosomal storage diseases. *BMB Rep.* **2015**, *48*, 438–444. [CrossRef]
149. Kiang, A.; Hartman, Z.C.; Liao, S.; Xu, F.; Serra, D.; Palmer, D.J.; Ng, P.; Amalfitano, A. Fully Deleted Adenovirus Persistently Expressing GAA Accomplishes Long-Term Skeletal Muscle Glycogen Correction in Tolerant and Nontolerant GSD-II Mice. *Mol. Ther.* **2006**, *13*, 127–134. [CrossRef]
150. Rastall, D.P.W.; Seregin, S.S.; Aldhamen, Y.A.; Kaiser, L.M.; Mullins, C.; Liou, A.; Ing, F.; Pereria-Hicks, C.; Godbehere-Roosa, S.; Palmer, D.; et al. Long-term, high-level hepatic secretion of acid α-glucosidase for Pompe disease achieved in non-human primates using helper-dependent adenovirus. *Gene Ther.* **2016**, *23*, 743–752. [CrossRef]
151. Byrne, B.J.; Fuller, D.D.; Smith, B.K.; Clement, N.; Coleman, K.; Cleaver, B.; Vaught, L.; Falk, D.J.; McCall, A.; Corti, M. Pompe disease gene therapy: Neural manifestations require consideration of CNS directed therapy. *Ann. Transl. Med.* **2019**, *7*, 290. [CrossRef]
152. Hermening, S.; Kügler, S.; Bähr, M.; Isenmann, S. Improved high-capacity adenoviral vectors for high-level neuron-restricted gene transfer to the CNS. *J. Virol. Methods* **2006**, *136*, 30–37. [CrossRef] [PubMed]
153. Ghulam Muhammad, A.K.M.; Xiong, W.; Puntel, M.; Farrokhi, C.; Kroeger, K.M.; Salem, A.; Lacayo, L.; Pechnick, R.N.; Kelson, K.R.; Palmer, D.; et al. Safety Profile of Gutless Adenovirus Vectors Delivered into the Normal Brain Parenchyma: Implications for a Glioma Phase 1 Clinical Trial. *Hum. Gene Ther. Methods* **2012**, *23*, 271–284. [CrossRef] [PubMed]
154. VanderVeen, N.; Raja, N.; Yi, E.; Appelman, H.; Ng, P.; Palmer, D.; Zamler, D.; Dzaman, M.; Lowenstein, P.R.; Castro, M.G. Preclinical Efficacy and Safety Profile of Allometrically Scaled Doses of Doxycycline Used to Turn "On" Therapeutic Transgene Expression from High-Capacity Adenoviral Vectors in a Glioma Model. *Hum. Gene Ther. Methods* **2016**, *27*, 98–111. [CrossRef] [PubMed]
155. Zou, L.; Zhou, H.; Pastore, L.; Yang, K. Prolonged Transgene Expression Mediated by a Helper-Dependent Adenoviral Vector (hdAd) in the Central Nervous System. *Mol. Ther.* **2000**, *2*, 105–113. [CrossRef]
156. Butti, E.; Bergami, A.; Recchia, A.; Brambilla, E.; Franciotta, D.; Cattalini, A.; Stornaiuolo, A.; Lachapelle, F.; Comi, G.; Mavilio, F.; et al. Absence of an intrathecal immune reaction to a helper-dependent adenoviral vector delivered into the cerebrospinal fluid of non-human primates. *Gene Ther.* **2008**, *15*, 233–238. [CrossRef]
157. Piersanti, S.; Astrologo, L.; Licursi, V.; Costa, R.; Roncaglia, E.; Gennetier, A.; Ibanes, S.; Chillon, M.; Negri, R.; Tagliafico, E.; et al. Differentiated Neuroprogenitor Cells Incubated with Human or Canine Adenovirus, or Lentiviral Vectors Have Distinct Transcriptome Profiles. *PLoS ONE* **2013**, *8*, e69808. [CrossRef]
158. Martina, Y.; Avitabile, D.; Piersanti, S.; Cherubini, G.; Saggio, I. Different modulation of cellular transcription by adenovirus 5, ΔE1/E3 adenovirus and helper-dependent vectors. *Virus Res.* **2007**, *130*, 71–84. [CrossRef]
159. Thomas, C.E.; Schiedner, G.; Kochanek, S.; Castro, M.G.; Lowenstein, P.R. Preexisting Antiadenoviral Immunity is Not a Barrier to Efficient and Stable Transduction of the Brain, Mediated by Novel High-Capacity Adenovirus Vectors. *Hum. Gene Ther.* **2001**, *12*, 839–846. [CrossRef]
160. Lowenstein, P.; Mandel, R.; Xiong, W.-D.; Kroeger, K.; Castro, M. Immune Responses to Adenovirus and Adeno-Associated Vectors Used for Gene Therapy of Brain Diseases: The Role of Immunological Synapses in Understanding the Cell Biology of Neuroimmune Interactions. *Curr. Gene Ther.* **2007**, *7*, 347–360. [CrossRef]
161. Xiong, W.; Goverdhana, S.; Sciascia, S.A.; Candolfi, M.; Zirger, J.M.; Barcia, C.; Curtin, J.F.; King, G.D.; Jaita, G.; Liu, C.; et al. Regulatable Gutless Adenovirus Vectors Sustain Inducible Transgene Expression in the Brain in the Presence of an Immune Response against Adenoviruses. *J. Virol.* **2006**, *80*, 27–37. [CrossRef]
162. Xiong, W.; Candolfi, M.; Kroeger, K.M.; Puntel, M.; Mondkar, S.; Larocque, D.; Liu, C.; Curtin, J.F.; Palmer, D.; Ng, P.; et al. Immunization against the Transgene but not the TetON Switch Reduces Expression from Gutless Adenoviral Vectors in the Brain. *Mol. Ther.* **2008**, *16*, 343–351. [CrossRef] [PubMed]
163. King, G.D.; Muhammad, A.K.M.G.; Xiong, W.; Kroeger, K.M.; Puntel, M.; Larocque, D.; Palmer, D.; Ng, P.; Lowenstein, P.R.; Castro, M.G. High-Capacity Adenovirus Vector-Mediated Anti-Glioma Gene Therapy in the Presence of Systemic Antiadenovirus Immunity. *J. Virol.* **2008**, *82*, 4680–4684. [CrossRef] [PubMed]
164. Puntel, M.; Muhammad, A.K.M.G.; Candolfi, M.; Salem, A.; Yagiz, K.; Farrokhi, C.; Kroeger, K.M.; Xiong, W.; Curtin, J.F.; Liu, C.; et al. A Novel Bicistronic High-Capacity Gutless Adenovirus Vector That Drives Constitutive Expression of Herpes Simplex Virus Type 1 Thymidine Kinase and Tet-Inducible Expression of Flt3L for Glioma Therapeutics. *J. Virol.* **2010**, *84*, 6007–6017. [CrossRef] [PubMed]
165. Stevenson, P.G.; Hawke, S.; Sloan, D.J.; Bangham, C.R. The immunogenicity of intracerebral virus infection depends on anatomical site. *J. Virol.* **1997**, *71*, 145–151. [CrossRef] [PubMed]

166. Matyszak, M. Inflammation in the CNS: Balance between immunological privilege and immune responses. *Prog. Neurobiol.* **1998**, *56*, 19–35. [CrossRef]
167. Matyszak, M.; Perry, V. The potential role of dendritic cells in immune-mediated inflammatory diseases in the central nervous system. *Neuroscience* **1996**, *74*, 599–608. [CrossRef]
168. Bechmann, I.; Galea, I.; Perry, V.H. What is the blood–brain barrier (not)? *Trends Immunol.* **2007**, *28*, 5–11. [CrossRef]
169. McMenamin, P.G. Distribution and phenotype of dendritic cells and resident tissue macrophages in the dura mater, leptomeninges, and choroid plexus of the rat brain as demonstrated in wholemount preparations. *J. Comp. Neurol.* **1999**, *405*, 553–562. [CrossRef]
170. Einfeld, D.A.; Schroeder, R.; Roelvink, P.W.; Lizonova, A.; King, C.R.; Kovesdi, I.; Wickham, T.J. Reducing the Native Tropism of Adenovirus Vectors Requires Removal of both CAR and Integrin Interactions. *J. Virol.* **2001**, *75*, 11284–11291. [CrossRef]
171. Salinas, S.; Zussy, C.; Loustalot, F.; Henaff, D.; Menendez, G.; Morton, P.E.; Parsons, M.; Schiavo, G.; Kremer, E.J. Disruption of the Coxsackievirus and Adenovirus Receptor-Homodimeric Interaction Triggers Lipid Microdomain- and Dynamin-dependent Endocytosis and Lysosomal Targeting. *J. Biol. Chem.* **2014**, *289*, 680–695. [CrossRef]
172. Salinas, S.; Junyent, F.; Coré, N.; Cremer, H.; Kremer, E.J. What is CAR doing in the middle of the adult neurogenic road? *Neurogenesis* **2017**, *4*, e1304790. [CrossRef] [PubMed]
173. Zhang, Y.; Bergelson, J.M. Adenovirus Receptors. *J. Virol.* **2005**, *79*, 12125–12131. [CrossRef] [PubMed]
174. Zussy, C.; Loustalot, F.; Junyent, F.; Gardoni, F.; Bories, C.; Valero, J.; Desarmenien, M.G.; Bernex, F.; Henaff, D.; Bayo-Puxan, N.; et al. Coxsackievirus Adenovirus Receptor Loss Impairs Adult Neurogenesis, Synapse Content, and Hippocampus Plasticity. *J. Neurosci.* **2016**, *36*, 9558–9571. [CrossRef] [PubMed]
175. Mestre-Francés, N.; Serratrice, N.; Gennetier, A.; Devau, G.; Cobo, S.; Trouche, S.G.; Fontès, P.; Zussy, C.; De Deurwaerdere, P.; Salinas, S.; et al. Exogenous LRRK2G2019S induces parkinsonian-like pathology in a nonhuman primate. *JCI Insight* **2018**, *3*, 1–18. [CrossRef] [PubMed]
176. Persson, A.; Fan, X.; Widegren, B.; Englund, E. Cell type- and region- dependent coxsackie adenovirus receptor expression in the central nervous system. *J. Neurooncol.* **2006**, *78*, 1–6. [CrossRef]
177. Fueyo, J.; Alemany, R.; Gomez-Manzano, C.; Fuller, G.N.; Khan, A.; Conrad, C.A.; Liu, T.-J.; Jiang, H.; Lemoine, M.G.; Suzuki, K.; et al. Preclinical Characterization of the Antiglioma Activity of a Tropism-Enhanced Adenovirus Targeted to the Retinoblastoma Pathway. *JNCI J. Natl. Cancer Inst.* **2003**, *95*, 652–660. [CrossRef]
178. Hotta, Y.; Honda, T.; Naito, M.; Kuwano, R. Developmental distribution of coxsackie virus and adenovirus receptor localized in the nervous system. *Dev. Brain Res.* **2003**, *143*, 1–13. [CrossRef]
179. Xu, R.; Mohanty, J.G.; Crowell, R.L. Receptor proteins on newborn Balb/c mouse brain cells for coxsackievirus B3 are immunologically distinct from those on HeLa cells. *Virus Res.* **1995**, *35*, 323–340. [CrossRef]
180. Chen, M.; Kato, T.; Higuchi, M.; Yoshida, S.; Yako, H.; Kanno, N.; Kato, Y. Coxsackievirus and adenovirus receptor-positive cells compose the putative stem/progenitor cell niches in the marginal cell layer and parenchyma of the rat anterior pituitary. *Cell Tissue Res.* **2013**, *354*, 823–836. [CrossRef]
181. Chen, M.; Kato, T.; Kato, Y. Data on localization of coxsackievirus and adenovirus receptor (CAR) in the embryonic rat brain. *Data Br.* **2019**, *23*, 103726. [CrossRef]
182. Candolfi, M.; Curtin, J.F.; Xiong, W.-D.; Kroeger, K.M.; Liu, C.; Rentsendorj, A.; Agadjanian, H.; Medina-Kauwe, L.; Palmer, D.; Ng, P.; et al. Effective High-Capacity Gutless Adenoviral Vectors Mediate Transgene Expression in Human Glioma Cells. *Mol. Ther.* **2006**, *14*, 371–381. [CrossRef] [PubMed]
183. Ogawa, N.; Terashima, T.; Oka, K.; Chan, L.; Kojima, H. Gene therapy for neuropathic pain using dorsal root ganglion–targeted helper-dependent adenoviral vectors with GAD67 expression. *PAIN Rep.* **2018**, *3*, e695. [CrossRef] [PubMed]
184. Lang, F.F.; Conrad, C.; Gomez-Manzano, C.; Yung, W.K.A.; Sawaya, R.; Weinberg, J.S.; Prabhu, S.S.; Rao, G.; Fuller, G.N.; Aldape, K.D.; et al. Phase I Study of DNX-2401 (Delta-24-RGD) Oncolytic Adenovirus: Replication and Immunotherapeutic Effects in Recurrent Malignant Glioma. *J. Clin. Oncol.* **2018**, *36*, 1419–1427. [CrossRef] [PubMed]
185. Schwarz, L.A.; Miyamichi, K.; Gao, X.J.; Beier, K.T.; Weissbourd, B.; DeLoach, K.E.; Ren, J.; Ibanes, S.; Malenka, R.C.; Kremer, E.J.; et al. Viral-genetic tracing of the input–output organization of a central noradrenaline circuit. *Nature* **2015**, *524*, 88–92. [CrossRef]

186. Ridoux, V.; Robert, J.J.; Xia, Z.; Perricaudet, M.; Mallet, J.; La Salle, G.L.G. Adenoviral vectors as functional retrograde neuronal tracers. *Brain Res.* **1994**, *648*, 171–175. [CrossRef]
187. Nair, S.G.; Strand, N.S.; Neumaier, J.F. DREADDing the lateral habenula: A review of methodological approaches for studying lateral habenula function. *Brain Res.* **2013**, *1511*, 93–101. [CrossRef]
188. Kritzinger, A.; Ferger, B.; Gillardon, F.; Stierstorfer, B.; Birk, G.; Kochanek, S.; Ciossek, T. Age-related pathology after adenoviral overexpression of the leucine-rich repeat kinase 2 in the mouse striatum. *Neurobiol. Aging* **2018**, *66*, 97–111. [CrossRef]
189. Dong, X.; Zong, S.; Witting, A.; Lindenberg, K.S.; Kochanek, S.; Huang, B. Adenovirus vector-based in vitro neuronal cell model for Huntington's disease with human disease-like differential aggregation and degeneration. *J. Gene Med.* **2012**, *14*, 468–481. [CrossRef]
190. Wang, D.D.; Bordey, A. The astrocyte odyssey. *Prog. Neurobiol.* **2008**, *86*, 342–367. [CrossRef]
191. Verhaart, I.E.C.; Aartsma-Rus, A. Therapeutic developments for Duchenne muscular dystrophy. *Nat. Rev. Neurol.* **2019**, *15*, 373–386. [CrossRef]
192. Kawano, R.; Ishizaki, M.; Maeda, Y.; Uchida, Y.; Kimura, E.; Uchino, M. Transduction of Full-length Dystrophin to Multiple Skeletal Muscles Improves Motor Performance and Life Span in Utrophin/Dystrophin Double Knockout Mice. *Mol. Ther.* **2008**, *16*, 825–831. [CrossRef] [PubMed]
193. Jiang, Z.; Schiedner, G.; Van Rooijen, N.; Liu, C.; Kochanek, S.; Clemens, P.R. Sustained Muscle Expression of Dystrophin from a High-Capacity Adenoviral Vector with Systemic Gene Transfer of T Cell Costimulatory Blockade. *Mol. Ther.* **2004**, *10*, 688–696. [CrossRef] [PubMed]
194. Ishizaki, M.; Maeda, Y.; Kawano, R.; Suga, T.; Uchida, Y.; Uchino, K.; Yamashita, S.; Kimura, E.; Uchino, M. Rescue from Respiratory Dysfunction by Transduction of Full-length Dystrophin to Diaphragm via the Peritoneal Cavity in Utrophin/Dystrophin Double Knockout Mice. *Mol. Ther.* **2011**, *19*, 1230–1235. [CrossRef]
195. Gonçalves, M.A.F.V.; Holkers, M.; Cudré-Mauroux, C.; Van Nierop, G.P.; Knaän-Shanzer, S.; Van der Velde, I.; Valerio, D.; De Vries, A.A.F. Transduction of myogenic cells by retargeted dual high-capacity hybrid viral vectors: Robust dystrophin synthesis in duchenne muscular dystrophy muscle cells. *Mol. Ther.* **2006**, *13*, 976–986. [CrossRef] [PubMed]
196. Guse, K.; Suzuki, M.; Sule, G.; Bertin, T.K.; Tyynismaa, H.; Ahola-Erkkilä, S.; Palmer, D.; Suomalainen, A.; Ng, P.; Cerullo, V.; et al. Capsid-Modified Adenoviral Vectors for Improved Muscle-Directed Gene Therapy. *Hum. Gene Ther.* **2012**, *23*, 1065–1070. [CrossRef] [PubMed]
197. Blum, S.; Shapir, N.; Miari, R.; Lerner, B.; Koren, B.; Doenyas-Barak, K.; Efrati, S.; Pergola, P.E.; Schwartz, D.; Chernin, G.; et al. TARGT Gene Therapy Platform for Correction of Anemia in End-Stage Renal Disease. *N. Engl. J. Med.* **2017**, *376*, 189–191. [CrossRef] [PubMed]
198. Shapir, N.; Miari, R.; Blum, S.; Schwartz, D.; Chernin, G.; Neil, G.A.; Afik, D.; Panet, A. Preclinical and Preliminary Clinical Evaluation of Genetically Transduced Dermal Tissue Implants for the Sustained Secretion of Erythropoietin and Interferon α. *Hum. Gene Ther. Clin. Dev.* **2015**, *26*, 216–227. [CrossRef]
199. Zafir-Lavie, I.; Sherbo, S.; Goltsman, H.; Badinter, F.; Yeini, E.; Ofek, P.; Miari, R.; Tal, O.; Liran, A.; Shatil, T.; et al. Successful intracranial delivery of trastuzumab by gene-therapy for treatment of HER2-positive breast cancer brain metastases. *J. Control. Release* **2018**, *291*, 80–89. [CrossRef]
200. Gil, J.S.; Gallaher, S.D.; Berk, A.J. Delivery of an EBV episome by a self-circularizing helper-dependent adenovirus: Long-term transgene expression in immunocompetent mice. *Gene Ther.* **2010**, *17*, 1288–1293. [CrossRef]
201. Boehme, P.; Zhang, W.; Solanki, M.; Ehrke-Schulz, E.; Ehrhardt, A. A High-Capacity Adenoviral Hybrid Vector System Utilizing the Hyperactive Sleeping Beauty Transposase SB100X for Enhanced Integration. *Mol. Ther. Nucleic Acids* **2016**, *5*, e337. [CrossRef]
202. Saydaminova, K.; Ye, X.; Wang, H.; Richter, M.; Ho, M.; Chen, H.; Xu, N.; Kim, J.; Papapetrou, E.; Holmes, M.C.; et al. Efficient genome editing in hematopoietic stem cells with helper-dependent Ad5/35 vectors expressing site-specific endonucleases under microRNA regulation. *Mol. Ther. Methods Clin. Dev.* **2015**, *2*, 14057. [CrossRef] [PubMed]
203. Palmer, D.J.; Turner, D.L.; Ng, P. A Single "All-in-One" Helper-Dependent Adenovirus to Deliver Donor DNA and CRISPR/Cas9 for Efficient Homology-Directed Repair. *Mol. Ther. Methods Clin. Dev.* **2020**, *17*, 441–447. [CrossRef] [PubMed]

204. Ran, F.A.; Hsu, P.D.; Lin, C.-Y.; Gootenberg, J.S.; Konermann, S.; Trevino, A.E.; Scott, D.A.; Inoue, A.; Matoba, S.; Zhang, Y.; et al. Double Nicking by RNA-Guided CRISPR Cas9 for Enhanced Genome Editing Specificity. *Cell* **2013**, *154*, 1380–1389. [CrossRef] [PubMed]
205. Qi, L.S.; Larson, M.H.; Gilbert, L.A.; Doudna, J.A.; Weissman, J.S.; Arkin, A.P.; Lim, W.A. Repurposing CRISPR as an RNA-Guided Platform for Sequence-Specific Control of Gene Expression. *Cell* **2013**, *152*, 1173–1183. [CrossRef] [PubMed]
206. Colasante, G.; Lignani, G.; Brusco, S.; Di Berardino, C.; Carpenter, J.; Giannelli, S.; Valassina, N.; Bido, S.; Ricci, R.; Castoldi, V.; et al. dCas9-Based Scn1a Gene Activation Restores Inhibitory Interneuron Excitability and Attenuates Seizures in Dravet Syndrome Mice. *Mol. Ther.* **2020**, *28*, 235–253. [CrossRef]
207. Song, C.; Jiang, T.; Richter, M.; Rhym, L.H.; Koblan, L.W.; Zafra, M.P.; Schatoff, E.M.; Doman, J.L.; Cao, Y.; Dow, L.E.; et al. Adenine base editing in an adult mouse model of tyrosinaemia. *Nat. Biomed. Eng.* **2020**, *4*, 125–130. [CrossRef]
208. Lim, C.K.W.; Gapinske, M.; Brooks, A.K.; Woods, W.S.; Powell, J.E.; Winter, J.; Perez-Pinera, P.; Gaj, T. Treatment of a Mouse Model of ALS by in Vivo Base Editing. *Mol. Ther.* **2020**, *28*, 1–13. [CrossRef]
209. Charlesworth, C.T.; Deshpande, P.S.; Dever, D.P.; Camarena, J.; Lemgart, V.T.; Cromer, M.K.; Vakulskas, C.A.; Collingwood, M.A.; Zhang, L.; Bode, N.M.; et al. Identification of preexisting adaptive immunity to Cas9 proteins in humans. *Nat. Med.* **2019**, *25*, 249–254. [CrossRef]
210. Xia, E.; Zhang, Y.; Cao, H.; Li, J.; Duan, R.; Hu, J. TALEN-Mediated Gene Targeting for Cystic Fibrosis-Gene Therapy. *Genes (Basel)* **2019**, *10*, 39. [CrossRef]
211. Xia, E.; Duan, R.; Shi, F.; Seigel, K.E.; Grasemann, H.; Hu, J. Overcoming the Undesirable CRISPR-Cas9 Expression in Gene Correction. *Mol. Ther. Nucleic Acids* **2018**, *13*, 699–709. [CrossRef]
212. Holkers, M.; Maggio, I.; Henriques, S.F.D.; Janssen, J.M.; Cathomen, T.; Gonçalves, M.A. Adenoviral vector DNA for accurate genome editing with engineered nucleases. *Nat. Methods* **2014**, *11*, 1051–1057. [CrossRef] [PubMed]
213. Palmer, D.J.; Grove, N.C.; Ing, J.; Crane, A.M.; Venken, K.; Davis, B.R.; Ng, P. Homology Requirements for Efficient, Footprintless Gene Editing at the CFTR Locus in Human iPSCs with Helper-dependent Adenoviral Vectors. *Mol. Ther. Nucleic Acids* **2016**, *5*, e372. [CrossRef]
214. Ohbayashi, F.; Balamotis, M.A.; Kishimoto, A.; Aizawa, E.; Diaz, A.; Hasty, P.; Graham, F.L.; Caskey, C.T.; Mitani, K. Correction of chromosomal mutation and random integration in embryonic stem cells with helper-dependent adenoviral vectors. *Proc. Natl. Acad. Sci. USA* **2005**, *102*, 13628–13633. [CrossRef]
215. Barzel, A.; Paulk, N.K.; Shi, Y.; Huang, Y.; Chu, K.; Zhang, F.; Valdmanis, P.N.; Spector, L.P.; Porteus, M.H.; Gaensler, K.M.; et al. Promoterless gene targeting without nucleases ameliorates haemophilia B in mice. *Nature* **2015**, *517*, 360–364. [CrossRef]
216. Cao, H.; Machuca, T.N.; Yeung, J.C.; Wu, J.; Du, K.; Duan, C.; Hashimoto, K.; Linacre, V.; Coates, A.L.; Leung, K.; et al. Efficient Gene Delivery to Pig Airway Epithelia and Submucosal Glands Using Helper-Dependent Adenoviral Vectors. *Mol. Ther. Nucleic Acids* **2013**, *2*, e127. [CrossRef] [PubMed]
217. Cao, H.; Ouyang, H.; Grasemann, H.; Bartlett, C.; Du, K.; Duan, R.; Shi, F.; Estrada, M.; Seigel, K.E.; Coates, A.L.; et al. Transducing Airway Basal Cells with a Helper-Dependent Adenoviral Vector for Lung Gene Therapy. *Hum. Gene Ther.* **2018**, *29*, 643–652. [CrossRef] [PubMed]
218. Palmer, D.J.; Turner, D.L.; Ng, P. Bi-allelic Homology-Directed Repair with Helper-Dependent Adenoviruses. *Mol. Ther. Methods Clin. Dev.* **2019**, *15*, 285–293. [CrossRef] [PubMed]
219. Li, C.; Lieber, A. Adenovirus vectors in hematopoietic stem cell genome editing. *FEBS Lett.* **2019**, *593*, 3623–3648. [CrossRef]
220. Li, C.; Psatha, N.; Gil, S.; Wang, H.; Papayannopoulou, T.; Lieber, A. HDAd5/35++ Adenovirus Vector Expressing Anti-CRISPR Peptides Decreases CRISPR/Cas9 Toxicity in Human Hematopoietic Stem Cells. *Mol. Ther. Methods Clin. Dev.* **2018**, *9*, 390–401. [CrossRef]
221. Li, C.; Psatha, N.; Sova, P.; Gil, S.; Wang, H.; Kim, J.; Kulkarni, C.; Valensisi, C.; Hawkins, R.D.; Stamatoyannopoulos, G.; et al. Reactivation of γ-globin in adult β-YAC mice after ex vivo and in vivo hematopoietic stem cell genome editing. *Blood* **2018**, *131*, 2915–2928. [CrossRef]
222. Li, C.; Mishra, A.S.; Gil, S.; Wang, M.; Georgakopoulou, A.; Papayannopoulou, T.; Hawkins, R.D.; Lieber, A. Targeted Integration and High-Level Transgene Expression in AAVS1 Transgenic Mice after in Vivo HSC Transduction with HDAd5/35++ Vectors. *Mol. Ther.* **2019**, *27*, 2195–2212. [CrossRef]

223. Wang, H.; Liu, Z.; Li, C.; Gil, S.; Papayannopoulou, T.; Doering, C.B.; Lieber, A. High-level protein production in erythroid cells derived from in vivo transduced hematopoietic stem cells. *Blood Adv.* **2019**, *3*, 2883–2894. [CrossRef]
224. Sessa, M.; Lorioli, L.; Fumagalli, F.; Acquati, S.; Redaelli, D.; Baldoli, C.; Canale, S.; Lopez, I.D.; Morena, F.; Calabria, A.; et al. Lentiviral haemopoietic stem-cell gene therapy in early-onset metachromatic leukodystrophy: An ad-hoc analysis of a non-randomised, open-label, phase 1/2 trial. *Lancet* **2016**, *388*, 476–487. [CrossRef]
225. Goncalves, M.A.F.V.; Van Nierop, G.P.; Tijssen, M.R.; Lefesvre, P.; Knaan-Shanzer, S.; Van der Velde, I.; Van Bekkum, D.W.; Valerio, D.; De Vries, A.A.F. Transfer of the Full-Length Dystrophin-Coding Sequence into Muscle Cells by a Dual High-Capacity Hybrid Viral Vector with Site-Specific Integration Ability. *J. Virol.* **2005**, *79*, 3146–3162. [CrossRef]
226. Maggio, I.; Stefanucci, L.; Janssen, J.M.; Liu, J.; Chen, X.; Mouly, V.; Gonçalves, M.A.F.V. Selection-free gene repair after adenoviral vector transduction of designer nucleases: Rescue of dystrophin synthesis in DMD muscle cell populations. *Nucleic Acids Res.* **2016**, *44*, 1449–1470. [CrossRef]
227. Muhammad, A.K.M.G.; Puntel, M.; Candolfi, M.; Salem, A.; Yagiz, K.; Farrokhi, C.; Kroeger, K.M.; Xiong, W.; Curtin, J.F.; Liu, C.; et al. Study of the Efficacy, Biodistribution, and Safety Profile of Therapeutic Gutless Adenovirus Vectors as a Prelude to a Phase I Clinical Trial for Glioblastoma. *Clin. Pharmacol. Ther.* **2010**, *88*, 204–213. [CrossRef]
228. Morsy, M.A.; Harvey, D.M.; Caskey, C.T. Helper-dependent adenoviral vectors as gene delivery vehicles. *Gene Ther. Mol. Biol.* **1999**, *3*, 223–232.
229. Gonzalez-Aparicio, M.; Alzuguren, P.; Mauleon, I.; Medina-Echeverz, J.; Hervas-Stubbs, S.; Mancheno, U.; Berraondo, P.; Crettaz, J.; Gonzalez-Aseguinolaza, G.; Prieto, J.; et al. Oxaliplatin in combination with liver-specific expression of interleukin 12 reduces the immunosuppressive microenvironment of tumours and eradicates metastatic colorectal cancer in mice. *Gut* **2011**, *60*, 341–349. [CrossRef] [PubMed]
230. Poutou, J.; Bunuales, M.; Gonzalez-Aparicio, M.; Garcia-Aragoncillo, E.; Quetglas, J.I.; Casado, R.; Bravo-Perez, C.; Alzuguren, P.; Hernandez-Alcoceba, R. Safety and antitumor effect of oncolytic and helper-dependent adenoviruses expressing interleukin-12 variants in a hamster pancreatic cancer model. *Gene Ther.* **2015**, *22*, 696–706. [CrossRef] [PubMed]
231. Poutou, J.; Bunuales, M.; Gonzalez-Aparicio, M.; German, B.; Zugasti, I.; Hernandez-Alcoceba, R. Adaptation of vectors and drug-inducible systems for controlled expression of transgenes in the tumor microenvironment. *J. Control. Release* **2017**, *268*, 247–258. [CrossRef] [PubMed]
232. Tuettenberg, A.; Jonuleit, H.; Tüting, T.; Brück, J.; Biermann, V.; Kochanek, S.; Knop, J.; Enk, A.H. Early Adenoviral Gene Expression Mediates Immunosuppression by Transduced Dendritic Cell (DC): Implications for Immunotherapy Using Genetically Modified DC. *J. Immunol.* **2004**, *172*, 1524–1530. [CrossRef] [PubMed]
233. Kron, M.W.; Engler, T.; Schmidt, E.; Schirmbeck, R.; Kochanek, S.; Kreppel, F. High-capacity adenoviral vectors circumvent the limitations of ΔE1 and ΔE1/ΔE3 adenovirus vectors to induce multispecific transgene product-directed CD8 T-cell responses. *J. Gene Med.* **2011**, *13*, 648–657. [CrossRef] [PubMed]
234. Zong, S.; Kron, M.W.; Epp, C.; Engler, T.; Bujard, H.; Kochanek, S.; Kreppel, F. ΔE1 and high-capacity adenoviral vectors expressing full-length codon-optimized merozoite surface protein 1 for vaccination against *Plasmodium falciparum*. *J. Gene Med.* **2011**, *13*, 670–679. [CrossRef]
235. Harui, A.; Roth, M.D.; Kiertscher, S.M.; Mitani, K.; Basak, S.K. Vaccination with helper-dependent adenovirus enhances the generation of transgene-specific CTL. *Gene Ther.* **2004**, *11*, 1617–1626. [CrossRef]
236. Gray, G.; Buchbinder, S.; Duerr, A. Overview of STEP and Phambili trial results: Two phase IIb test-of-concept studies investigating the efficacy of MRK adenovirus type 5 gag/pol/nef subtype B HIV vaccine. *Curr. Opin. HIV AIDS* **2010**, *5*, 357–361. [CrossRef]
237. Del Moral-Sánchez, I.; Sliepen, K. Strategies for inducing effective neutralizing antibody responses against HIV-1. *Expert Rev. Vaccines* **2019**, *18*, 1127–1143. [CrossRef]
238. Fuchs, J.D. Safety and Immunogenicity of a Recombinant Adenovirus Serotype 35-Vectored HIV-1 Vaccine in Adenovirus Serotype 5 Seronegative and Seropositive Individuals. *J. AIDS Clin. Res.* **2015**, *6*, 461. [CrossRef]
239. Baden, L.R.; Karita, E.; Mutua, G.; Bekker, L.-G.; Gray, G.; Page-Shipp, L.; Walsh, S.R.; Nyombayire, J.; Anzala, O.; Roux, S.; et al. Assessment of the Safety and Immunogenicity of 2 Novel Vaccine Platforms for HIV-1 Prevention: A Randomized Trial. *Ann. Intern. Med.* **2016**, *164*, 313–322. [CrossRef]

240. Gurwith, M.; Lock, M.; Taylor, E.M.; Ishioka, G.; Alexander, J.; Mayall, T.; Ervin, J.E.; Greenberg, R.N.; Strout, C.; Treanor, J.J.; et al. Safety and immunogenicity of an oral, replicating adenovirus serotype 4 vector vaccine for H5N1 influenza: A randomised, double-blind, placebo-controlled, phase 1 study. *Lancet Infect. Dis.* **2013**, *13*, 238–250. [CrossRef]
241. Khurana, S.; Coyle, E.M.; Manischewitz, J.; King, L.R.; Ishioka, G.; Alexander, J.; Smith, J.; Gurwith, M.; Golding, H. Oral Priming with Replicating Adenovirus Serotype 4 Followed by Subunit H5N1 Vaccine Boost Promotes Antibody Affinity Maturation and Expands H5N1 Cross-Clade Neutralization. *PLoS ONE* **2015**, *10*, e0115476. [CrossRef]
242. Ledgerwood, J.E.; DeZure, A.D.; Stanley, D.A.; Coates, E.E.; Novik, L.; Enama, M.E.; Berkowitz, N.M.; Hu, Z.; Joshi, G.; Ploquin, A.; et al. Chimpanzee Adenovirus Vector Ebola Vaccine. *N. Engl. J. Med.* **2017**, *376*, 928–938. [CrossRef] [PubMed]
243. Yang, X.; Wang, X.; Song, Y.; Zhou, P.; Li, D.; Zhang, C.; Jin, X.; Huang, Z.; Zhou, D. Chimpanzee adenoviral vector prime-boost regimen elicits potent immune responses against Ebola virus in mice and rhesus macaques. *Emerg. Microbes Infect.* **2019**, *8*, 1086–1097. [CrossRef] [PubMed]
244. Jia, W.; Channappanavar, R.; Zhang, C.; Li, M.; Zhou, H.; Zhang, S.; Zhou, P.; Xu, J.; Shan, S.; Shi, X.; et al. Single intranasal immunization with chimpanzee adenovirus-based vaccine induces sustained and protective immunity against MERS-CoV infection. *Emerg. Microbes Infect.* **2019**, *8*, 760–772. [CrossRef] [PubMed]
245. Folegatti, P.M.; Bittaye, M.; Flaxman, A.; Lopez, F.R.; Bellamy, D.; Kupke, A.; Mair, C.; Makinson, R.; Sheridan, J.; Rohde, C.; et al. Safety and immunogenicity of a candidate Middle East respiratory syndrome coronavirus viral-vectored vaccine: A dose-escalation, open-label, non-randomised, uncontrolled, phase 1 trial. *Lancet Infect. Dis.* **2020**, *3099*, 1–11. [CrossRef]
246. Aurisicchio, L.; De Tomassi, A.; La Monica, N.; Ciliberto, G.; Traboni, C.; Palombo, F. Regulated and Liver-Specific Tamarin Alpha Interferon Gene Delivery by a Helper-Dependent Adenoviral Vector. *J. Virol.* **2005**, *79*, 6772–6780. [CrossRef]
247. Crettaz, J.; Otano, I.; Ochoa, L.; Benito, A.; Paneda, A.; Aurrekoetxea, I.; Berraondo, P.; Rodriguez-Madoz, J.R.; Astudillo, A.; Kreppel, F.; et al. Treatment of Chronic Viral Hepatitis in Woodchucks by Prolonged Intrahepatic Expression of Interleukin-12. *J. Virol.* **2009**, *83*, 2663–2674. [CrossRef]
248. Schiwon, M.; Ehrke-Schulz, E.; Oswald, A.; Bergmann, T.; Michler, T.; Protzer, U.; Ehrhardt, A. One-Vector System for Multiplexed CRISPR/Cas9 against Hepatitis B Virus cccDNA Utilizing High-Capacity Adenoviral Vectors. *Mol. Ther. Nucleic Acids* **2018**, *12*, 242–253. [CrossRef]